UNIVERSITÀ DEGLI STUDI DI MILANO

Scuola di Dottorato in Fisica, Astrofisica e Fisica Applicata
Dipartimento di Fisica

Corso di Dottorato in Fisica, Astrofisica e Fisica Applicata
Ciclo XXVI

Observational tests on the dynamics of Globular Clusters

Settore Scientifico Disciplinare FIS/05

Supervisore: Professor Giuseppe BERTIN

Coordinatore: Professor Marco BERSANELLI

Tesi di Dottorato di:
Alice ZOCCHI

Anno Accademico 2012-2013

Commission of the final examination:

External Referee:
Professor Enrico Vesperini, Indiana University Bloomington, Department of Astronomy

External Member:
Doctor Barbara Lanzoni, Università degli Studi di Bologna, Dipartimento di Fisica e Astronomia

Internal Member (Ph.D. Supervisor):
Professor Giuseppe Bertin, Università degli Studi di Milano, Dipartimento di Fisica

Final examination:

Saturday, April 12, 2014

Università degli Studi di Milano, Dipartimento di Fisica, Milano, Italy

Cover illustration:

Subaru Telescope image of the globular cluster NGC 2419
Credit: Subaru Telescope, National Astronomical Observatory of Japan

Internal illustrations:

Very Large Telescope image (edited) of the globular cluster NGC 6254 (M10)
Credit: European Southern Observatory (see Chapter 8)

Design:

Anna Lisa Varri, Paola Zocchi

MIUR subjects:

FIS/05 - Astronomia e Astrofisica

PACS:

98.10.+z	Stellar dynamics and kinematics
98.20.-d	Stellar clusters and associations
98.20.Gm	Globular clusters in the Milky Way

Contents

List of Figures

List of Tables

Introduction

General motivation and objectives

Galactic globular clusters are nearly gas-free, self-gravitating stellar systems characterized by an apparently simple geometry, with finite size probably determined by tidal truncation. These unique properties make them excellent laboratories for studies of stellar dynamics, and ideal targets for N-body simulations. For a long time, they have been treated as spherically symmetric, nonrotating, isotropic systems. The spherical King (1966) models, constructed to match this physical picture, are usually considered as the correct zeroth-order dynamical reference model, and are sometimes successful in representing the observed characteristics of these systems.

In reality, this simple physical picture suffers from a number of limitations, which become more evident now that much improved observations have become available. In particular, deviations from sphericity have been observed (see Geyer et al. 1983; White & Shawl 1987; Chen & Chen 2010), and should be explained, even when assuming the simplest idealized stellar dynamical scenario, in which the effects of discreteness and binaries are ignored. Three physical ingredients are expected to affect the observed shapes of stellar systems: internal rotation, external tides, and pressure anisotropy. A proper identification of the physical ingredients that shape the internal dynamics of globular clusters will lead to draw conclusions on their origin, and on the origin of their host systems. In particular, a detailed characterization of the role played by internal rotation and pressure anisotropy in present-day globular clusters would be a crucial element to discriminate among different formation scenarios for this class of stellar systems; indeed, the main goal of this Thesis is to clarify the role of these two important dynamical factors. We will not address here the effect of tides because they are expected to act mainly in the outer parts of these stellar systems, in regions outside the focus of the present investigation, and often beyond the range of the available data.

For the purpose of giving a detailed and more realistic description of globular clusters, dynamical studies such as those that will be described in this Thesis are an important counterpart to the stellar populations analyses often carried out for these systems. Dynamical studies are meaningful only when both photometric and kinematic data are taken into account, but unfortunately for globular clusters the application (and thus the test) of dynamical models is frequently carried out only in relation to the available photometric profiles (see Trager et al. 1995 and McLaughlin & van der Marel 2005), without the corresponding tests on the associated kinematical profiles, in contrast to what is routinely done in studies of early-type galaxies. We recall that spherical King (1966) models

have long been considered to provide an adequate description of the dynamics of globular clusters, only on the basis of their ability in reproducing the observed surface brightness profiles; then it was basically taken for granted that the kinematical properties of globular clusters should conform to the King models, even if, in practice, direct tests of this assumption were not available. On the galactic side, from the study of ellipticals it has been learned that structurally different models (as diagnosed by their kinematics or characterized by their virial coefficients) may have remarkably similar photometric profiles (see for example Bertin 2000). Therefore, it is important to take into account the kinematical measurements, because they can give stringent constraints on alternative dynamical scenarios, and determine the principal dynamical ingredients that can be considered responsible for the observed properties of globular clusters. We will address this issue, point out the need for more kinematic data, and discuss what specific data are currently missing and should be acquired for decisive answers.

Thesis overview

Main results

The present Thesis is devoted to the study of the internal dynamics of globular clusters, by means of models that take into account fundamental physical ingredients such as internal rotation and anisotropy in velocity space. The main results of the Thesis are summarized below.

Pressure anisotropy as signature of partial relaxation in Galactic globular clusters: We performed a combined photometric and kinematic analysis of a sample of 13 Galactic globular clusters under different relaxation conditions, based on their core relaxation time, by means of two well-known families of spherical stellar dynamical models. Systems characterized by shorter relaxation time scales are expected to be better described by isotropic King (1966) models, while less relaxed systems might be interpreted by means of non-truncated, radially-biased anisotropic $f^{(\nu)}$ models, originally designed to represent stellar systems produced by a violent relaxation formation process (Bertin & Trenti 2003). The comparison between dynamical models and observations is performed by fitting simultaneously surface brightness and velocity dispersion profiles. We found that King models usually offer a good representation of the observed photometric profiles, but often lead to less satisfactory fits to the kinematic profiles, independently of the relaxation condition of the systems. For some less relaxed clusters, $f^{(\nu)}$ models indeed provide a good description of both observed profiles. The analysis confirms that, to answer some important dynamical questions that bear on the formation and evolution of globular clusters, it would be highly desirable to acquire larger numbers of accurate kinematic data-points, well distributed over the cluster field.

Analysis of different density profiles for the globular cluster NGC 6341: We presented new number density and surface brightness profiles for the globular cluster NGC 6341 (M92). We performed detailed fits of spherical isotropic King (1966) and spherical nonrotating Wilson (1975) models to the observed profiles, and we found that the best-fit models underestimate the number density inside the core radius. Wilson models better represent the observations, in particular in the outermost cluster regions: the good global agreement of these models with the observations suggests that there is no need to introduce an extra-tidal halo to explain the radial distribution of stars at large radial distances because the truncation is softer than that assumed

by King models. Interestingly, we found that the best-fit models for the number density and the surface brightness profiles are different, even though they are based on the same observations. Additional tests support the evidence that this fact reflects the difference in the radial distribution of the stellar tracers that determine the observed profiles (main-sequence stars for the number density, bright evolved stars for the surface brightness).

Internal rotation: We carried out a dynamical analysis of the photometry and three-dimensional kinematics of 47 Tuc (NGC 104), M15 (NGC 7078), and ω Cen (NGC 5139), by means of a recently introduced family of self-consistent axisymmetric rotating models Varri & Bertin (2012). The three clusters show evidence of differential rotation and deviations from sphericity. The well-relaxed cluster 47 Tuc is interpreted very well by the rotating model, which is found to explain the observed morphology. For M15, we provide a global model in good agreement with the data, including the central behavior of the rotation profile and the shape of the ellipticity profile. For the partially relaxed cluster ω Cen, the selected model reproduces the complex three-dimensional kinematics, in particular the observed anisotropy profile; the discrepancy found for the steep central gradient in the observed line-of-sight velocity dispersion profile and for the ellipticity profile is ascribed to the condition of only partial relaxation of this cluster and the interplay between rotation and radial anisotropy.

Observational proposals: From the results of the investigations summarized above, it is particularly evident that kinematical data are crucial to provide an adequate description of globular clusters. We therefore submitted two observational proposals to the European Southern Observatory (ESO), to measure radial velocities of single stars in four Galactic globular clusters. With the first, we proposed to use the spectrograph VIMOS mounted at the Very Large Telescope (VLT) to carry out a pilot project, by measuring velocities for about 600 stars in the globular cluster NGC 6254 (M10). This program provided us with data, that are currently under analysis. With the second project, we proposed to use the multi-object spectrograph FLAMES/GIRAFFE mounted at the VLT to obtain high resolution spectra for more than 300 stars in each of three flattened Galactic globular clusters, NGC 5897, NGC 6273, and NGC 6541. The data from this program will become available soon, in the next months.

Analysis of the output of numerical simulations: We considered the results of two numerical simulations, and we treated them as we would treat real observational data: we calculated from the simulated samples of stars the profiles that are obtained from standard photometric and kinematic observations, and we analyzed them by means of both isotropic and anisotropic dynamical models, with the aim of obtaining an estimate of the total mass and of the half-mass radius of the systems. The first simulation describes a cluster of equal-mass stars in a tidal field, the second describes an isolated cluster made of stars of different masses. In the first case, we analyzed the effect of considering only a subset of the total number of stars to study its dynamics; we found that, as expected, the estimated value of the mass of the cluster is smaller than the one obtained when all the stars are considered, whereas the value of the half-mass radius is more stable. In the second case, we analyzed the number, the mass, and the luminosity profiles, and we found that the best- fit model obtained for the mass density is the one that best reproduces the velocity dispersion profile. We then explored the effects introduced by the observational limitations on the density profiles, by excluding from our analysis the faint stars that would not be observable with the available instruments and telescopes. We obtained a description of the sim-

ulated clusters that reflects the one found in the case of the globular cluster NGC 6341. We also compared the results obtained when the velocity dispersion profile is calculated with all the stars in the clusters with those obtained when only the red giant branch stars are considered, as generally done in real data-sets: in the second case, we obtained smaller values of the mass of the systems, and larger errors on the parameters.

Line profiles: We made a test on the possibility to use the global line-of-sight velocity distribution to study the dynamics of globular clusters. We considered spherical isotropic King (1966) models, spherical nonrotating Wilson (1975) models, and axisymmetric differentially rotating models (Varri & Bertin 2012). Within each of these three families of models, we identified the best-fit models to three Galactic clusters (47 Tuc, M15, and ω Cen), and we generated from each of their distribution functions a set of discrete particle realizations. We then calculated for each of the generated samples the line-of-sight velocity distribution, and we convolved it with a Gaussian function, to simulate the measurements error. By comparing the line profiles predicted for the different models for each globular cluster, we found that only very accurate observations could discriminate between the different predicted profiles.

Organizational note

The present Thesis consists of a total of ten Chapters. The introductory Chapters 1, 2, and 3 outline the basic properties of Galactic globular clusters and the models and observations that can be used to study their dynamics. The remaining Chapters are divided into two Parts. Part I comprises Chapters 4 to 6. It presents dynamical studies carried out on Galactic clusters by means of dynamical models that take into account different dynamical factors. Part II, from Chapter 7 to Chapter 10, is dedicated to recent efforts we made in order to provide a more realistic description of the dynamics of globular clusters: we proposed to carry out observations to increase the number of clusters for which kinematic measurements are available, we studied the effects of observational limits by analyzing dedicated simulations, and we explored the possibility of using a new diagnostic tool to study the dynamics of globular clusters. Part I is basically made of refereed publications already appeared in scientific journals; co-authors of the relevant articles are mentioned below. Some variations have been made in the presentation of previously published results, to maintain consistency of style and content structure through the manuscript.

Chapter 1: Basic properties of globular clusters: We introduce some basic structural and dynamical properties of the Galactic globular clusters.

Chapter 2: Dynamical models: We describe the modeling techniques that can be used to describe the dynamics of a stellar system.

Chapter 3: Observations and model testing: We give an overview of the available observational data and of the methods that can be used to interpret them in terms of dynamical models.

Chapter 4: Globular clusters in different relaxation conditions: We present the results of an observational investigation of pressure anisotropy as signature of partial relaxation for a sample of Galactic globular clusters. The main part of this work has been carried out in collaboration with G. Bertin and A. L. Varri and has been published as an article in *Astronomy & Astrophysics* (Zocchi et al. 2012).

Chapter 5: A signature of mass segregation in the globular cluster NGC 6341 (M92): We describe the density profiles obtained from observations of the globular cluster NGC 6341 by means of spherical isotropic models. This work has been carried out in collaboration with A. Di Cecco, A. L. Varri, M. Monelli, G. Bertin, G. Bono, P. B. Stetson, M. Nonino, R. Buonanno, I. Ferraro, G. Iannicola, A. Kunder, and A. R. Walker, and has been published as an article in *Astronomical Journal* (Di Cecco et al. 2013).

Chapter 6: Rotating globular clusters: We explore the role of internal rotation in determining the observed morphology of three Galactic globular clusters. This work has been carried out in collaboration with P. Bianchini, A. L. Varri, and G. Bertin, and has been published as an article in *Astrophysical Journal* (Bianchini et al. 2013).

Chapter 7: Measuring accurate radial velocities with FLAMES: We describe the observations we will obtain with FLAMES, and we make predictions on the expected velocity dispersion profiles, by means of spherical isotropic and anisotropic models. This work is carried out in collaboration with N. Lützgendorf, M. Hilker, G. Bono, G. Bertin, H. Baumgardt, P. Bianchini, A. Di Cecco, M. Fabrizio, A. Kunder, M. Nonino, N. Neumayer, P. B. Stetson, and A. L. Varri.

Chapter 8: A pilot project with VIMOS: We describe the observations obtained with VIMOS, and we analyze the data by means of different families of dynamical models. This work has been carried out in collaboration with N. Lützgendorf, M. Hilker, G. Bono, G. Bertin, P. Bianchini, A. Di Cecco, M. Fabrizio, A. Kunder, M. Nonino, N. Neumayer, P. B. Stetson, and A. L. Varri.

Chapter 9: A study of simulated observations: We analyze the output of numerical simulations by mimicking the observations of real globular clusters. We explore the effects introduced by observational limitations on the description of the systems.

Chapter 10: Global line profiles: We analyze the possibility to use the global line-of-sight velocity distribution as a diagnostic tool to discriminate between different dynamical models for globular clusters.

Appendix A: Definition of some dynamical models: We present some details of the dynamical models used throughout the Thesis.

Appendix B: Radial velocity data-sets for Galactic globular clusters: We provide a list of all the line-of-sight velocities data-sets currently available for Galactic globular clusters.

CHAPTER 1

Basic properties of globular clusters

Galactic globular clusters are gas-free, self-gravitating stellar systems, with masses in the range between 10^4 and 10^6 $M_\odot$. They are among the first recognizable stellar structures that were born on sub-galactic scales and their typical age is comparable to the age of the Universe.

There are almost 160 known globular clusters in the Milky Way, which can be divided into two sub-systems, associated with the disk and with the halo, respectively (Ashman & Zepf 2008). These sub-systems are mainly determined according to the distance of globular clusters from the Galactic center, but the classification is also based on a number of other properties, such as the metallicity or the morphology of the horizontal branch in the color-magnitude diagram. The majority of clusters are located at a distance $d_{\rm GC} < 15$ kpc from the Galactic center, and only about 15 of them are outside a sphere of radius 30 kpc. The mean distance of clusters from the Sun is $d_\odot \sim 15.4$ kpc; this is an important variable to take into account, because it determines the amount of systems for which detailed observations are possible.

For the astronomical community, this class of stellar systems has been valuable in many ways. As a frequently observed prominent component of many galaxies, globular clusters are useful tools to shed lights on the formation and evolution of their host systems. As individual objects, they provide insights into the study of stellar evolution, and they allow us to study exotic stellar populations. Moreover, the study of their internal dynamics can provide an estimate of the relevant mass-to-light ratio, thus excluding or requiring the presence of significant amounts of dark matter in these systems. This is particularly important because at the typical mass range of globular clusters a puzzling dichotomy is observed: on the one hand, the available observations suggest that globular clusters do not contain dark matter and can generally be well described by Newtonian gravity, on the other hand, the dynamics of the more spatially extended dwarf galaxies appears to be dark matter dominated.

In this Chapter, the basic properties of these systems will be outlined, and some recent discoveries will be illustrated.

1.1 Structural properties and observed morphology

Globular clusters have long been modeled as spherically symmetric systems, and their dynamics is commonly described by means of the spherical and isotropic King (1966) models (see Appendix A.1). In this framework, the structure of a globular cluster can be characterized by considering the values of some typical radii. The core radius, $R_{\rm c}$, is defined as the projected radius[1] at which the surface brightness is half its central value.

[1] In this Thesis, we indicate with R the projected (two-dimensional) radial distance from the center, and with r the intrinsic (three-dimensional) radial distance.

Quantity	Mean value
$d_\odot$	15.40 kpc
R_c	1.68 pc
R_h	3.42 pc
r_tr	27.69 pc
ε	0.08

Table 1.1: Mean values for selected properties of Galactic globular clusters (Harris 2010). In the latest version of the Harris catalog, the values of the truncation radii are not listed; we calculated them from the available values of the core radius R_c and of the concentration parameter C (see Appendix A.1), as: $r_\mathrm{tr} = R_\mathrm{c}\, 10^C$.

The half-light radius, R_h, is the radius of the disk that contains half of the total light emitted from the cluster. In one-component models with constant mass-to-light ratio, the half-mass radius R_M and the half-light radius coincide[2]. Finally, the truncation radius, r_tr, gives an estimate of the radial extent of the cluster. Mean values of these parameters for Galactic globular clusters are given in Table 1.1.

Deviations from spherical symmetry for Galactic globular clusters are observed. The flattening can be quantified by the ellipticity parameter

$$\varepsilon = 1 - \frac{b}{a}\,, \tag{1.1}$$

where a and b are the projected semi-major and semi-minor axes, respectively.

White & Shawl (1987) (hereafter indicated as WS87) measured ellipticity profiles for a sample of 100 Galactic clusters, and gave the mean of the values in each profile as a measure of the global flattening of each cluster. The ellipticities reported in the Harris (2010) catalog are those obtained from this work, with the only exception of the ellipticity of ω Cen, for which the measurement of Geyer et al. (1983) was considered. For a long time, this has been the only comprehensive collection of measurements of the ellipticity of Galactic globular clusters; recently, Chen & Chen (2010) (hereafter indicated as CC10) used 2MASS (Two Micron All Sky Survey) infrared observations to provide an alternative database of ellipticities, consisting of a sample of 116 clusters.

The two distributions of ellipticity values appear significantly different, as shown in Fig. 1.1. The distribution of WS87 (represented by a red solid line in the figure) has a peak near $\varepsilon \approx 0$. The distribution of ellipticity values from CC10 (gray dashed line) has a peak near $\varepsilon \approx 0.10$, with the majority of the values falling in the range [0.05, 0.25]; the maximum value of the entire sample, $\varepsilon \approx 0.45$ is 1.5 times larger than the one in the other distribution. Another difference in the two distributions is found in the orientation of the measured major axes: in the former the axes are randomly oriented, whereas in the latter, especially for the clusters in the region of the Galactic Bulge, they preferentially point toward the Galactic Center (see Fig. 1.2).

The apparent discrepancies between the two studies should be interpreted by taking into account several factors. WS87 obtained their values from an optical study, with the use of a surface photometry technique consisting of consecutive blurring of the digitized images of blue sensitive photographic plates, while CC10 values were determined with a number count technique, based on 2MASS observations in infrared bands. Because of

[2]The intrinsic (three-dimensional) half-light and half-mass radii are indicated with r_h and r_M, respectively; the values of the projected quantities are smaller than the correspondent intrinsic ones.

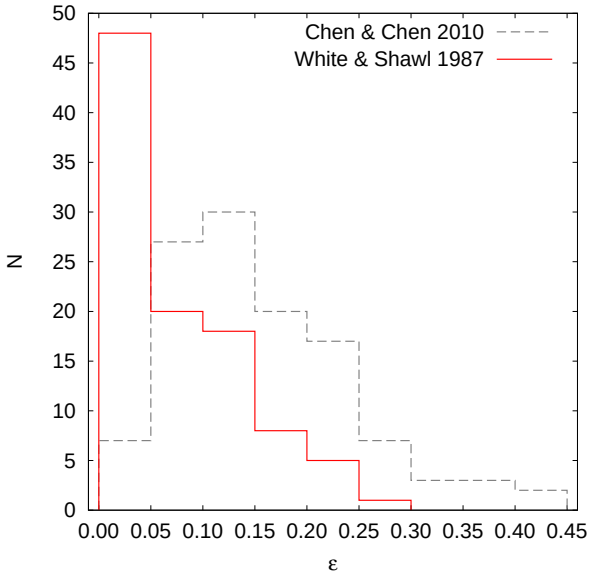

Figure 1.1: Distribution of the ellipticities of 100 Galactic globular clusters from White & Shawl (1987) and of 116 clusters from Chen & Chen (2010).

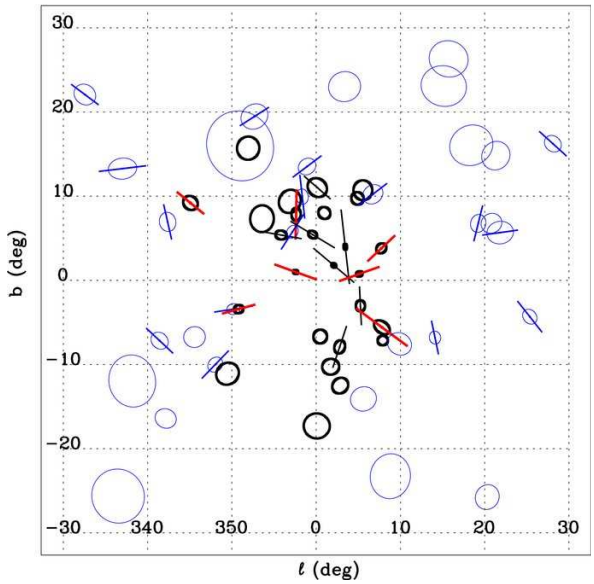

Figure 1.2: Spatial distribution of 57 Galactic globular clusters. Thick ellipses mark globular clusters with $d_{\rm GC} < 2.7$ kpc and thin ellipses mark those beyond. For clusters flatter than the average ($\varepsilon > 0.13$), a line is drawn through the corresponding ellipse depicting the axial ratio, with a longer length meaning a flatter shape. There are 14 flattened bulge clusters, marked by lines in thick ellipses. For half of these, highlighted in red, the angle between the direction of the major axis and the one of the Galactic center is less than 20°. Figure taken from Chen & Chen (2010).

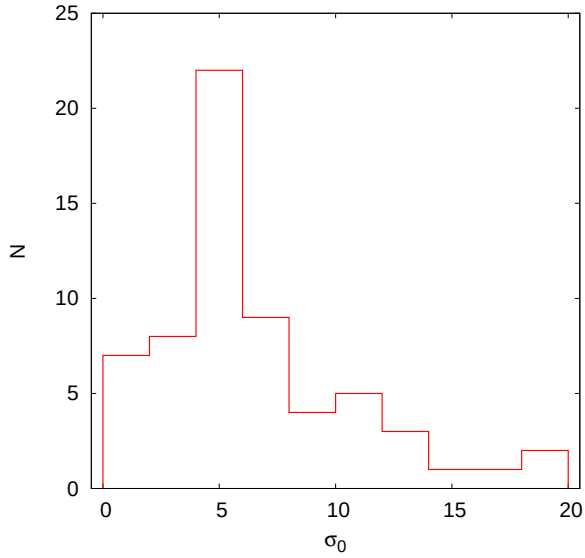

Figure 1.3: Distribution of the central velocity dispersions for Galactic globular clusters, as published in the Harris (2010) catalog.

the different resolution limits of the two approaches, the measurements made by WS87 mainly refer to the inner regions of the clusters, whereas the ones by CC10 focus on the outer parts. In both cases, the cluster flattening values do not refer to a standard isophote: WS87 axial ratios are derived from the averaged values of the ellipticity of the isodensity contours at various distances from the center, while CC10 axial ratios are measured at the location at which a given value of the density contrast with respect to the background is reached. This limitation is crucial because there is observational evidence that the ellipticity of a cluster depends on radius (see also Geyer et al. 1983). We conclude that the two databases carry complementary information about the morphology of Galactic globular clusters.

In Sect. 3.1 we give further details on the photometric data usually used to describe the structure and morphology of Galactic globular clusters.

1.2 Kinematical properties

From the kinematical point of view, Galactic globular clusters are generally considered as pressure-supported stellar systems, characterized by isotropy in the velocity space, as expected for systems close to a thermodynamically relaxed state (see Sect. 1.3). The kinematics of these systems can be studied by means of line-of-sight (radial) velocities and proper motions (the kinematic observable quantities will be described in more detail in Sect. 3.2). Unfortunately, only for a very small sample of Galactic globular clusters there are data-sets accurate and large enough to provide a good description of their kinematics. A list of the published measurements of line-of-sight velocities for these systems is presented in Appendix B. Chapters 7 and 8 describe the observations that we proposed to the European Southern Observatory (ESO), and that constitute a first step towards the acquisition of more kinematic data for Galactic clusters.

Table 1.2: Rotation in Galactic globular clusters.

Globular Cluster	σ_0 km s^{-1}	$V_{\rm rot}$ km s^{-1}	ε	Ref.
NGC 104$^{(a,b)}$	9.6 ± 0.6	4.4 ± 0.4	0.09	(3)
NGC 288$^{(a)}$	2.7 ± 0.8	0.5 ± 0.3	...	(3)
NGC 1851	10.4 ± 0.5	1.6 ± 0.5	0.05	(1), (2)
NGC 1904	5.3 ± 0.4	0.6 ± 0.5	0.01	(1), (2)
NGC 2808	13.4 ± 1.2	3.3 ± 0.5	0.12	(1), (2)
NGC 3201$^{(a)}$	4.5 ± 0.5	1.2 ± 0.3	0.12	(8)
NGC 4590	2.4 ± 0.9	1.2 ± 0.4	0.05	(3)
NGC 5024	4.4 ± 0.9	0.0 ± 0.5	0.01	(3)
NGC 5139$^{(a,b)}$	19.0 ± 1.0	6.0 ± 1.0	0.17	(6), (7)
NGC 5904	7.5 ± 1.0	2.6 ± 0.5	0.14	(1)
NGC 6121$^{(a)}$	3.9 ± 0.7	1.8 ± 0.2	0.00	(3)
NGC 6171	4.1 ± 0.3	2.9 ± 1.0	0.02	(1), (2)
NGC 6218$^{(a)}$	4.7 ± 0.9	0.3 ± 0.2	0.04	(3)
NGC 6254$^{(a)}$	6.6 ± 0.8	0.4 ± 0.5	0.00	(1), (2)
NGC 6388	18.9 ± 0.8	3.9 ± 1.0	0.01	(1), (2)
NGC 6397	4.5 ± 0.6	0.2 ± 0.5	0.07	(1), (9)
NGC 6441	18.0 ± 0.2	12.9 ± 2.0	0.02	(1), (2)
NGC 6656$^{(a)}$	6.8 ± 0.6	1.5 ± 0.4	0.14	(3)
NGC 6715	16.4 ± 0.4	2.0 ± 0.5	0.06	(4), (5)
NGC 6752	5.7 ± 0.7	0.0 ± 0.0	0.04	(3)
NGC 6809$^{(a)}$	2.7 ± 0.5	0.5 ± 0.2	0.02	(3)
NGC 6838	2.3 ± 0.2	1.3 ± 0.5	0.00	(1), (2)
NGC 7078$^{(a,b)}$	13.5 ± 0.9	3.8 ± 0.5	0.05	(1), (2)
NGC 7099	5.0 ± 0.9	0.0 ± 0.0	0.01	(3)

Notes. Summary of the kinematical properties of selected Galactic globular clusters, as recently presented by Bellazzini et al. (2012). From left to right: cluster identification, central velocity dispersion (with associated error), rotation amplitude (with associated error), and ellipticity (from White & Shawl 1987). The references in the last column indicate the source of the velocity dispersions and of the rotation amplitudes. The $V_{\rm rot}$ values from Lane et al. (2010) have been multiplied by a factor 2, to directly compare them with the scale adopted by Bellazzini et al. (2012).
$^{(a)}$ See also the values we list in Table 4.2 for the central velocity dispersion of these clusters.
$^{(b)}$ We list our estimates of rotation amplitude for these three clusters in Table 6.2.

References. (1) Bellazzini et al. (2012); (2) Harris (2010); (3) Lane et al. (2010); (4) Ibata et al. (2009); (5) Bellazzini et al. (2008); (6) van de Ven et al. (2006); (7) Pancino et al. (2007); (8) Cote et al. (1995); (9) Meylan & Mayor (1991)

With the available data, it is possible to measure velocity dispersion profiles only for a few globular clusters (see for example Chapter 4); for the majority of Galactic clusters,

instead, only the value of this quantity at the center of the system, indicated with σ_0, is commonly available. The distribution of the values of σ_0 for Galactic clusters is shown in Fig. 1.3. The mean value of this quantity is 6.30 km s^{-1}; the large majority of these values ($\sim 80\%$) is smaller than 10 km s^{-1}, and only for a very few clusters values as large as 20 km s^{-1}are found. The globular cluster ω Cen is the one with the largest measured σ_0.

Several studies have shown that velocity dispersion anisotropy may have a role in determining the dynamics of these systems. Indeed, indications of the presence of radially-biased pressure anisotropy have been found in some clusters: more details on this topic will be given in Chapter 4.

Internal rotation has been measured in an increasing number of objects; in Table 1.2 we list the values of the rotational velocities that have been measured so far for Galactic globular clusters. The detection of internal rotation in star clusters is a challenging task, because the typical value of the ratio of mean velocity to velocity dispersion is only of a few tenths, and σ_0 is small (for example $V_{\rm rot}/\sigma_0 \approx 0.46$, 0.32 for 47 Tuc and ω Cen, respectively; see Bellazzini et al. 2012). Chapter 6 will address the issue of rotation of globular clusters.

Ground-based work on nearby Galactic globular clusters has already demonstrated the power of three-dimensional kinematics (van Leeuwen et al. 2000). The Hubble Space Telescope (for ω Cen, see Anderson & van der Marel 2010; for 47 Tuc, see Anderson & King 2003) and Gaia, with the planned acquisition of the proper motions of thousands of stars in globular clusters, make this goal within reach, supplemented by the kinematical information derived from radial velocity measurements. These measurements would also allow us to obtain an anisotropy profile for the clusters, and to probe directly the type of anisotropy that is present, as already done for example by Anderson & van der Marel (2010) (see also Chapter 6).

1.3 Relaxation times and ages

In our Galaxy, globular clusters are among the oldest known objects. The age $T_{\rm age}$ of these stellar systems can be determined based on the intrinsic luminosity of their main sequence turnoff. Measures of this kind are subject to very large uncertainties, whereas measures of relative ages of globular clusters can be determined more precisely (Stetson et al. 1996). By considering a sample of 36 Galactic globular clusters, Richer et al. (1996) found an age distribution with dispersion of about 1 Gyr and a total age spread of about 4 Gyr. Before the current modern estimates of the relevant cosmological parameters, Vandenberg et al. (1996) have shown that the age of Galactic globular clusters is $T_{\rm age} \sim 15$ Gyr, and that values $T_{\rm age} < 12$ Gyr or $T_{\rm age} > 20$ Gyr are very unlikely. We could therefore consider, as also suggested by McLaughlin & van der Marel (2005), a common age of $T_{\rm age} = 13$ Gyr for globular clusters in the Milky Way.

In Fig. 1.4 we show the distribution of the core and half-mass relaxation times (for a definition, see Sect. 2.1.1) for Galactic globular clusters, as reported in the Harris (2010) catalog. The values of the core relaxation times are spread on 6 orders of magnitude; the mean value of this quantity is $T_{\rm c} = 9.28 \times 10^7$ yr. The distribution of the half-mass relaxation times has a very sharp peak, with all but a handful of clusters having values included within two orders of magnitude; the mean value is $T_{\rm M} = 9.51 \times 10^8$ yr.

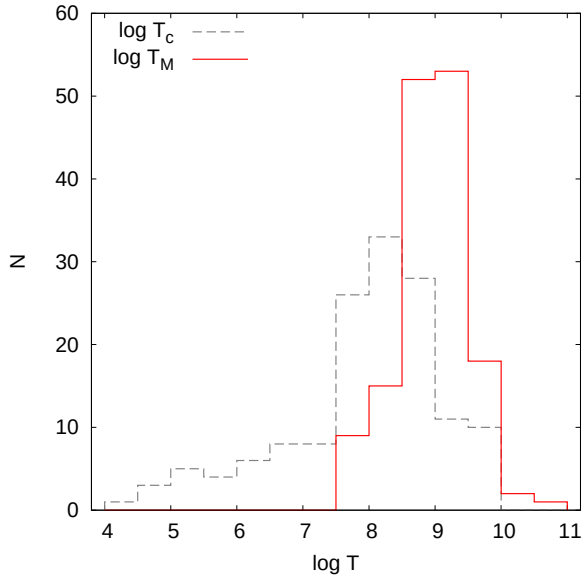

Figure 1.4: Distribution of the values of the core (gray, dashed line) and half-mass (red, solid line) relaxation times for Galactic globular clusters, as published in the Harris (2010) catalog.

1.3.1 Relaxation classes

From the typical values just reported, it is apparent that for globular clusters the relaxation times are generally shorter than their age. This means that the relaxation process has a key role in determining the internal dynamics of these systems. The differences observed in the distribution of core and half-mass relaxation times suggest that Galactic globular clusters are in different stages of their dynamical evolution: some globular clusters appear to be well relaxed, while others seem to be only partially relaxed (and therefore in a dynamical state that is close to that of elliptical galaxies).

It is possible to characterize the different relaxation conditions of globular clusters by means of the central (core) relaxation times $T_{\rm c}$ as listed in the Harris (2010) catalog. The core relaxation time appears to be more adequate for this purpose than the half-mass relaxation time, because in general $T_{\rm c}$ is less model-dependent (this issue will be addressed in more depth in Sect. 4.2).

Looking at Fig. 1.4, we see that the distinction between relaxed and partially relaxed globular clusters is not sharp. Therefore, we introduce a simple criterion to classify globular clusters according to their relaxation state. We consider three relaxation classes:

- relaxed globular clusters, for which $\log T_{\rm c} < 8$ (first class);
- globular clusters in an intermediate relaxation condition, for which $8 < \log T_{\rm c} < 9$ (second class);
- partially relaxed globular clusters, for which $\log T_{\rm c} > 9$ (third class);

we recall that here $T_{\rm c}$ is expressed in years. When considering the values listed in the Harris (2010) catalog, we find that 61 clusters belong to the first class, 61 to the second, and only 21 to the third. Throughout the Thesis, we will refer to this classification when

discussing the dynamical state of specific clusters. We checked that, by classifying the clusters with respect to the half-mass relaxation time, some changes in the composition of the three classes identified above would occur, but with minor effects in relation to the general description.

1.4 Hot topics

In this section we summarize some recent surprising discoveries that have received new interest in the field of globular clusters. We present the recent findings about intermediate-mass black holes in Sect. 1.4.1, about multiple stellar populations in Sect. 1.4.2, and about blue straggler stars in Sect. 1.4.3.

Some issues related to the possible discovery of intermediate-mass black holes in several Galactic globular clusters, in particular with regards to the central slope of observational profiles of clusters, will be discussed in Sect. 4.3.3. In this Thesis, we will not deal with the other two topics in great detail, but we will take them into account when analyzing the data we requested with the proposals described in Chapters 7 and 8. In particular, we will look for the presence of kinematic evidence of multiple populations, and we will determine the binary fraction of the clusters, which could explain the origin of their blue straggler stars (Dalessandro et al. 2011).

1.4.1 Intermediate-mass black holes

Black holes with masses larger than $10^6 M_\odot$ are found in the centers of almost all galaxies (Davis et al. 2013; van den Bosch et al. 2012), including the Milky Way (Schödel et al. 2002). The discovery of central super-massive black holes at high redshift (Fan 2006) indicates that these objects already existed at a very early stage of structure formation. If we imagine that these objects grew from ordinary stellar black holes, with a mass of up to a few tens of solar masses, the required growth time would be too high and hard to justify. It has thus been suggested (Ebisuzaki et al. 2001) that intermediate-mass black holes, with masses between 10^2 and $10^5 M_\odot$, could be the seeds for super-massive black holes. Two popular theories for the formation of intermediate-mass black holes exist: they could be the end product of Population III stars (Madau & Rees 2001), or they could be the result of runaway stellar collisions in dense young globular clusters (Portegies Zwart et al. 2004, but see also Glebbeek et al. 2009). The extrapolation of the empirical relation between super-massive black holes masses and the velocity dispersion of their host spheroid (Ferrarese & Merritt 2000) to the mass range of intermediate-mass black holes also encourages to look for them in globular clusters. For these reasons great efforts have been made in order to find signatures of the presence of these objects in several Galactic globular clusters.

Direct detection of an intermediate-mass black hole in globular clusters is problematic. Strader et al. (2012) searched for the signal of accreting intermediate-mass black holes in three Galactic clusters, by means of radio observations; no sources were observed in the clusters considered, suggesting either that intermediate-mass black holes are rare in clusters, or that they accrete in a very inefficient manner. In direct connection with topics addressed in this Thesis, an intermediate-mass black hole may leave a signature in its immediate surrounding, in particular a density cusp (Bahcall & Wolf 1976) is expected. Intermediate-mass black hole detections in globular clusters are mostly claimed on the basis of the discovery of a shallow cusp in the surface brightness profile and a rise in the velocity dispersion profile towards the center (for example, see Anderson & van der Marel 2010, Lützgendorf et al. 2013a). However, similar features can also

be produced by different processes. For example, mass segregation, core collapse, or the presence of binary stars in the center can also generate a shallow cusp in the brightness profile, as shown by means of dedicated N-body simulations (Vesperini & Trenti 2010). Some kinematical properties can be explained by the presence of pressure anisotropy, without a central intermediate-mass black hole (van der Marel & Anderson 2010; Zocchi et al. 2012, see also Sect. 4.3.3). Therefore, conclusive evidence for the existence of intermediate-mass black holes in globular clusters is still unavailable (Volonteri 2010).

An illustrative example of this issue is given by the controversial case of ω Cen. Noyola et al. (2008) measured its central surface brightness profile with the Advanced Camera for Surveys on board of the Hubble Space Telescope, and its central velocity dispersion with the Integral Field Units of the spectrograph GMOS mounted on the Gemini telescope. They found a cusp in the surface brightness and a rise in the velocity dispersion towards the center. Their analysis, carried out by means of an isotropic and spherical dynamical model, suggests the presence of an intermediate-mass black hole of mass $M_\bullet = 4.0^{+0.75}_{-1.0} \times 10^4 M_\odot$. van der Marel & Anderson (2010) considered star counts and proper-motion measurements obtained by the Hubble Space Telescope near the cluster center. They analyzed the profiles by means of two sets of anisotropic models, with either a flat core or a shallow cusp; the anisotropy is constrained by the observed profile that they obtained from proper-motion data (the cluster is isotropic in the center, radially anisotropic in the intermediate part, and tangentially anisotropic in the outermost region; see also Chapter 6). The flat core models provide a good fit to both kinematic and photometric observations, without requiring the presence of dark mass. The best-fit cusp model instead requires the presence of an intermediate-mass black hole of $M_\bullet = (8.7 \pm 2.9) \times 10^3 M_\odot$ (or of a dark cluster with radius $\lesssim 0.16$ pc), a value that is not compatible with the estimate from Noyola et al. (2008). Noyola et al. (2010) claimed that these different results could be due to a misidentification of the cluster center. They calculated the position of the center by using kinematical data obtained by the spectrograph FLAMES mounted on the Very Large Telescope, and performed a new dynamical analysis by means of isotropic models. Their analysis implies the presence of an intermediate-mass black hole of mass $3.0 \times 10^4 M_\odot < M_\bullet < 5.2 \times 10^4 M_\odot$, depending on the considered position of the center.

A similar controversy has originated around the massive globular cluster NGC 6388. Lützgendorf et al. (2011) studied the velocity dispersion profile they measured with FLAMES Integral Field Units, together with a surface brightness profile measured from the Hubble Space Telescope data. They argue that the observed steep rise towards the center in the velocity dispersion profile, reaching almost 25 km s^{-1}, may correspond to the presence of an intermediate-mass black hole of mass $M_\bullet = (1.7 \pm 0.9) \times 10^4 M_\odot$. However, Lanzoni et al. (2013) analyzed the velocity dispersion profile calculated from radial velocities of single stars measured by FLAMES. Their velocity dispersion profile is flat in the center, with a value of ~ 13 km s^{-1}; the dynamical analysis carried out on this profile rules out the presence of an intermediate-mass black hole more massive than $2 \times 10^3 M_\odot$.

Lützgendorf et al. (2013b) collected all the existing studies providing masses (or upper limits) of intermediate-mass black holes in globular clusters, and checked the presence of trends with several cluster parameters. By using the 14 globular clusters in their sample, they found a correlation between the mass of the intermediate-mass black holes and the velocity dispersion of the cluster; the slope of this correlation, however, is different from the one observed for super-massive black holes. In turn, correlations between the mass of the black hole and the total mass and the total luminosity of the cluster are associated with slopes more similar to the ones observed for super-massive black holes.

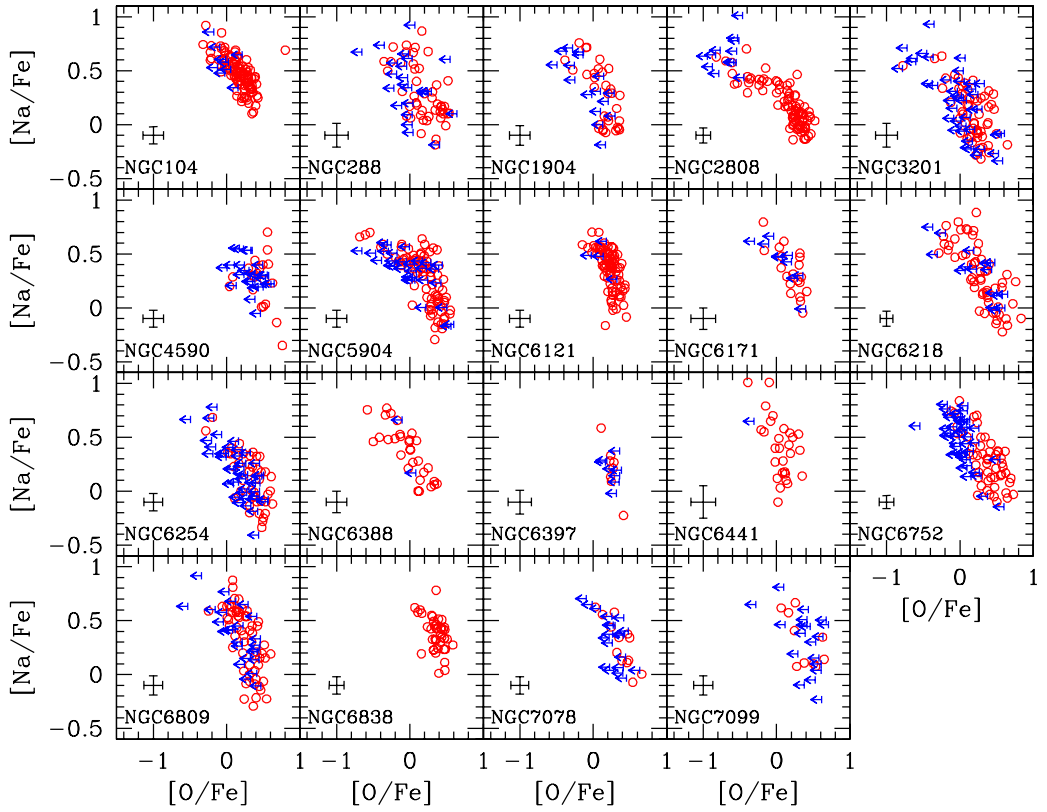

Figure 1.5: The Na-O anticorrelation observed in 19 globular clusters. Sodium and Oxygen abundances for the represented stars were measured from GIRAFFE and UVES spectra. Star-to-star error bars are indicated in each panel. Upper limits in Oxygen abundances are shown as arrows, detections are indicated as open circles. Figure taken from Carretta et al. (2009).

1.4.2 Multiple stellar populations

For a long time globular clusters have been considered as an assembly of stars all characterized by the same age and initial chemical composition (Helium content and metallicity), and with masses distributed according to an initial mass function. A similar set of stars would be treated as a prototype of a simple stellar population, thus characterized by a single isochrone in the color-magnitude diagram. Several photometric and spectroscopic observations have now shown that there is evidence of the presence of multiple stellar populations in all the clusters that have been examined in greater detail so far. The best pieces of evidence of the presence of multiple stellar populations in globular clusters are the finding that different stars in the same cluster may be characterized by different chemical composition and the splitting of the evolutionary sequences in the color-magnitude diagram (Gratton et al. 2012a; Piotto et al. 2007; Piotto 2009).

Therefore, the suggested picture is that clusters have been the site of multiple generations of stars. It is argued that second-generation stars formed in the central region of the system from material polluted by the ejecta of some first-generation stars. Most of the stars that are presently found in globular clusters belong to the second-generation; first-generation stars, with a composition similar to that of field stars, are still present in

the clusters, making up to one third of the current total population (D'Ercole et al. 2008; Vesperini et al. 2010). Second-generation stars appear to be more centrally concentrated with respect to the first-generation stars (Bellini et al. 2009; Lardo et al. 2011; Milone et al. 2012).

Chemical inhomogeneities in globular clusters were already detected about forty years ago. The first detection of unusual chemical abundances was found in red giant branch stars in the globular clusters NGC 5904 (M5) and NGC 6254 (M10) by Osborn (1971); Hesser & Bell (1980) found anomalies in the abundances of main sequence stars in the cluster 47 Tuc. A related recent discovery is the detection, by means of spectroscopic observations (Carretta et al. 2009), of a Na-O anticorrelation in 19 Galactic globular clusters (see Fig. 1.5).

The first photometric evidence of the presence of multiple stellar populations in a globular cluster was the discovery of a splitting of the main sequence of ω Cen into two branches (blue and red), down to a few magnitudes below the turnoff (Bedin et al. 2004). Sollima et al. (2007) showed that the multiple main sequence is present in the entire spatial extent of the cluster, but that the stars belonging to the blue main sequence are more concentrated towards the center, with respect to the other main sequence stars. A spectroscopic follow-up analysis showed that stars in the blue main sequence have metal abundances twice as large as the ones of stars in the dominant red main sequence (Piotto et al. 2005). Moreover, the sub-giant branch of ω Cen is spread into four distinct components, characterized by different metallicities and ages (Villanova et al. 2007). The results obtained from the observations of ω Cen stimulated a number of similar studies devoted to investigate the phenomenon in other globular clusters. Piotto et al. (2007) showed that the main sequence of NGC 2808 splits into three separate branches, with different Helium abundances; this feature was also connected to the peculiar morphology of the horizontal branch (D'Antona & Caloi 2004; D'Antona et al. 2005). A split is also observed in the sub-giant branch of NGC 1851 (Milone et al. 2008; Gratton et al. 2012b), and is connected to the presence of two different stellar populations. Recently, Milone et al. (2012) have shown that ultraviolet observations are particularly adequate to reveal the presence of a splitting of the evolutionary sequences in the color-magnitude diagrams of globular clusters; as a consequence, a significant effort to obtain observations in this band has been made (see for example Piotto et al. 2013).

1.4.3 Blue straggler stars

Blue straggler stars are main sequence stars that are brighter and bluer than the turnoff: they are therefore younger and more massive than the other stars in the cluster. They were first discovered by Sandage (1953) in the globular cluster NGC 5272 (M3), and recently have been the target of numerous studies in Galactic globular clusters. Observing these objects in optical bands is challenging, because they are very faint with respect to asymptotic giant branch and red giant branch stars. In ultraviolet bands, instead, blue stragglers and horizontal branch stars are the brightest objects, and are easily identified in the color-magnitude diagram. An example is the study carried out by Ferraro et al. (1999) for the cluster NGC 6093 (M80): they observed 305 blue stragglers, the largest sample ever observed in a Galactic globular cluster.

Two possible mechanisms have been suggested to be responsible for the formation of these exotic stars in globular clusters. One possibility is that they are formed in collisions or mergers between two single main sequence stars (Sandquist et al. 1997; Sills et al. 1997). The other scenario suggests that blue stragglers are produced via mass transfer within primordial binaries (Sollima et al. 2008; Knigge et al. 2009). Blue stragglers

formed from stellar collisions are expected to be located near the center of the cluster, whereas the distribution of blue stragglers outside the cluster core seems to be due to objects generated by mass transfer in primordial binary systems (Davies et al. 2004).

The radial distribution of blue stragglers in different clusters shows significant variations (e.g., see Ferraro et al. 1993 for M3 and Ferraro et al. 2006 for ω Cen), but it appears to be very similar within distinct groups of Galactic clusters. Ferraro et al. (2012) have recently suggested to use the radial distribution of the blue straggler stars in globular clusters as a "dynamical clock", that is, a tracer of their dynamical age. The observed distribution, in fact, contains important signatures of the dynamical evolution of these systems, being mainly modeled by the long-term effects of the dynamical friction that acts on the population of binaries in the cluster since the early stages of its evolution.

1.5 Extragalactic globular clusters

Globular clusters are also found in external galaxies (Ashman & Zepf 2008); their properties can give useful insights into the study of the formation mechanisms of these stellar systems, especially with regards to the different environment in which they are located.

The first observational efforts in this topic were aimed at studying globular clusters in the nearby Magellanic Clouds. An example is the measure of surface brightness profiles, based on star counts and aperture photometry, for 10 young star clusters in the Large Magellanic Cloud, carried out by Elson et al. (1987). Lately, by using the Hubble Space Telescope, it has been possible to determine high resolution photometric profiles for large samples of globular clusters in several galaxies. Barmby et al. (2007) explored the morphologies of clusters in the Andromeda galaxy (M31), and proposed a first interpretation of the observed profiles in terms of simple dynamical models; a similar work was also done by Harris et al. (2002) and Harris et al. (2006) for clusters in the elliptical galaxy NGC 5128, by Mackey & Gilmore (2003a,b,c) for clusters in the Magellanic Clouds and in the Sagittarius dwarf spheroidal galaxy, and by Madrid et al. (2009) for clusters in the Virgo elliptical galaxy M87.

Bellazzini (1998) considered a sample of non-post-core-collapse clusters, and found that their configuration in the fundamental plane defined by the parameters[3] ($\log R_{\rm c}$, $\log \sigma_0$, μ_0), is similar to a straight line. This finding was later confirmed by Pasquato & Bertin (2010), who considered the half-light quantities ($\log R_{\rm h}$ and $\mu_{\rm h}$, i.e. the half-light radius and average surface brightness within it) corresponding to the central ones used by Bellazzini (1998). By studying a sample of 129 clusters in the Milky Way, in the Magellanic Clouds and in the Fornax dwarf, they found the following linear relation between $\mu_{\rm h}$ (measured in mag arcsec^{-2}) and $\log R_{\rm h}$ (expressed in pc):

$$\mu_{\rm h} = (5.25 \pm 0.44) \log R_{\rm h} + (15.58 \pm 0.28) \, . \tag{1.2}$$

Both young and old clusters follow this scaling law, which has a scatter of approximately 1 mag in $\mu_{\rm h}$. Young clusters display more of a scatter and a clear trend in this with age, whereas this is not seen for old clusters; this trend becomes tighter if cluster age is measured in units of the cluster half-light relaxation time. It is therefore apparent that two-body relaxation plays a major role, together with stellar population evolution, in shaping the relation between $\mu_{\rm h}$, $\log R_{\rm h}$, and cluster age. These findings lead to conclude that this fundamental line scaling law does not have a primordial origin, but is instead the result of a combination of stellar evolution and collisional dynamical evolution.

[3] We recall that $R_{\rm c}$ is the core radius and σ_0 the central velocity dispersion (see Sect. 1.1 and 1.2 for their definition). We indicate with μ_0 the central surface brightness.

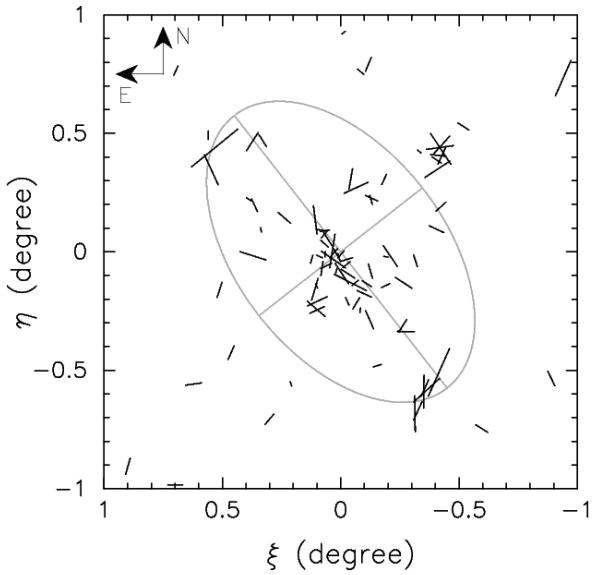

Figure 1.6: Cluster elongations and orientations shown with respect to M31. The sizes of the vectors are correlated with the ellipticities. The ellipse has a radius of 10 kpc and is flattened to $b/a = 0.6$. Figure taken from Wang & Ma (2013).

When analyzing 291 globular clusters in M31, the Milky Way, Magellanic Clouds, the Fornax dwarf spheroidal, and NGC 5128, Barmby et al. (2007) found that they define a very tight fundamental plane with identical slopes in the parameter space. They argue that their findings reinforces the view that old globular clusters have near-universal structural properties, regardless of the host environment. Very recently, this was also confirmed by Wang & Ma (2013), who presented surface brightness profiles for 79 globular clusters in M31, and derived structural and dynamical parameters for them. They also analyzed the distribution of the clusters in the galaxy, with particular attention to the ellipticity and the orientation in the galaxy, as shown in Fig. 1.6. They concluded that the elongation of the clusters in M31 is not entirely related to tidal effects induced by the galactic potential, but could be due to other dynamical factors, such as internal rotation and pressure anisotropy.

Harris et al. (2013) have compiled a catalog of 422 galaxies with published measurements of their globular cluster populations. Among various correlations of the total number of globular clusters, $N_{\rm GC}$, with other global galaxy properties, they found that the number of clusters correlates with the dynamical mass of the host galactic bulge. They also present a plot showing the specific frequency[4] $S_{\rm N}$ of the clusters versus the host galaxy luminosity: it is reproduced in Fig. 1.7. This graph exhibits the known U-shape: highest specific frequency occurs for either very faint or very bright systems, while in the middle range of galaxy luminosity the specific frequency has a minimum. Rhode (2012) considered 20 giant galaxies, and presented an analysis of the correlation between their total number of globular clusters $N_{\rm GC}$ and several other properties, such as total stellar mass and luminosity, bulge mass and luminosity, and mass of the central

[4]The specific frequency is defined as $S_{\rm N} \equiv N_{\rm GC} \times 10^{0.4(M_{\rm V}+15)}$, where $M_{\rm V}$ is the total absolute magnitude of the galaxy in V band. The specific frequency therefore connects the galaxy size and the globular cluster population (Harris & van den Bergh 1981).

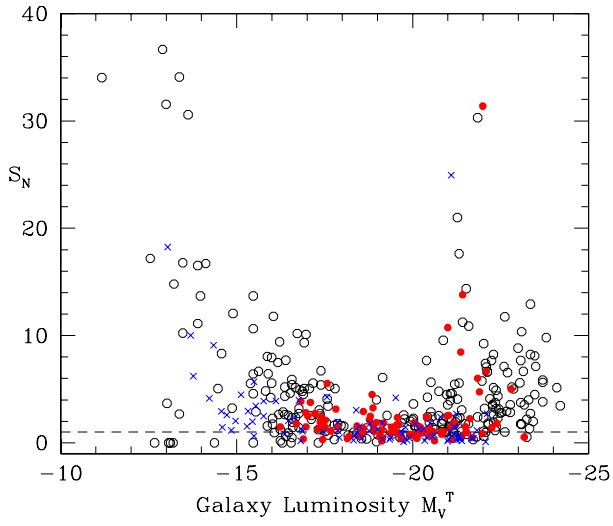

Figure 1.7: Specific frequency of globular clusters versus the absolute visual magnitude of the host galaxy. Elliptical and dwarf elliptical galaxies are plotted as open circles, lenticular galaxies as solid red circles, and spirals or irregulars as blue crosses. The horizontal line at bottom shows specific frequency = 1. Figure taken from Harris et al. (2013).

super-massive black hole. The strongest correlation appears to be that between $N_{\rm GC}$ and the total stellar mass of the galaxy; the correlation with the largest scatter is that between $N_{\rm GC}$ and the mass of the central black hole: the author argued that this behavior reflects the connection between these quantities and the galaxy potential.

CHAPTER 2

Dynamical models

This Chapter is dedicated to the description of the modeling techniques that can be used to provide a description of the dynamics of a stellar system. In Sect. 2.1 we present the different approaches that could be adopted. In Sect. 2.2 we outline the characteristics of the method that uses models defined by a distribution function, and in Sect. 2.3 some properties of other available models. Section 2.4 will give an overview of what is commonly done to study the dynamics of Galactic globular clusters.

2.1 Dynamical description of self-gravitating stellar systems

There are two possible approaches to study the dynamics of a stellar system. The first is the "predictive" approach: specific physical hypotheses are formulated, in order to construct a theoretical model that will subsequently be compared with observations (see Sects. 2.1.2 and 2.1.3). The second, "descriptive", approach consists in extracting all the possible information from the data, before making physical assumptions, with the idea that a physical discussion will be made eventually after the structure of the system is determined from the data (see Sects. 2.1.4 and 2.3). In the following we summarize the key features of these approaches, especially in relation to applications to globular clusters. For a more detailed discussion on this topic, we refer the reader to Bertin (2000).

2.1.1 Fundamental time scales

To study the internal dynamics of stellar systems it is useful to introduce a time scale that measures the dynamical effects associated with the two-body encounters (see Chapter 7 of Bertin 2000). These encounters can be treated as events of Rutherford scattering, in which a star representing a "test mass" $m_{\rm t}$ is deflected by another "field star" of the cluster, of mass m. The relaxation time can be defined as the time scale beyond which the cumulative effects of subsequent encounters, as measured by the increase of the square of the transverse velocity component $v_\perp$ with respect to the original direction of motion, becomes comparable to the initial specific energy of a star

$$v_{\rm start}^2 = T \int (\Delta v_\perp)^2 2\pi v_{\rm start} \nu \, b \, db \tag{2.1}$$

where b is the impact parameter and ν is the number density of the system. The increment of the transverse velocity can be expressed as

$$\Delta v_\perp = 2 v_{\rm start} \frac{m}{m + m_{\rm t}} \sin\frac{\theta}{2} \cos\frac{\theta}{2} \, , \tag{2.2}$$

Time scale	Typical value
$\tau_{\rm d}$	$\sim 10^6$ yr
$T_{\rm c}$	$\sim 10^8$ yr
$T_{\rm M}$	$\sim 10^9$ yr
$T_{\rm age}$	$\sim 10^{10}$ yr

Table 2.1: Typical values for the relevant dynamical time scales of Galactic globular clusters.

where θ denotes the deflection angle, with $\sin(\theta/2) = \sqrt{1/[1+(b/b_0)^2]}$, and $b_0 = G(m+mt)/v_{\rm start}^2$. By substituting Eq. (2.2) in Eq. (2.1) and by integrating over $[0, b_{\rm max}]$ (with $b_{\rm max}$ maximum value allowed for the impact parameter), we obtain

$$T \approx \frac{v_{\rm start}^3}{8\pi G^2 \nu\, m^2 \ln\Lambda} \tag{2.3}$$

where $\ln\Lambda$ is often called Coulomb logarithm, with $\Lambda = b_{\rm max}/b_0$.

If we assume that the stars in the cluster have all the same mass m, and that the velocity distribution is approximately a Maxwellian distribution, we can consider the velocity dispersion σ as a good approximation for the initial velocity $v_{\rm start}$ (see Spitzer 1987). It is important to notice that the number density and the velocity dispersion are defined as a function of the distance from the center of the system (when considering it as spherically symmetric), therefore the relaxation time can also be expressed as a radial profile. For this reason, it is appropriate to distinguish between core $T_{\rm c} \propto \sigma(r_{\rm c})^3/\nu(r_{\rm c})$ and half-mass relaxation time $T_{\rm M} \propto \sigma(r_{\rm h})^3/\nu(r_{\rm h})$.

The half-mass relaxation time, from the virial theorem, can be expressed as

$$T_{\rm M} \approx \frac{N^{1/2} r_{\rm M}^{3/2}}{G^{1/2} m^2 \ln\Lambda}\,, \tag{2.4}$$

where N is the number of stars in the system, and the Coulomb logarithm can be expressed as $\ln\Lambda = \ln(0.4N)$, if we take $b_{\rm max} = r_{\rm M}$.

The relaxation times of the Galactic globular clusters shown in Fig. 1.4 have been calculated by means of these equations, by using the values of the structural and dynamical parameters given by King (1966) models, because in general the desired measurements of $\sigma(r)$ and $\nu(r)$ are not available directly.

It is important to compare the relaxation time scale with a typical dynamical time scale of the system. By defining the dynamical time as $\tau_{\rm d} = 2r_{\rm M}/\sigma$, the following relation can be obtained

$$\frac{T_{\rm M}}{\tau_{\rm d}} \propto \frac{N}{\ln(0.4N)}\,. \tag{2.5}$$

Typical values of the relevant time scales for Galactic globular clusters are listed in Table 2.1.

2.1.2 Kinetic description

To describe a stellar system containing a large number of stars it can be useful to consider the continuous limit, and to refer to the single-star distribution function $f(\mathbf{x}, \mathbf{v}, t)$,

defined in the phase space. The evolution of this function in phase space is described by the Boltzmann equation:

$$\frac{\partial f}{\partial t} + \mathbf{v} \cdot \frac{\partial f}{\partial \mathbf{x}} + \mathbf{a} \cdot \frac{\partial f}{\partial \mathbf{v}} = \left(\frac{\partial f}{\partial t} \right)_{\text{coll}} , \tag{2.6}$$

where the right-hand term takes into account the collisions between stars in the system (usually expressed by means of the Fokker-Planck term), and $\mathbf{a} = -\partial\Phi/\partial\mathbf{x}$, with Φ mean potential of the system.

If a description of the long-term evolution of a stellar system is not needed, it is appropriate to refer to the homogeneous equation associated with Eq. (2.6), that is, the "collisionless" Boltzmann equation. Since the relaxation time of globular clusters is long with respect to their dynamical time, the clusters can be considered non-collisional, and described in these terms. Moreover, for globular clusters, the dynamical time is much shorter than their age, so it is reasonable to imagine that in their lifetime they evolved into a quasi-equilibrium state: it is therefore possible to neglect the explicit time-dependence in the distribution function, which becomes then $f(\mathbf{x}, \mathbf{v})$.

In Eq. (2.6), the potential Φ is determined by the total mass distribution by means of the Poisson equation: the fact that the distribution function depends on the potential makes the problem non-linear. For fully self-consistent problems, the potential is completely determined by the density associated with f (in this case the stars), so that the Poisson equation becomes:

$$\nabla^2 \Phi = 4\pi G \int f d^3 v \, , \tag{2.7}$$

where the mass density is expressed as:

$$\rho = \int f d^3 v \, . \tag{2.8}$$

A number of macroscopic quantities can be defined from the distribution function, in particular the mean velocity vector, the pressure tensor, and the velocity dispersion tensor:

$$\langle v \rangle_i = \int f v_i d^3 v \tag{2.9}$$

$$P_{ij} = \int (\mathbf{v} - \langle \mathbf{v} \rangle)_i (\mathbf{v} - \langle \mathbf{v} \rangle)_j f d^3 v \tag{2.10}$$

$$\sigma_{ij}^2 = \frac{P_{ij}}{\rho} = \frac{1}{\rho} \int (\mathbf{v} - \langle \mathbf{v} \rangle)_i (\mathbf{v} - \langle \mathbf{v} \rangle)_j f d^3 v \, . \tag{2.11}$$

An equilibrium solution of the collisionless Boltzmann equation must be an integral of the motion. In fact the Jeans theorem states that an equilibrium solution of the collisionless Boltzmann equation depends on the phase space coordinates only through the isolating integrals of the motion (e.g., see Chapter 9 of Bertin 2000).

2.1.3 Fluid and virial description

We can resort to descriptions that are less detailed than the kinetic description.

A first possibility is that of the fluid equations. By taking velocity moments of the Boltzmann equation it is possible to obtain a hierarchy of fluid equations. Every new

moment that is considered introduces a new variable. Formally, in order to keep all the information contained in the collisionless Boltzmann equation, it would be necessary to consider an infinite number of moment equations. In general, there is no way to break the system into a finite and complete set of fluid equations. For collisionless systems, no equations of state are available to reduce the problem to a closed finite set of fluid equations. In general, fluid equations are then used as a diagnostic tool to interpret stellar dynamics data, more than as a tool to construct models that are related to a specific distribution function.

At a different level, the virial description consists in taking moments of the fluid equations with respect to the spatial coordinates, and in integrating on the volume occupied by the system. This procedure provides a kind of backbone of a macroscopic description: the details not only on stellar orbits but also on density and velocity profiles are lost. The reference equation for this approach is the second-order virial set of equations for a self-gravitating system:

$$\frac{1}{2}\frac{d^2 I_{ij}}{dt^2} = 2\left(K_{ij} + \frac{\Pi_{ij}}{2}\right) + W_{ij} \ , \tag{2.12}$$

where I_{ij} is the generalized moment of inertia tensor, K_{ij} and $\Pi_{ij}/2$ are the ordered and random components of the kinetic energy tensor, respectively, and W_{ij} is the gravitational energy tensor, which has been shown by S. Chandrasekhar to be very useful for the study of self-gravitating homogeneous ellipsoids. For inhomogeneous stellar systems, these give global constraints that may be useful in relation to simple arguments. Often, the condition of virial equilibrium is used to test the quality of results obtained from numerical integrations.

2.1.4 N-body simulations

The most detailed analysis that is possible to obtain for stellar systems is the one done by means of numerical N-body simulations; with this method, in fact, the objects are studied as discrete systems.

This tool of investigation has been largely developed for the study of stellar systems like globular clusters, because there is concrete hope to consider a number of particles N comparable with the number of stars of the system that we wish to study (see Heggie & Hut 2003). This approach is particularly suited to the study of their dynamical evolution, with respect to specific problems like merging, mass segregation or external time-dependent problems, that are particularly difficult to treat with analytical methods.

In N-body simulations the stars are modeled as point-like masses, even if in general the number of particles N in the simulations is (much) smaller than the number of stars in the real systems. If the finite size of the stars plays a role, some interesting phenomena in stellar encounters can occur. These phenomena are difficult to study analytically, but can be introduced in the simulations, once the underlying mechanisms have been clarified. Since in many cases the number of particles in the code is smaller than the real number of stars in the system, every particle in the code is actually a super-particle that represents the mass of more than one star, unrealistically grouped exactly in the same place in the phase space. This produces unrealistic granularity and potential fluctuations.

2.2 Dynamical models defined by distribution functions

The ("predictive") approach largely used in the present Thesis to describe the dynamics of globular clusters is based on models defined by a distribution function. In this Section we outline the assumptions from which the distribution functions are defined and the properties of the models.

2.2.1 Assumptions, truncation, and physical ingredients

In the case of globular clusters, physically justified assumptions are based on the properties of the systems that have been described in Chapter 1, and can be summarized as follows. The system is:

- described as continuous, by using a mean field description that neglects the real granularity of the stellar system;
- assumed to be in a quasi-stationary state, that is, the distribution function and the self-consistent potential are taken to be time independent.
- considered to be composed by a single component: we consider it as formed by a homogeneous population of stars with a constant mass-to-light ratio;
- characterized by the presence of a spatial truncation, as a result of the tidal effects of the host galaxy.

In a first approximation globular clusters may be considered as spherically symmetric systems (as shown in Sect. 1.1, they are indeed only moderately flattened). In this case the construction of the models is greatly simplified, because the gravitational potential depends only on r, the distance from the center of the system, and the distribution function depends only on the variables r, $v_{\rm r}$, and $v_{\rm t}$ (the latter being the radial and tangential components of the velocity). Moreover, many globular clusters can be considered to be close to a thermodynamically relaxed state (see Sects. 2.1.1 and 1.3). Therefore the distribution function should depend only on the single-star energy E and the pressure tensor should be isotropic.

Spherical isotropic models

The simplest models are spherically symmetric and isotropic, and provide a good zeroth-order description of globular clusters. In particular, two families of models have been considered, that differ in the definition of the spatial truncation.

King (1966) models have been widely used to study the dynamical properties of globular clusters. These quasi-relaxed models are defined as a Maxwellian distribution function, with an energy truncation:

$$f_{\rm K}(E) = \begin{cases} A\left[\exp(-aE) - \exp(-aE_0)\right] & E \leq E_0 \\ 0 & E > E_0 \end{cases} . \tag{2.13}$$

The cut-off energy E_0 can be interpreted as the threshold value beyond which a star is no longer considered as part of the system. Because of the assumed spherical symmetry, this energy truncation translates into the existence of a truncation radius $r_{\rm tr}$. More details of this family of models are given in Appendix A.1.

The truncation prescription is not unique. Therefore it is possible to define several families of models with similar physical properties but a different truncation in phase space. In this respect, the family of models defined as:

$$f_{\rm W}(E) = \begin{cases} A\left\{\exp(-aE) - \exp(-aE_0)[1 - a(E - E_0)]\right\} & E \leq E_0 \\ 0 & E > E_0 \ , \end{cases} \tag{2.14}$$

represents the spherical isotropic nonrotating limit of a family of rotating models originally introduced by Wilson (1975) (see also Appendix A.2).

Spherical anisotropic models

As shown in Sect. 1.3, some globular clusters have very long relaxation times. These less relaxed clusters might conform to the picture of formation via incomplete violent relaxation, which has the characteristic signature of radially-biased pressure anisotropy in the outer parts. To test this scenario it is necessary to consider models including pressure anisotropy as a physical ingredient.

In this Thesis (in particular, see Chapter 4), we have decided to analyze globular clusters by means of models (the $f^{(\nu)}$ models; see Bertin & Trenti 2003, and references therein) explicitly constructed for the context of violently relaxed elliptical galaxies. They are defined from the following distribution function

$$f^{(\nu)}(E, J^2) = \begin{cases} A \exp\left[-aE - d\left(\frac{J^2}{|E|^{3/2}}\right)^{\nu/2}\right] & E \leq 0 \\ 0 & E > 0 \ , \end{cases} \tag{2.15}$$

where J indicates the single-star total angular momentum. Additional details on these models are provided in Appendix A.3.

Here the use of $f^{(\nu)}$ models is preferred to other options (for example to the use of King-Michie models, Michie 1963), because these models are based on a physical justification and have been shown to perform well both in relation to the observations of bright elliptical galaxies and to the properties of the products of incomplete violent relaxation found in numerical simulations of collisionless collapse (Trenti et al. 2005).

Non-spherical models

One way to interpret the observed small flattening of some globular clusters is in terms of tidal interactions. A family of triaxial isotropic models has been introduced for this purpose by Bertin & Varri (2008): as a generalization of the family of spherical King models, they constructed a family of triaxial models in which the deviations from sphericity induced by the presence of an external tidal field are taken into account self-consistently. A full characterization of the resulting configurations in terms of the relevant intrinsic and projected properties has been given by Varri & Bertin (2009); the range of the predicted flattening is consistent with that observed in most Galactic globular clusters. In this Thesis, we did not take into account these models, because the effects of tides are expected to act mainly in the outer parts of these stellar systems, in regions outside the focus of our investigation, and often beyond the range of the available data.

There are also some indications of rotation in several Galactic globular clusters (see Sect. 1.2). The family of self-consistent axisymmetric rotating models introduced by Varri & Bertin (2012, see Appendix A.4) is characterized by differential rotation, approximately rigid in the center and vanishing in the outer parts. The velocity dispersion

calculated by these models is characterized by isotropy in the central region of the system, weak radial anisotropy in the intermediate regions, and tangential anisotropy in the outer parts. In Chapter 6, we will present a detailed dynamical analysis of three Galactic globular clusters by means of this family of rotating models.

2.2.2 Projections along the line of sight

To compare the predictions of the dynamical models with some observable quantities, it is necessary to project the relevant profiles along the line of sight. For a spherically symmetric system, profiles can be given either in terms of the intrinsic radial coordinate r, or the projected radial coordinate R.

The projected surface mass density is therefore expressed as:

$$\Sigma(R) = 2 \int_0^{+\infty} \rho(r) dz \ , \tag{2.16}$$

where $r^2 = R^2 + z^2$, and z is in the direction of the line of sight. Obviously, in the case of systems characterized by a truncation radius $r_{\rm tr}$, the integration will be carried out only to $z_{\rm tr} = \sqrt{r_{\rm tr}^2 - R^2}$.

The projection of the velocity dispersion is given by the following integral:

$$\Sigma(R)\sigma_{\rm P}^2(R) = 2 \int_0^{+\infty} \rho(r)\sigma_{\rm L}^2(r) dz \ , \tag{2.17}$$

where $\sigma_{\rm L}^2$ represents the line-of-sight velocity dispersion component. For isotropic models, $\sigma_{\rm L}^2 = \sigma^2$, where σ^2 indicates a component of the velocity dispersion. For anisotropic models, it is possible to calculate:

$$\sigma_{\rm L}^2 = \sigma_{\rm r}^2 \cos^2(\xi) + \sigma_\theta^2 \sin^2(\xi) \ , \tag{2.18}$$

where $\sin\xi = R/r$, and spherical coordinates are used, so that $\sigma_{\rm r}^2$, σ_θ^2, and σ_φ^2 are the components of the velocity dispersion[1]. If we define the anisotropy α as:

$$\alpha(r) = 2 - \frac{\sigma_{\rm t}^2}{\sigma_{\rm r}^2} \ , \tag{2.19}$$

and recall that $\sigma_{\rm t}^2 = 2\sigma_\theta^2$, we can express the line-of-sight component of the velocity dispersion as:

$$\sigma_{\rm L}^2 = \sigma_{\rm r}^2 \left(1 - \frac{\alpha(r)}{2}\frac{R^2}{r^2}\right) \ . \tag{2.20}$$

Therefore, the projection of the velocity dispersion along the line of sight is in general calculated by using the radial component of the dispersion and the anisotropy function.

Projections of non-spherical models

In the case of non-spherical models, the projection for comparison with the observations is complicated by the fact that a different orientation of the system produces a different projection on the sky.

[1] The component σ_φ^2 does not contribute to $\sigma_{\rm L}^2$ because it is perpendicular to the direction of the line of sight. We also recall that $\sigma_\theta^2 = \sigma_\varphi^2$.

When considering the axisymmetric rotating models described above, for example, the inclination angle between the line of sight and the rotation axis of the systems must be taken into account in order to properly determine the properties of the projection. To simplify the calculations, the projection can be performed by sampling from the relevant distribution function a discrete set of particles and then by performing a rotation of such a discrete system to match the desired inclination angle. The theoretical kinematic and photometric profiles can then be constructed by following the procedures described in Sects. 3.1 and 3.2. By sampling a large number of particles (we chose $N = 2{,}048{,}000$) it is possible to obtain smooth profiles and an accurate description of the system (for an application of this method, see Sect. 6.2).

2.3 Other approaches

Some alternative methods that do not require a definition of a distribution function exist and can be used to describe the dynamics of stellar systems. In this Section, we briefly describe these alternative methods and procedures.

2.3.1 Jeans equations

The Jeans equations are obtained by taking velocity moments of the collisionless Boltzmann equation. In the case of spherically symmetric systems, there is only one equation for the radial coordinate, which can be written as

$$\frac{d(\rho\sigma_{\rm r}^2)}{dr} + \frac{\alpha}{r}\rho\sigma_{\rm r}^2 + \rho\frac{d\Phi}{dr} = 0\,, \tag{2.21}$$

where the mass density ρ, the radial component of the velocity dispersion $\sigma_{\rm r}$, and the anisotropy α depend only on the radial coordinate r; we recall that the last term can be expressed in terms of the mass contained within a certain radius, because $d\Phi/dr = GM(r)/r^2$. This equation is often used to obtain the velocity dispersion of a stellar system from the surface brightness profile properly deprojected by assuming a radial profile for the mass-to-light ratio and for the anisotropy function.

An example of the application of this method can be found in Lützgendorf et al. (2011), to probe the dynamics of the central region of the globular cluster NGC 6388. The first input needed in this approach is the surface brightness profile, which is deprojected into the intrinsic density profile of the cluster. This can be done for example by applying the multi-Gaussian expansion (MGE) method developed by Emsellem et al. (1994); the basic approach of this method is to parametrize the projected surface brightness with a sum of Gaussians (this is done because the deprojection of a Gaussian function leads to a Gaussian function). To apply this parametrization and to compare the velocity profile derived from the Jeans equation to their data, Lützgendorf et al. (2011) used the Jeans Anisotropic MGE (JAM) equations for spherical systems, and the multi-Gaussian expansion developed by Cappellari (2002, 2008).

One of the shortcomings of this approach is that it is not a priori guaranteed that there exist a supporting distribution function corresponding to the fluid solutions that are found. Because the anisotropy type and profile are assumed arbitrarily, and manually changed until the obtained velocity dispersion reproduces the data, the modeling is degenerate: different assumed anisotropies could produce similar observable features.

2.3.2 Schwarzschild orbit superposition method

Schwarzschild (1979) computed a numerical model to describe a triaxial stellar system in dynamical equilibrium. To do that, he first chose a density distribution, and calculated the corresponding potential. Then he computed about 1500 orbits within this potential, each covering typically 100 oscillations through the system; the considered orbits belong to two families: box orbits and tube orbits around the long axis of the system. Finally, he reproduced the chosen density distribution by superposition of a subset of the available orbits, each populated by an appropriate number of stars.

This method was developed for elliptical galaxies. It is flexible and efficient and does not make any assumptions about the degree of velocity anisotropy, but starts from a given intrinsic density distribution.

An example of the use of this method is the description of the dynamics of ω Cen given by van de Ven et al. (2006). Under the assumption of axisymmetry, they obtained the mass model from a MGE parametrization of the observed surface brightness. This would be best obtained from a two-dimensional image, which gives direct information about the flattening and radial variations in the two-dimensional structure of the object. Instead, the authors decided to perform a one-dimensional MGE fit to the radial surface brightness profile, and after that use the available ellipticity profile to include flattening in the mass model. At first, they calculated models for a range of values in distance, inclination and constant V-band mass-to-light ratio; next, by setting the distance and the inclination at their measured best-fit values, they also calculated a large set of models with mass-to-light ratio varying with radius. All these models were then used to fit simultaneously the two-dimensional light distribution, and the mean velocity and velocity dispersion of both proper-motion components and along the line of sight, calculated in polar apertures on the plane of the sky. By comparing the predicted values with the observations, they obtained the model parameters and a goodness-of-fit parameter. van den Bosch et al. (2006) followed this same procedure to probe the dynamics of the globular cluster NGC 7078 (M15).

2.3.3 Dedicated N-body simulations

Recent improvements in computational speed of the codes for performing N-body simulations and the availability of accelerator hardware (GRAvity PipEs, Graphic Processing Units) have enabled the study of the entire dynamical evolution of globular clusters on a star-by-star basis. These numerical simulations can model in a realistic way the important effects of discreteness, mass segregation, binaries, rotation, core collapse, and time-dependent tides, which are known to govern the evolution of globular clusters. The possibility to study stellar systems in such a level of detail is surely interesting, but the contributions of so many different ingredients could generate some degeneracy, and the results need to be considered very carefully. Very recently, this method has been used to obtain a detailed description of individual globular clusters.

Zonoozi et al. (2011) performed a series of N-body simulations to create a realistic model for the outer halo Galactic globular cluster Pal 14. They computed a set of 66 models to find the initial conditions that best reproduce the observations, after being evolved for 11 Gyr; the number of stars they used in each simulation was in the range $7\times10^4 < N < 10^5$. The cluster Pal 14 was chosen because its low density, its large radius, and its small estimated mass make it the ideal target for this type of analysis.

Recently, D. C. Heggie started a simulation of the nearby Galactic globular cluster NGC 6121 (M4)[2]. He used as initial conditions those determined by Heggie & Giersz (2008), with a starting configuration containing more than 10^5 stars. The main goal of

[2] `http://www.maths.ed.ac.uk/~heggie/m4/intro.html`

this project was to clarify the importance of this type of dynamical analysis, and to point out its limits and difficulties.

2.4 Apparent lack of complete tests of dynamical models

As shown previously in this Chapter, a great variety of models and techniques is available to test the dynamics of globular clusters. Unfortunately, very often these tests are carried out only in relation to the available photometric profiles, without the corresponding tests on the associated kinematical profiles, in contrast to what is routinely done in the studies of early-type galaxies. Yet it would be important to take into account the kinematical measurements, because they can give stringent constraints on alternative dynamical scenarios, and determine the principal dynamical ingredients that can be considered responsible for the observed properties of globular clusters.

An example of this unsatisfactory situation is the fact that spherical King (1966) models have long been considered adequate in describing the dynamics of globular clusters, only on the basis of their ability in reproducing the observed surface brightness profiles (Trager et al. 1995; McLaughlin & van der Marel 2005). Essentially, it was taken for granted that the kinematical properties of globular clusters are similar to those of King models, even if direct tests of this assumption were in practice unavailable.

Some studies of Galactic globular clusters, constrained simultaneously by density and velocity dispersion profiles, are actually available, mainly based on multi-mass Michie-King models (e.g., see Gunn & Griffin 1979, Meylan et al. 1995, and Meylan & Mayor 1991 for NGC 5272, ω Cen, and NGC 6397, respectively), but a systematic and homogeneous investigation is still missing.

We point out that, on the galactic side, deep investigations of these issues, starting with the mid 1970s, have led to the remarkable discovery that bright ellipticals are generally supported by anisotropic pressure and contain significant amounts of dark matter inside the effective radius (e.g., see Chapter 24 in Bertin 2000). From the study of elliptical galaxies it has also been learned that structurally different models (as diagnosed by their kinematics or characterized by their virial coefficients) may have remarkably similar photometric profiles (e.g., see Appendix D of Bertin et al. 2002).

In Chapter 3 we will present the observable quantities that can be used to obtain a satisfactory dynamical description of globular clusters. In Chapters 4 and 6 we will show that it is crucial to consider the kinematical information available for these systems, in order to provide a satisfactory analysis of their dynamical properties.

CHAPTER 3

Observations and model testing

To determine whether a dynamical model offers a good representation of the dynamics of globular clusters, and in particular to determine which dynamical ingredients need to be considered in describing these systems, it is necessary to compare the profiles calculated by the models with the observed ones. Following the description of the available modeling techniques offered in the previous Chapter, in the present Chapter we give an overview of the available observational data, and on the methods that can be used to compare them with the models. In Sect. 3.1 and 3.2 we provide a description of the observable quantities giving information on the distribution of stars in the space and on their kinematic properties, respectively. Section 3.3 illustrates a possible model fitting procedure, and Sect. 3.4 gives some details on alternative methods.

3.1 Observations of the distribution of stars in globular clusters

The use of photographic plates marked the beginning of the studies of the distribution of stars in globular clusters. These observations provided the possibility to count stars in these systems, and were first used already at the end of the $19^{\rm th}$ century. The advantage of this technique is the large field of view, that allows to obtain an image that includes the entire cluster just with one exposure. It is particularly adequate to investigate the external parts of the clusters, but its poor spatial resolution prevents the astronomers from resolving the innermost parts of the systems, due to the extreme crowding conditions.

A way to overcome this issue was made possible by the development of photoelectric devices that measure the surface brightness through different apertures. Photoelectric techniques applied to astronomy were developed in 1940s, and since 1950s they were used to study the cores of globular clusters. This technique, combined with the previous one, has provided composite density profiles from the center to the very outermost parts of clusters.

Only in the 1980s, with the development of Charge-Coupled Devices (CCDs) for astronomical applications, coupled with software improvement for photometry in crowded fields (e.g., DAOPHOT by Stetson 1987, DOPHOT by Schechter et al. 1993), the brightest stars in the cores of all globular clusters have been at last fully resolved.

Photoelectric and, especially, CCD observations have allowed a systematic investigation of the inner surface brightness profiles of a large number of Galactic globular clusters. Clusters in the Magellanic Clouds were also studied, and the Hubble Space Telescope has finally provided the possibility of studying the surface brightness profiles of globular clusters in the nearby spiral galaxy M31.

3.1.1 Number density profiles

To construct the number density radial profile of a globular cluster it is necessary to have observational data able to provide star counts in the region occupied by the cluster. The usual procedure to build a number count profile is to divide the cluster into concentric annuli and count the number of stars per square arcminute that fall inside each annulus. A radial position is then associated to each annulus, and usually the middle radial position of each annulus is chosen. The error on each of the points is calculated as the square root of the number of stars, divided by the area of the annulus.

King et al. (1968) collected number count profiles for 54 Galactic globular clusters based on photometric plates. This work was followed by a study of the outer structure of 12 globular clusters carried out by Grillmair et al. (1995). They used deep photographic photometry in two colors to select and count member stars according to their position in the color-magnitude diagram; in this way, they reduced the contamination of foreground and background stars, and reached significantly low surface densities better than previously possible.

The measurements of star count density profiles were only obtained for this small set of Galactic globular clusters some decades ago. In the majority of cases the study of the structure of globular clusters is carried out by means of surface brightness profiles (see below). Recently, Miocchi et al. (2013) used an appropriate combination of high-resolution Hubble Space Telescope observations and wide-field, ground-based data to derive the radial stellar density profiles of 26 Galactic globular clusters from resolved star counts.

3.1.2 Surface brightness profiles

In analogy to what is done for number density profiles, the surface brightness profile is measured by dividing the cluster into concentric annuli, by summing the flux contribution of the stars located inside each of them, and by dividing the result by the area of the annulus. Again, the radial position associated with each annulus is usually its middle position. The error on the surface brightness is estimated by propagating the error on individual measurements of star magnitudes, which are calculated as the sum of this intrinsic photometric error, of the error of the absolute photometric zero-points, and of the mean calibration error.

A catalog of surface brightness profiles for Galactic globular clusters

Trager et al. (1995) (hereafter indicated as TKD95), presented a catalog of surface brightness profiles of 124 Galactic globular clusters, the largest collection ever gathered. These profiles are measured from inhomogeneous data, containing both surface brightness in different bands and star count data, that were combined by assuming that the color does not change with the radius. The authors divided the data in three sets, each with a different weight, according to the reliability of the measurements. For each globular cluster, the profile measured by TKD95 is composed of $N_{\rm p}$ photometric data-points, determined by the radius R_i measured in arcseconds, by the V band surface brightness $m_{\rm V}(R_i)$ measured at the radial position R_i and expressed in mag arcsec^{-2}, and by w_i, a weight that the authors assign to each measurement. We remark here that these surface brightness profiles are relative to the V band, even if observations in different bands were used to calculate them.

For the globular clusters analyzed in Chapters 4, 6, and 7, among those available, we decided to use the surface brightness profiles published in this catalog, to deal with a

homogeneous sample. This choice guarantees that the profiles have been constructed with the same method, even though the actual data come from different sources. This is the same starting point of McLaughlin & van der Marel (2005), who tested three spherical dynamical models (King, Wilson and power-law models) on a very wide sample of globular clusters, by considering only their photometric profiles.

The surface brightness data by TKD95 have to be properly corrected and treated before a comparison can be made with theoretical models. First, an extinction correction must be introduced, under the assumption that such extinction can be considered to be constant over the entire extent of each globular cluster. The extinction $A_{\rm V}$ can be estimated from the reddening listed in the Harris (2010) catalog and the correction on the surface brightness measurements can be calculated as $m(R_i) = m_{\rm V}(R_i) - A_{\rm V}$, for $i = 1, \ldots, N_{\rm p}$. This is the only correction that is necessary to apply to the data, assuming that TKD95 already removed any foreground and background contamination that could affect the measurements. Then, by following the procedure described by McLaughlin & van der Marel (2005), it is possible to estimate the uncertainties δm_i on the data: starting from the weights, they are calculated[1] as $\delta m_i = \sigma_\mu / w_i$. In the surface brightness profiles that we used for the dynamical analyses in Chapters 4, 6, and 7, we considered only the points with weights $w_i \geq 0.15$ in the original profile, as suggested by McLaughlin & van der Marel (2005).

More recent sources

Noyola & Gebhardt (2006) used the Hubble Space Telescope to study the central regions of a sample of Galactic globular clusters; they obtained surface brightness profiles by using integrated light with a method they developed and tested on simulated images. When compared with previous ground-based measurements, their profiles show different shapes for the inner regions. The new measured values of the central surface brightness are brighter than previously reported: this is mainly due to the higher spatial resolution of the Hubble Space Telescope.

Usually, the less reliable parts in the profiles published by TKD95 are the central regions: therefore, in the analyses described in Chapters 4 and 6, we decided to combine their profiles with the more recent and accurate surface brightness profiles we just described, when available. For the globular clusters NGC 104 (47 Tuc) and NGC 6341 (M92), we simply combined the profiles taken from TKD95 and from Noyola & Gebhardt (2006); for NGC 6254 (M10) and NGC 7078 (M15), we decided to combine the two data-sets by removing the points from the oldest source, when they do not match the more recent profile. In the case of NGC 7078, it should be emphasized that, with this treatment, the profile changes significantly in the central regions, and the central slope becomes steeper. For the analyses we carried out on NGC 5139 (ω Cen) in Chapters 4 and 6, we added to the surface brightness profile of TKD95 the inner points that Eva Noyola kindly provided us (Noyola et al. 2008); we notice however that the number of data-points in our final composite surface brightness profile of this cluster is significantly smaller than that of the other clusters, despite its larger extension (see Table 4.3).

3.1.3 Ellipticity profiles and isodensity contours

As outlined in Sect. 1.1, globular clusters present deviations from spherical symmetry that are measured by means of the ellipticity parameter ε. For the globular cluster ω

[1] σ_μ is a constant that varies from cluster to cluster, the value of which can be found in Table 6 in McLaughlin & van der Marel (2005).

Cen, an ellipticity profile was published by Geyer et al. (1983): it is the most extended ellipticity profile available for a Galactic cluster, as it reaches $\approx 0.5\, r_{\rm tr}$, where $r_{\rm tr}$ represents the standard truncation radius. In addition, Anderson & van der Marel (2010) report the ellipticity profile of the central region ($R \lesssim 250\ ''$) of this cluster. For most clusters, however, the only available profile is the one given by White & Shawl (1987).

In their star count analysis, Grillmair et al. (1995) found that most of their sample clusters show extra-tidal wings in their surface density profiles, which show a shape that is consistent with numerical studies of the tidal stripping of globular clusters; they identified the extra-tidal material with stars still in the process of leaving the clusters. Jordi & Grebel (2010) also found indications of the presence of tidal tails around some of the clusters they analyzed, and in one case they also detected a two-arm morphology. In all the other clusters in their sample, they found an extra-tidal halo, which in some cases they argue to be associated with the Sagittarius stream (Bellazzini et al. 2003; Forbes & Bridges 2010).

3.2 Observations of the kinematics of stars in globular clusters

The acquisition of kinematic data provides information on the amount and the distribution of mass in globular clusters; unfortunately, it is difficult to obtain large and accurate data-sets to be used for this purpose. Two types of kinematic data are available: those that provide measurements of velocities along the line of sight (often called radial velocities), and those that provide velocities on the plane of the sky, that is proper motions.

During the first half of the $20^{\rm th}$ century, stellar radial velocities were acquired from techniques using photographic plates; the typical errors of these measurements were 10 km s^{-1}, that is of the same order of magnitude of the expected value of velocity dispersion in globular clusters. The development of cross-correlation techniques provided an efficient way to determine radial velocities (Griffin 1967; Griffin & Gunn 1974); with the advent of such techniques, the typical errors on the measurements dropped to 0.5 km s^{-1}, providing an adequate tool for investigating the internal dynamics of globular clusters. At the beginning, technological developments were mainly driven by the need of small errors on radial velocity measurements, as required in order to probe the low values of the internal velocity dispersion of globular clusters. More recently, improvements in the design of the instruments have also been motivated by the need of increasing the number of measurements that can be obtained at one time.

Fiber-fed, multi-object spectrographs like FLAMES at the Very Large Telescope, HYDRA at Kitt Peak, and AAOmega at the Anglo Australian Observatory can obtain velocities for a large sample of stars in one time. Similar results can be obtained by using Fabry-Perot interferometers (Gebhardt et al. 1995). Slit spectroscopy is instead only rarely used for these systems (but see Chapter 8). In Appendix B we provide a list of the published data-sets of radial velocities for stars in Galactic globular clusters.

The value of the velocity dispersion near the cluster center is important for the understanding of cluster dynamical evolution, in particular with reference to the phenomenon of core collapse and to the presence of an intermediate-mass black hole. This value is difficult to obtain for high-concentration globular clusters by means of radial velocities of individual stars, because of serious crowding problems. A possibility to overcome this difficulty is to measure the broadening of integrated-light spectra obtained from an area of a few square arcseconds at the center of the cluster. The first observations of this type, which is a standard technique for elliptical galaxies, are those obtained for 10 clusters and described by Illingworth (1976). With the advent of modern Integral Field

Units mounted on spectrographs at large telescopes, it has been possible to measure accurate velocity dispersion in the center of Galactic globular clusters; for example, see Lützgendorf et al. (2011, 2012, 2013a).

Proper motions provide two-dimensional kinematic information (see, e.g. Wybo & Dejonghe 1995, 1996). For a cluster at a distance of 5 kpc, a velocity dispersion of 5 km s^{-1}corresponds to a displacement of 20 milliarcseconds per century. For a long time, even in the best studied clusters, the errors in the measurement of proper motions have been comparable in size to the motions themselves. This explains why only very few studies of cluster internal proper motions have been made (Lupton et al. 1987; Leonard et al. 1992).

The advent of the Hubble Space Telescope has made it possible to obtain proper-motion measurements for a sample of Galactic globular clusters. Bellini et al. (2013) presented preliminary results of a large project aimed at measuring this quantity for more than 20 Galactic clusters[2]. For these objects there are two or more well-separated epochs in the archive, spanning up to more than 10 years. The photometric and astrometric techniques developed by the authors have allowed them to measure the positions of tens of thousands of stars per cluster within one arcminute from the center, with typical proper-motion errors of ~ 0.02 mas yr^{-1}, which translates into ~ 0.8 km s^{-1} for a typical cluster.

3.2.1 Velocity dispersion profiles

In the following we will describe a procedure that can be used to measure the velocity dispersion profile of globular clusters, starting from a set of line-of-sight (radial) velocities of single stars. We used this method to calculate the profiles presented in Chapters 4, 6, 7, and 8.

First, it is necessary to divide the data in several radial bins containing an equal number of stars. It is important to carefully chose the binning prescription that represents the best compromise between having a profile with a large number of points and having accurate points: on the one hand, in fact, by increasing the number of bins, that is by decreasing the number of data per bin, a profile with a very large number of points would be obtained, but each of the points would have large velocity dispersion errors; on the other hand, by considering bins with a very large number of data the resulting profile would have a small number of points, even if the single points would have very small errors (we refer the reader to Sects. 4.1.1 and 7.2.1 for a discussion on the number of velocity data that would be needed in order to have a satisfactory velocity dispersion profile).

Secondly, the mean velocity and the velocity dispersion in each bin are measured by means of the procedure described by Pryor & Meylan (1993). Initially, the mean velocity $\langle v_{\rm r} \rangle$ and the dispersion[3] $\sigma_{\rm c}$ are estimated for the entire set of velocities; the mean velocity represents the overall velocity of the entire cluster. Then, taking this value as a constant for the entire cluster, the line-of-sight velocity dispersion $\sigma(R_i)$ and the related accuracy $\delta\sigma_i$ are determined inside each of the bins in which the data have been divided. For each bin, the distance from the center R_i can be indicated as the mean of the radial positions of the stars that it contains. We notice that, in following this procedure, we ignored the possible presence of rotation and therefore considered the various kinematical data-

[2]Among these 20 clusters, there are 8 of the clusters we analyzed in Chapter 4

[3]We note that the velocity dispersion $\sigma_{\rm c}$ is sometimes used as an estimate for the central velocity dispersion σ_0 (see Sect.1.2), even if it is not in principle guaranteed that the two quantities have a similar value. In this Thesis, we will keep the notation introduced here to differentiate these quantities.

points in each bin, after subtraction of the systemic velocity, to contribute only to velocity dispersion (random motions).

A similar procedure can be used also to produce velocity dispersion profiles from proper-motion data: the profiles are generated by dividing the data-sets in radial bins, by considering the mean velocity of the entire data-set as a constant value throughout the cluster, and by measuring the velocity dispersion and the associated uncertainty for each bin, using the mean of the radial positions of the stars that it contains as an estimate of its distance from the center. The difference with respect to the case in which line-of-sight velocities are used is that in this case two profiles are calculated: $\sigma_{\rm T}(R)$ and $\sigma_{\rm R}(R)$, the projected tangential and radial component of proper-motion velocity dispersion, respectively.

In principle, we might consider using unbinned data, to avoid loss of information (more on this topic can be found in Sect. 3.4). In this Thesis, however, we preferred to follow the more traditional approach of constructing the associated one-dimensional profiles, a method that can be applied in a similar way to both kinematical and photometric data and that allows us to follow well-established fitting procedures used in the past (especially in studies of elliptical galaxies; see Sect. 3.3).

3.2.2 Rotation profiles

To calculate the rotation profile from a data-set of line-of-sight velocities, the following standard procedure is usually used (e.g., see Cote et al. 1995; Bellazzini et al. 2012); we adopted this method to calculate the rotation profiles presented in Chapter 6.

Before building a rotation profile it is necessary to identify the position angle ϕ of the projected rotation axis in the plane of the sky, defined as the angle between the rotation axis and the north direction, measured east of north. To do that, the line-of-sight velocities data-set is divided in two halves by a line passing through the center of the cluster with a given position angle, and for each subsample the mean line-of-sight velocity $\langle v_{\rm r} \rangle$ is computed. The position angle is then varied in fixed steps (for example, in Chapter 6 we considered steps of 10°), and the difference between the mean velocities $\Delta\langle v_{\rm r} \rangle$ is plotted against the position angle ϕ. A fit of a sine function to this pattern is then carried out: the position angle at which the maximum difference in mean velocities is reached corresponds to the rotation axis and the amplitude of the sine function gives an estimate of the significance of the internal rotation. The value obtained in this way for the position angle is then used to rotate the Cartesian coordinate system in the plane of the sky by aligning it with the directions of the major and minor axes.

At this point, it is possible to proceed to build the rotation profiles. First, the measured mean systemic velocity is subtracted from each data-set. Then, the line-of-sight velocities data-set are divided in bins along the major axis, and finally each bin is assigned the average position on the major axis, the mean velocity of the stars that it contains, and the associated uncertainty to this measure.

When dealing with a proper-motion data-set, the rotation profile can be constructed by dividing the data-set in radial bins and by calculating for each bin the mean radial distance and the mean velocity, separately for the tangential and projected radial components (for an example, see Fig. 6.7).

3.2.3 Anisotropy profiles

In principle, if the three components of the velocity are available for a set of stars in a globular cluster, it is possible to calculate its anisotropy profile, as defined in Eq. (2.19),

from the components of the velocity dispersion associated with each bin. Unfortunately, this is not usually possible, because the sets of line-of-sight velocities and of proper motions (when available) are not composed by the same sample of stars.

Therefore, a different definition of anisotropy is adopted. This is the ratio of the velocity dispersion in the tangential component to the velocity dispersion in the radial component, $\sigma_{\rm T}(R)/\sigma_{\rm R}(R)$. This quantity is useful to obtain an immediate indication of the type of anisotropy that is present in the cluster: values of $\sigma_{\rm T}/\sigma_{\rm R} \approx 1$ indicate isotropy in velocity space, values of $\sigma_{\rm T}/\sigma_{\rm R} > 1$ indicate the presence of tangential anisotropy, and values of $\sigma_{\rm T}/\sigma_{\rm R} < 1$ indicate radial anisotropy. We calculated this quantity for three Galactic globular clusters, as shown in Chapter 6.

3.2.4 Line-of-sight velocity distribution

To conclude the list of observable quantities that can be used to probe the kinematics of stellar systems, we consider here the line-of-sight velocity distribution, which is widely used to study the internal dynamics of ultra compact dwarf galaxies, dwarf spheroidals, and elliptical galaxies. Only a brief introduction is given here: a more detailed discussion about this quantity is postponed to Chapter 10.

Observed spectra of the stellar systems mentioned above are usually obtained by means of slit spectroscopy, and are assumed to be the convolution of a suitably chosen template spectrum and a broadening function. This broadening function corresponds to the distribution of stars over line-of-sight velocities, and it is sometimes referred to as the "line profile" (van der Marel & Franx 1993). To recover the line-of-sight velocity distribution, it is necessary to deconvolve the spectra using the template. Many techniques have been developed to recover the line-of-sight velocity distribution from the data, their evolution being mainly driven by the improvements in the observational techniques and in the quality of the data. Early methods mostly used Fourier-based techniques (i.e., see Tonry & Davis 1979), but more recently several methods that allow for the fitting of the line-of-sight velocity distribution directly in the pixel space have been developed (see Rix & White 1992 and Cappellari & Emsellem 2004).

This observable quantity is not commonly used to study the dynamics of Galactic globular clusters, because it is usually not possible to obtain spectra for a significant part of these systems (as can be done instead for larger and more distant systems by means of slit spectroscopy), and because the available radial velocity data-sets are too small to enable the construction of such function from discrete data. An analysis of the dynamics of extra-galactic globular clusters in terms of their line-of-sight velocity distribution might be possible.

3.3 Fitting procedure

In the following we describe a procedure that can be adopted to perform the statistical analysis of the data. We basically follow Bertin et al. (1988).

This Section describes in detail the procedure we employed for the dynamical analysis presented in Chapter 4. We therefore consider here the case of a cluster for which both the surface brightness and the velocity dispersion profiles are available, and we compare these observed profiles to the ones calculated by some dynamical models (e.g., in the case of Chapter 4, King and $f^{(\nu)}$ models). In Chapters 5, 6, 7, and 8 we will present the results of fits obtained by means of procedures similar to the ones described here.

3.3.1 Photometric fit

The photometric fit determines which equilibrium model (within a considered family of dynamical models) has the projected mass distribution that best reproduces the surface brightness profile, under the assumption that:

$$\Sigma(R) = \frac{M}{L}\lambda(R) \,, \tag{3.1}$$

where $\Sigma(R)$ is the model surface mass density, $\lambda(R)$ the model surface luminosity density, and the mass-to-light ratio M/L is considered to be constant in the cluster. From the photometric data, we perform a fit that allows us to determine three parameters for each model:

- Ψ, the concentration parameter, which determines the shape of the surface brightness and velocity dispersion profiles;
- r_0, the scale radius;
- μ_0, the central surface brightness.

We might determine the values of these parameters by minimizing the quantity:

$$\sum_{i=1}^{N_\mathrm{p}} \left[\frac{m(R_i) - S(R_i/r_0) + \mu_0}{\delta m_i} \right]^2 \,, \tag{3.2}$$

where S is the surface density expressed in magnitudes, but we found that it is more convenient to minimize:

$$\chi^2_\mathrm{p} = \sum_{i=1}^{N_\mathrm{p}} \left[\frac{l(R_i) - k\hat{\Sigma}(R_i/r_0)}{\delta l_i} \right]^2 \,, \tag{3.3}$$

because the chi-squared function turns out to be more stable, as already pointed out by McLaughlin & van der Marel (2005). The connection between Eqs. (3.2) and (3.3) is easily made, by taking into account the following relations:

$$\begin{aligned} &m(R_i) - m_0 = -2.5\log[l(R_i)] \\ &S(R_i/r_0) = -2.5\log[\hat{\Sigma}(R_i/r_0)] \\ &\mu_0 - m_0 = 2.5\log k \,, \end{aligned} \tag{3.4}$$

where the zero-point $m_0 = 26.422$ allows us to express the observed surface brightness $m(R_i)$ in solar units; the observed luminosities $l(R_i)$ are expressed in solar units and δl_i are calculated from δm_i and represent the errors on luminosities. The quantity $\hat{\Sigma}(R_i/r_0)$ is the surface density, normalized to its central value; from this point of view, the parameter k is related to the mass-to-light ratio.

Even if we calculated the parameters from the luminosities, we report the results in terms of magnitudes, because in this way a comparison with the data is more natural. To calculate the surface brightness profile $\mu(R)$ that best reproduces the data, we choose the model identified by Ψ, we calculate the normalized projected mass-density profile, and then we rescale it radially with r_0 and vertically with μ_0.

We notice that there are only two independent fit parameters, because $k = k(\Psi, r_0)$. Hence, the value of the reduced $\chi^2_{\rm p}$ is:

$$\widetilde{\chi}^2_{\rm p} = \frac{\chi^2_{\rm p}}{N_{\rm p} - 2} \, . \tag{3.5}$$

To have a quantitative estimate of the quality of the fit, it is convenient to calculate also the mean and maximum residuals:

$$\begin{aligned} &\langle \Delta\mu \rangle = \tfrac{1}{N_{\rm p}^{1/2}} \left\{ \textstyle\sum_{i=1}^{N_{\rm p}} [m(R_i) - \mu(R_i)]^2 \right\}^{1/2} \\ &(\Delta\mu)_{\rm max} = \max_{i=1,\ldots,N_{\rm p}} |m(R_i) - \mu(R_i)| \, . \end{aligned} \tag{3.6}$$

3.3.2 Kinematic fit

The parameters identified by the photometric fit determine a model, characterized by the parameter Ψ, the profiles of which are rescaled with r_0. At this point, we perform a fit to the kinematic data to find the central line-of-sight velocity dispersion, that is the velocity scale needed to rescale vertically the normalized projected velocity dispersion profile calculated from the dynamical models. We calculate the value of this scale, σ_0, as the one that minimizes:

$$\chi^2_{\rm k} = \sum_{i=1}^{N_{\rm k}} \left[\frac{\sigma(R_i) - \sigma_0 \sigma_{\rm P}(R_i)}{\delta\sigma_i} \right]^2 \, , \tag{3.7}$$

where $\sigma_{\rm P}(R_i)$ is the projected velocity dispersion calculated from the model, dependent on the rescaled radial coordinate. In this case, the values of the reduced χ^2 and of the residuals can be found from the following expressions:

$$\begin{aligned} &\widetilde{\chi_{\rm k}}^2 = \tfrac{\chi^2_{\rm k}}{N_{\rm k} - 1} \\ &\langle \Delta\sigma \rangle = \tfrac{1}{N_{\rm k}^{1/2}} \left\{ \textstyle\sum_{i=1}^{N_{\rm k}} [\sigma(R_i) - \sigma_0 \sigma_{\rm P}(R_i)]^2 \right\}^{1/2} \\ &(\Delta\sigma)_{\rm max} = \max_{i=1,\ldots,N_{\rm k}} |\sigma(R_i) - \sigma_0 \sigma_{\rm P}(R_i)| \, . \end{aligned} \tag{3.8}$$

One might argue that a more sensible way to perform the fit would be by means of a single fit procedure, using the combined $\chi^2_{\rm tot} = \chi^2_{\rm p} + \chi^2_{\rm k}$, defined as the sum of the photometric and of the kinematic contribution. We did perform tests of this different procedure and found that the results are equivalent to those obtained by performing the photometric fit first and then the kinematic fit at fixed Ψ and r_0. This confirms the qualitative expectation that the kinematical data, being less numerous and less accurate with respect to the photometric ones, have little weight in determining Ψ and r_0 and are only needed to determine the scale σ_0, that is, the relevant mass-to-light ratio.

3.3.3 Goodness of the photometric and kinematic fits

To measure the goodness of the photometric and kinematic fits, we referred to the confidence intervals on the χ^2-distribution. The probability density function of the χ^2 distribution is defined as:

$$f(x; n) = \frac{e^{(-x/2)} x^{(n/2-1)}}{2^{n/2} \Gamma(n/2)} \tag{3.9}$$

when $x \geq 0$, and zero otherwise. The parameter n corresponds to the number of degrees of freedom and Γ denotes the gamma function (e.g., see Abramowitz & Stegun 1972, Sect. 26.4).

The two-sided confidence interval relative to a confidence level ζ on the χ^2 probability density function is defined as the interval $[\chi^2_{\rm inf}, \chi^2_{\rm sup}]$ such that

$$\zeta = \int_{\chi^2_{\rm inf}}^{\chi^2_{\rm sup}} f(x;n)dx \; ; \tag{3.10}$$

and that:

$$1 - \frac{\zeta}{2} = \int_0^{\chi^2_{\rm inf}} f(x;n)\, dx = \int_{\chi^2_{\rm sup}}^{\infty} f(x;n)\, dx \; . \tag{3.11}$$

3.3.4 Errors on the best-fit parameters

For the methods described below, we refer mainly to Press et al. (2007). In the case of the photometric fit, we used the following procedure to calculate the formal errors on the parameters. First we calculated the Hessian matrix:

$$H_{ij} = \frac{\partial^2 \chi^2}{\partial x_i \partial x_j} \; , \tag{3.12}$$

where $i = 1, 2, 3$ and $x_1 = \Psi$, $x_2 = r_0$ and $x_3 = \mu_0$; then we calculated the covariance matrix:

$$[E] = 2[H]^{-1} \; . \tag{3.13}$$

Finally, we obtained the errors:

$$\delta x_i = (E_{ii})^{1/2} \; . \tag{3.14}$$

In the case of the kinematic fit, in which $\chi^2_{\rm k}$ depends analytically only on the parameter σ_0, we can immediately calculate:

$$\delta\sigma_0 = \left(\frac{2}{\partial^2 \chi^2_{\rm k} / \partial \sigma_0^2} \right)^{1/2} \; . \tag{3.15}$$

In addition to errors, we identified the relevant confidence regions and intervals for the various parameters, after defining a likelihood function $\Lambda = e^{-\chi^2/2}$. First, we calculated confidence regions in the (Ψ, r_0) plane, after marginalizing the likelihood function on k, in the following way:

$$\Lambda(\Psi, r_0) = \int e^{-\chi^2/2} dk \; . \tag{3.16}$$

We identified the regions corresponding to confidence levels of 68.3% and 95.4%. To check the results, we compared them with the regions defined by the curves of constant χ^2 with the appropriate values (see Sect. 15.6 in Press et al. 2007). For each globular cluster and for the families of models, we notice that the regions identified with these two methods overlap in a consistent way.

We also calculated the confidence intervals on the parameters Ψ, r_0 and σ_0 (for the last parameter, the calculation can be done immediately, because the kinematic likelihood

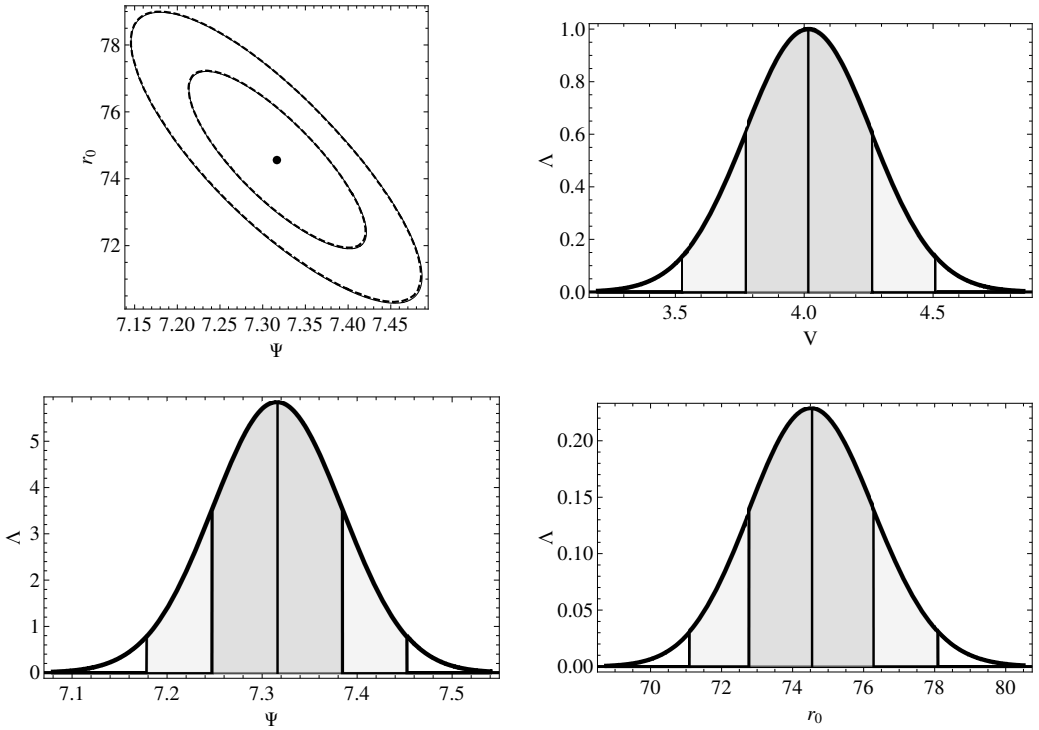

Figure 3.1: Confidence regions and confidence intervals on NGC 6121 King model parameters. The top left figure shows the overlap of the confidence regions, corresponding to confidence levels of 68.3% and 95.4% (solid lines), and the curves of constant χ^2 (dashed lines); the black dot marks the position of the maximum of the likelihood (that is the minimum of χ^2). The top right figure shows the confidence intervals for the likelihood depending on σ_0; the bottom figures show the confidence intervals on the parameter Ψ and r_0; the dark gray area corresponds to the confidence level of 68.3%, the light gray area to the confidence level of 95.4%; a solid vertical line marks the position of the maximum of the likelihood (that is the minimum of χ^2).

depends only on σ_0; for the other parameters, we have to marginalize once more the likelihood function), corresponding to confidence levels of 68.3% and 95.4%. Comparing them with the errors calculated with the covariance matrix method, we found that the results are consistent.

In Fig. 3.1 we show an example of the confidence regions and intervals calculated for the King best-fit model for the globular cluster NGC 6121. The top left panel shows the overlap of the confidence regions (solid lines) corresponding to confidence levels of 68.3% and 95.4%, and the curves of constant χ^2 (dashed lines). It is clear that there is a good agreement between the two relevant pairs of curves. The bottom panels show the confidence intervals calculated on the marginalized likelihood for the parameters Ψ and r_0, and the top right panel those for the parameter σ_0; in these figures the confidence intervals are shown as shaded areas. By comparing the extent of the dark gray area with the values of the uncertainties on the corresponding parameters (see Table 4.2 in Chapter 4), we see that the different methods lead to consistent results.

3.4 Dealing with discrete kinematic tracers

As shown previously in this Chapter, discrete tracers are commonly used to study the kinematics of a stellar system. The population of tracers to use needs to be chosen carefully, as the one best representing the dynamics of the system.

Discrete tracers can be used in two different ways. The first has been discussed in Sect. 3.2, and requires the binning of the data in reasonable spacial intervals, to recover a specific quantity, such as the velocity dispersion or the rotation profile. This is the method usually used when analyzing globular clusters data. Even if they give useful indications, and allow us to compare observed profiles with theoretical ones, binning methods suffer from a loss of information. In fact, in order to estimate the desired quantity, each bin must contain a sufficient number of stars, as explained in Sect. 3.2. By following this approach, a data-set of a few hundred stars will be therefore reduced to only almost ten bins.

Another method, commonly used to study the dynamics of dwarf spheroidals and galaxies, is to test a dynamical model by maximizing the likelihood function of the data-set, without binning the data. This method has been widely described by Wilkinson & Evans (1999) and Wilkinson et al. (2002). It was originally proposed by Little & Tremaine (1987) and further developed by Kochanek (1996). The procedure involves the calculation of the probability $P(\{R_i, v_{\mathrm{r},i}\}_{i=1,\dots,N}|\vartheta)$, where ϑ represents the sets of parameters of the model to be tested, and $\{R_i, v_{\mathrm{r},i}\}_{i=1,\dots,N}$ is the set of data. P is calculated by scanning a grid of values for the parameters. Using the Bayes theorem and assuming the shape of prior probabilities for the values of these parameters, the most likely parameter values can then be determined by maximizing the probability P.

Recently, a discrete approach to dynamical modeling has been proposed by Watkins et al. (2013), and applied to study the properties of the globular cluster ω Cen. First, they used Jeans models to calculate the predicted mean velocity and velocity dispersion, under a given set of model parameters. Then, they adopted a maximum likelihood approach to identify the best models to reproduce the data, by exploring the parameter space. They included a contaminating population in the models, instead of eliminating suspected non-member stars a priori: in this way, they used all the available data, avoiding the chance to eliminate a member star mistakenly considered an interloper.

The work done by Watkins et al. (2013) on ω Cen has been possible mainly because for this cluster very accurate and rich data-sets of proper motions and line-of-sight velocities are available; recently, the same method has been applied by den Brok et al. (2014) to study the globular cluster NGC 7078. Other Galactic clusters do not have such an abundance of data, and this method might not give equally satisfactory results.

Part I

Exploring the role of pressure anisotropy and rotation in the dynamics of globular clusters

CHAPTER 4

Globular clusters in different relaxation conditions

As shown in Sect. 1.3.1, Galactic globular clusters are characterized by different relaxation conditions. For many of them, the relevant relaxation times are shorter than their age, so that they are commonly considered to be close to thermodynamical relaxation, with a distribution function close to a Maxwellian. King (1966) models are defined by a distribution function of this type, and provide a good representation of quasi-relaxed stellar systems (see Appendix A.1): for this reason they are in principle well suited to describe globular clusters.

However, some large globular clusters have very long relaxation times, and thus need not be in a quasi-relaxed state: their structure might be more similar to that of elliptical galaxies, for which pressure anisotropy is thought to play an important role. This feature is well represented by the distribution function that defines the family of non-truncated radially-biased anisotropic $f^{(\nu)}$ models (see Bertin & Trenti 2003, and references therein); these models were constructed to describe the products of (incompletely) violently relaxed elliptical galaxies (see Appendix A.3).

It is therefore reasonable to expect that more relaxed globular clusters would be better described by isotropic King models, whereas less relaxed systems might be better represented by means of anisotropic $f^{(\nu)}$ models. This scenario has been tested by comparing these dynamical models with observations of Galactic globular clusters in different relaxation conditions. The comparison is performed by fitting both surface brightness and velocity dispersion profiles, with the method described in Sect. 3.3.

This Chapter is organized as follows. In Sect. 4.1 we introduce the sample of globular clusters selected for this study, and we describe the available data-sets. In Sect. 4.2 we present the results of our work and in Sect.4.3 we discuss our findings in view of previous results and known issues. Finally, in Sect. 4.4 we draw our conclusions.

This Chapter is based on the article Zocchi et al. (2012).

4.1 The selected sample

4.1.1 Selection criteria

The sample of globular clusters is selected on the basis of the following criteria.

1. We exclude post-core-collapse globular clusters, that is, we reject the clusters labeled as post-core-collapse by Harris (2010). The reason is that we wish to test dynamical models on the global scale, avoiding the subtle modeling issues that characterize the central regions of these systems, especially if phenomena a priori known to go beyond the considered modeling are involved.

2. We choose globular clusters for which an accurate and extended surface brightness profile is available.

3. We select clusters for which at least 140 stellar radial (line-of-sight) velocities have already been measured. We impose a lower limit to the number of measured velocities, because we wish to extract from the data a reasonably well-defined velocity dispersion profile; the value of this limit is fixed in a way that it allows us to include in the analysis globular clusters that belong to the different relaxation classes defined in Sect. 1.3.1.

4. We exclude from our list the clusters that have less than 35 stellar radial velocities inside the projected half-light radius[1] $R_{\rm h}$. We introduce this further requirement, because we wish to analyze velocity dispersion profiles that characterize the stellar systems on the largest radial extent, and the central regions are crucial to test how well the dynamical models perform in describing the systems.

For only few globular clusters the desired data are available. Indeed, of the 31 Galactic globular clusters with a reasonable number of radial velocities (i.e., at least 40 line-of-sight velocity measures on the entire spatial extent of the cluster), 3 are flagged as post-core-collapse, 9 have less than 140 velocity data, and 6 have less than 35 data inside their projected half-light radius (see Table B.2). In the Harris (2010) catalog, NGC 362 and NGC 7078 are indicated as possible post-core-collapse clusters (as suggested by Trager et al. 1995), but we decided to keep them because, according to their concentration parameter in the Harris catalog, it is still possible to obtain an acceptable fit with King models. In this way, we are left with 13 globular clusters that match our selection criteria. In relation to the relaxation classes defined in Sect. 1.3.1, our set of globular clusters contains 5 well-relaxed clusters, 6 clusters in an intermediate relaxation condition, and 2 partially relaxed clusters.

To better characterize our sample in terms of the radial extent of their radial velocity data, we consider the ratio of the radius of the last kinematical point to the projected half-light radius[2], $R_{\rm V}/R_{\rm h}$, and the ratio of the radius of the last kinematical point to the truncation radius, $R_{\rm V}/r_{\rm tr}$. We judge the following values of the two ratios, $R_{\rm V}/R_{\rm h} \geq 3$ and $R_{\rm V}/r_{\rm tr} \geq 0.8$, to be satisfactory. All the selected globular clusters satisfy the first relation, and all but four globular clusters satisfy the second condition.

Table 4.1 gives the sample of selected globular clusters, listed in order of increasing core relaxation time $\log T_{\rm c}$. The upper part of the table contains relaxed globular clusters, the middle part those in an intermediate relaxation condition; partially relaxed clusters are shown in the lower part. For each object, the values of the adopted cluster distance from the Sun $d_\odot$ (expressed in kpc), the concentration parameter[3] C, the logarithm of the core relaxation time $\log T_{\rm c}$, the logarithm of the half-mass relaxation time $\log T_{\rm M}$ (where $T_{\rm c}$ and $T_{\rm M}$, in other papers often indicated with the symbols $t_{\rm rc}$ and $t_{\rm rh}$, are expressed in years) and the ellipticity ε are recorded (as listed in the Harris 2010 catalog). In addition, the maximum rotational velocity $V_{\rm rot}$ (in km s^{-1}; the references for these values are Lane et al. 2011 for the globular clusters for which we use the kinematic data published in this paper, and Meylan & Heggie 1997 for the others), the number of velocity data-points

[1] The values of this quantity are reported in the Harris (2010) catalog, where the notation is $r_{\rm h}$. In other studies, this quantity is often referred to as the effective radius, and is indicated as $R_{\rm e}$.

[2] We recall that, as noted in Sect. 2.2, we indicate with R the projected (two-dimensional) radial distance from the center, and with r the intrinsic (three-dimensional) radial distance.

[3] We distinguish here between the concentration parameter c, defined by Eq. (A.3), and the concentration parameter C defined using the core radius $R_{\rm c}$ in place of r_0 in Eq. (A.3).

Table 4.1: The selected globular clusters.

Globular Cluster	$d_\odot$	C	$\log T_\mathrm{c}$	$\log T_\mathrm{M}$	ε	V_rot	N_V	$N_\mathrm{V,h}$	$R_\mathrm{V}/R_\mathrm{h}$	$R_\mathrm{V}/r_\mathrm{tr}$	Ref.
NGC 362	8.6	1.76	7.76	8.93	0.01	0.0	208	92	4.22	0.33	(1)
NGC 7078 (M15)	10.4	2.29	7.84	9.32	0.05	1.7	1777	1298	16.94	0.62	(2)
NGC 104 (47 Tuc)	4.5	2.07	7.84	9.55	0.09	2.2	2475	709	19.27	1.44	(3), (4)
NGC 6121 (M4)	2.2	1.65	7.90	8.93	0.00	0.9	200	55	10.36	0.87	(4)
NGC 6341 (M92)	8.3	1.68	7.96	9.02	0.10	2.5	295	42	13.96	1.14	(5)
NGC 6218 (M12)	4.8	1.34	8.19	8.87	0.04	0.15	242	58	10.38	1.06	(4)
NGC 6254 (M10)	4.4	1.38	8.21	8.90	0.00	...	147	47	5.22	0.55	(6)
NGC 6656 (M22)	3.2	1.38	8.53	9.23	0.14	1.5	345	116	8.40	0.88	(4)
NGC 3201	4.9	1.29	8.61	9.27	0.12	1.2	399	201	10.35	1.27	(7)
NGC 6809 (M55)	5.4	0.93	8.90	9.29	0.02	0.25	728	311	7.79	1.44	(4)
NGC 288	8.9	0.99	8.99	9.32	...	0.25	171	68	5.53	0.93	(4), (6)
NGC 5139 (ω Cen)	5.2	1.31	9.60	10.09	0.17	7.9	2060	554	5.97	0.62	(8), (9)
NGC 2419	82.6	1.37	9.87	10.63	0.03	0.6	166	38	14.63	1.74	(10)

Notes. From left to right, the following quantities are displayed: distance from the Sun (kpc), concentration parameter, logarithm of the core relaxation time (years), logarithm of the half-mass relaxation time (years), ellipticity, rotational velocity (km s^{-1}), total number of velocity data-points available, number of velocity data-points inside the projected half-light radius, ratio of the radius of the outermost velocity point to the projected half-light radius, and ratio of the radius of the outermost velocity point to the truncation radius. The sources of the kinematical data are listed in the last column (see main text for references of the other quantities).

References. (1) Fischer et al. 1993; (2) Gebhardt et al. 2000; (3) Gebhardt et al. 1995; (4) Lane et al. 2011; (5) Drukier et al. 2007; (6) Carretta et al. 2009; (7) Cote et al. 1995; (8) Mayor et al. 1997; (9) Reijns et al. 2006; (10) Ibata et al. 2011.

available $N_{\rm V}$, the number of velocity data-points inside the projected half-light radius $N_{\rm V,h}$, the ratios of the radius of the outermost velocity point $R_{\rm V}$ to the projected half-light radius $R_{\rm h}$ and to the truncation radius $r_{\rm tr}$, and the sources of the kinematic data are given in the last columns.

4.1.2 Data-sets

The surface brightness profiles

To deal with a homogeneous sample, we decided to use the surface brightness profiles provided by Trager et al. (1995), as previously done also by McLaughlin & van der Marel (2005). This choice guarantees that the profiles have been constructed with the same method, even though the actual data come from different sources. For some clusters, more accurate surface brightness profiles have been recently measured by Noyola & Gebhardt (2006) in the innermost regions of several Galactic globular clusters. For the clusters in our sample, when available, we combined these recent profiles with the ones provided by Trager et al. (1995) (see Sect. 3.1.2 for a more detailed description).

The velocity dispersion profiles

We calculated velocity dispersion profiles as described in Sect. 3.2.1, starting from the radial velocities data-sets of the selected clusters. As shown in Table 4.1, for the majority of the clusters in our sample, only one data-set of stellar radial velocities is used for the dynamical analysis presented here. In the following we discuss in detail the cases in which a composition of different data-sets has been performed or which require some additional comments.

For the majority of the clusters of the sample, other data-sets are available, as listed in Table B.1. For the globular clusters NGC 6121, NGC 6656 and NGC 6809, we decided to consider only the data-sets from Lane et al. (2011), because they are more complete and more radially extended. In the case of NGC 3201, NGC 6341, and NGC 7078, we preferred to consider only older data-sets; in fact, the more recent data-points from Carretta et al. (2009), Mészáros et al. (2009), and Smolinski et al. (2011) are not very numerous and not as well distributed radially as those of the older sources we used.

For NGC 104, three data-sets of radial velocities are available. We decided to consider only data from the two most numerous ones (the third, by Carretta et al. 2009, is discarded because of its limited radial extent). The data from Gebhardt et al. (1995) are more centrally concentrated than those from Lane et al. (2011).[4] In order to have a complete sampling on the entire radial extent of the cluster, we decided to define a mixed data-set, composed of 499 data from Gebhardt et al. (1995), located inside $100''$, and 1976 data from Lane et al. (2011), located outside that radius.

NGC 288 has been studied by Carretta et al. (2009) and by Lane et al. (2011). Since these papers publish the coordinates of each star, we were able to identify the stars in common between the two data-sets: for the stars in the overlap, velocity measures by Carretta et al. (2009), being more accurate, have been preferred. Finally, we excluded three stars for which the value of the velocity deviates by more than $4\sigma_{\rm c}$ from the mean

[4] Giersz & Heggie (2011) make some cautionary remarks about the velocity dispersion profile reported by these authors. In particular, the selection criteria adopted by Lane et al. (2011) could lead to the exclusion of some high-velocity stars, with consequent lowering of the central velocity dispersion, and to the inclusion of nonmember stars affecting the outer part of the profile. By using the composite data-set described above, we should be able to obtain reliable values of the velocity dispersion in the central regions, while the outermost points may still be affected by the inclusion of nonmember stars.

radial velocity $\langle v_{\rm r} \rangle$ (for the definition of these quantities, see Sect. 3.2.1), obtaining a final sample of 171 data.

In the case of NGC 5139, we merged the largest sample of velocity data available (Reijns et al. 2006) with the sample provided by Mayor et al. (1997), which provides measurements for stars located in the central region of the cluster. A delicate issue regarding this cluster is the controversial position of its center, which plays an important role also in our analysis, because we wish to build a radial-dependent velocity dispersion profile, starting from stellar positions expressed in right ascension and declination (for Reijns et al. 2006). To carry out a proper merging of the two data-sets, we have used the position of the center proposed by Mayor et al. (1997); to calculate radial distances, we have followed the procedure described by van de Ven et al. (2006). Other data-sets are available for this cluster, but they have not been considered for the dynamical analysis presented in this Chapter.

4.2 Fits and trends for the different relaxation classes

The values of the dimensionless parameters and the physical scales of the two families of models determined by the photometric and kinematic fits are presented in Table 4.2 (the fitting procedure is described in Sect. 3.3). Note that, in general, for the $f^{(\nu)}$ models relatively low values of the concentration parameter Ψ are identified (see Appendix A.3). Quantitative information about the best-fit models and the observational profiles, such as the number of the photometric and kinematic points, the values of the relevant reduced chi-squared, and the corresponding residuals, are listed in Table 4.3. To evaluate the quality of the fits, in Table 4.4 we compare the values of the reduced photometric and kinematic chi-squared, denoted by $\widetilde{\chi}^2_{\rm p}$ and $\widetilde{\chi}^2_{\rm k}$ respectively, with the two-sided 90% confidence interval, calculated with respect to the reduced χ^2-distribution, characterized by the appropriate number of degrees of freedom (see Sect. 3.3.3 for details).

The surface brightness and the line-of-sight velocity dispersion profiles determined by the fit procedure for the models, together with the observed profiles for the clusters in the first, second, and third relaxation class, are shown in Figs. 4.1, 4.2, and 4.3, respectively. In the panels, solid lines correspond to the best-fit King models and dashed lines to the best-fit $f^{(\nu)}$ models. The vertical solid (dashed) lines mark the position of the King ($f^{(\nu)}$) model projected half-light radii. For the surface brightness profiles, the data from Trager et al. (1995) are indicated with circles, the data from other sources with squares. For the velocity dispersion data, the horizontal bars indicate the length of the radial bin in which the data-points have been calculated; they do not have a role in determining the fit. For each data-point the errors are shown as vertical error bars. Note that, even if we insisted on selecting clusters with a reasonable number of data inside $R_{\rm h}$, for about half of the clusters, the kinematic profiles are undersampled in their central region.

In the following part of this section we will try to give a general assessment of the quality of the fits in the various cases. The properties of the fits are best obtained by checking directly the values provided in Tables 4.3 and 4.4 and by inspection of Figs. 4.1-4.3. Table 4.3 shows that generally, for a given cluster, $\widetilde{\chi}^2_{\rm p} > \widetilde{\chi}^2_{\rm k}$, because the photometric profiles are characterized by a larger number of data-points with reported smaller errorbars. Table 4.4 shows that NGC 6656 is the only cluster for which the values of $\widetilde{\chi}^2_{\rm p}$ and $\widetilde{\chi}^2_{\rm k}$ for the two models are inside the relevant 90% confidence interval. Within the King modeling, four clusters have $\widetilde{\chi}^2_{\rm p}$ inside the 90% confidence interval and nine have $\widetilde{\chi}^2_{\rm k}$ inside the 90% confidence interval; within the $f^{(\nu)}$ modeling, six clusters have $\widetilde{\chi}^2_{\rm k}$ inside the 90% confidence interval. A visual inspection of the fits (in particular, see the kinematic

Table 4.2: Dimensionless parameters and physical scales of the best-fit models.

	King Models				$f^{(\nu)}$ Models			
NGC	Ψ	r_0	μ_0	σ_0	Ψ	r_0	μ_0	σ_0
(1)	(2)	(3)	(4)	(5)	(6)	(7)	(8)	(9)
104	8.58 ± 0.01	23.09 ± 0.23	14.33 ± 0.01	12.27 ± 0.19	8.21 ± 0.02	250.44 ± 1.46	14.29 ± 0.01	14.07 ± 0.22
288	4.82 ± 0.10	91.03 ± 2.86	20.02 ± 0.03	2.85 ± 0.19	3.91 ± 0.24	79.54 ± 5.37	19.88 ± 0.03	3.70 ± 0.25
362	7.80 ± 0.03	10.21 ± 0.11	14.66 ± 0.01	8.31 ± 0.44	6.86 ± 0.05	52.73 ± 1.09	14.70 ± 0.01	9.26 ± 0.50
2419	6.62 ± 0.04	19.70 ± 0.31	19.43 ± 0.03	5.04 ± 0.43	4.24 ± 0.09	29.86 ± 0.83	19.44 ± 0.04	7.28 ± 0.61
3201	6.17 ± 0.11	76.99 ± 3.05	18.35 ± 0.08	4.28 ± 0.19	4.09 ± 0.40	103.48 ± 11.71	18.33 ± 0.08	5.01 ± 0.23
5139	6.27 ± 0.05	136.94 ± 2.33	16.42 ± 0.04	14.83 ± 0.25	4.31 ± 0.07	150.63 ± 3.07	16.35 ± 0.04	23.41 ± 0.40
6121	7.32 ± 0.07	74.56 ± 1.76	17.00 ± 0.11	4.01 ± 0.30	7.39 ± 0.09	464.49 ± 20.40	17.01 ± 0.11	4.21 ± 0.31
6218	6.11 ± 0.07	51.56 ± 1.51	17.65 ± 0.07	3.93 ± 0.30	4.00 ± 0.14	60.69 ± 2.52	17.57 ± 0.07	5.58 ± 0.42
6254	6.26 ± 0.04	53.63 ± 0.60	16.88 ± 0.09	6.21 ± 0.37	2.67 ± 0.13	51.48 ± 1.45	16.84 ± 0.09	9.69 ± 0.59
6341	7.54 ± 0.02	14.72 ± 0.13	15.31 ± 0.01	9.28 ± 0.41	5.99 ± 0.04	50.00 ± 0.80	15.44 ± 0.01	12.77 ± 0.56
6656	6.47 ± 0.11	86.18 ± 2.34	16.41 ± 0.11	6.47 ± 0.38	5.99 ± 0.26	241.58 ± 26.46	16.41 ± 0.11	7.19 ± 0.42
6809	4.44 ± 0.11	129.11 ± 4.06	19.12 ± 0.04	2.92 ± 0.13	3.92 ± 0.19	101.53 ± 5.39	18.99 ± 0.04	3.61 ± 0.17
7078	8.09 ± 0.02	7.72 ± 0.13	14.07 ± 0.03	11.83 ± 0.24	8.17 ± 0.05	65.88 ± 0.94	13.59 ± 0.06	12.79 ± 0.26

Notes. For each cluster, named in column (1), for King and $f^{(\nu)}$ models, we list: the concentration parameter Ψ, in other papers often indicated as W_0 (Col. (2) and (6)), the scale radius r_0, expressed in arcsec (Col. (3) and (7), as defined in equations (A.2) and (A.10); note that they are intrinsic quantities; they are recorded here in arcseconds for easier comparison with the observations, as shown in Figs. 4.1-4.3), the V band central surface brightness μ_0 in mag arcsec^{-2} (Col. (4) and (8)), and the central line-of-sight velocity dispersion σ_0 in km s^{-1} (Col. (5) and (9)). Formal errors on the various parameters are also recorded (see Sect. 3.3.4).

Table 4.3: Quality of the fits.

			King Models						$f^{(\nu)}$ Models					
NGC	$N_{\rm p}$	$N_{\rm k}$	$\widetilde{\chi}^2_{\rm p}$	$\langle\Delta\mu\rangle$	$(\Delta\mu)_{\rm max}$	$\widetilde{\chi}^2_{\rm k}$	$\langle\Delta\sigma\rangle$	$(\Delta\sigma)_{\rm max}$	$\widetilde{\chi}^2_{\rm p}$	$\langle\Delta\mu\rangle$	$(\Delta\mu)_{\rm max}$	$\widetilde{\chi}^2_{\rm k}$	$\langle\Delta\sigma\rangle$	$(\Delta\sigma)_{\rm max}$
(1)	(2)	(3)	(4)	(5)	(6)	(7)	(8)	(9)	(10)	(11)	(12)	(13)	(14)	(15)
104	231	16	3.487	0.41	4.68	7.411	1.03	3.39	6.433	0.24	1.53	10.367	1.34	2.98
288	85	6	1.251	0.30	0.98	0.442	0.21	0.33	3.891	0.46	1.10	2.040	0.46	0.78
362	239	8	3.113	0.58	7.09	1.307	0.99	1.74	1.563	0.15	0.92	3.345	1.55	2.45
2419	137	6	1.983	0.21	1.10	1.344	0.98	2.21	1.492	0.16	0.83	0.471	0.50	0.83
3201	80	16	1.308	0.38	1.49	1.783	0.83	1.73	1.289	0.36	1.48	4.005	1.21	2.29
5139	72	37	3.750	0.36	2.08	1.974	1.73	4.90	21.742	0.80	1.62	3.406	2.07	4.38
6121	228	10	1.460	0.27	1.33	0.450	0.47	0.94	1.710	0.29	1.33	0.581	0.52	0.93
6218	143	11	1.185	0.32	1.12	0.584	0.54	0.91	2.663	0.40	1.12	0.765	0.59	1.10
6254	162	6	5.046	0.37	2.75	0.606	0.48	0.65	4.372	0.22	1.12	1.844	0.89	1.15
6341	118	8	8.439	0.41	2.51	1.418	0.51	1.02	20.589	0.33	1.06	2.354	1.01	2.37
6656	143	7	1.019	0.23	0.66	0.942	0.67	1.36	1.056	0.23	0.66	1.699	0.89	1.83
6809	114	13	1.165	0.32	1.04	1.103	0.40	0.96	4.404	0.59	1.34	2.967	0.64	1.35
7078	310	35	6.136	0.75	5.00	3.229	1.33	3.06	3.813	0.36	1.41	1.981	1.37	3.25

Notes. For each cluster, named in column (1), we provide the number of points in the surface brightness (2) and in the velocity dispersion (3) profile. For King and $f^{(\nu)}$ models, we list: the reduced best-fit photometric chi-squared $\widetilde{\chi}^2_{\rm p}$ (Col. (4) and (10)), the mean (Col. (5) and (11)) and maximum (Col. (6) and (12)) photometric residuals, the reduced best-fit kinematic chi-squared $\widetilde{\chi}^2_{\rm k}$ (Col. (7) and (13)), the mean (Col. (8) and (14)) and maximum (Col. (9) and (15)) kinematic residuals.

Table 4.4: Two-sided confidence intervals for the reduced χ^2-distribution with n degrees of freedom.

	Photometric Fits					Kinematic Fits				
NGC	n	King $\widetilde{\chi}^2_{\rm p}$	$f^{(\nu)}$ $\widetilde{\chi}^2_{\rm p}$	$\widetilde{\chi}^2_{\rm inf}$	$\widetilde{\chi}^2_{\rm sup}$	n	King $\widetilde{\chi}^2_{\rm k}$	$f^{(\nu)}$ $\widetilde{\chi}^2_{\rm k}$	$\widetilde{\chi}^2_{\rm k,inf}$	$\widetilde{\chi}^2_{\rm k,sup}$
(1)	(2)	(3)	(4)	(5)	(6)	(7)	(8)	(9)	(10)	(11)
104	229	3.49	6.43	0.85	1.16	15	7.41	10.37	0.48	1.67
288	83	1.25	3.89	0.76	1.27	5	0.44	2.04	0.23	2.21
362	237	3.11	1.56	0.85	1.16	7	1.31	3.35	0.31	2.01
2419	135	1.98	1.49	0.81	1.21	5	1.34	0.47	0.23	2.21
3201	78	1.31	1.29	0.75	1.28	15	1.78	4.01	0.48	1.67
5139	70	3.75	21.74	0.74	1.29	36	1.97	3.41	0.65	1.42
6121	226	1.46	1.71	0.85	1.16	9	0.45	0.58	0.37	1.88
6218	141	1.19	2.66	0.81	1.20	10	0.58	0.77	0.39	1.83
6254	160	5.05	4.37	0.82	1.19	5	0.61	1.84	0.23	2.21
6341	116	8.44	20.59	0.79	1.23	7	1.42	2.35	0.31	2.01
6656	141	1.02	1.06	0.81	1.20	6	0.94	1.70	0.27	2.10
6809	112	1.17	4.40	0.79	1.23	12	1.10	2.97	0.44	1.75
7078	308	6.14	3.81	0.87	1.14	34	3.23	1.98	0.64	1.43

Notes. For each cluster, named in column (1), separately for the photometric and the kinematic fits, we provide the number of degrees of freedom of each fit (Col. (2) and (7)), the reduced best-fit chi-squared for King (Col. (3) and (8)) and for $f^{(\nu)}$ (Col. (4) and (9)) models, and the lower (Col. (5) and (10)) and upper (Col. (6) and (11)) boundaries of the two-sided 90% confidence level interval for the reduced χ^2-distribution with n degrees of freedom.

fits for NGC 362, NGC 3201, NGC 6121, NGC 6656, NGC 6809 and the inner photometric profiles of NGC 3201, NGC 6121, NGC 6218, NGC 6656, and NGC 7078) also suggests that some systematic trends are clearly missed by both families of models.

First class

Within the class of relaxed globular clusters, for NGC 362 and NGC 7078 it is evident that the King models cannot reproduce the observed surface brightness profiles, and that the $f^{(\nu)}$ models perform better, especially for describing the outer parts of the cluster. As to the observed velocity dispersion profiles, we see that for NGC 7078 the $f^{(\nu)}$ profile is formally more adequate (at the 99.9% confidence level), while for NGC 362 the King profile is the closer to the observations (at the 90% confidence level). We should recall that these two globular clusters are flagged in the Harris (2010) catalog as post-core-collapse clusters, although the listed value of the concentration parameter C is smaller than 2.5. Indeed, the observations indicate that there are some processes that cannot be captured by King models (with particular reference to the shallow cusp in the photometric profile of NGC 7078), even if it is possible to obtain a global satisfactory fit.

By looking at the plots in Fig. 4.1, NGC 104 and NGC 6341 appear to have both observed surface brightness and velocity dispersion profiles well represented by King models (for NGC 6341 the King $\widetilde{\chi}^2_{\rm k}$ falls within the 90% confidence interval), in spite of

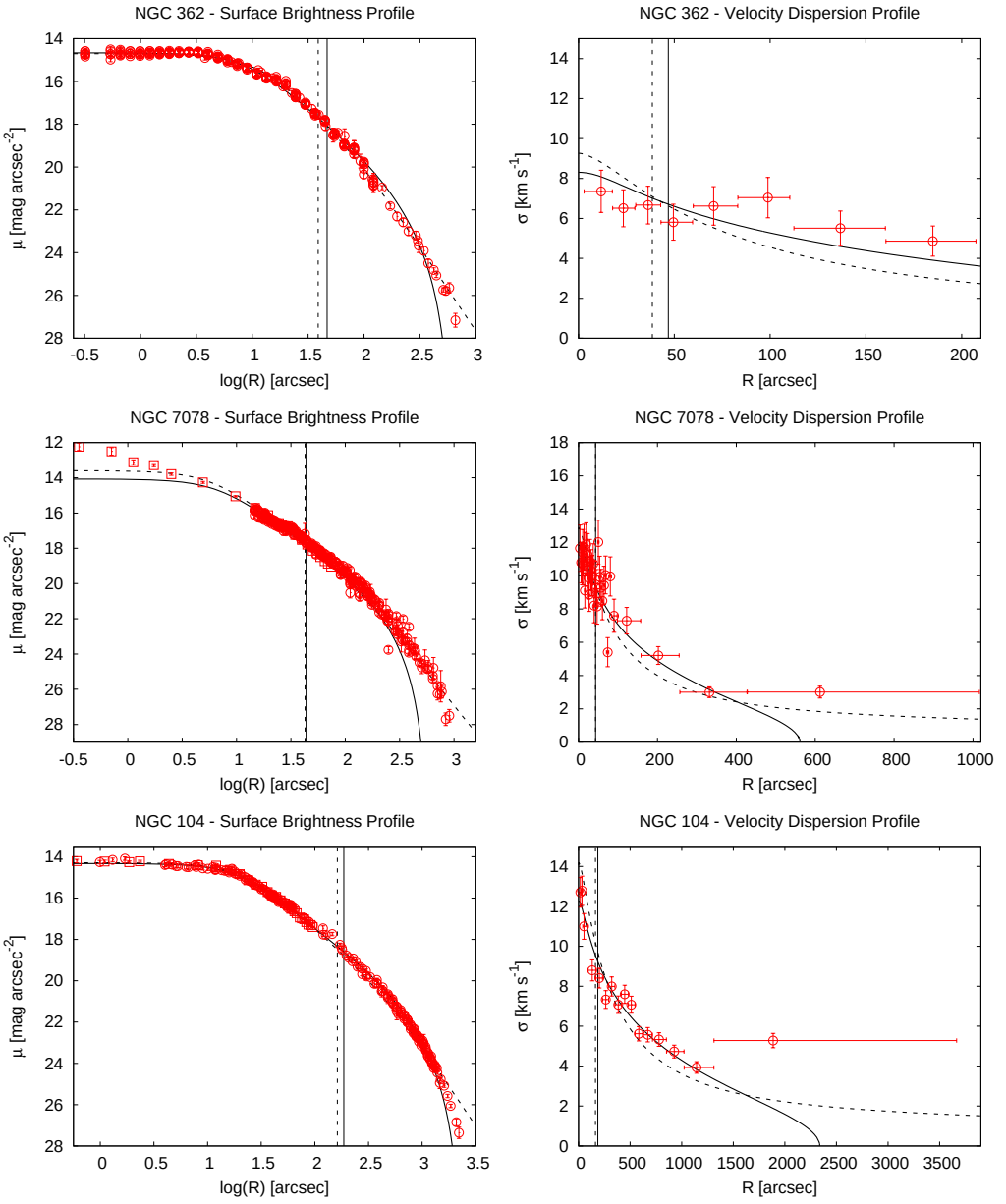

Figure 4.1: Fits by King models and anisotropic $f^{(\nu)}$ models to the surface brightness profiles and to the line-of-sight velocity dispersion profiles of relaxed globular clusters. In all panels, solid lines correspond to the King-model fits, dashed lines to $f^{(\nu)}$-model fits; the vertical solid lines mark the position of the King model projected half-light radii, $R_{\rm h}$, the dashed ones the position of the $f^{(\nu)}$ model projected half-light radii. For the surface brightness profiles, the data from Trager et al. (1995) are indicated with circles, the data from other sources (see Sect. 4.1.2) with squares. For each data-point, errors are shown as vertical error bars; in the case of the velocity dispersion profile, the horizontal bars indicate the length of the radial bin in which the data-points have been calculated and have no role in the fitting procedure (see Sect. 3.3).

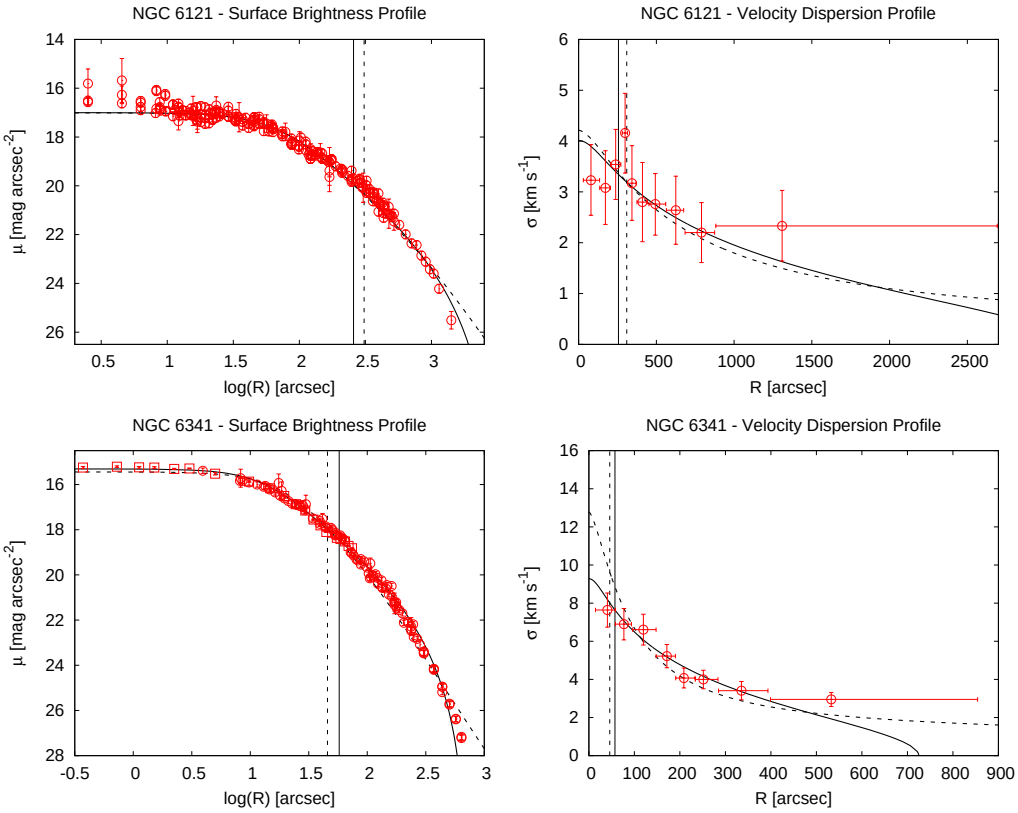

Figure 4.1: (continued)

the fact that, from Table 4.4, the fits cannot be considered entirely satisfactory. Curiously, NGC 6121 is equally well described by the two models; the values of the reduced chi-squared are slightly lower for the King model, but in practice the quality of the two fits is similar.

We notice that for NGC 104 and NGC 6121 it is particularly evident that the last point in the velocity dispersion profile is significantly higher than expected by both models. A partial explanation of this fact could be the very large extent of the radial interval in which it is calculated. Therefore, it is important to obtain more velocity data-points in the outer regions to clarify this issue.

Second class

Best-fit profiles for globular clusters in the intermediate relaxation class are shown in Fig. 4.2. For NGC 288, NGC 6218, and NGC 6809 King models provide a better fit to both the surface brightness and the velocity dispersion profile (at the 90% confidence level in all cases).

For the other globular clusters in this relaxation class the results are less sharp. In fact, for NGC 3201 and NGC 6254 the surface brightness profiles are formally better reproduced by $f^{(\nu)}$ models (for the first, at 95% confidence level), while the corresponding velocity dispersion profiles are formally better described by King models (at the 95%

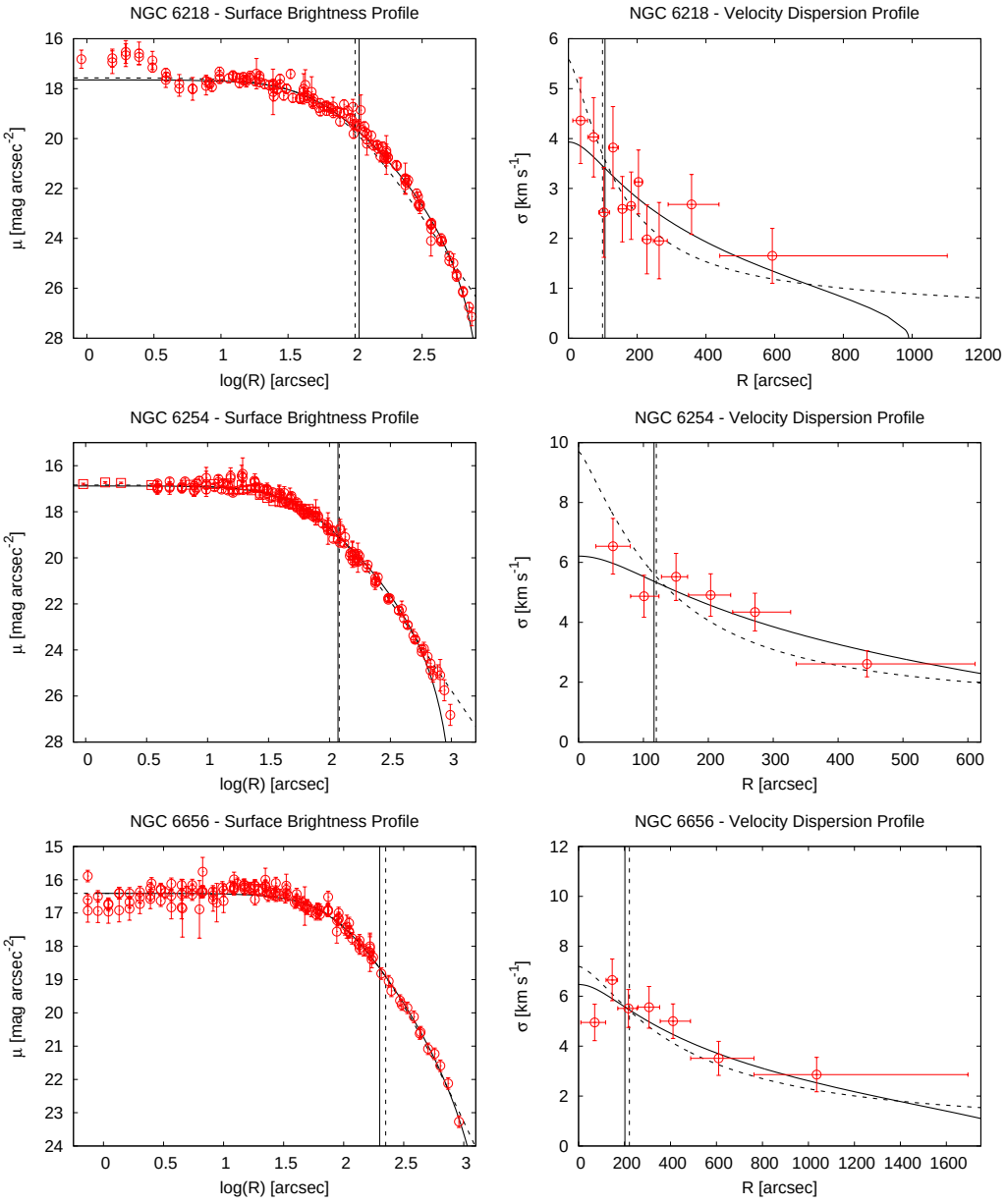

Figure 4.2: Fits by King models and anisotropic $f^{(\nu)}$ models to the surface brightness profiles and to the line-of-sight velocity dispersion profiles of globular clusters in the intermediate relaxation condition, in the same format as in Fig. 4.1.

and 90% confidence level, respectively). The best-fit concentration parameter obtained by means of $f^{(\nu)}$ models for the globular cluster NGC 6254 is very small; we recall that for these models low concentration models exhibit a sizable core (see Appendix A.3). For NGC 6656 both the surface brightness and the velocity dispersion profile are approx-

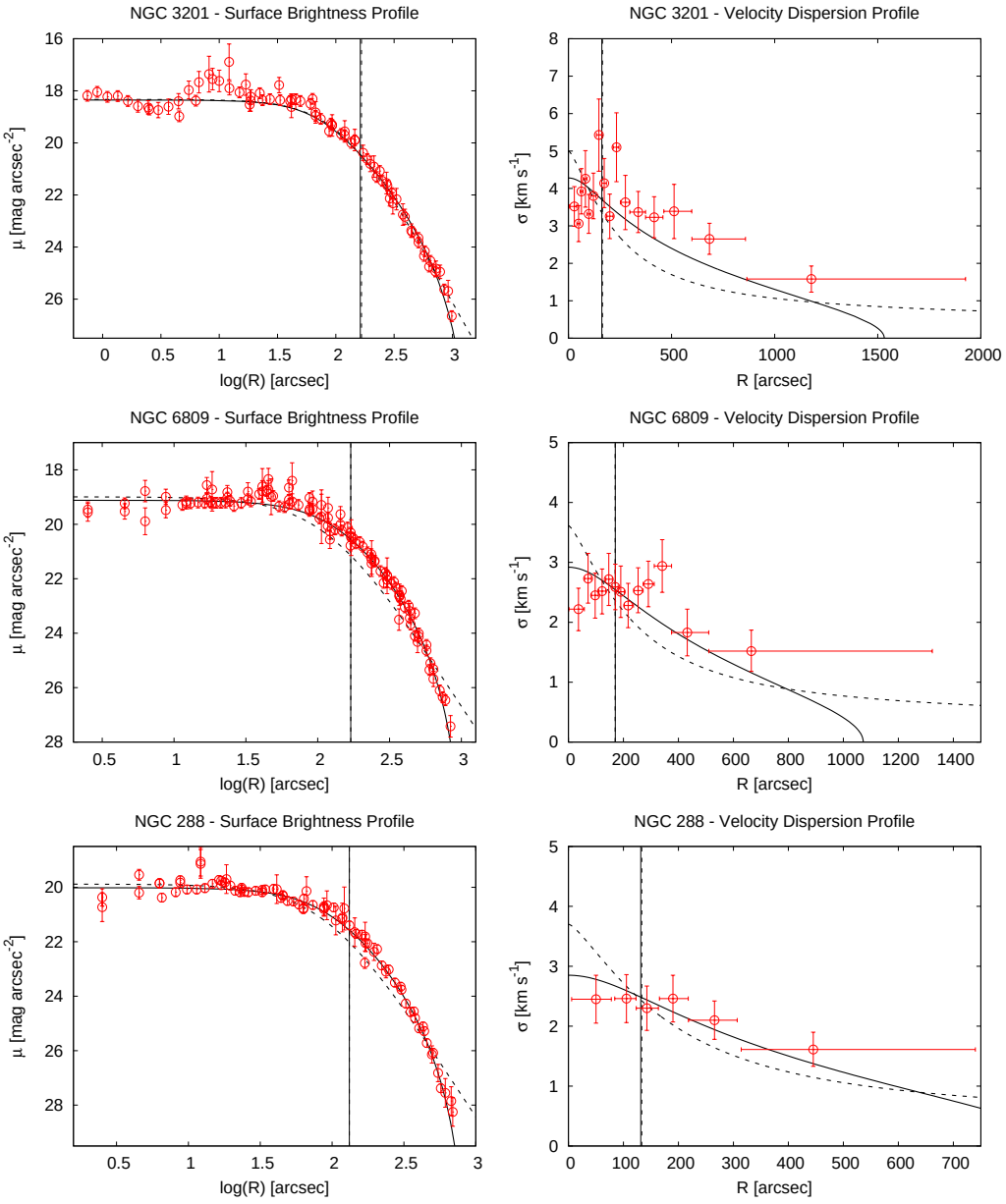

Figure 4.2: (continued)

imately equally well reproduced by the two families of models (at the 90% confidence level in all cases).

For NGC 3201, NGC 6656, and NGC 6809 the velocity dispersion profiles have an irregular shape in the central regions: even if King models formally perform better than $f^{(\nu)}$ models, they are unable to reproduce the observations. We tried to choose a different binning for the data and we found that this irregularity does not depend on the way in

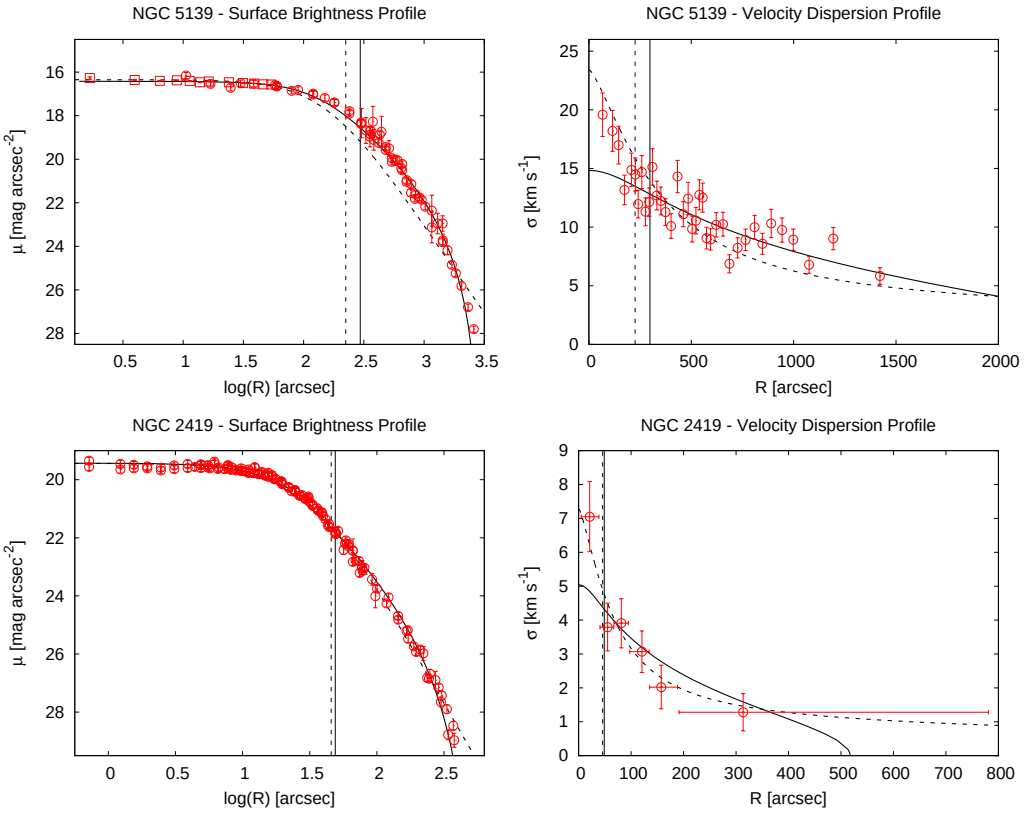

Figure 4.3: Fits by King models and anisotropic $f^{(\nu)}$ models to the surface brightness profiles and to the line-of-sight velocity dispersion profiles of partially relaxed globular clusters, in the same format as in Fig. 4.1.

which the observed velocity dispersion profile is constructed from the available dataset. Clearly, more data are necessary in order to obtain a more convincing description of these systems.

Third class

In Fig. 4.3, we show the best-fit profiles for partially relaxed globular clusters. For these two clusters we see discordant results: for NGC 2419 $f^{(\nu)}$ models are more adequate for describing the data (at the 99.99% and 90% confidence level for the photometric and kinematic fit, respectively), while for NGC 5139 King models provide a better fit to the observed profiles. However, even if formally King models perform better in describing the kinematic profiles of NGC 5139, they do not provide a satisfactory description of the kinematics of the central parts of the cluster (see Fig. 4.3); in this respect, the $f^{(\nu)}$ models give a better representation of the inner kinematics.

General results

To summarize, we found that, as expected, $f^{(\nu)}$ models tend to perform globally better than King models for the least relaxed globular cluster of our sample, NGC 2419. For NGC 2419, the good performance of $f^{(\nu)}$ models might correspond to the partial relaxation condition of the cluster, consistent with the physical picture that motivates the definition of the $f^{(\nu)}$ models, as outlined at the beginning of this Chapter. In addition, for three clusters in the second relaxation class (NGC 3201, NGC 6254, and NGC 6656), $f^{(\nu)}$ models are competitive with King models. Furthermore, $f^{(\nu)}$ models can describe well a relatively steep central slope of the velocity dispersion profile, even when the corresponding photometric profile is cored, while King models and other isotropic models (such as Wilson 1975 models) are unable to reproduce this kinematical behavior. This fact is evident from the kinematic fits for NGC 2419, NGC 5139 and for possibly one cluster in the intermediate relaxation condition (NGC 6218).

As far as the behavior of the photometric profiles at large radii is concerned, we see that, especially for NGC 104, NGC 362, NGC 6254, NGC 6341, and NGC 7078 King models do not provide a good description of the truncation, as noted in a number of previous studies (in particular, see McLaughlin & van der Marel 2005; Jordi & Grebel 2010; Küpper et al. 2010, in which the outermost parts of the surface brightness profiles are appropriately modeled by using N-body simulations). In some cases, the observed profile falls between the King and the $f^{(\nu)}$ profiles. This suggests that truncated $f^{(\nu)}$ models might behave systematically better than King models for describing these stellar systems. To a large extent, the modification by truncation in phase space of the anisotropic (non-truncated) $f^{(\nu)}$ models is complementary to the generalization of the isotropic (truncated) King models to models characterized by anisotropic pressure, that is, the so-called Michie-King models (in which the truncated Maxwellian is associated with the anisotropic factor of the Eddington models; see Michie 1963, Gunn & Griffin 1979). Of course, the simple physical picture offered by King, $f^{(\nu)}$, and Michie-King models still suffers from a number of limitations. Such a simple picture is bound to fail in the modeling of clusters in which core collapse has taken place. Therefore, it is not surprising that clusters such as NGC 362 and NGC 7078, even if they belong to the first relaxation class, are not described by isotropic King models as well as expected.

We wish to reiterate that, in general, the kinematic fits are crucial to assess if a model is actually able to describe a given globular cluster (as we anticipated in Sect. 2.4). Unfortunately, the observed velocity dispersion profiles are generally less accurate and less reliable, with respect to the surface brightness profiles; not only the outer parts (radii close to the truncation radius), but also the inner parts (inside the half-light radius) are often not well sampled as would be desired. The present study confirms that in the future it would be desirable to acquire new and better kinematic data (our effort is described in Chapters 7 and 8).

4.3 Isotropic vs. anisotropic models

4.3.1 Global results

The values of the relevant structural parameters derived from the best-fit models are presented in Table 4.5. To compare quantitatively the properties of the best-fit models selected in the two families of models for each globular cluster, we can correlate the values of the derived parameters, such as the half-mass radius $r_{\rm M}$, the total mass M, the

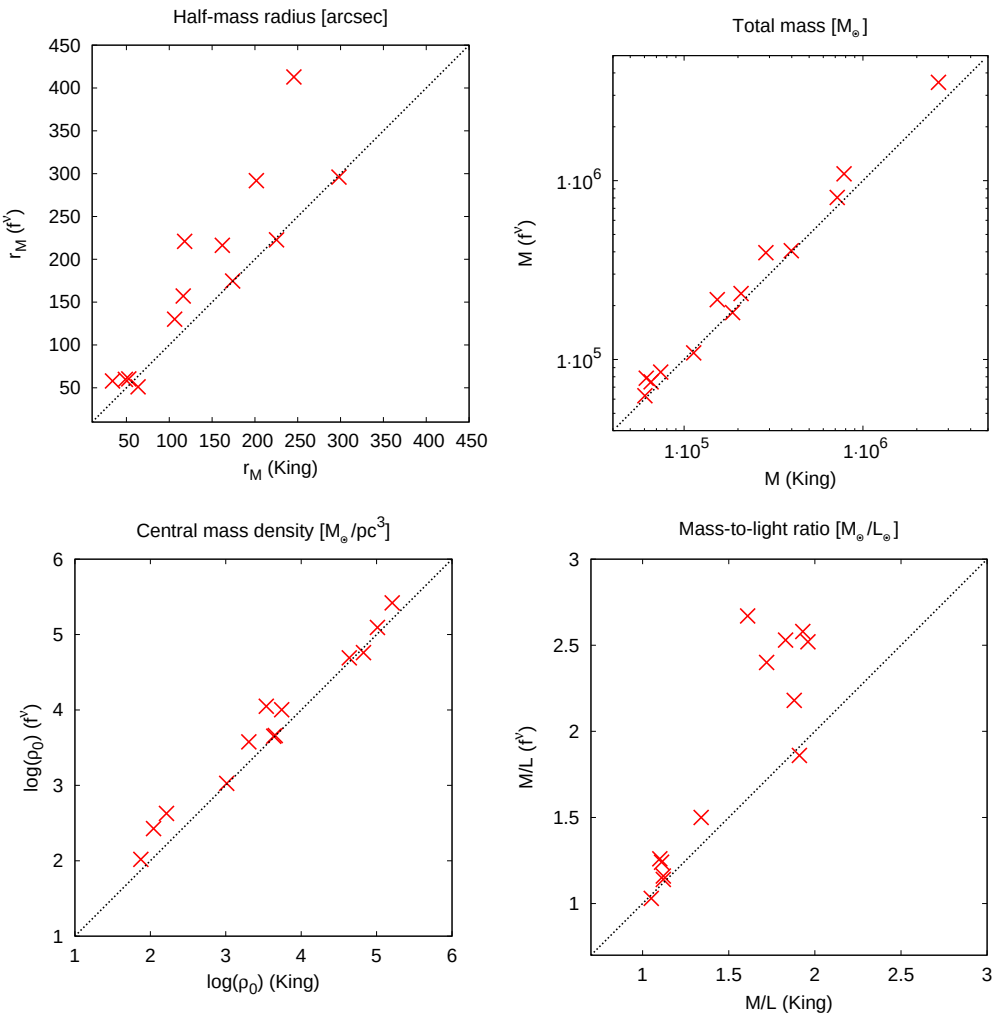

Figure 4.4: Comparison between the values of the structural parameters derived from King and $f^{(\nu)}$ best-fit models. The top left panel shows, as crosses, the values of half-mass radii, the top right panel the total masses, the bottom left panel the central mass density and the bottom right panel the mass-to-light ratios. In each panel, the x-axis refers to the values calculated with King models, and the y-axis to those calculated with $f^{(\nu)}$ models; the dotted diagonal line denotes the identity relation. The intrinsic quantity $r_{\rm M}$ would be best given in parsecs, but it is reported here in arcseconds for easier comparison with the observed profiles and with the projected half-light radius $R_{\rm h}$ represented in the previous figures.

central mass density ρ_0 and the mass-to-light ratio M/L. These correlations are illustrated in Fig. 4.4.

For the majority of the globular clusters considered in our sample, the values of the half-mass radius from $f^{(\nu)}$ models are larger than those obtained from King models; only for NGC 362 the opposite is true. For NGC 288, NGC 5139 and NGC 6809 the values calculated from the two models basically coincide. By comparing the values of the total

Table 4.5: Derived structural properties.

	King Models							$f^{(\nu)}$ Models						
NGC	c	$R_{\rm c}$	$r_{\rm M}$	$r_{\rm tr}$	M	M/L	ρ_0	$R_{\rm c}$	$r_\alpha/r_{\rm M}$	$r_{\rm M}$	r_α	M	M/L	ρ_0
(1)	(2)	(3)	(4)	(5)	(6)	(7)	(8)	(9)	(10)	(11)	(12)	(13)	(14)	(15)
104	2.00	22.60	2.57	2335.74	7.181	1.34	5.011	23.25	1.783	4.82	8.59	8.047	1.50	5.094
288	0.99	79.49	7.51	896.85	0.740	1.88	2.043	58.24	0.866	7.53	6.53	0.850	2.18	2.427
362	1.77	9.88	2.65	605.79	1.867	1.05	4.826	11.34	1.786	2.13	3.80	1.828	1.03	4.761
2419	1.42	18.58	19.56	516.97	7.843	1.72	1.874	20.01	0.958	23.97	22.95	10.912	2.40	2.081
3201	1.30	71.58	3.85	1532.62	1.131	1.91	3.012	72.31	0.915	5.14	4.70	1.088	1.86	3.026
5139	1.32	127.68	7.51	2861.08	26.446	1.93	3.537	98.89	0.978	7.46	7.30	35.427	2.58	4.049
6121	1.62	71.31	2.62	3144.17	0.654	1.10	3.656	72.45	1.868	4.40	8.23	0.750	1.26	3.661
6218	1.28	47.81	2.47	982.45	0.614	1.96	3.306	43.45	0.890	3.03	2.69	0.786	2.52	3.577
6254	1.32	50.02	2.48	1125.66	1.532	1.61	3.741	47.97	0.564	3.35	1.89	2.161	2.67	4.003
6341	1.69	14.18	2.12	724.28	2.866	1.83	4.638	17.12	1.523	2.43	3.70	3.956	2.53	4.691
6656	1.38	80.92	3.13	2057.81	2.081	1.11	3.636	82.71	1.523	4.53	6.89	2.337	1.24	3.652
6809	0.92	110.09	5.90	1072.17	0.604	1.12	2.214	74.28	0.867	5.83	5.06	0.627	1.16	2.628
7078	1.86	7.51	1.70	560.55	3.976	1.12	5.207	6.27	1.793	2.92	5.24	4.056	1.14	5.420

Notes. For each cluster, listed in column (1), for the King models, we provide (2) the concentration index $c = \log(r_{\rm tr}/r_0)$ (see Eqs. (A.2), (A.3)) and (5) the truncation radius $r_{\rm tr}$, in arcsec; for the $f^{(\nu)}$ models, in Col. (10) the ratio between the anisotropy and the half-mass radius and in Col. (12) the anisotropy radius r_α, defined as $\alpha(r_\alpha) = 1$ (see Eq. (2.19) for the definition of α), in pc. For both King and $f^{(\nu)}$ models, we list: the core radius $R_{\rm c}$ (defined in the standard way) in arcsec (Col. (3) and (9)), the intrinsic half-mass radius $r_{\rm M}$, in pc (Col. (4) and (11), respectively), the total mass M of the cluster (Col. (6) and (13)) expressed in units of $10^5\ M_\odot$, the V band mass-to-light ratio in solar units (Col. (7) and (14)) and the logarithm of the central mass density ρ_0 in $M_\odot$ pc^{-3} (Col. (8) and (15)).

Table 4.6: Core and half-mass relaxation times for the best-fit King and $f^{(\nu)}$ models.

	King Models		$f^{(\nu)}$ Models	
NGC	$\log T_c$	$\log T_M$	$\log T_c$	$\log T_M$
(1)	(2)	(3)	(4)	(5)
362	7.565	8.971	7.713	8.825
7078	7.620	8.820	7.491	9.176
6121	7.818	8.774	7.836	9.137
104	7.846	9.198	7.922	9.629
6341	7.881	8.904	8.142	9.052
6218	8.140	8.725	8.142	8.902
6254	8.269	8.892	8.334	9.150
6656	8.418	9.099	8.451	9.361
3201	8.523	9.123	8.545	9.305
6809	8.835	9.289	8.529	9.288
288	8.969	9.482	8.750	9.509
5139	9.515	10.140	9.429	10.191
2419	9.812	10.537	9.970	10.731

mass and of the central mass density calculated with the two families of models, we see that for the whole sample (with few exceptions) the values calculated with $f^{(\nu)}$ models are larger than those calculated with King models; this fact is not at all surprising, since the $f^{(\nu)}$ models are not truncated. As to the mass-to-light ratios, we see that there is not a tight correlation between the values calculated with King and $f^{(\nu)}$ models, the latter being almost always larger. Similar trends are noted also in the structural properties derived from (isotropic) models characterized by a more spatially extended truncation, such as the Wilson models (see McLaughlin & van der Marel 2005).

In Table 4.6, we list the values of the core and half-mass relaxation times calculated by using the two best-fit dynamical models for each globular cluster; the clusters are listed in order of increasing King core relaxation times, and the separation in three classes of relaxation here adopted is marked with horizontal lines. Figure 4.5 illustrates the correlation between the values of these parameters.

When considering the core relaxation times (calculated according to Eq. (10) of Djorgovski (1993), as in the Harris 2010 catalog), we see that the original division in the relaxation classes proposed in Sect. 1.3.1 on the basis of the values listed in the Harris catalog is confirmed. The only exception is NGC 6341: according to the value of the core relaxation time calculated with its best-fit $f^{(\nu)}$ model, this cluster should belong to the second class, rather than to the first. When we list globular clusters according to increasing core relaxation times estimated with the models identified in this work, we see that the order of relaxed globular clusters changes with respect to that of Table 4.1. However, there is a general agreement between values of these quantities calculated with the two families of models.

To calculate the half-mass relaxation times we followed the definition of Eq. (5) in Spitzer & Hart (1971), which is based on the half-mass radius (see also Sect.2.1.1). We see that the values from $f^{(\nu)}$ models are larger than those from King models, except for

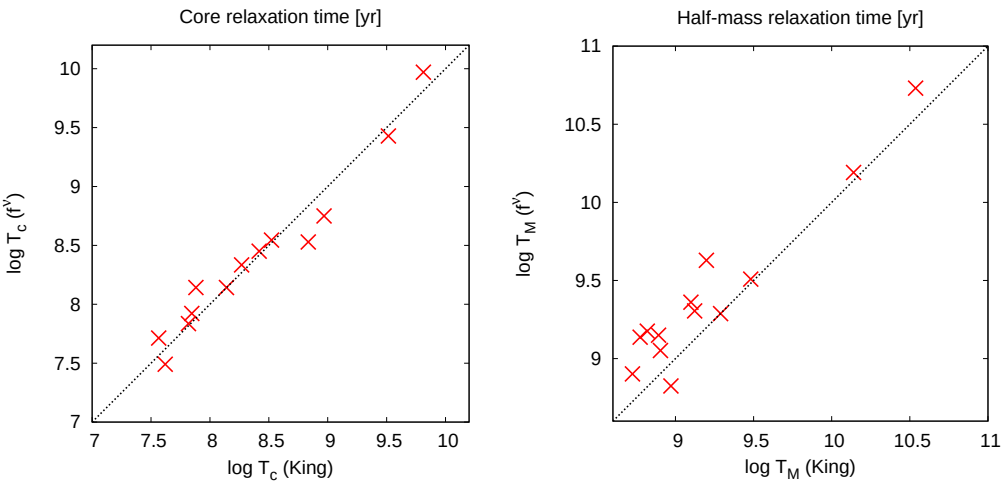

Figure 4.5: Comparison between the values of the relaxation times derived from King and $f^{(\nu)}$ best-fit models. The left panel shows the values of core relaxation times, the right panel the half-mass relaxation times. The format is the same as in Fig. 4.4.

NGC 362 and NGC 6809 (for the latter cluster, the estimated values are approximately equal). In contrast with the case of the core relaxation times, the values of the half-mass relaxation time turn out to be more model-dependent. Such dependence is likely to be due to the differences between the density profiles of the two families of models, which, in general, are less significant in the central regions and become more evident at radii larger than the half-mass radius. The introduction of a truncation for $f^{(\nu)}$ models would also lead to different values of these parameters. We notice that usually the half-mass relaxation time is calculated by inserting in the relevant definition directly the (projected) half-light radius (see, for example, Harris 2010 and McLaughlin & van der Marel 2005). By following the same procedure, we found that the values of the half-mass relaxation times are less model dependent, and closer to the values listed in the Harris catalog.

4.3.2 Comparison with previous studies

In the case of King models, it is interesting to compare the values of the structural parameters found in the present investigation with those obtained in previous studies, as summarized in Table 4.7. By combining the formal errors from both analyses, the comparison of our results with those of McLaughlin & van der Marel (2005) is the most significant because their values result from a fitting procedure which is similar to the one we have followed; for this reason, it is also, to some extent, the most surprising. We recall that the errors on the parameters can be found in Table 4.2. McLaughlin & van der Marel (2005) list the formal errors on the parameters in their Tables 10 and 12. No similarly detailed comparison with other papers could be made, because in general error analysis is not provided.

We notice that for ten globular clusters (all but NGC 2419, NGC 6254, and NGC 7078) our values of Ψ agree, within the errors, with the values of McLaughlin & van der Marel (2005); for the scale radius, agreement is found for eight objects (all but NGC 2419, NGC 6121, NGC 6254, NGC 6341, and NGC 7078). We may argue that the discrepancy is

Table 4.7: Comparison between the values of structural parameters from best-fit King models found in our analysis and in previous studies. See Table 4.2 for the description of column entries.

NGC	Ref.	Ψ	r_0	μ_0	σ_0	NGC	Ref.	Ψ	r_0	μ_0	σ_0
104	(0)	8.58	23.09	14.33	12.27	288	(0)	4.82	91.03	20.02	2.85
	(1)	9.33	15.25	14.42	11.5		(1)	4.33	94.05	20.00	2.9
	(2)	8.70	22.84	14.42	...		(2)	4.65	98.41	20.00	...
	(3)	8.6	23.19	14.36	15.27		(3)	4.8	92.87	20.00	2.79
	(4)	8.81	22.01	14.38	11.0		(4)	4.80	92.79	20.05	2.9
362	(0)	7.80	10.21	14.66	8.31	2419	(0)	6.62	19.70	19.43	5.04
	(1)	8.93	7.19	14.79	6.4		(1)	6.55	19.88	19.77	3.0
	(2)	6.80	10.79	14.79	...		(2)	6.55	22.19	19.77	...
	(3)	7.9	10.05	14.66	11.12		(3)	6.5	20.60	19.44	5.32
	(4)	7.76	11.16	14.80	6.4		(4)	6.44	20.47	19.67	4.0
3201	(0)	6.17	76.99	18.35	4.28	5139	(0)	6.27	136.94	16.42	14.83
	(1)	6.17	86.22	18.96	5.2		(1)	5.77	157.85	16.81	16.0
	(2)	6.21	93.55	18.96	...		(2)	5.94	168.01	16.81	...
	(3)	6.1	77.68	18.30	4.21		(3)	6.2	141.20	16.44	13.75
	(4)	6.14	83.98	19.00	5.0		(4)	6.21	152.73	16.81	16.8
6121	(0)	7.32	74.56	17.00	4.01	6218	(0)	6.11	51.56	17.65	3.93
	(1)	7.24	45.38	17.88	4.2		(1)	6.55	37.57	18.00	4.5
	(2)	7.20	52.37	17.88	...		(2)	6.48	42.38	18.00	...
	(3)	7.4	72.57	16.94	5.25		(3)	6.1	51.74	17.62	4.66
	(4)	7.40	72.42	17.95	4.0		(4)	6.33	50.70	18.10	4.5
6254	(0)	6.26	53.63	16.88	6.21	6341	(0)	7.54	14.72	15.31	9.28
	(1)	6.55	48.45	17.70	6.6		(1)	8.22	11.27	15.46	5.9
	(2)	6.55	54.49	17.70	...		(2)	7.92	14.56	15.46	...
	(3)	6.5	49.41	16.85	6.17		(3)	7.5	16.15	15.61	8.71
	(4)	6.48	49.19	17.70	6.6		(4)	7.50	16.20	15.47	6.0
6656	(0)	6.47	86.18	16.41	6.47	6809	(0)	4.44	129.11	19.12	2.92
	(1)	6.17	83.19	17.40	9.0		(1)	3.17	192.94	19.40	4.9
	(2)	6.21	91.41	17.40	...		(2)	3.53	215.54	19.40	...
	(3)	6.5	85.15	16.38	8.56		(3)	4.5	126.41	19.07	3.73
	(4)	6.48	84.96	17.42	7.8		(4)	4.49	126.22	19.36	4.0
7078	(0)	8.09	7.72	14.07	11.83						
	(1)	12.32	1.96	14.21	12.0						
	(2)	10.75	4.09	14.21	...						
	(4)	9.72	8.49	14.21	13.5						

Notes. For NGC 7078 the entry marked with (3) is missing: the authors of this work decided to exclude this globular cluster from their analysis because it is core-collapsed. In references (2) and (4) only the core radii are given; therefore we used the values of R_c and Ψ to calculate r_0 (see Appendix A.1).

References. (0) This work; (1) Pryor & Meylan 1993; (2) Trager et al. 1995; (3) McLaughlin & van der Marel 2005; (4) Harris 2010.

partly due to the fact that our surface brightness profiles usually contain a larger number of data-points with respect to those of the cited paper, even when we do not merge the original profiles by Trager et al. (1995) with those of other sources.

The discrepancies between the values of the central surface brightness derived here and those resulting from previous studies are primarily due to the correction for the extinction, usually neglected, introduced in our analysis, following McLaughlin & van der Marel (2005). In fact, such discrepancies are not severe; only three objects (NGC 6341, NGC 6809, and NGC 7078) have values which are not consistent, within the errors, with respect to values determined in previous studies. The reason for this is the fact that we added to these profiles the more recent and more accurate data from Noyola & Gebhardt (2006).

The structural parameter for which the differences between the values obtained in our analysis and those in the literature are the most relevant is the central line-of-sight velocity dispersion. For NGC 288, NGC 2419, NGC 3201, NGC 6121, NGC 6254, and NGC 7078 we see that our values agree, within the errors, with at least one of the values found in the literature (only four of them with McLaughlin & van der Marel 2005). This discrepancy is not at all surprising, because the kinematic data are the most uncertain. This fact gives one further argument for the need for more numerous and more accurate kinematic data for these systems.

4.3.3 Central slope of the photometric and kinematic profiles

When considering the surface brightness profiles of our selected globular clusters, we note that there are cases in which the observed photometric profiles deviate from the calculated ones at small radii. In particular, by focusing on the innermost regions of the profiles, we see that this is the case for NGC 6121, NGC 6218, and NGC 7078, for which the models are underluminous, and NGC 288, NGC 6656, and NGC 6809, in which the models are overluminous, and NGC 3201, for which the observed central surface brightness appears to oscillate. A convincing explanation for the disagreement found in these cases is still lacking. In spite of these local discrepancies, the global values of the statistical indicators may be satisfactory (see Table 4.4).

As far as the velocity dispersion profiles are concerned, in four cases (NGC 288, NGC 3201, NGC 6121, and NGC 6656), both models overpredict the central data-points, while, as mentioned in Sect. 4.2, four clusters (NGC 2419, NGC 5139, and, possibly, NGC 6218 and NGC 6254) show a relatively large gradient of the profile in the central regions. At variance with the study of elliptical galaxies, the kinematic profiles of globular clusters are often undersampled inside the half-light radius.

As described in Sect. 1.4.1, recently, the central cusps in the observed photometric and kinematic profiles of some globular clusters have been interpreted as clues of the presence of an intermediate-mass black hole in the center of the system (see the analytical model by Bahcall & Wolf 1976 and the N-body simulations by Baumgardt et al. 2005 and Noyola & Baumgardt 2011), and a variety of dynamical models (either defined from distribution functions or as solutions of the Jeans equations), have been used in order to constrain the mass of such central object (the best known example is the controversial case of ω Cen, studied by Noyola et al. 2008 and van der Marel & Anderson 2010, with different conclusions). However, Vesperini & Trenti (2010) showed that these shallow photometric cusps are not decisive signatures of the presence of an intermediate-mass black hole, and that they might be related to other dynamical processes; moreover, the authors emphasize the fact that the typical accuracy in the data may be insufficient to characterize the slope of the profile as desired.

As shown in the previous sections, the presence of radially-biased pressure anisotropy (which occurs in the context of the family of $f^{(\nu)}$ models or of the Michie-King models, see Michie 1963) can also produce a relatively rapid decline in the central part of the velocity dispersion profile. Therefore, here we are reiterating a point already noted in the literature, that the presence of a central intermediate-mass black hole should not be considered as the only physical explanation of the existence of a central kinematical peak. Unfortunately, our independent conclusion only confirms that the interpretation of this interesting kinematical feature is more model dependent than desired. We recall that $f^{(\nu)}$ models are characterized by a "realistic" anisotropy profile (see Fig. 6 in Trenti & Bertin 2005, and Fig. A.4 in this Thesis): the central regions are more isotropic than the outer ones in velocity space, because the models represent a scenario in which violent relaxation has acted more efficiently in the center. This differential kinematical feature is not always present in dynamical models based on the Jeans approach, which, to obtain a fast decline in the velocity dispersion profile in the absence of a central intermediate-mass black hole, usually requires very high values of the anisotropy parameter, even in the central regions of the cluster (see, for example, Sect 4.2 in Noyola et al. 2008 or Sect 5.3 in Lützgendorf et al. 2011).

4.3.4 Radial orbit instability

Systems in which there is a great amount of radial kinetic energy with respect to tangential kinetic energy are subject to the radial orbit instability.

Polyachenko & Shukhman (1981) (see also Fridman & Polyachenko 1984) introduced a parameter defined as:

$$\kappa = \frac{2K_{\rm r}}{K_{\rm t}} \tag{4.1}$$

where $K_{\rm r}$ and $K_{\rm t}$ represent the radial and the tangential component of the total kinetic energy, respectively, and argued that when:

$$\kappa > 1.7 \pm 0.25 \tag{4.2}$$

radial orbit instability occurs. Actually, different families of models generally have different threshold values for the instability. A detailed discussion of the onset of the radial orbit instability for the family of $f^{(\nu)}$ models can be found in Trenti & Bertin (2005), Trenti et al. (2005), and Trenti & Bertin (2006), where the validity of the criterion expressed in Eq. (4.2) is discussed.

We calculated the values of the parameter κ for the $f^{(\nu)}$ models that provide the best fit to the observed profiles of the globular clusters of the sample (see Table 4.8). It is interesting to note that globular clusters belonging to a given relaxation class tend to have similar values of the stability parameter ($\kappa \approx 1.3, 1.8, 1.7$ for the first, second, and third relaxation class, respectively; in this respect, NGC 6656 and NGC 6254 appear to exhibit an exceptional behavior). In other words, the relaxed class is found to be more isotropic by the $f^{(\nu)}$ diagnostics.

The majority of the globular clusters that have $\kappa \gtrsim 1.7$ are likely to be in a condition of *marginal* instability. The case of NGC 6254 does remain problematic: the value of its stability parameter κ is significantly larger than the threshold, and this cluster appears to be unstable with respect to the radial-orbit instability. From their analysis on this issue for the $f^{(\nu)}$ family of models, Trenti et al. (2005) concluded that low-concentrated models (with $\Psi \lesssim 4$) should be unstable: indeed, the best-fit concentration parameter for NGC 6254 is the lowest among those obtained for the globular clusters in our sample.

Table 4.8: Global anisotropy parameter for the best-fit $f^{(\nu)}$ models.

Relaxed		Intermediate		Partially Relaxed	
NGC	κ	NGC	κ	NGC	κ
362	1.353	6218	1.835	5139	1.754
7078	1.301	6254	2.307	2419	1.771
104	1.301	6656	1.443		
6121	1.320	3201	1.810		
6341	1.443	6809	1.859		
		288	1.859		

We argue that the introduction of a truncation in phase space to the family of $f^{(\nu)}$ models might have a stabilizing effect, since such truncation will affect primarily the outer parts of a given configuration, which are dominated by radially-biased pressure anisotropy. Therefore the truncation is likely to reduce the global value of the radial component of the total kinetic energy.

4.4 Discussion and conclusions

We have performed a detailed combined photometric and kinematic study of a sample of Galactic globular clusters, representing systems under different relaxation conditions. For these objects, surface brightness and velocity dispersion profiles have been fitted by means of two different families of dynamical models, the truncated isotropic King models and the non-truncated, anisotropic $f^{(\nu)}$ models. The analysis has been carried out by following the same procedure used in the past to study the dynamics of elliptical galaxies and described in Sect. 3.3. Each globular cluster is then associated with two best-fit models. The main conclusions can be summarized as follows.

- The expected trend, that King models should perform better for more relaxed globular clusters, has been checked to exist but it is not as sharp as anticipated. The two clusters (NGC 104 and NGC 6341) for which the global fit by King models is most convincing indeed belong to the class of relaxed objects. King models tend to offer a good representation of the observed photometric profiles (as is commonly reported), regardless of the relaxation condition of the system (but a statement of this kind should also be supported by the relevant statistical indicators; see Table 4.4). However, the quality of the fits by King models to the kinematic profiles remains to be proved, even for relaxed clusters, because of the few data-points and the large error bars in the observed profiles. Three clusters for which the King models appear to be inadequate do not actually come as a surprise: NGC 2419 is the least relaxed cluster of the sample and NGC 362 and NGC 7078 are suspected to be post-core-collapse clusters.

- The second expected trend, that less relaxed clusters might exhibit the characteristic signature of incomplete violent relaxation, is also partly present but is not as sharp as might have been hoped for. Some cases indeed point to a significant role of radially-biased pressure anisotropy. The least relaxed cluster, NGC 2419, is well described by the $f^{(\nu)}$ models. For the second least relaxed cluster, NGC 5139,

the central shallow cusp in the velocity dispersion profile appears to be well captured by the $f^{(\nu)}$ models. A marginal indication in favor of the $f^{(\nu)}$ models also comes from inspection of the inner kinematic profiles of NGC 6218 and NGC 6254, although these two clusters are not among the least relaxed objects. In contrast, King models and other isotropic models (such as the spherical Wilson models) have difficulty in matching significant velocity gradients inside the half-light radius. Therefore, the partial success of the $f^{(\nu)}$ models suggests that for some globular clusters radially-biased pressure anisotropy may be important. This property could be examined further by means of better spatially-resolved kinematic data in the inner regions (i.e., at radii out to approximately the half-light radius). This result is in line with the conclusions of recent papers: in particular, see Ibata et al. (2011) and references therein, based on the application of King-Michie models.

- In some clusters, regardless of the relaxation condition, some qualitative characteristics of the observed profiles are missed by both families of models here considered. It may be that part of these cases would be resolved by a study in terms of *truncated* $f^{(\nu)}$ models. But it may also be that other ingredients, such as rotation (solid-body or differential), play a role (see for example Chapter 6).

- This work demonstrates that the values of some structural parameters, such as the total mass and the half-mass radius, can be significantly model-dependent. In view of the results listed in the previous items, this is a clear warning against an indiscriminate use of structural parameters for globular clusters based on only one family of models (the spherical King models).

- In general, the kinematic fits are crucial to assess if a model is actually suited to describe a given globular cluster. The main issue in testing dynamical models on globular clusters is therefore the general lack of good kinematic data: the data are available for a small fraction of the population of Galactic globular clusters and generally made of a small number of data-points, not well distributed in radius. Surprisingly, the kinematic profile is often not well sampled as desired inside the half-mass radius. As discussed above this is a key region for confronting the performance of different dynamical models. In addition, accurate data in the outermost parts, close to the truncation radius, would touch on other important issues, such as the role of tides. To address this problem, we submitted two proposals to ESO: we will discuss them in Chapters 7 and 8.

- Some of the clusters considered in this Chapter have been also analyzed by means of other dynamical models. In Chapter 5 we present a study of new density profiles of NGC 6341 by means of King (1966) and Wilson (1975) spherical isotropic models. Axisymmetric rotating models (Varri & Bertin 2012) have been used to describe the globular clusters NGC 104, NGC 5139, and NGC 7078 (see Chapter 6). We postpone a comparison between the results found here and the results of those investigations to the mentioned Chapters.

CHAPTER 5

A signature of mass segregation in the globular cluster NGC 6341 (M92)

The dynamics of stars located in the outermost regions of globular clusters is influenced by the effects induced by the external tidal field of their host galaxy (Spitzer & Chevalier 1973; Aguilar et al. 1988). One of the expected effects is the evaporation of low-mass stars (Spitzer & Harm 1958): by escaping from the cluster, they can form halos or extended tidal tails, that are indeed sometimes observed around these systems. The first observational evidence of these structures around globular clusters was found from photographic plates data (Grillmair et al. 1995; Lehmann & Scholz 1997; Testa et al. 2000; Leon et al. 2000). Investigations based on more accurate CCD photometry also presented evidence of tidal tails (Odenkirchen et al. 2001, 2003; Grillmair & Johnson 2006; Chun et al. 2010) and of surrounding halos (Lee et al. 2003; Olszewski et al. 2009; Jordi & Grebel 2010; Correnti et al. 2011) around more than 30 Galactic globular clusters.

The investigation presented here originated from the idea of confirming the possible presence of extra-tidal material around the cluster NGC 6341 (M92) , and to accurately determine the distribution of stars in the outermost regions of the cluster. We decided to consider this particular cluster because, even if it has already been the target of several studies on this topic, an accurate determination of the density distribution in its external regions was still missing. Indeed, by using photographic plates, Testa et al. (2000) have provided evidence of the presence of extra-tidal stars at a distance of about $30'$ from the cluster center, and have computed a surface density map, which shows marginal evidence for an elongation in the extra-tidal extension orthogonal to the direction of the Galactic center. More recently, by using data obtained with a mosaic CCD camera, Lee et al. (2003) confirmed the presence of extra-tidal stars and showed that the elongation of the isodensity contours is observed only for the brightest stars. Jordi & Grebel (2010) analyzed the Sloan Digital Sky Survey (SDSS) photometric catalog and found an elongation in the density contours in the same direction as that detected by Testa et al. (2000), even though their data do not cover uniformly the entire area around the cluster.

The surface brightness profile obtained for this cluster by Trager et al. (1995), supplemented by the one of Noyola & Gebhardt (2006), which covers the central region of the cluster, was used for the dynamical analysis presented in Chapter 4. Another profile, focusing on the outer regions of the cluster NGC 6341 is given by Lee et al. (2003). These radial profiles do not give any indication of the size of deviations from spherical symmetry (for these, an inspection of the density contours would be required); anyway, they may give useful indications of the presence of extra-tidal material.

The analysis presented in this Chapter does not provide evidence for the presence of these effects, but a comparison between number density and surface brightness data obtained from the same set of observations led to identifying another interesting and

Table 5.1: Details of ACS observations.

Pointing	Band	N. of exp.	Exp. time
α - HRC$^{(a)}$	F435W	6	340 s
	F555W	155	10-100s
β - WFC$^{(b)}$	F606W	3	0.5, 5, 90 s
	F814W	3	0.5, 6, 100 s
γ - WFC$^{(c)}$	F475W	3	3, 20, 40 s
	F814W	3	1, 10, 20 s

Notes. Pointing α has been obtained by means of the ACS High Resolution Channel (HRC), pointings β and γ by means of the ACS Wide Field Channel (WFC).
$^{(a)}$ GO-10335, PI: H. Ford; $^{(b)}$ GO-9453, PI: T. Brown; $^{(c)}$ GO-10505, PI: C. Gallart.

important problem. The analysis of the different profiles has indeed shown that different dynamical tracers are distributed in a different way in the cluster: this can be interpreted as a signature of mass segregation.

This Chapter is organized as follows. In Sect. 5.1 we present the observational data used in this study, and we provide details on the calculation of the number density and surface brightness profiles, and of the isodensity contours. In Sect. 5.2 we give a description of these data by means of isotropic dynamical models, and we discuss the interpretation of our results as a signature of mass segregation. Finally, in Sect. 5.3 we draw our conclusions.

The work described in this Chapter is based on the article Di Cecco et al. (2013). Some variations have been made in the presentation of this study: we decided to dedicate more space, here, to the dynamical analysis of the cluster, and we included an analysis of its kinematics (not present in the article).

5.1 Observations and data

To obtain a good coverage of the entire extent of the cluster, we combined ground-based data collected by means of the mosaic camera MegaCam at the Canada-France-Hawaii Telescope (CFHT) with data collected by the Advanced Camera for Surveys (ACS) on board of the Hubble Space Telescope (HST). The MegaCam images were collected in g', r', i', z' bands[1]. The ACS data have been obtained by means of three different pointings, whose details are given in Table 5.1 (see also Di Cecco et al. 2010 for a description of the procedure adopted to reduce these data). In order to increase the radial extent of the area covered by our data-set, we supplemented our data with multiband (g, r, i, z) data collected by the Sloan Digital Sky Survey (SDSS) (Aihara et al. 2011). These ground-based data cover an area of $\sim 4^\circ \times 4^\circ$ around the cluster center, but they are not uniformly distributed. Figure 5.1 displays the sky coverage of the considered data-sets.

The completeness of each data-set was estimated, and the star counts were accordingly corrected to take this into account. In summary, we are dealing with three different data-sets, that cover different regions of the cluster:

1. $R \leq 1.25'$, ACS-WFC pointing β.
   For radial distances $R < 0.18'$ the completeness was estimated using the data from

[1]Proposal ID: 2004AC03, PI: J. Clem

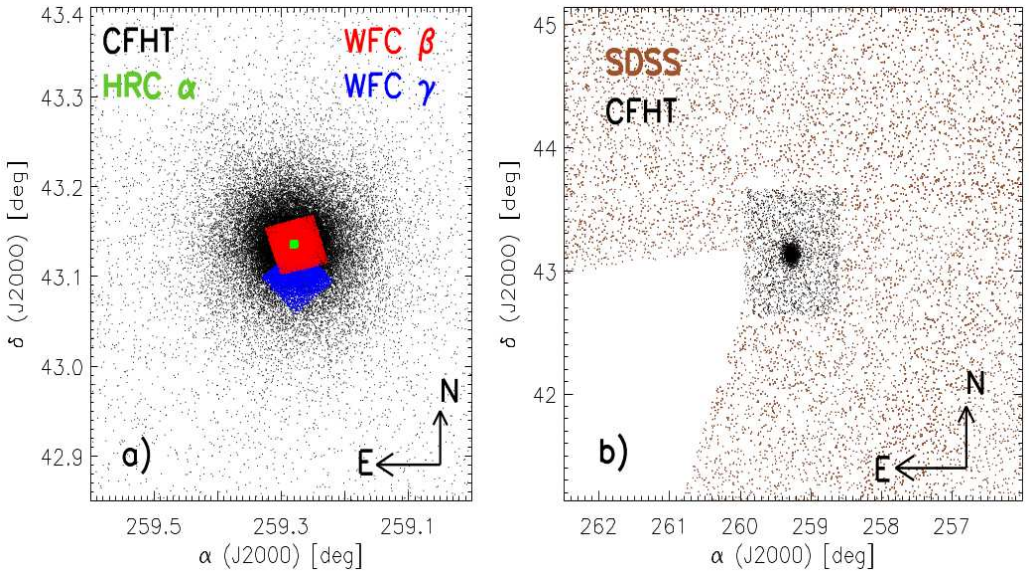

Figure 5.1: Extent of the considered data-sets in the region centered on the globular cluster NGC 6341. **Panel (a).** Images collected with the ACS on board the HST: the red and the blue squares show the images collected with the WFC (pointings β and γ respectively), the small green square those collected by the HRC (pointing α). Stars observed in ground-based images collected with CFHT are displayed as black dots. The field of view of this plot is $1^\circ \times 1^\circ$. **Panel (b).** Images collected with ground-based telescopes, namely CFHT (black dots) and SDSS (brown dots). Note that the SDSS data-set does not uniformly cover the area of the sky around NGC 6341. The field of view of this plot is $4^\circ \times 4^\circ$. In both panels, the orientation is shown in the bottom right corner.

pointing α, that were obtained with the ACS-HRC. In the region between $0.18'$ and $1.25'$, these data display a gap of $2.5''$ due to the separation of the CCDs; to correct this, we selected two regions of $2.5''$ at the edges of the gap and we randomly extracted half of the stars in each of the two regions.

2. $1.25' < R \leq 30'$, CFHT.
   For radial distances $1.25' < R \leq 3.33'$ the completeness was estimated using ACS-WFC data from pointing γ; the comparison of these data-sets indicates that for $i \leq 22$ mag the CFHT data-set can be considered complete at larger distances.

3. $30' < R \leq 2^\circ$, SDSS.
   The completeness was estimated using CFHT data. SDSS data are complete for $i \leq 22$ mag and radial distances larger than $11.7'$, but by inspecting Fig. 5.1 it is evident that they do not uniformly cover the entire region around the cluster; a correction was applied to star counts to account for this.

To provide homogeneous star counts across the entire globular cluster, the i and the r band from the SDSS, as well as the F814W and the F606W band of pointing β were transformed into the i' and the r' band of the MegaCam photometric system; in the following, we will omit the prime, when referring to CFHT bands. The accuracy in these transformations is better than 0.02 mag (Di Cecco et al. 2010). We decided to convert all the magnitudes into i and r bands because they are common to all the considered data-

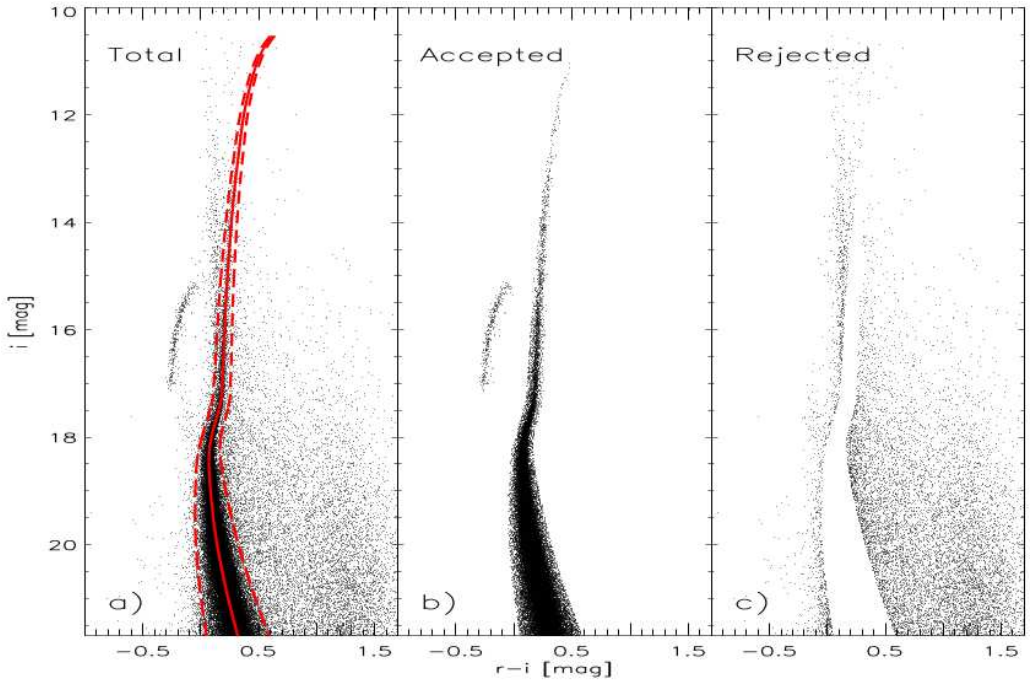

Figure 5.2: Panel (a). Color-magnitude diagram $(i, r-i)$ of stars in the CFHT and ACS-WFC data-sets. **Panels (b) and (c).** Color-magnitude diagrams for candidate NGC 6341 member (accepted) stars and for candidate field (rejected) stars, respectively.

sets, and because the data in these bands have good photometric accuracy, $\delta_{r-i} = 0.06$ mag. In particular, the i band is minimally affected by saturation problems: for this reason, it was chosen to compute the density profiles.

5.1.1 Number density and surface brightness profiles

The field of view of the CFHT and of the SDSS data-set fully encloses the estimated radial extent of NGC 6341 (see Table 5.2 for a collection of the published values of the estimated truncation radius). Our objective is to determine the extent of the cluster, and to study its outermost regions, with particular reference to the presence of tidal tails: for this reason, it is particularly important to accurately distinguish candidate cluster members from field stars. The method used to identify these two different groups of stars is described in the following.

A fiducial photometric catalog was built by selecting stars with intrinsic photometric error $\delta_{r-i} \leq 0.10$ mag, separation index[2] $sep \geq 2.5$, and distance from the cluster center $10'' \leq R \leq 180''$. This catalog of stars was used to compute a fiducial line (ridgeline) in the $(i, r-i)$ color-magnitude diagram of these stars (a description of the method used is given by I. Ferraro et al. 2014, in preparation). We stress that the selection criteria listed above were only applied to identify the stars to be used to estimate the ridgeline. The position of the ridgeline marks the center of the acceptance region, that is the region of

[2]The separation index quantifies the degree of crowding, i.e., the amount of spurious light due to neighboring stars, that affects the magnitude of individual stars (Stetson et al. 2003).

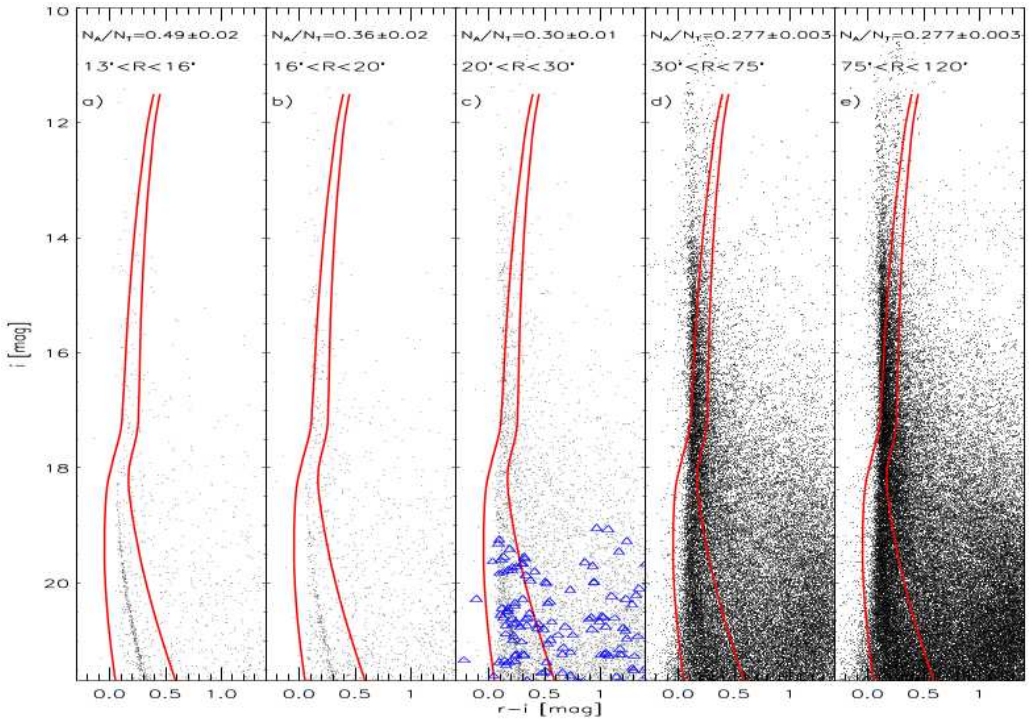

Figure 5.3: Panel (a). Color-magnitude diagram $(i, r-i)$ based on CFHT data. The red solid lines display the acceptance region defined in Fig. 5.2. The radial extent of the bin and the value of the ratio $N_{\rm A}/N_{\rm T}$ are given at the top of the panel. **Panels (b) and (c).** Same as for panel (a), but for stars located at larger radial distances. The blue triangles plotted in panel (c) are the objects located inside the candidate galaxy clusters (Wen et al. 2009), as described in the main text. **Panels (d) and (e).** Same as for panel (a), but for stars from the SDSS data-set.

the color-magnitude diagram where we assume that the candidate main sequence and red giant branch cluster stars lie. The acceptance region is centered on the ridgeline and the width in color goes from 0.01 mag close to the tip of the red giant branch up to 0.30 mag for magnitudes fainter than the main sequence turnoff. We consider $i = 21.7$ mag as the lower limit for the acceptance region, because at fainter magnitudes the photometric error in the color increases and the ridgeline is less well determined.

Panel (a) of Fig. 5.2 shows the $(i, r-i)$ color-magnitude diagram for the entire sample of stars; the calculated ridgeline is also shown with a solid line, and the acceptance region is delimited by the dashed lines. Panel (b) of Fig. 5.2 shows the candidate NGC 6341 member stars; the main sequence, the red giant branch, and the horizontal branch are clearly recognizable in this plot. The stars selected as main sequence and red giant branch member stars likely include field stars with colors and magnitudes similar to those of the cluster; the horizontal branch stars instead can be easily separated from the field stars, because they have bluer colors. Panel (c) of Fig. 5.2 shows the color-magnitude diagram of candidate field stars with their typical peaks in color at $0 < r-i < 0.2$ and at $1.2 < r-i < 1.4$ mag.

To probe the radial extent of candidate cluster stars, we investigated the ratio between the number of accepted stars $N_{\rm A}$ and the total number of stars $N_{\rm T}$ that are found in

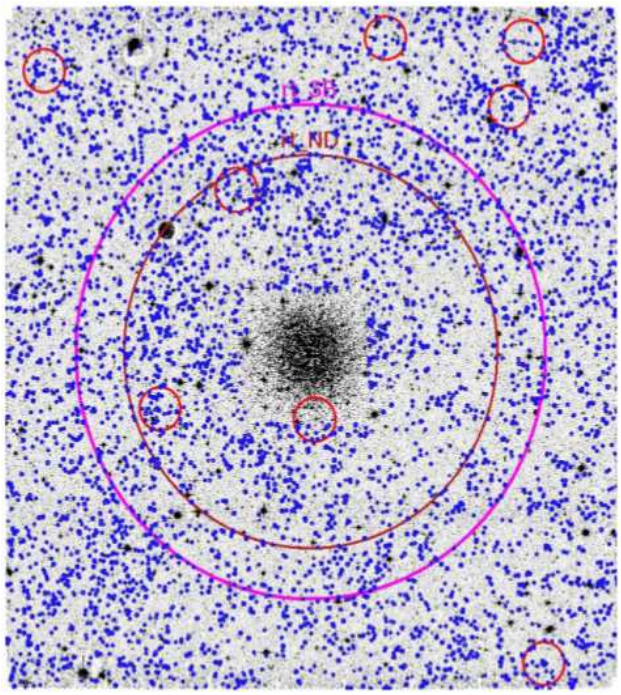

Figure 5.4: NGC 6341 r-band image obtained with MegaCam at CFHT. Blue dots display the non-point-like sources identified using Sextractor, the large purple and red circles display the Wilson truncation radius according to the surface brightness and the number density profile (see Table 5.2). The small orange circles show the candidate galaxy clusters identified by Wen et al. (2009). North is up and east left; the field of view is $1^\circ \times 1^\circ$.

five radial bins located between $13'$ and 2° from the cluster center. Data plotted in Fig. 5.3 show the $(i, r-i)$ color-magnitude diagram of stars in each of these radial bins. The first three considered radial bins are entirely composed of stars in the CFHT data-set, the last two bins are entirely located in the region covered by the SDSS data-set. The photometric precision of observations in this region is confirmed by the narrow distribution of main sequence stars; in particular, the morphology of the color-magnitude diagrams of stars located in the three innermost radial bins suggests that main sequence stars are good tracers of the radial extent of the cluster. We found that, as expected, the ratio between the number of cluster stars and the total number of stars is steadily decreasing when moving toward the outermost cluster regions. It decreases from $N_{\rm A}/N_{\rm T} = 0.49 \pm 0.02$ at $R \sim 14.5'$ to $N_{\rm A}/N_{\rm T} = 0.30 \pm 0.01$ at $R \sim 25'$: this radial distance appears to be a preliminary plausible lower limit for the truncation radius, and indeed the ratio $N_{\rm A}/N_{\rm T}$ attains a smaller constant value in the two outermost radial bins.

To check the plausibility of this first estimate of the radial extent of NGC 6341, the radial distribution of extragalactic sources was also investigated. The entire set of r-band images collected with MegaCam at CFHT was adopted, a new independent photometry was performed by using Sextractor (Bertin & Arnouts 1996), and the non-point-like sources were selected by using the procedure described by Evans et al. (2010). Figure 5.4 shows the radial distribution of these sources (blue dots) in the field of view of the CFHT data-set. The red and the purple circles represent the truncation radius of the cluster as

calculated by means of Wilson models, based on the number density and the surface brightness profile, respectively (see Sect. 5.2.1). The smaller orange circles show the candidate galaxy clusters identified from the SDSS data (Wen et al. 2009). By inspecting this figure it is apparent that the candidate galaxy clusters are located either close to the truncation radius or beyond it; the innermost circle, being located in a region with high density, is considered suspicious. When selecting the objects included in the regions occupied by the five candidate galaxy clusters beyond the truncation radius and plotting them in the color-magnitude diagram, we found that only about the 35% of them are located inside the acceptance region (blue triangles in panel (c) of Fig. 5.3), a fraction that agrees, within the errors, with the value of $N_{\rm A}/N_{\rm T}$ found in the considered bin.

To remove spurious stars that were erroneously accepted as cluster members, we used the method described by Walker et al. (2011) for the globular cluster IC 4499. After having corrected the SDSS data-set to account for its non-homogeneous coverage of the area around NGC 6341, we divided the region occupied by the data into radial bins, and we counted the number of field (rejected) stars $N_{\rm R}$ falling into each bin. We calculated for each bin the logarithmic surface density η of field stars. We considered η as a function of the inverse of the radial distance from the cluster center, and we performed a linear fit to these data-points; by extrapolating to infinite radial distance we found that the asymptotic value is $\eta = 0.42 \pm 0.10$ (logarithmic number of stars per arcmin^2). We obtained another estimate of this quantity by taking the mean of the five outermost data-points, thus finding $\eta = 0.36 \pm 0.10$. We then adopted as the final value for this quantity the mean of these estimates, $\eta = 0.39 \pm 0.14$.

We then computed the logarithm of the ratio between the number of accepted stars and the number of rejected stars, $N_{\rm A}/N_{\rm R}$, by considering the entire data-set. We calculated the mean asymptotic value of this quantity by taking the mean of the values it assumes in the three outermost radial bins; we obtained $\log(N_{\rm A}/N_{\rm R}) = -0.41 \pm 0.03$.

Finally, by multiplying the number of rejected stars per arcmin^2 by $N_{\rm A}/N_{\rm R}$, we found the number of candidate field stars that were erroneously classified as candidate NGC 6341 stars, ~ 0.95 star arcmin^{-2}. By subtracting this value from the number of the accepted stars per unit area, we obtained the final *Count Catalog* of candidate NGC 6341 stars. This catalog was used to compute the number density (ND) radial profile, by following the procedure described in Sect. 3.1.1. This profile extends from $R \sim 1.5''$ out to $R \sim 2^\circ$; the error on each point is calculated as the square root of the number of stars, divided by the area of the annulus.

A similar procedure was followed to determine the luminosity from erroneously accepted field stars. By subtracting the value of this quantity from the accepted stellar luminosity, we obtained an independent *Luminosity Catalog* of candidate NGC 6341 stars. This catalog was used to calculate the surface brightness (SB) radial profile, with the procedure described in Sect. 3.1.2. The ratio between the number of accepted and rejected stars is more robust than the ratio between the luminosity of accepted and rejected stars, since the intrinsic error of the former is at least a factor of two smaller than that of the latter. The reason for this is that the value of the luminosity ratio depends on the radial distribution of bright evolved stars, which can cause fluctuations in the local values of the luminosity density.

5.1.2 Isodensity contours

We evaluated the circular symmetry of the number density as a function of the radial distance by using the *Count Catalog*. To avoid possible systematic uncertainties in the radial distribution, the symmetry of the number density was estimated by using only

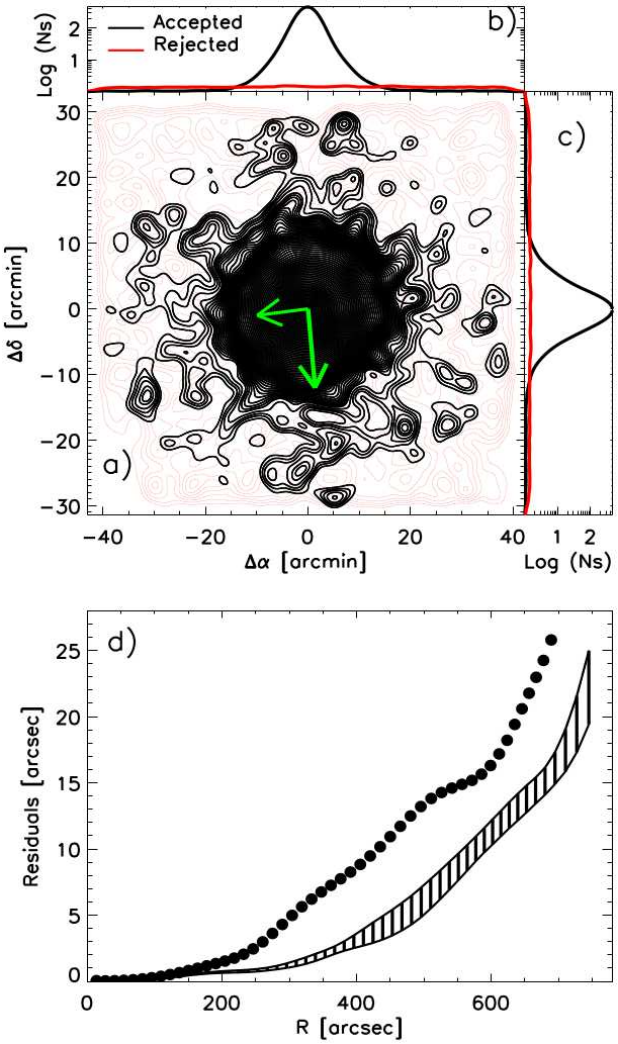

Figure 5.5: Panel (a). Contour levels for candidate NGC 6341 (black) and field (red) stars projected onto the sky. The long green arrow marks the direction of the Galactic Center, the short one the proper motion of the cluster. **Panels (b) and (c).** Projected logarithmic distribution for candidate NGC 6341 (black) and field (red) stars along the horizontal and the vertical axis. **Panel (d).** The black filled circles show the residuals of the fits to the contour levels plotted in panel (a) with circles of variable radius as a function of the radial distance. The vertically hatched area shows the results of simulations.

ACS and CFHT data; the results are not affected by the exclusion of the SDSS dataset. We computed the contour levels for the candidate cluster and field stars, and we show them respectively as black and red lines in panel (a) of Fig. 5.5. By inspecting the figure, it is apparent that the contour levels become asymmetric at a distance of $\sim 13'$, which is almost equivalent to the values of the truncation radius of NGC 6341 found in the literature (see Col. 5 in Table 5.2). Beyond this radius, the distribution of candidate cluster stars becomes clumpy. Panels (b) and (c) of Fig. 5.5 show the linear density of the

candidate NGC 6341 and field stars (black and red lines, respectively), projected along the axes.

To trace in detail the departure of the contour levels from circular symmetry, we performed a fit to each contour with a circle. The center of the circles is identical to the center of the contours, which coincides with the cluster center, and the radius of the circles is the fitting parameter. Then, we computed the residuals between individual contours and best-fit circles, from the very center of the cluster out to a radial distance of $R \sim 800''$. The residuals plotted in panel (d) of Fig. 5.5 show that the innermost contour levels appear to be symmetric, as indicated by the vanishing values of the residuals out to $R \sim 150''$. Contours become asymmetric at a radial distance $500'' \lesssim R \lesssim 600''$, where the residuals show a shoulder clearly connected to the density drop detected in the contour plot. At $R \sim 700''$ the contours become even more asymmetric; the fit in the outermost regions fails to converge because of the large asymmetries.

The increasing asymmetry that we found in the outer regions could be the consequence of the fluctuations associated with the decrease in density. To validate this working hypothesis we performed a series of simulations by using the observed density profile to compute synthetic globular clusters, that are required to have symmetric density distribution. We applied to these globular clusters the same procedure to evaluate the contour levels and we performed the same fit with circles of variable radius. The vertical hatched area plotted in panel (d) of Fig. 5.5 represents the residuals calculated for the synthetic globular clusters. By comparing this area and the plotted points it is apparent that the asymmetry in the real cluster is at least 3σ larger than in the synthetic clusters.

To further characterize the nature of the asymmetries in the contour levels, we show two green arrows, in the top panel of Fig. 5.5, indicating the direction of the Galactic center (long arrow) and of the NGC 6341 proper motion (short arrow) according to Dinescu et al. (1999). We found no clear correlation between these directions and the clumpy distribution of candidate NGC 6341 stars at large radial distances. Evidence of a clumpy stellar distribution in the outskirts of NGC 6341 was also present in the stellar density maps provided by Testa et al. (2000, see their Fig. 6), by Lee et al. (2003, see their Fig. 12) and by Jordi & Grebel (2010, see their Fig. 17). The results presented here support the conclusions presented by Testa et al. (2000), who found marginal evidence of an elongation of the outermost clumpy stars in the direction orthogonal to the direction of the Galactic center.

5.2 Description of density profiles by means of isotropic dynamical models

We carried out fits of dynamical models to the observed radial profiles. We considered the King (1966) and the Wilson (1975) spherical and isotropic dynamical models (see AppendixA.1 and A.2 for a more detailed description). We chose these particular families of models because, as shown in Chapter 4, NGC 6341 is well described by isotropic models. We consider here Wilson models in addition to the more traditional King models because we want to explore the effects of a different truncation prescription in the representation of the most external regions of this cluster. We recall here that a description by means of a one-component dynamical model assumes that the stellar populations are distributed homogeneously in the cluster.

To identify the best-fit model we adopted the procedure described in Sect. 3.3. The results are shown in Fig. 5.6 and 5.7; the values of the relevant parameters of the best-fit models are listed in the upper part of Table 5.2.

Table 5.2: Best-fit parameters.

Profile	King Models				Spherical Wilson Models			
	Ψ	c	r_0	$r_{\rm tr}$	Ψ	c	r_0	$r_{\rm tr}$
ND	6.91 ± 0.02	1.50 ± 0.01	34.25 ± 0.38	18.11 ± 0.44	5.84 ± 0.02	1.73 ± 0.01	48.03 ± 0.42	42.63 ± 1.19
SB	8.40 ± 0.01	1.95 ± 0.00	15.22 ± 0.02	22.80 ± 0.18	6.65 ± 0.01	2.14 ± 0.00	21.08 ± 0.05	48.80 ± 0.85
SB-15	7.20 ± 0.01	1.59 ± 0.00	19.43 ± 0.05	12.56 ± 0.10	6.52 ± 0.01	2.06 ± 0.00	24.33 ± 0.06	46.67 ± 0.42
SB-17	6.95 ± 0.01	1.51 ± 0.00	23.17 ± 0.06	12.63 ± 0.12	6.29 ± 0.01	1.94 ± 0.00	29.04 ± 0.06	41.97 ± 0.53
T95	7.92	1.81	23.67	15.20				
T00				12.33				
L03	8	1.83	12.42	14.00				
MLvdM05	7.5	1.68	16.15	12.88	5.9	1.75	26.51	24.85
JG10	6.93	1.51	23.37	12.55				
T95+N06	7.54	1.69	14.72	12.07	6.34	1.96	19.33	29.58
L03+N06	7.84	1.78	13.46	13.67	6.61	2.12	18.94	41.72

Notes. For each model, we list the dimensionless parameter Ψ, the concentration c, the scale radius r_0 (arcsec), and the truncation radius $r_{\rm tr}$ (arcmin). The different profiles are identified by the label in the first column. The cases indicated as T95+N06 and L03+N06 refer to the fits we performed on composite profiles, obtained by combining the profiles from Trager et al. (1995) and Lee et al. (2003) with the profile from Noyola & Gebhardt (2006), which covers the innermost region of the cluster.

References. (T95) Trager et al. 1995; (T00) Testa et al. 2000; (L03) Lee et al. 2003; (MLvdM05) McLaughlin & van der Marel 2005; (N06) Noyola & Gebhardt 2006; (JG10) Jordi & Grebel 2010.

5.2.1 Density tracers and mass segregation

The fit to the number density ND profile is shown in the top panel of Fig. 5.6. Both King and Wilson models underestimate the central number density, failing to represent the four innermost points. A quantitative interpretation of this discrepancy remains unavailable, but the problem is likely to be related to the failure of the assumptions at the basis of a one-component description in the central regions. The good agreement of King models to the observations in the middle part of the profile breaks down around $700''$, where the profile approaches the background level (0.95 star arcsec^{-2}). In the case of the Wilson models, instead, only the two outermost points are discrepant, and the model fits the data out to a distance larger than $1000''$. We note that the two outermost points in the profile are likely to be affected by errors in the subtraction of background stars.

The bottom panel of Fig. 5.6 shows the fits to the surface brightness SB profile. When compared to the King best-fit model, the Wilson best-fit model provides a more adequate overall description, not only in relation to the outermost points, as in the number density profile, but also in the central part of the profile. The satisfactory performance of the Wilson models indicates that the observations can be explained by means of a less abrupt truncation radius, with no need to introduce extra-tidal halos. In this case, the two outermost points were not taken into account to calculate the best-fit parameters, since they are expected to be even more affected by errors in the subtraction of background stars, with respect to the corresponding points in the number density profile.

Surprisingly, even if the number density and the surface brightness profiles come from the same set of observations, the best-fit parameters determined by the fits are significantly different. We argue that this behavior is due to the fact that each profile represents a different aspect of the density distribution of the cluster. On the one hand, the number density profile, derived by considering the radial distribution of both luminous and faint stars, is dominated by the main sequence stars, which greatly outnumber evolved (red giant branch and horizontal branch) stars (Castellani et al. 2007). On the other hand, the surface brightness profile is heavily affected by the presence of the brighter red giant branch stars. The difference in the best-fit models reflects the intrinsic difference in the radial distribution of the stellar tracer that determines each profile. This behavior should be interpreted as a signature of mass segregation[3]. Indeed, the evolved slightly more massive stars[4] appear to be more centrally concentrated compared to stars with lower masses (see the values of the concentration parameter c in Table 5.2).

This interpretation is confirmed by an additional test. We calculated two other surface brightness profiles, by considering only the stars in the *Luminosity Catalog* that are fainter than a limiting magnitude of $i = 15$ and $i = 17$ mag; in the following, we indicate these profiles as SB-15 and SB-17, respectively. We carried out the fitting procedure on these profiles, and we list the resulting parameters in the third and fourth rows of Table 5.2; the fits are shown in Fig. 5.7. By inspecting the values of the best-fit parameters, it appears that by eliminating the brightest stars, the profiles tend to approach to the number density profile. Indeed, the values of the concentration parameter c and of the radial scale r_0 follow a monotonic trend from the surface brightness SB profile to the SB-15, to the SB-17, and finally to the number density ND profile.

Interestingly enough, for the SB-15 and SB-17 profiles, formally the King models reproduce the data better than the Wilson models, in contrast to what we found for the

[3]The occurrence of mass segregation in NGC 6341 was also suggested by Andreuzzi et al. (2000).

[4]Note that hot horizontal branch stars are less massive than main sequence turnoff stars, but they are a minor fraction of evolved cluster stars.

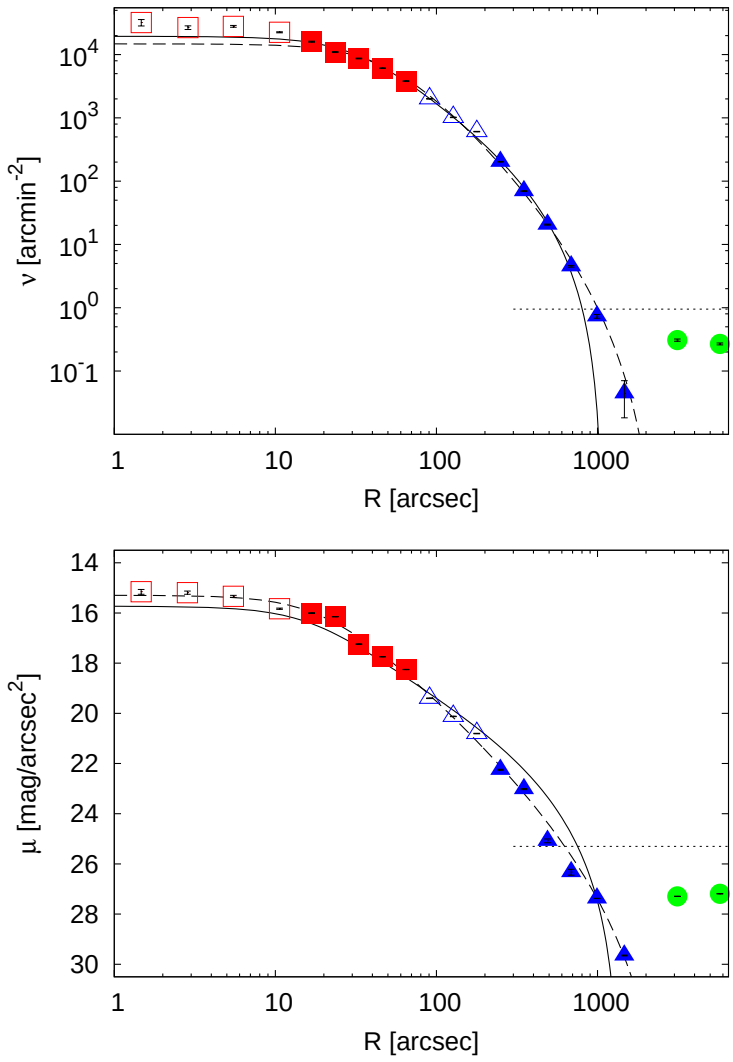

Figure 5.6: Fits by King and Wilson spherical models to the number density (ND, top) and surface brightness (SB, bottom) profiles. Solid lines correspond to the King-model fits, dashed lines to Wilson-model fits; the horizontal dotted lines show the background level; errors are shown as vertical error bars. Red squares indicate data obtained from pointing γ, blue triangles those from the CFHT data-set, and green circles those from the SDSS. Empty symbols mark regions where a completeness correction was applied.

previously described ND and SB profiles. A reason for this can be found when comparing the radial extent of the different profiles. The three surface brightness profiles are limited by the fact that the cut of candidate cluster stars brighter than a limiting magnitude causes a decrease in the radial extent and a more abrupt truncation of the profile. Indeed, the outermost radial point for the SB-15 profile is located at $R \sim 700''$, and for the SB-17 profile at only $R \sim 500''$; for these profiles, the outermost four and five points

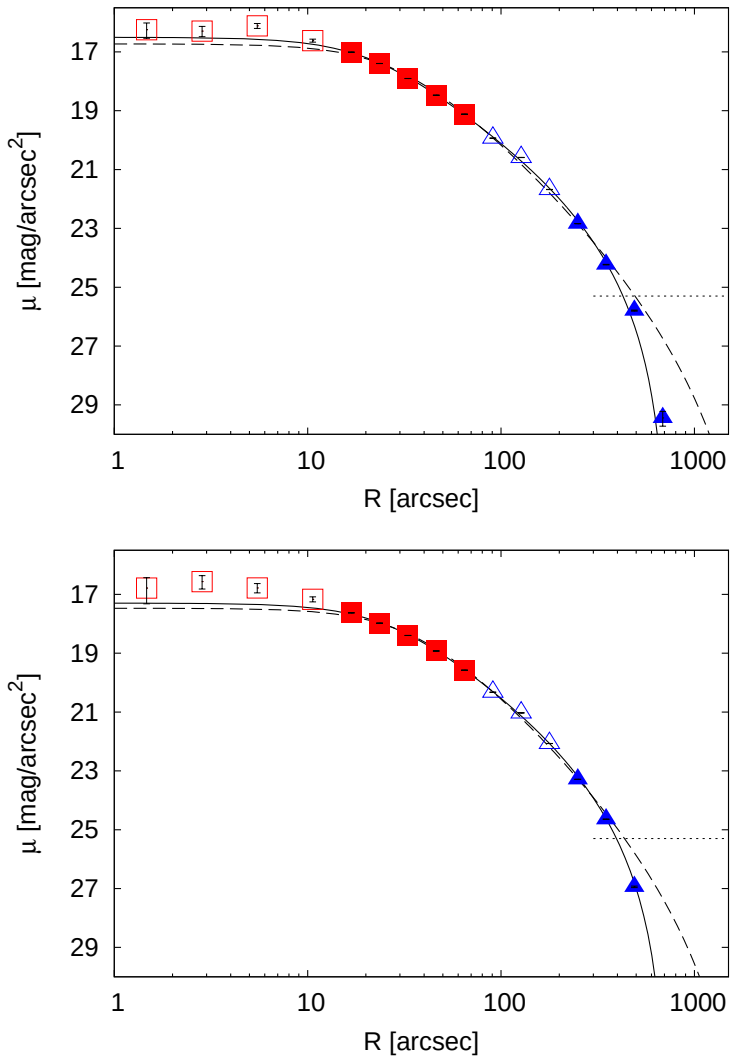

Figure 5.7: Fits by King and Wilson spherical models to the surface brightness SB-15 (top) and SB-17 (bottom) profiles, in the same format as in Fig. 5.6.

(respectively) are missing, with respect to those available in the case of ND and SB. The larger radial extent of the surface brightness SB profile is caused by the presence of a few bright giants that keep the profile well above the background level.

Another interesting feature is that the four innermost points of the profiles are not well reproduced by the models, that always underestimate the central density. This does not hold for the case of the SB-17 profile, for which Wilson models accurately account for the innermost slope of the observed profile. The discrepancy between models and observations was already found and discussed in Sect. 4.3.3, but its cause is yet to be found, and more accurate data are needed to determine it.

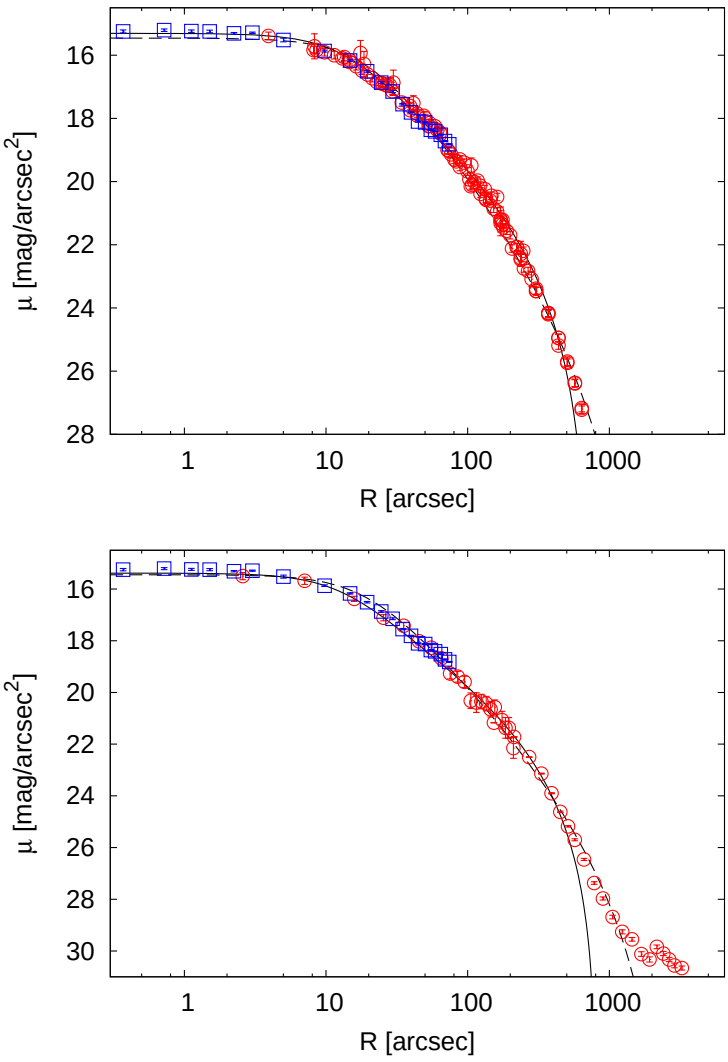

Figure 5.8: Fits by King and Wilson spherical models to the composite T95+N06 (top) and L03+N06 (bottom) profiles. Solid lines correspond to the King-model fits, dashed lines to Wilson-model fits; errors are shown as vertical error bars. Blue squares indicate data from N06, red circles those from other sources.

5.2.2 Comparison with previous studies

For comparison, the central part of Table 5.2 lists the most recent best-fit parameters published for NGC 6341 (only in a few cases the Wilson parameters are available). Acronyms in the first column identify the papers in which the results have been published.

The lower part of Table 5.2 lists the results of the fits to the only two[5] available (V-

[5]Another surface brightness profile was presented by Jordi & Grebel (2010), but the data-set is not publicly available.

Table 5.3: Central velocity dispersion and total mass.

Profile	King Models		Wilson Models	
	σ_0	M	σ_0	M
ND	7.16 ± 0.31	3.07	7.13 ± 0.31	3.05
SB	7.58 ± 0.33	3.02	8.77 ± 0.38	2.69
SB-15	8.75 ± 0.38	2.91	8.45 ± 0.37	2.74
SB-17	8.48 ± 0.37	2.96	8.16 ± 0.36	2.80

Notes. For each profile, listed in the first column, we list the central velocity dispersion σ_0 in km s^{-1}and the total mass of the cluster in units of $10^5 M_{\odot}$, as estimated by both King and Wilson models.

band) surface brightness profiles in the literature, the one by Trager et al. (1995), T95, and the one by Lee et al. (2003), L03. We decided to add to both data-sets the surface brightness data by Noyola & Gebhardt (2006), N06, which are relative to the innermost region of the cluster. The results of these fits are shown in Fig. 5.8.

The profile identified here as T95+N06 was analyzed in Chapter 4, and the values of the King model parameters listed here are the ones obtained there (see Tables 4.2 and 4.5). For this profile, the models provide an equally good fit to the data; Wilson models perform better than King models in representing the outermost points of the profile, while the opposite holds for the innermost ones. We note that this profile reaches a maximum radial distance of $R < 700''$, comparable with the one of our SB-15 profile. For the L03+N06 profile, the good agreement with observations that is seen in the inner and middle parts of the profile breaks down around $600''$ for the King model, and at more than $1000''$ for the Wilson model; a similar behavior was also found for the fit to the ND profile described above. In the L03+N06 profile, the outermost points are not reproduced by any of the considered models.

The values of the parameters listed in Table 5.2 are not consistent with each other, within the errors. In conclusion, we believe that a proper comparison of the values of the best-fit parameters found by fitting models to different (number density or surface brightness) profiles requires that we take into account the role played by the different stellar tracers in determining their shape, which makes standard one-component dynamical models questionable.

5.2.3 Kinematics and an estimate of total mass

Finally, we decided to carry out a kinematic fit to the velocity dispersion profile presented for this cluster in Chapter 4. As described in Sect. 3.3, we determined the velocity scale (i.e., the central velocity dispersion σ_0) by starting from the best-fit models identified within the two considered families by means of the photometric fit to each of the four considered profiles (ND, SB, SB-15, and SB-17). We list in Table 5.3 the values of σ_0 obtained in the four cases by both King and Wilson models.

Figure 5.9 shows the results of the kinematic fits. We see that in general the models determined by the surface brightness profiles (especially SB-15 and SB-17) better reproduce the observations, in particular at small radii. With respect to King models, Wilson models appear to give a better description of the data, over the entire extent of the observed profile. We notice that the values obtained here for the central velocity dispersion

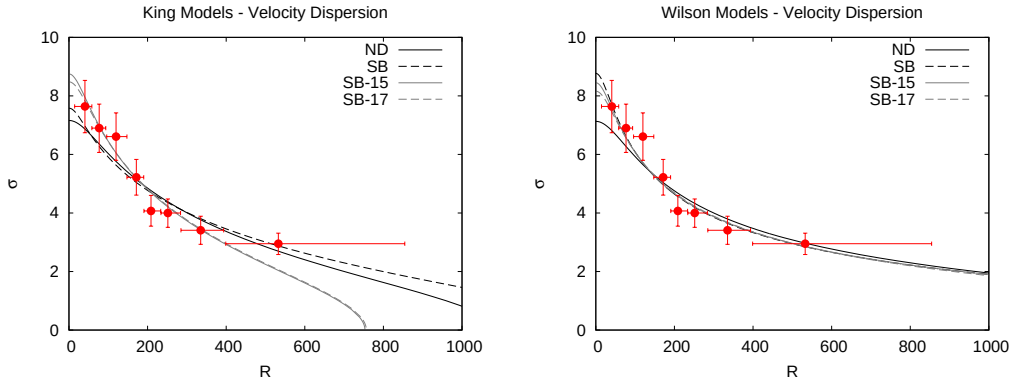

Figure 5.9: King (left panel) and Wilson (right panel) velocity dispersion best-fit models. The best-fit models identified for the ND profile are represented as black solid lines, the ones for SB by black dashed lines, the ones for SB-15 by gray solid lines, and the ones for SB-17 by gray dashed lines. The data are indicated with circles. For each data-point, errors are shown as vertical error bars; horizontal bars indicate the length of the radial bin in which the data-points have been calculated and have no role in the fitting procedure (see Sect. 3.3).

are not compatible with each other, and are smaller than those obtained from the study described in Chapter 4 ($\sigma_0 = 9.28 \pm 0.41$ for King models, and $\sigma_0 = 12.77 \pm 0.56$ for $f^{(\nu)}$ models, see Table 4.2).

An important result is that the best-fit models obtained by the surface brightness profiles reproduce the velocity dispersion better than those obtained by the number density profiles. This fact supports the interpretation given above for the results of the photometric fits. Indeed, the line-of-sight velocities used to calculate the velocity dispersion profile were measured for bright stars, that is, for the tracers that determine the shape of the surface brightness profiles. It is therefore reasonable that a model is found to reproduce better the observations when kinematic and photometric profiles calculated from the same population of tracers are considered.

We also calculated the total mass of this cluster, for each considered case (see Table 5.3). The values estimated by means of King models are larger than those estimated by Wilson models, even if the latter describe more extended systems; they are also larger than the value we obtained by means of King models from the analysis presented in Chapter 4 ($M = 2.87 \times 10^5 M_\odot$, see Table 4.5).

5.3 Discussion and conclusions

We studied the radial distribution of stars of the globular cluster NGC 6341 by using ground-based (MegaCam at CFHT, SDSS) and space (ACS on HST) data.

The contour levels, based on star count data, are symmetric in the innermost regions, and exhibit an increasing asymmetry for radial distances between $3'$ and $10'$. For distances larger than $\sim 13'$ the stellar distribution becomes clumpy. The contour levels do not exhibit a preferred orientation in space.

We calculated two independent radial profiles, to describe the distribution of stars in the cluster, the number density (ND) and the surface brightness (SB) profile. We performed fits of spherical isotropic King and Wilson models to these profiles. Wilson mod-

els appear to reproduce better than King models the behavior of the outermost regions of the cluster with no need of extra-tidal halos. Interestingly, for the number density profile, both models significantly underestimate the observations in the innermost regions.

We also found that the best fit to the ND and to the SB profile are provided by two different models for the two families, even though the profiles are derived from the same data-sets. We argue that this difference is caused by a difference in the radial distribution of the stellar tracers that characterize the two observed profiles. The number density profile traces the radial distribution of main sequence stars, whereas the surface brightness profile that of bright evolved stars. This conclusion is also supported by the results of a test that has been carried out on two additional profiles, calculated by considering only stars fainter than a given magnitude. Furthermore, the results of the kinematic fits to the velocity dispersion profile of this cluster appear to be in agreement with this interpretation.

To our knowledge, this is the first investigation in which independent estimates of both number density and surface brightness profiles derived by the same set of data are provided and compared. In the literature, there are many examples of papers in which a combination of number density and surface brightness profiles is performed to enlarge the extent of the available profiles to describe a given globular cluster. The results presented here show that this procedure is to be avoided, because the mixing of profiles that are determined by different tracers provides a distorted description of the system.

Hopefully, a thorough discussion of the behavior of different profiles in this and other clusters should determine which of the various considered profiles is best suited for a study in terms of one-component models. We refer to Chapter 9 for a first discussion on this topic, based on the analysis of the results of N-body simulations.

In this context a key role can be played by the new generation of wide field imagers that are available at the 4-8 m class telescopes (Dark Energy Camera and Survey at the CTIO[6] 4 m Blanco telescope, Mohr et al. 2012; Hyper SuprimeCam at Subaru[7]). In a single pointing they can cover the entire extent of a large number of globular clusters and with modest exposure times they make it possible to perform homogeneous and accurate photometry several magnitudes fainter than the main sequence turnoff.

[6] `http://www.ctio.noao.edu/noao/content/Dark-Energy-Camera-DECam`
[7] `http://www.naoj.org/Projects/HSC/index.html`

CHAPTER 6

Rotating globular clusters

Internal rotation, external tides, and pressure anisotropy are the main physical factors that could be responsible for the observed flattening of globular clusters, but we still do not know which is the dominant cause of the observed deviations from spherical symmetry (van den Bergh 2008). For the moment, we do not address the effect of tides because they are expected to act mainly in the outer parts of these stellar systems, in regions outside the focus of the present investigation. The suggestion that internal rotation plays a role in determining the structure and morphology of globular clusters is not new (King 1961; Fall & Frenk 1985). However, while several investigations have been carried out to probe the role of anisotropy, in only few cases internal rotation has been studied by a quantitative application of non-spherical rotating dynamical models. So far, the most significant examples are the orbit-based axisymmetric modeling of ω Cen and M15 (van de Ven et al. 2006 and van den Bosch et al. 2006, respectively), the study of ω Cen by means of axisymmetric Wilson (1975) models (Sollima et al. 2009) and oblate rotator nonparametric models (Merritt et al. 1997), and the analysis of the internal dynamics of a small sample of Galactic globular clusters by means of dedicated two-dimensional Fokker-Planck models (Fiestas et al. 2006).

In this framework, the present investigation is motivated by the need to provide a more realistic dynamical interpretation of selected rotating Galactic globular clusters. Recently, a new family of self-consistent axisymmetric models has been introduced, specifically designed to describe quasi-relaxed stellar systems with finite global angular momentum (Varri & Bertin 2012, hereafter indicated as VB12); the models are characterized by differential rotation, approximately rigid in the center and vanishing in the outer parts, and pressure anisotropy. In this Chapter we discuss the application of this family of differentially rotating global models to three Galactic globular clusters, namely 47 Tuc (NGC 104), M15 (NGC 7078), and ω Cen (NGC 5139), that have been observed in detail and are known to exhibit evidence for rotation.

The dynamical models will be compared with the relevant photometric and kinematic data, with particular attention to the global characteristics of the three-dimensional kinematics. The role of kinematic data, which, as shown in Chapter 4, are crucial for a meaningful description of these stellar system, is here particularly important, thanks to the possibility of dealing with both line-of-sight and proper-motion data. The selection of the appropriate dynamical models will allow us to obtain also an estimate of the distance to the clusters. Furthermore, by taking into consideration the inclination angle of the rotation axis of the stellar systems with respect to the line of sight, we will perform a detailed analysis of the morphology of the three clusters, thus testing whether, for these cases, the observed deviations from spherical symmetry can indeed be explained by rotation. Finally, since the three clusters are in different relaxation states (47 Tuc and M15, with $\log T_c < 8$, fall in the class of fully relaxed clusters, whereas ω Cen, with $\log T_c > 9$,

should be considered as only partially relaxed, according to the classification introduced in Sect. 1.3.1; T_c indicates the core relaxation time expressed in years) we will be able to test the role of internal rotation under different relaxation conditions.

This Chapter is organized as follows. In Sect. 6.1 we present the available data-sets for these three globular clusters and describe the procedure followed to construct the profiles of the relevant photometric and kinematic quantities. In Sect. 6.2 we summarize the properties of the adopted family of self-consistent rotating dynamical models and introduce the method used to identify the model to describe the data available for the three clusters. The detailed results on 47 Tuc, M15, and ω Cen are reported in Sect. 6.3. In Sect. 6.4 we discuss the results of this work and compare them with those obtained from previous studies. Finally, in Sect. 6.5 we summarize the conclusions that can be drawn from our study.

The work described in this Chapter has been published recently (Bianchini et al. 2013); some variations have been made in the presentation of this study, to allow for a comparison of the results obtained for the different clusters at each step of the followed procedure. My main contribution to this analysis is the determination of the physical scales and of the distance of the clusters by means of the fitting procedures described in Sects. 6.2.2 and 6.2.3.

6.1 Selected globular clusters and their observational profiles

To carry out the proposed analysis, we decided to select, among those already analyzed in Chapter 4, globular clusters that exhibit evidence for rotation, for which proper-motion data are available. This leads us to select three globular clusters, namely 47 Tuc, ω Cen, and M15; their basic properties are summarized in Table 6.1.

In this section we describe the kinematic and photometric data-sets that we will use in the dynamical analysis. The data are referred to a Cartesian coordinate system $(x_{\rm p}, y_{\rm p})$, with $x_{\rm p}$ and $y_{\rm p}$ aligned with the major and minor axes, respectively (van de Ven et al. 2006). The $z_{\rm p}$ axis identifies the line-of-sight direction. Proper motions are then decomposed into projected tangential $u_{\rm T}$ and radial $u_{\rm R}$ components[1].

6.1.1 Kinematic profiles

The present dynamical study is based on a combined analysis of the rotation profiles, the velocity dispersion profiles, and the pressure anisotropy profile. The kinematic profiles are constructed with the traditional binning approach, as described in Sect. 3.2. In particular, radial bins are used to construct the velocity dispersion and anisotropy profiles, whereas the line-of-sight rotation profile is constructed by binning along the observed major axis, in intervals of $x_{\rm p}$. We choose a number of bins that represents the best compromise between having a rich radial sampling and accurate points,[2] as outlined in Sect. 3.2. A brief description of the data-sets and some details of the procedure used to obtain the different profiles are given below.

Line-of-sight velocities data-sets

For 47 Tuc and M15, the line-of-sight velocities data-sets are the same used for the analysis described in Chapter 4. The sample adopted for the first is composed of $N_{\rm V}$ = 2475 ve-

[1] The notation u (instead of v) indicates velocities measured in mas yr^{-1}, as shown in Eq. (6.1).

[2] The number of stars per bin is chosen to be large enough to limit the uncertainties associated with low-number statistics (for the profiles constructed in this Chapter the number of data per bin is > 90).

Table 6.1: Properties of ω Cen, 47 Tuc, and M15.

Globular cluster	$d_\odot$ (1)	R_c (2)	C (3)	$\log T_\mathrm{c}$ (4)	ϕ (5)	ϕ_k (6)
47 Tuc	4.5 ± 0.2	21.60 ± 1.31	2.07 ± 0.03	7.85 ± 0.07	123 ± 1	136 ± 1
M15	10.4 ± 0.8	8.40 ± 0.95	2.29 ± 0.18	7.62 ± 0.06	215 ± 1	106 ± 1
ω Cen	5.2 ± 0.7	142.20 ± 8.26	1.31 ± 0.04	9.52 ± 0.04	6 ± 0	12 ± 1

Globular	ε		i	N_V	N_pm
cluster	(7)	(8)	(9)	(10)	(11)
47 Tuc	0.16 ± 0.02	0.09 ± 0.01	≈ 45	2476	12 974
M15	0.19 ± 0.10	0.05 ± 0.00	60 ± 15	1777	703
ω Cen	0.21 ± 0.02	0.17 ± 0.00	50 ± 4	1868	2740 + 72 970

Notes. For each cluster we list: (1) the distance from the Sun $d_\odot$ in kpc; (2) the core radius R_c in arcsec; (3) the concentration parameter C; (4) the logarithm of the core relaxation time T_c in years (from spherical King models); the position angle of (5) the photometric minor axis ϕ and of (6) the kinematic rotation axis ϕ_k on the plane of the sky, measured in degrees (East of North); the ellipticity ε as reported by (7) CC10 and (8) WS87; (9) the inclination i of the rotation axis with respect to the line of sight measured in degrees; the number of data-points for the samples of (10) line-of-sight velocities N_V and of (11) proper motions N_pm.

References. From Col. (1) to Col. (3), Harris (2010); Col. (4) Chapter 4 (Zocchi et al. 2012); Cols. (5) and (8) WS87; Col. (7) CC10; Col. (9) van de Ven et al. (2006), Anderson & King (2003), van den Bosch et al. (2006) (from top to bottom, that is, for ω Cen, 47 Tuc, and M15, respectively); Cols. (6), (10), and (11) considered in this Chapter.

locities covering the entire extent of the cluster and with an average error of 2.29 km s^{-1}. The data-set of the second is composed of N_V = 1777 line-of-sight velocities; this sample is centrally concentrated, with $\approx 80\%$ of the stars being inside $10\,R_c$ and with an average error of 3.79 km s^{-1}.

For ω Cen, we consider here a different combination of data-sets, with respect to the one adopted in Chapter 4. We decided to combine the 1589 line-of-sight velocities from Reijns et al. (2006) with the 649 line-of-sight velocities from Pancino et al. (2007), which are mainly located in the central part of the cluster. The final combined data-set, obtained after identifying the stars in common between the two samples and keeping those with the lower associated error, is composed of 1868 data, and reaches a radial extent of approximately half truncation radius, with an average error of 1.98 km s^{-1}. In Chapter 4, in place of the data-set from Pancino et al. (2007), we used the data-set from Mayor et al. (1997) because it allowed us to obtain a final data-set containing more than 2000 velocities. Here, it is not possible to use that same combination of data-sets, because Mayor et al. (1997) only give radial distances for the stars in their sample, preventing us to calculate the observed rotation profile.

Proper-motion data-sets

The proper motions for the globular cluster 47 Tuc are taken from McLaughlin et al. (2006); the data-set is composed of $N_{\rm pm}$ = 12 974 Hubble Space Telescope (HST) proper motions, and covers only the central region of the cluster, out to ≈100 arcsec (approximately $4\,R_{\rm c}$). The measurements have an average error of 0.27 mas yr^{-1} (corresponding to 5.76 km s^{-1}at a distance of 4.5 kpc).

For M15, we used the sample of $N_{\rm pm}$ = 703 HST proper motions in the central region of the cluster ($R < 2\,R_c$), as reported by McNamara et al. (2003), with an average error of 0.14 mas yr^{-1} (corresponding to 6.79 km s^{-1}at a distance of 10.2 kpc).

The proper-motion data available for ω Cen are the ones from van Leeuwen et al. (2000), with a total of 9847 ground-based measurements, and the ones from Anderson & van der Marel (2010), with a total of 72 970 HST measurements. We treat the two data-sets as distinct. From the van Leeuwen et al. (2000) data-set we selected a subsample composed of stars with a membership probability higher than 68%, non-disturbed from neighboring stars, and with error measurements lower than 0.25 mas yr^{-1} (for a similar selection, see van de Ven et al. 2006): in this way we obtained a sample composed of $N_{\rm pm}$ = 2740 proper motions, with a radial extent of approximately half truncation radius and an average error of 0.16 mas yr^{-1} (corresponding to 3.89 km s^{-1}for an assumed distance of 5.2 kpc). The data-set from Anderson & van der Marel (2010) is composed of two fields: a central field within $R \lesssim R_{\rm c}$ and a field positioned along the major axis between $0.7R_{\rm c} \lesssim R \lesssim 2.5R_{\rm c}$. The average error of the data is 0.078 mas yr^{-1} (corresponding to 1.92 km s^{-1}for an assumed distance of 5.2 kpc).

We recall that the procedure used to obtain the proper-motion data-sets described above will not reveal any solid body rotation in the plane of the sky, as well as any systematic motions of contraction or expansion (e.g., see Vasilevskis et al. 1979; McLaughlin et al. 2006; Anderson & van der Marel 2010), because the proper-motion measurements are relative measurements (no absolute reference frame is available for measuring the star displacements at different epochs). van de Ven et al. (2006) show how to compensate for the missed solid body component under the assumption of axisymmetry in the proper-motion sample of van Leeuwen et al. (2000), by combining line-of-sight velocities and proper motions. We apply the suggested correction to the ω Cen proper-motion sample of van Leeuwen et al. (2000), but we do not correct the data from Anderson & van der Marel (2010). For 47 Tuc and M15, given the fact that the data-sets are centrally concentrated, we argue that, in the very central regions of the clusters, the amount of solid body rotation associated with this effect is negligible and therefore we do not apply any correction (see van den Bosch et al. 2006, who first noted that the result of the correction for M15 is below the measurement errors and therefore can be ignored). Therefore, for the last two clusters no sign of rotation in the plane of the sky is expected from the proper-motion data-sets considered above; however, rotation in the plane of the sky has been clearly detected for 47 Tuc by Anderson & King (2003), using as an absolute reference the background stars of the Small Magellanic Cloud.

Finally, an additional correction is applied to the ω Cen and 47 Tuc data, to correct for the apparent rotation resulting from their large angular extent and their global orbital motion in the Galaxy; to this purpose, we followed the procedure described by van de Ven et al. (2006).

Rotation profiles

As outlined in Sect. 3.2.2, the first step in building a rotation profile consists in identifying the position angle $\phi_{\rm k}$ of the projected rotation axis in the plane of the sky. The

value obtained for this angle is then used to rotate the Cartesian coordinate system in the plane of the sky by aligning $x_{\rm p}$ and $y_{\rm p}$ with the major and minor axes, respectively. The position angles calculated for the clusters here under examination are listed in Table 6.1, where they can be compared to the position angles of the photometric minor axes ϕ reported by WS87.

The position angles of the kinematic minor axes of 47 Tuc and ω Cen are in reasonable agreement with the photometric ones, suggesting a direct connection between the presence of internal rotation and observed flattening. A discrepancy is found instead for M15: for this cluster the small observed flattening makes the identification of the minor axis nontrivial. Various estimates of the photometric position angle are given in the literature, ranging from 215° to 135°, suggesting a possible twisting[3] of the position angle of both the photometric and kinematic minor axes (Gebhardt et al. 2000; van den Bosch et al. 2006).

After identifying the rotation axis, we can proceed to build the rotation profiles from line-of-sight and proper-motion data. We calculate three mean-velocity profiles, one for the line of sight, $V_{\rm rot}(x_{\rm p})$, and two for the proper motions, $V_{\rm T}(R)$ and $V_{\rm R}(R)$.

Velocity dispersion and anisotropy profiles

The velocity dispersion profiles are computed as described in Sect. 3.2.1, by dividing the data-sets into radial bins. The profiles obtained are $\sigma(R)$, $\sigma_{\rm T}(R)$, and $\sigma_{\rm R}(R)$, respectively for the line-of-sight velocities, projected tangential component of proper motions, and projected radial component of proper motions.

From the dispersion profiles of the proper motions we also calculate the anisotropy profile (see Sect. 3.2.3), $\sigma_{\rm T}(R)/\sigma_{\rm R}(R)$. We recall here that values of $\sigma_{\rm T}/\sigma_{\rm R} \approx 1$ indicate isotropy in velocity space, $\sigma_{\rm T}/\sigma_{\rm R} > 1$ indicate the presence of tangential anisotropy, and $\sigma_{\rm T}/\sigma_{\rm R} < 1$ radial anisotropy.

6.1.2 Photometric profiles

The photometric quantities that we will use in the dynamical analysis are the surface brightness profile and the ellipticity profile.

Surface brightness profiles

The surface brightness profiles are the same used in Chapter 4: they are the V-band surface brightness profiles given by Trager et al. (1995). The profiles are extinction corrected, under the assumption of constant extinction over the entire extent of the cluster. The more accurate data available from Hubble Space Telescope measurements in the inner parts of the three clusters are also used (Noyola & Gebhardt 2006; Noyola et al. 2008).

Ellipticity

For 47 Tuc and M15 we refer to the ellipticity profiles shown in Fig. 5 in WS87. They reach $\approx 0.2\, r_{\rm tr}$ and $\approx 0.4\, r_{\rm tr}$, respectively. For ω Cen we consider the ellipticity profile taken from Geyer et al. (1983). This is the most extended ellipticity profile available for a Galactic globular cluster, as it reaches $\approx 0.5\, r_{\rm tr}$, where $r_{\rm tr}$ represents the standard

[3] Additional tests on the twisting of the rotation axis and on the radial variation of the rotation amplitude can be found in Appendix B of Bianchini et al. (2013).

truncation radius (see Sect. 1.1). In addition, Anderson & van der Marel (2010) report the ellipticity profile of the central region ($R \lesssim 250$ arcsec); in the following analysis both data-sets will be taken into consideration. We note that a significant radial variation is present in the three ellipticity profiles. This is particularly evident for ω Cen, which exhibits a nonmonotonic behavior.

6.2 Model identifications and predictions

To carry out the comparison between the differentially rotating models and the observations, we have to specify:

- three dimensionless parameters: the concentration Ψ, the rotation strength χ, and the parameter $\bar{b}$;
- three physical scales: the radial scale r_0, the central surface brightness μ_0, and the velocity scale v_0;
- the inclination angle i between the rotation axis and the line-of-sight direction;
- the distance to the cluster (required to convert the proper motions in km s^{-1}).

Such a highly-dimensional parameter space is likely to lead to a high degree of degeneracy. Therefore, we decided to separate the modeling procedure in three steps, by starting from the focus of interest of this work, that is the presence of internal rotation. First, we determine the dimensionless structural parameters by following a few natural selection criteria based on the observed kinematics, then we set the physical scales by means of standard statistical fits (this information will be summarized in Tables 6.3 and 6.4), and finally we test some properties of the models as predictions in relation to other observational data not used in the first two steps. In the remaining of this Section, we give more details on each of these steps.

6.2.1 Dimensionless parameters

The exploration of the complete three-dimensional parameter space is guided by the following general properties of the models: (1) large values of the concentration parameter Ψ determine spatially extended configurations, in terms of the relevant units of length; (2) configurations characterized by a given value of concentration and increasing values of the rotation strength parameter χ are progressively more compact because of the adopted truncation prescription in phase space; (3) the parameter $\bar{b}$ determines the shape of the line-of-sight rotation profile, in particular, it regulates the radial position of the velocity peak (see Appendix A.4 and Varri & Bertin 2012 for additional details).

Since the three selected clusters are characterized by significant global internal rotation, it is reasonable to start from the observed rotation properties, in order to identify the natural ranges of the three dimensionless parameters. In particular, the parameters should lead to configurations that successfully reproduce the following observations:

1. the observed value of $V_{\rm rot}^{\rm max}/\sigma_0$, that is, the ratio of the peak of the rotation velocity profile to the central velocity dispersion for the line-of-sight kinematic data;
2. the observed shape of the rotation profile along the line of sight, in particular the position $R_{\rm rot}^{\rm max}$ of the rotation peak (relative to the cluster half-light radius);

Table 6.2: Kinematic quantities to identify the dimensionless parameters of a model.

Globular cluster	σ_0 (1)	$V_{\rm rot}^{\rm max}$ (2)	$V_{\rm rot}^{\rm max}/\sigma_0$ (3)	$R_{\rm h}$ (4)
47 Tuc	13.06 ± 1.00	3.26 ± 0.40	0.25 ± 0.04	190.22 ± 3.06
M15	12.93 ± 1.06	3.00 ± 0.63	0.23 ± 0.05	60.26 ± 9.70
ω Cen	17.31 ± 1.72	5.80 ± 0.32	0.34 ± 0.04	300.06 ± 3.51

Globular cluster	$R_{\rm rot}^{\rm max}$ (5)	$R_{\rm rot}^{\rm max}/R_{\rm h}$ (6)	$R_{\rm a}$ (7)	$R_{\rm a}/R_{\rm h}$ (8)
47 Tuc	342.40 ± 5.13	1.80 ± 0.04	...	...
M15	79.34 ± 12.54	1.32 ± 0.30	...	...
ω Cen	510.10 ± 10.21	1.69 ± 0.04	1035.21±32.10	3.45 ± 0.11

Notes. For each cluster we report in Col. (1) the observed central line-of-sight velocity dispersion σ_0 in km s^{-1}, in Col. (2) the maximum of the line-of-sight rotation profile $V_{\rm rot}^{\rm max}$ in km s^{-1}, in Col. (3) the ratio $V_{\rm rot}^{\rm max}/\sigma_0$, in Col. (4) the half-light radius $R_{\rm h}$ in arcsec from Harris (2010), in Col. (5) the position of the maximum of the rotation profile $R_{\rm rot}^{\rm max}$ expressed in arcsec, in Col. (6) the ratio $R_{\rm rot}^{\rm max}/R_{\rm h}$, in Col. (7) the position $R_{\rm a}$ of the transition from the regime of radial anisotropy to tangential anisotropy in arcsec, and in Col. (8) the ratio $R^{\rm a}/R_{\rm h}$. A blank space in the last two columns indicates that the desired information is not available from the data. Columns (3), (6), and (8) guide our choice of the three dimensionless parameters that characterize the internal structure of the models.

3. the qualitative behavior of the anisotropy profile (when available), in particular the radial position $R_{\rm a}$ (relative to the half-light radius) of the transition from radial anisotropy to tangential anisotropy.

The relevant observational quantities to be matched by application of the above selection criteria are calculated and listed in Table 6.2. Specifically, the central velocity dispersions σ_0 and associated errors are calculated from the kinematic data within $R_{\rm c}/2$; the peak of rotation $V_{\rm rot}^{\rm max}$, its radial position $R_{\rm rot}^{\rm max}$ and the radial position of the transition from radial anisotropy to tangential anisotropy $R_{\rm a}$ are calculated by fitting a polynomial to the rotation profile and to the anisotropy profile, in the relevant radial ranges.

Given a set of parameters $(\Psi, \chi, \bar{b})$, the models are projected on the plane of the sky by assuming a known inclination angle i (reported in Table 6.1), as described in Sect. 2.2.2. The projection is performed by sampling from the relevant distribution function a discrete set of $N = 2\,048\,000$ particles and then by performing a rotation of such discrete system to match the relevant inclination angle. The theoretical kinematic and photometric profiles[4] are then constructed by following the procedures described in Sect. 3.1 and 3.2. The central dispersion σ_0, the maximum of the rotation profile $V_{\rm rot}^{\rm max}$, and its position $R_{\rm rot}^{\rm max}$ are calculated in view of the above-mentioned selection criteria. As to the morphological aspects, the projected isodensity contours are calculated based on the projected number density distribution. The relevant ellipticity profiles are then constructed by considering the ratio of the principal axes of approximately one hundred

[4]The profiles thus constructed are discrete profiles, which are then interpolated to obtain continuous profiles. The statistical scatter associated with the use of discrete model-points is well under control, given the high number of sampling particles considered.

isodensity contours, corresponding to selected values of the normalized projected number density in the range $[0.9, 10^{-3}]$; smooth profiles are then obtained by performing an average on subsets made of ten to twenty individual ellipticity values (depending on the concentration of the configuration).

The dimensionless parameters are varied until the kinematic selection criteria are reasonably met,[5] that is, until we obtain models consistent within the uncertainties with the observed quantities listed in Table 6.2.

6.2.2 Physical scales

Once a set of dimensionless parameters is identified, we proceed to determine the relevant physical scales, by fitting the models to the observed profiles, that is, by minimizing the related chi-squared. Two fits are performed. With the photometric fit to the surface brightness profile we determine two scales: the central surface brightness μ_0 and the radial scale[6] r_0. Once μ_0 and r_0 have been fixed, the velocity scale v_0 is determined by means of the kinematic fit, which is performed by minimizing a combined chi-squared defined as the sum of the contributions from the line-of-sight rotation and the line-of-sight velocity dispersion profiles. Finally, the mass-to-light ratio is directly connected to the central surface brightness by the following relation $M/L_{\rm V} = \hat{\Sigma}(0)10^{\mu_0/2.5}$, where $\hat{\Sigma}(0)$ denotes the central surface density expressed in the relevant units. The details of the fitting procedure and of the calculation of the errors are given in Sect 3.3.

6.2.3 Dynamical distance measurement

The kinematic information associated with the proper motions is used to measure the distance to the cluster. The relation between proper motions u measured in mas yr^{-1} and proper motions v expressed in km s^{-1} is

$$\left[\frac{v}{\text{km s}^{-1}}\right] = 4.74 \left[\frac{d_\odot}{\text{kpc}}\right] \left[\frac{u}{\text{mas yr}^{-1}}\right], \tag{6.1}$$

where $d_\odot$ is the distance from the observer to the globular cluster. Therefore, with all the dimensionless parameters and physical scales fixed from the previous analysis, we obtain a best-fit distance $d_{\odot,\rm dyn}$ (hereafter referred to as dynamical distance) by a combined fit to the observed tangential $\sigma_{\rm T}$ and radial $\sigma_{\rm R}$ velocity dispersion profiles (i.e., by minimizing a combined chi-squared defined as the sum of the contributions of the two velocity dispersion profiles in the plane of the sky).

6.2.4 Predicted profiles

At this stage for a given cluster the model and the relevant scales have all been determined. A number of other observable quantities are then predicted and can be compared to the available observations. In particular, we wish to include in this category the following quantities: the anisotropy profile $\sigma_{\rm T}/\sigma_{\rm R}$, the proper-motion mean-velocity profiles $V_{\rm T}$ and $V_{\rm R}$, the ellipticity profile ε, and the two-dimensional structure of the isodensity contours which need not be perfect ellipses.

[5] Note that the procedure adopted to determine the values of the dimensionless parameters that characterize the internal structure of the models does not allow us to calculate the related formal errors. In any case we will estimate the range of variation of reasonable models (also in relation to the lack of information on R_a for two of the three clusters) by performing a simple exploration of the available parameter space, as described in Sect. 6.2.5.

[6] The scale r_0 is the standard length scale of King models; e.g., see Eq. (A.2) in Appendix A

6.2.5 Exploration of the parameter space

The procedure adopted for the selection of a rotating model gives priority to the kinematic data, which are usually affected by large uncertainties and often do not cover a sufficiently wide radial extent. Therefore, it is important to check whether the selection procedure might be improperly sensitive to these uncertainties. In order to do so, we perform an exploration of the available dimensionless parameter space (Sect. 6.2.1) by estimating what range of parameters would be consistent with the uncertainties associated with the kinematic observed quantities listed in Table 6.2.

For each selected model that meets the kinematic criteria we calculated the physical scales by means of the fits described in Sects. 6.2.2 and 6.2.3. The best-fit model is taken to be the one that minimizes the total chi squared (defined as the sum of the calculated chi squared for the photometric, kinematic, and distance fits). As an example of this procedure, in Fig. 6.5 we show three different models for ω Cen, characterized by different values of the $V_{\rm rot}^{\rm max}/\sigma_0$ parameter, respectively 0.28, 0.34, and 0.36. The three models give comparable results for the kinematic profiles, very similar results for the photometric profile, and, most importantly, they all give similar trends in the predicted ellipticity profiles, as shown in Fig. 6.10. Therefore we conclude that our selection procedure can be considered to be sufficiently stable and reliable.

Moreover, we recall that the kinematic data on the plane of the sky for 47 Tuc and M15 (see Sect. 6.1.1) are not radially extended enough to allow us to determine the complete shape of the anisotropy profile. Therefore, in these cases the $R_{\rm a}$ scale, which marks the radial position of the transition from radial to tangential anisotropy, cannot be used as an additional criterion for the selection of the dimensionless parameters.

6.3 General results

The values of the dimensionless parameters, the physical scales, and the best-fit dynamical distance for the selected models are listed in Table 6.3. In Table 6.4 we report the derived structural properties of the clusters. The quality of the results is summarized in Figs. 6.1-6.6 for ω Cen, 47 Tuc, and M15, respectively. In each figure, the solid lines represent the model profiles, the open circles the data-points. For the kinematic profiles the data-points are associated with a horizontal bar, representing the size of the radial bin, and a vertical bar, indicating the errors associated with the measurements. Quantitative information about the quality of the fits for the determination of the physical scales is given in Table 6.5, where the reduced chi-squared, the corresponding two-sided 90% confidence interval, and the number of degrees of freedom are listed. In each case, the value of the photometric chi-squared $\widetilde{\chi}^2_{\rm p}$ is larger than the value of the kinematic chi-squared $\widetilde{\chi}^2_{\rm k}$: this is due to the fact that the kinematic profiles are characterized by a small number of points with larger error bars (this was also found in Sect. 4.2). Note that the value of the reduced chi-squared of the kinematic fit of M15 is inside the corresponding 90% confidence interval.

6.3.1 Photometric and kinematic fits

In the following we give, separately for the three clusters, a description of the results of the fitting procedure carried out on the photometric and kinematical observed profiles.

Table 6.3: Dimensionless parameters and physical scales of the best-fit models.

GC	Ψ	χ	$\bar{b}$	μ_0	r_0	v_0	$d_{\odot,\mathrm{dyn}}$
	(1)	(2)	(3)	(4)	(5)	(6)	(7)
47 Tuc	7.6	1.6×10^{-3}	0.008	14.30 ± 0.08	24.41 ± 0.14	13.35 ± 0.21	4.15 ± 0.07
M15	6.8	1.6×10^{-3}	0.035	14.65 ± 0.01	13.33 ± 0.20	12.52 ± 0.24	10.52 ± 0.38
ω Cen	5.8	14.4×10^{-3}	0.040	16.43 ± 0.05	134.54 ± 1.13	15.87 ± 0.27	4.11 ± 0.07

Notes. For each globular cluster (GC, indicated in the first column) we list: the concentration parameter Ψ in Col. (1), the rotation strength parameter χ in Col. (2), the $\bar{b}$ parameter in Col. (3), the V-band central surface brightness μ_0 in mag arcsec^{-2} in Col. (4), the radial scale r_0 in arcsec in Col. (5), the velocity scale v_0 in km s^{-1} in Col. (6), and the best-fit dynamical distance $d_{\odot,\mathrm{dyn}}$ in kpc in Col. (7); for the physical scales and the distance, the associated errors are also shown. Note that r_0 is an intrinsic quantity; it is recorded here in arcseconds, for easier comparison with the observations.

Table 6.4: Derived parameters.

GC	C	R_c	R_h	r_tr	M	M/L
	(1)	(2)	(3)	(4)	(5)	(6)
47 Tuc	1.87 ± 0.01	24.6 ± 0.1	162.8 ± 0.9	1814.9 ± 10.4	6.23 ± 0.04	1.69 ± 0.13
M15	1.94 ± 0.02	12.9 ± 0.2	43.7 ± 0.7	1118.9 ± 16.8	4.55 ± 0.07	1.45 ± 0.05
ω Cen	1.27 ± 0.01	127.8 ± 1.1	282.5 ± 2.4	2400.3 ± 20.2	19.53 ± 0.16	2.86 ± 0.14

Notes. For each globular cluster (GC, indicated in the first column) we provide the structural parameters derived for the best-fit models: (1) the concentration parameter $C = \log(r_\mathrm{tr}/R_\mathrm{c})$, (2) the projected core radius R_c in arcsec, (3) the projected half-mass radius R_h in arcsec, (4) the truncation radius r_tr in arcsec, (5) the total mass of the cluster M in units of $10^5 M_\odot$, (6) the V-band mass-to-light ratio in solar units.

Table 6.5: Quality of the fits.

GC	Photometric fit				Kinematic fit				Distance fit			
	n_p	$\widetilde{\chi}^2_\mathrm{p}$	$\widetilde{\chi}^2_\mathrm{inf}$	$\widetilde{\chi}^2_\mathrm{sup}$	n_k	$\widetilde{\chi}^2_\mathrm{k}$	$\widetilde{\chi}^2_\mathrm{inf}$	$\widetilde{\chi}^2_\mathrm{sup}$	n_d	$\widetilde{\chi}^2_\mathrm{d}$	$\widetilde{\chi}^2_\mathrm{inf}$	$\widetilde{\chi}^2_\mathrm{sup}$
	(1)	(2)	(3)	(4)	(5)	(6)	(7)	(8)	(9)	(10)	(11)	(12)
47 Tuc	229	5.55	0.85	1.16	39	4.00	0.66	1.40	39	1.35	0.66	1.40
M15	308	5.11	0.87	1.14	31	1.08	0.62	1.45	7	0.41	0.31	2.01
ω Cen	70	4.73	0.74	1.29	39	1.75	0.66	1.40	73	7.19	0.74	1.29

Notes. For each globular cluster (GC, indicated in the first column), separately for the photometric, kinematic, and distance fits, we provide the number of degrees of freedom [Cols. (1), (5), and (9)], the reduced best-fit chi-squared [Cols. (2), (6), and (10)], and the lower [Cols. (3), (7), and (11)] and upper [Cols. (4), (8), and (12)] boundaries of the two-sided 90% confidence level interval for the reduced χ^2-distribution with n degrees of freedom.

47 Tucanae

As illustrated in Fig. 6.1, the surface brightness profile and the line-of-sight rotation and velocity dispersion profiles are well reproduced by the selected model. In particular,

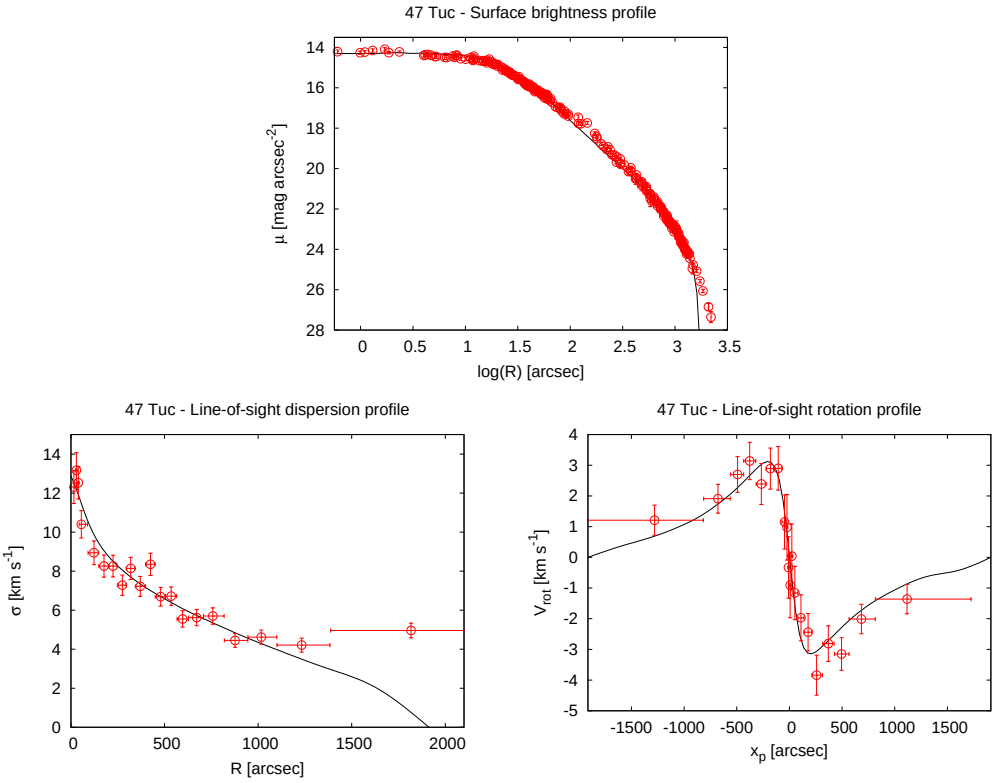

Figure 6.1: Surface brightness profile, line-of-sight velocity dispersion profile, and line-of-sight rotation profile (measured along the projected major axis; for the definition of the $x_{\rm p}$ coordinate and the way the data are binned, see Sect. 6.1) for 47 Tuc. Solid lines represent the selected model profiles and open circles the observational data-points. Vertical bars represent the measured errors and horizontal bars indicate the size of the bins. The fits on these profiles have been used to determine the three physical scales of the model (μ_0, r_0, v_0) (see Table 6.3); the associated photometric and kinematic reduced chi-squared and the number of degrees of freedom are listed in Table 6.5.

the rotation profile is well matched throughout the extension of the cluster, showing clearly the position of the maximum rotation velocity, the characteristic rigid rotation behavior in the central region, and the relatively sharp decrease in the outer parts. The observed line-of-sight velocity dispersion profile is characterized by one data-point at $R \gtrsim 1800$ arcsec deviating from the model profile (this fact has already been detected in Sect. 4.2, when the study of the observed profiles by means of spherical models was discussed). A corresponding discrepancy is found also for the surface brightness profile, at approximately the same radial position (the last four photometric data-points). These two features may be interpreted in terms of the population of "potential escapers" resulting from the tidal interaction between the cluster and the host Galaxy (see Küpper et al. 2010; Lane et al. 2012).

As to the proper-motion data, the relevant profiles, although limited to the central region, show a satisfactory agreement with the model predictions (see Fig. 6.2). In the intermediate regions ($50 \lesssim R \lesssim 1000$ arcsec) the model predicts weak radial anisotropy and tangential anisotropy in the outer parts. It would be interesting to acquire more

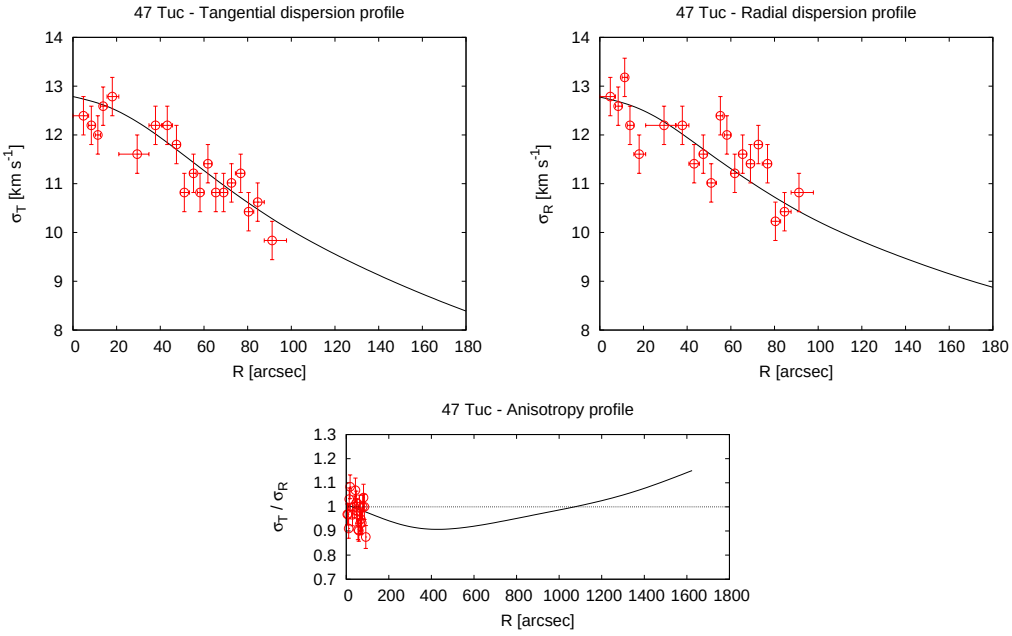

Figure 6.2: The top panels illustrate the fit to the proper-motion dispersion profiles along the projected tangential and radial directions for 47 Tuc; this fit has determined the dynamical distance $d_{\odot,\mathrm{dyn}}$. The associated reduced chi-squared and the number of degrees of freedom are shown in Table 6.5. The bottom panels show the predicted anisotropy profile against the available data. Solid lines represent the model profiles, open circles the observational data-points. Vertical bars indicate the measured errors and horizontal bars indicate the size of the bins.

spatially extended proper-motion measurements to confirm this prediction.

Rotation in the plane of the sky is not available from the proper-motion data-set of McLaughlin et al. (2006). However, proper-motion rotation has been measured for this cluster by Anderson & King (2003), by using the HST and by considering background stars of the Small Magellanic Cloud as an absolute reference frame. The observed rotation corresponds to a velocity of 4.97 ± 1.17 km s^{-1}(based on the assumed distance of 4.5 kpc) at a projected radius of 5.7 arcmin (corresponding approximately to the position of the rotation peak). Within the uncertainties, this is consistent with our model, which predicts a value of 4.13 km s^{-1}at 5.7 arcmin.

M15

Remarkably, except for the most central region, the selected model offers a good description of both the line-of-sight kinematic profiles and the surface brightness profile (see Fig. 6.3). The line-of-sight velocity dispersion profile is reproduced by the model out to the last available bin, located at approximately $0.5r_{\mathrm{tr}}$.

As to the line-of-sight rotation profile, a large scatter is present in the central regions, due to the high measurement errors, which have an average of 3.79 km s^{-1}(significantly higher than the average errors of ω Cen and 47 Tuc: 1.98 km s^{-1}and 2.29 km s^{-1}, respectively). Unfortunately, the kinematic data-set does not sample the region where the peak of the rotation curve is expected. More accurate and better distributed line-of-sight

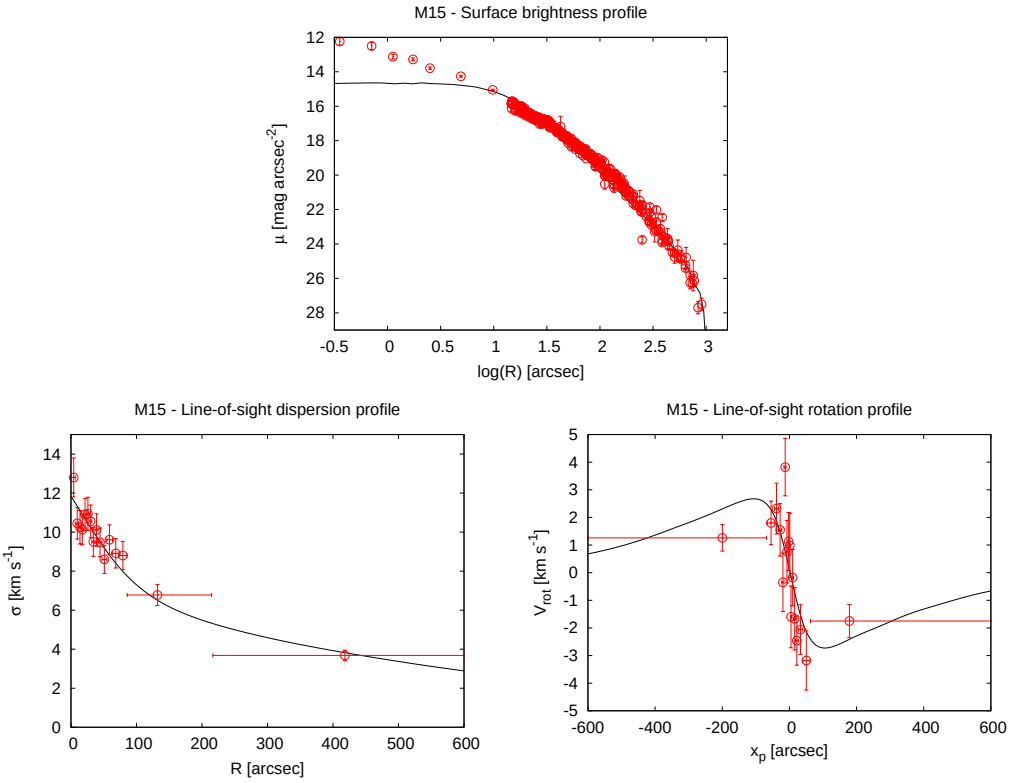

Figure 6.3: Surface brightness profile, line-of-sight velocity dispersion profile, and line-of-sight rotation profile (measured along the projected major axis) for M15. For description of symbols and curves see Fig. 6.1.

velocity measurements would be required to build a more reliable and complete rotation profile. However, it is interesting to note that the rotation profile in the central regions, characterized by a solid-body behavior, is well accounted for by the model, although high rotation is detected in the center and interpreted as a signature of the presence of a decoupled rotating core (for more details, see Appendix B of Bianchini et al. 2013).

For the proper motions, given the small number of data and the low accuracy of the measurements, we decided to divide the sample in only 4 bins to avoid excessive statistical noise; the relevant profiles are illustrated in Fig. 6.4. Such profiles can be used to constrain the kinematic behavior of the cluster only in relation to the very central regions. In turn, the selected model leads to specific predictions on the anisotropy profile in the intermediate and outer parts of the object, which are expected to first show weak radial anisotropy and then tangential anisotropy. Unfortunately, for this object no information about the rotation on the plane of the sky is yet available.

ω Centauri

In general, the selected model is in satisfactory agreement with the surface brightness profile and the line-of-sight kinematic profiles, as shown in Fig. 6.5. For the photometric profile, the model reproduces well the central regions and the intermediate parts, but it

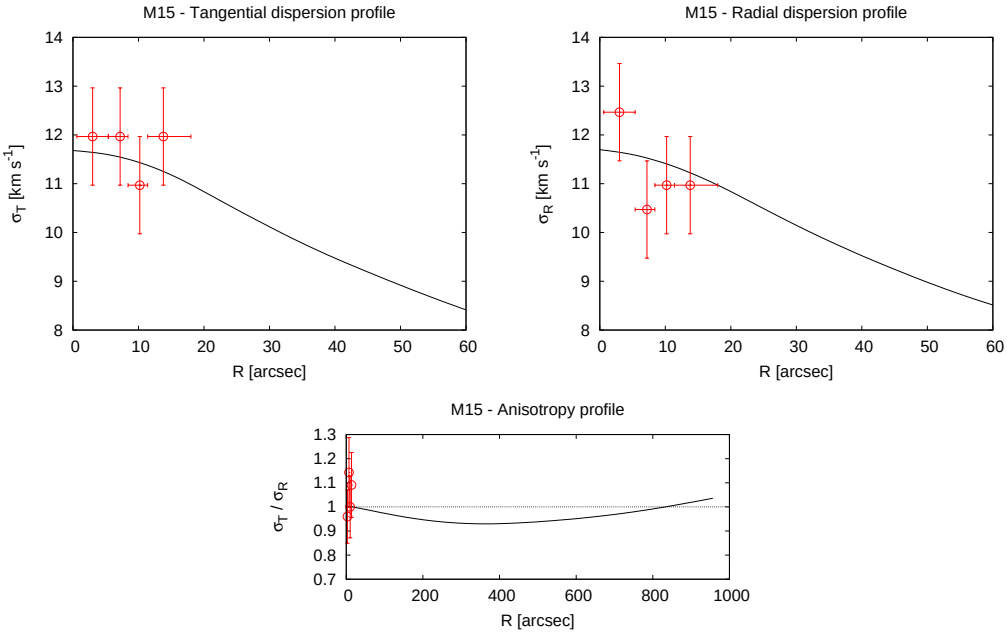

Figure 6.4: Tangential dispersion, radial dispersion, and anisotropy profile for M15. For description of symbols and curves see Fig. 6.2.

underestimates the last two data-points.

For the line-of-sight kinematic profiles, the model is able to reproduce simultaneously the shape of the rotation profile and the shape of the velocity dispersion profile, with one important failure: the central values (inside ≈ 200 arcsec) of the line-of-sight velocity dispersion are severely underestimated by our model. It is interesting to note that any quasi-Maxwellian dynamical model applied to ω Cen is unable to reproduce the cuspy behavior observed in the central regions (e.g., see the application of spherical King models and of spherical Wilson models presented by MLvdM05 in their Fig. 11; see also the fit by means of the rotating Wilson 1975 model performed by Sollima et al. 2009). In this respect, radially-biased anisotropic models appear to perform better (in particular, see the application of the $f^{(\nu)}$ models discussed in Chapter 4). On the one hand, this feature has sometimes been considered as evidence for the presence of a central intermediate-mass black hole (see Noyola et al. 2008). On the other hand, the same feature may indicate that ω Cen, because of its relatively high relaxation time (see Table 6.1), is only partially relaxed and characterized by a higher degree of radial anisotropy with respect to the case of more relaxed stellar systems, as suggested by Fig. 6.6 (see also van der Marel & Anderson 2010). A more detailed discussion of this issue is postponed to Sect. 6.4.2, where a comparison among models with different anisotropy profiles is presented. Curiously, even though the line-of-sight data indicate high rotation in the very central regions ($R < 0.5 R_c$, see Appendix B of Bianchini et al. 2013), which is naturally interpreted as the signature of a complex rotating central structure, this does not appear to affect the quality of our results on the rotation profile; in fact, the selected model reproduces the central part of the line-of-sight rotation curve surprisingly well (see Fig. 6.6).

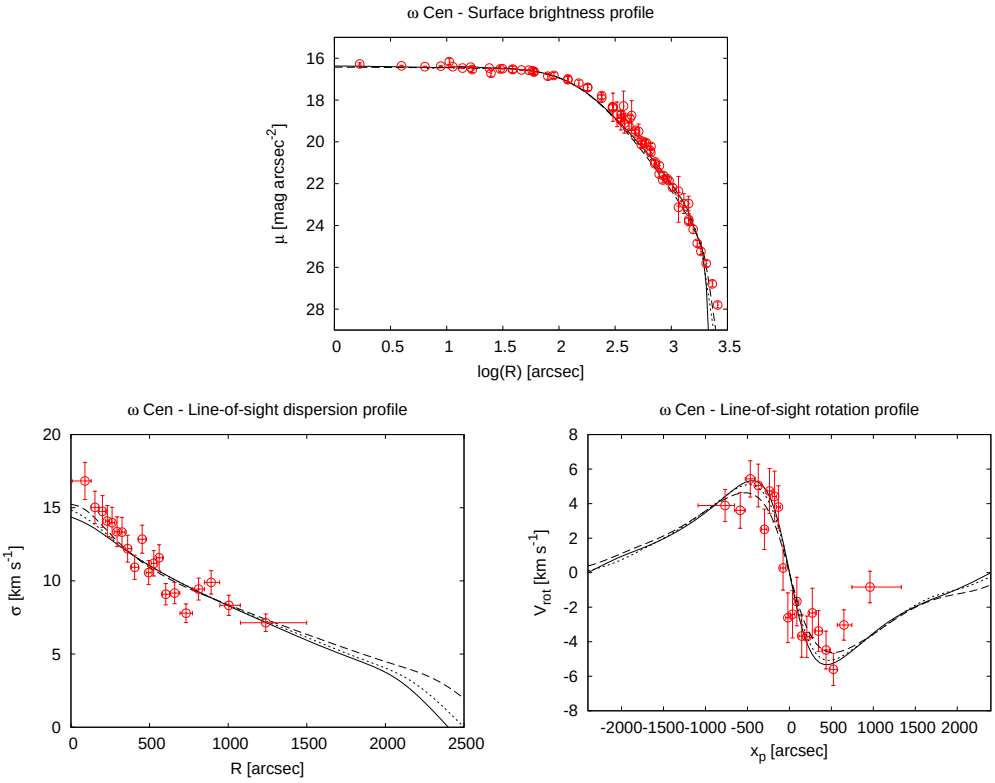

Figure 6.5: Surface brightness profile, line-of-sight velocity dispersion profile, and line-of-sight rotation profile (measured along the projected major axis) for ω Cen. Solid lines represent the selected model profiles and open circles the observational data-points; the dotted and dashed lines represent the profiles of the models used to test the sensitivity of the selection procedure to the specific choice of kinematical parameters on which the procedure in based, as described in Sect. 6.2.5.

In addition, the model identified by our procedure is able to reproduce all three components of the projected velocity dispersion tensor of ω Cen (both along the line of sight and on the plane of the sky; see Fig. 6.6). Interestingly, the shape of the observed anisotropy profile built from the proper-motion dispersions is consistent with the general properties of the selected model, which is characterized by isotropy in the central region, weak radial anisotropy in the intermediate region, and tangential anisotropy in the outer parts. The transition between the region characterized by radial anisotropy to the region characterized by tangential anisotropy takes place at $R \approx 1200$ arcsec. The data indeed show signs of radial anisotropy in the intermediate region (note that our model predicts a degree of radial anisotropy lower than the observed one) and of tangential anisotropy outside $R \approx 1000$ arcsec. The existence of tangential anisotropy found in the present study is consistent with the results of previous investigations, namely van de Ven et al. (2006) and van der Marel & Anderson (2010) (see their Fig. 6). We wish to emphasize that such behavior of the anisotropy profile in the outer parts is a natural property of the family of models at the basis of the present work.

Finally, we can also compare the rotation on the plane of the sky predicted by the

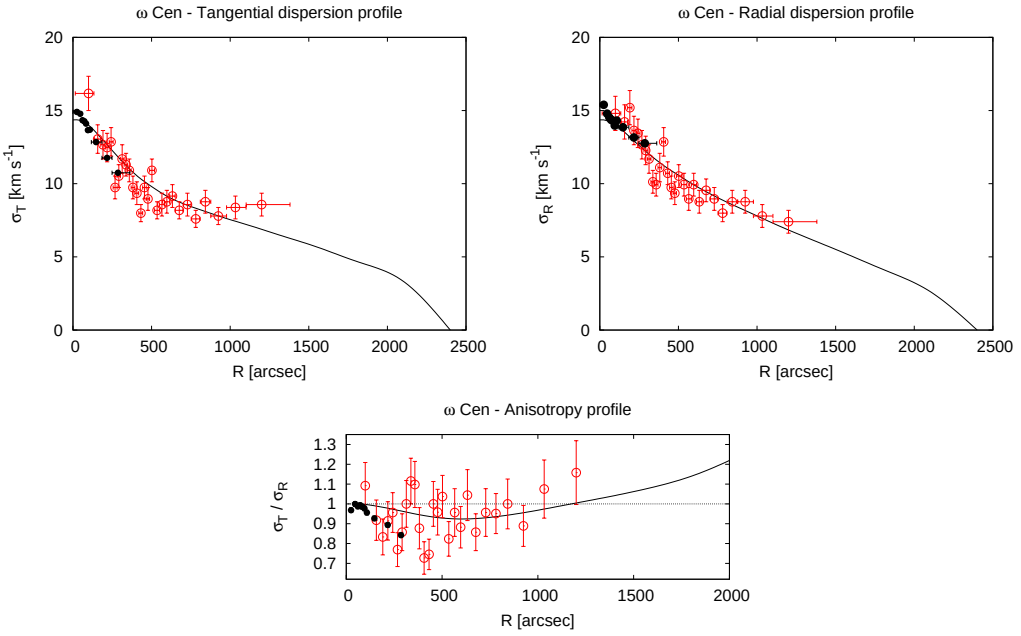

Figure 6.6: Tangential dispersion, radial dispersion, and anisotropy profile for ω Cen. Solid lines represent the model profiles, open circles the observational data-points from van Leeuwen et al. (2000) and black dots those from Anderson & van der Marel (2010). For more details see Fig. 6.2.

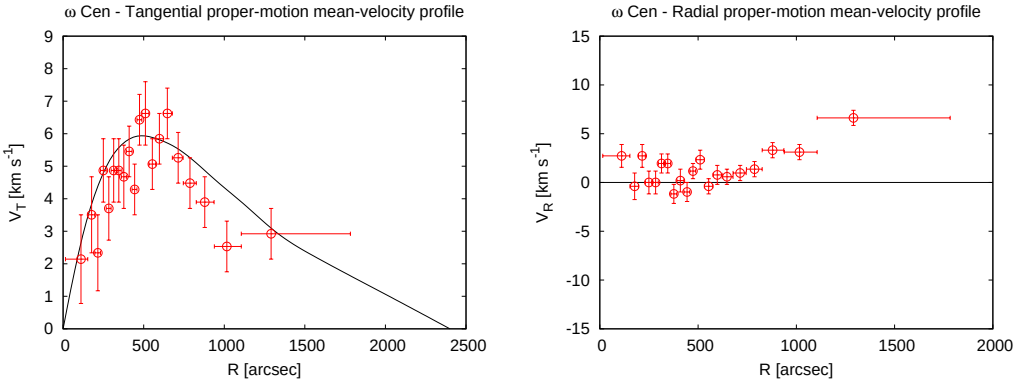

Figure 6.7: Predicted proper-motion mean-velocity profiles along the tangential and radial directions for ω Cen. Solid lines represent the model profiles and open circles the observational data-points. Vertical bars indicate the measured errors and horizontal bars the size of the bins. Note that the data give a hint of a possible overall expansion, which is obviously not present in the model.

model with the observed mean-velocity profiles along the tangential and radial directions. Figure 6.7 shows that the tangential proper-motion mean-velocity profile $V_{\rm T}(R)$ is well reproduced by the model, confirming the presence of differential rotation. In the radial direction the model predicts a flat profile with vanishing velocity; in the external

regions ($R > 1000$ arcsec), the observed proper-motion mean-velocity in the radial direction reaches a value of $V_{\rm R} \approx 5$ km s^{-1}, indicating the presence of a systematic expansion ascribed to systematic errors in the measurement procedures (van Leeuwen et al. 2000). At this point, we should also recall that, as discussed in Sect. 6.1.1, the procedure used to measure the proper motions removes any sign of solid-body rotation in the plane of the sky; therefore we apply to the data a correction to recover the solid-body mean velocity component, following van de Ven et al. (2006). This fact introduces some uncertainties in the final profiles and might account for some of the discrepancies between the model and the observed proper-motion mean-velocity profiles.

In conclusion, aside from the inner cusp problem, the generally good agreement between model and proper-motion mean-velocity and velocity dispersion profiles is quite remarkable, because the model was selected only to match the velocity-to-dispersion ratio along the line of sight $V_{\rm rot}^{\rm max}/\sigma_0$, the location of the peak in the rotation profile along the line of sight $R_{\rm rot}^{\rm max}$, and the location of the transition from radial to tangential anisotropy in the plane of the sky.

6.3.2 Dynamical distance

The rescaling of the model profiles to match the observed proper-motion dispersion profiles allows us to derive an estimate for the distance of the clusters, as described in the previous Section.

For 47 Tuc the best-fit distance is $d_{\odot,\rm dyn} = 4.15 \pm 0.07$ kpc, with associated reduced chi-squared $\widetilde{\chi}^2_{\rm d} = 1.35$ inside the corresponding 90% confidence interval. This value is consistent with the dynamical distance reported by McLaughlin et al. (2006) $d_{\odot,\rm dyn} = 4.02 \pm 0.35$ kpc, measured from the same proper-motion data-set used in the present work, under the simple assumptions of spherical symmetry, isotropy, and absence of internal rotation. Our value is lower than the standard value of $d_\odot = 4.5 \pm 0.2$ kpc reported in the Harris (2010) catalog and lower than other distance estimates obtained by means of photometric methods, such as main sequence fitting, RR Lyrae, and white-dwarf cooling sequence fitting (for a recent summary of results, see Table 1 of Woodley et al. 2012 or Bono et al. 2008).

The dynamical distance obtained for M15 is $d_{\odot,\rm dyn} = 10.52 \pm 0.38$ kpc, with a reduced chi-squared $\widetilde{\chi}^2_{\rm d} = 0.41$, inside the corresponding 90% confidence interval. This is consistent with the kinematic distance obtained by McNamara et al. (2004) of $d_{\odot,\rm dyn} = 9.98 \pm 0.47$ kpc and the value obtained by van den Bosch et al. (2006) of $d_{\odot,\rm dyn} = 10.3 \pm 0.4$ kpc; these two estimates are based on the same proper-motion data-set considered in the present work. In particular, the value obtained by McNamara et al. (2004), which is based on the simplifying assumptions of spherical symmetry, isotropy in velocity space, and no rotation, is lower than the value obtained in the present work and the one obtained by van den Bosch et al. (2006) (in which anisotropy, rotation, and flattening are taken into account). Moreover, our distance is in agreement with other distance estimates based on photometric methods, such as the one reported in the Harris (2010) catalog $d_\odot = 10.4 \pm 0.8$ kpc. In this case, the conclusion drawn by Bono et al. (2008), according to which distances obtained from kinematic data are systematically lower than distances obtained from other methods, does not hold.

The dynamical distance obtained for ω Cen is $d_{\odot,\rm dyn} = 4.11 \pm 0.07$ kpc, with an associated reduced chi-squared $\widetilde{\chi}^2_{\rm d} = 7.19$. This value is significantly smaller than the distance estimated with photometric methods (e.g., $d_\odot = 5.2 \pm 0.7$ kpc from Harris 2010) and also smaller than other estimates obtained by means of the application of different dynamical models (e.g., $d_{\odot,\rm dyn} = 4.70 \pm 0.06$ kpc from van der Marel & Anderson 2010;

$d_{\odot,\mathrm{dyn}} = 4.8 \pm 0.3$ kpc from van de Ven et al. 2006). As also noted by van de Ven et al. (2006), a low value of the distance is expected when either the line-of-sight velocity dispersion is underestimated or the proper-motion dispersion is overestimated. In our case, it is clear from the previous section and from Fig. 6.5, that our dynamical model underestimates the central value of the line-of-sight velocity dispersion. Therefore, our distance estimate is affected by a systematic bias (reflected also by the high value of the reduced chi-squared). The dynamical distances obtained by van der Marel & Anderson (2010) and van de Ven et al. (2006) are based on a Jeans model and on an orbit-based model, respectively; previous studies based on the application of quasi-Maxwellian dynamical models, such as spherical King or spherical Wilson models, do not report distance estimates for this object.

6.3.3 Deviations from spherical symmetry

The selected axisymmetric model is associated with a well defined ellipticity profile, which is the morphological counterpart to the presence of rotation.

Figure 6.8 shows the ellipticity profile predicted by our model plotted together with the ellipticity data available for 47 Tuc. In this cluster, the deviations from spherical symmetry are naturally explained by the selected model with a surprising degree of accuracy. In fact, the ellipticity profile derived by our model reproduces the radial variation of the observed ellipticity over the entire spatial range covered by the data (the flattening of 47 Tuc increases from a value of $\varepsilon \approx 0$ to a maximum value of $\varepsilon \approx 0.12$ at $R \approx 450$ arcsec). We recall that the ellipticity profile associated with the selected self-consistent model is a structural property completely determined by the dimensionless parameters and physical scales identified during the model selection procedure. In this case we can thus state with confidence that internal rotation is the physical ingredient responsible for the observed global deviations from spherical symmetry. In this respect, we emphasize that the relation between the shapes of the rotation profile and the ellipticity profile is highly nontrivial; in particular, the peak of the rotation profile does not correspond to a peak in the ellipticity profile (at variance with what is often believed, e.g. Meylan & Mayor 1986).

The comparison between the observed and the predicted ellipticity profiles of M15 is illustrated in Fig. 6.9. Our model predicts a value of ellipticity close to zero in the very central regions and an increase of the flattening thereafter, consistent with the observations. In particular, we note that the model profile seems to overlap smoothly with the observed profile in the region sampled by the data. Moreover, the observed average flattening is consistent with the value predicted by our model. We thus conclude that our dynamical model, and consequently the presence of internal rotation, can naturally explain the observed deviations from sphericity of M15.

The comparison of the predicted ellipticity of ω Cen with the corresponding observed profile is illustrated in Fig. 6.10; the open circles represent the profile from Anderson & van der Marel (2010), the black dots represent the profile from Geyer et al. (1983), and the solid line the profile derived from our model. The two observed profiles are consistent in the sampled radial range, except for the innermost region ($R < 100$ arcsec) where a large scatter dominates the data of Anderson & van der Marel (2010). The model ellipticity profile is characterized by a general trend similar to that of the Geyer et al. (1983) measurements, but it predicts the peak of maximum flattening too far out, at about $R \approx 1000$ arcsec. If we calculate the average ellipticity in the radial range covered by the data, we find an average flattening associated with the selected model ($\varepsilon = 0.10$) in agreement with the observed one ($\varepsilon = 0.12 \pm 0.02$). In other words, we are led to

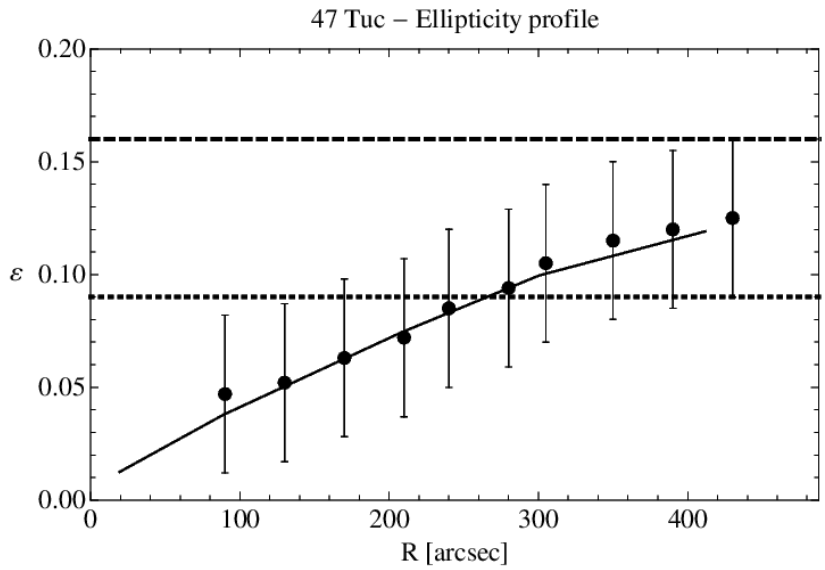

Figure 6.8: Ellipticity profile for 47 Tuc. The black dots mark the observed ellipticities presented by WS87, the solid line represents the profile derived from our axisymmetric rotating model. Dotted and dashed horizontal lines indicate the average values reported by WS87 and CC10, respectively.

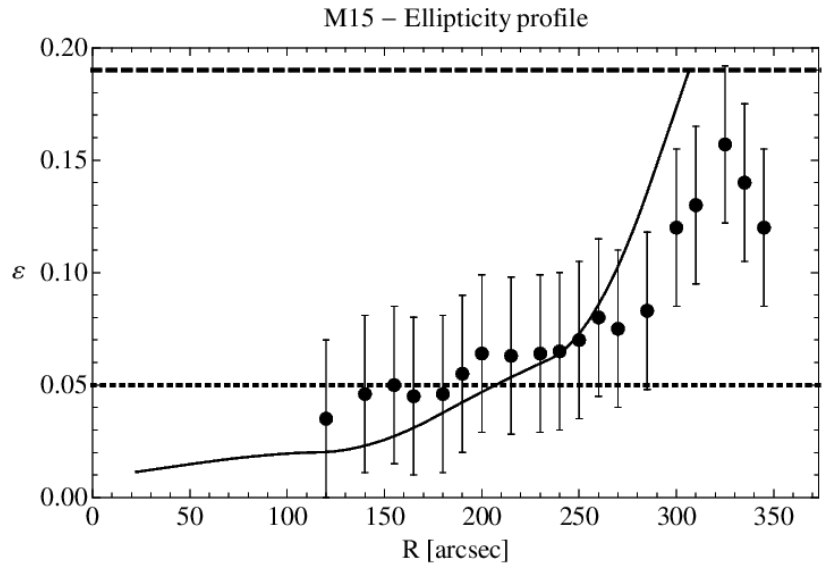

Figure 6.9: Ellipticity profile for M15. For a description of symbols and curves see Fig. 6.8.

conclude that the observed deviations from sphericity are likely to be originated by the presence of internal rotation. In Sect. 6.4 we will argue that the discrepancies between the predicted and observed ellipticity profiles are likely to be related to the complex nature of ω Cen, in particular to its conditions of partial relaxation and the interplay between

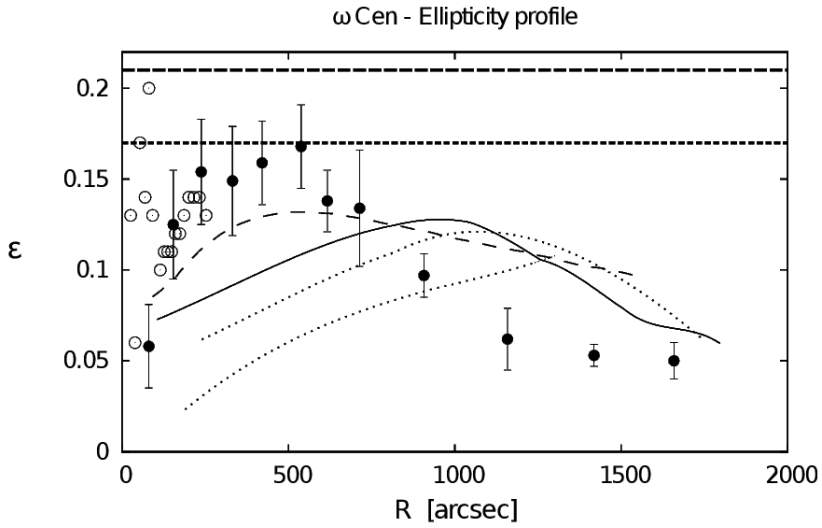

Figure 6.10: Ellipticity profile for ω Cen. Open circles mark the observed ellipticities from Anderson & van der Marel (2010), black dots those from Geyer et al. (1983). The solid line represents the predicted profile derived from the rotating axisymmetric model proposed in this work, whereas the thin dotted curves correspond to the models used to test the sensitivity of the selection procedure (see Sect. 6.2.5). Dotted and dashed horizontal lines indicate the average values from WS87 and CC10, respectively. Finally, the long-dashed line represents the ellipticity profile for the best-fit rotating Wilson (1975) model, from Sollima et al. (2009); see discussion in Sect. 6.4.

rotation and anisotropy in velocity space.

6.4 Discussion

6.4.1 Partially relaxed versus well relaxed clusters

The three globular clusters under consideration are known to be in different evolutionary states. In fact, the core relaxation time of ω Cen is significantly higher than the relaxation times of 47 Tuc and M15 (see Table 6.1). This suggests that ω Cen should be in a partially relaxed state, whereas 47 Tuc and M15 can be considered well-relaxed clusters.

When applied to the two more relaxed clusters, 47 Tuc and M15, our models perform very well; the systems are quasi-isotropic in their inner regions and internal rotation is able to explain the observed morphology. The most significant discrepancy left is probably that of the core structure of M15 (inside $\approx$ 10 arcsec), characterized by a cusp in the surface brightness that is likely to be related to the phenomenon of core collapse (Murphy et al. 2011), which goes beyond the objectives of our equilibrium models. For this cluster, the intermediate and outer regions (from 10 arcsec out to 1000 arcsec) are well fitted by our rotating model (Fig. 6.3), at variance with the spherical King model, which severely underestimates the surface brightness (beyond $\approx$ 300 arcsec; see Fig. 4.1).

In the case of ω Cen, we argue indeed that the main discrepancies noted between our model and observations are associated with the condition of partial relaxation of the cluster. This interpretation is supported by the fact that models with sizable radially-biased pressure anisotropy, such as the family of spherical $f^{(\nu)}$ models, are able to re-

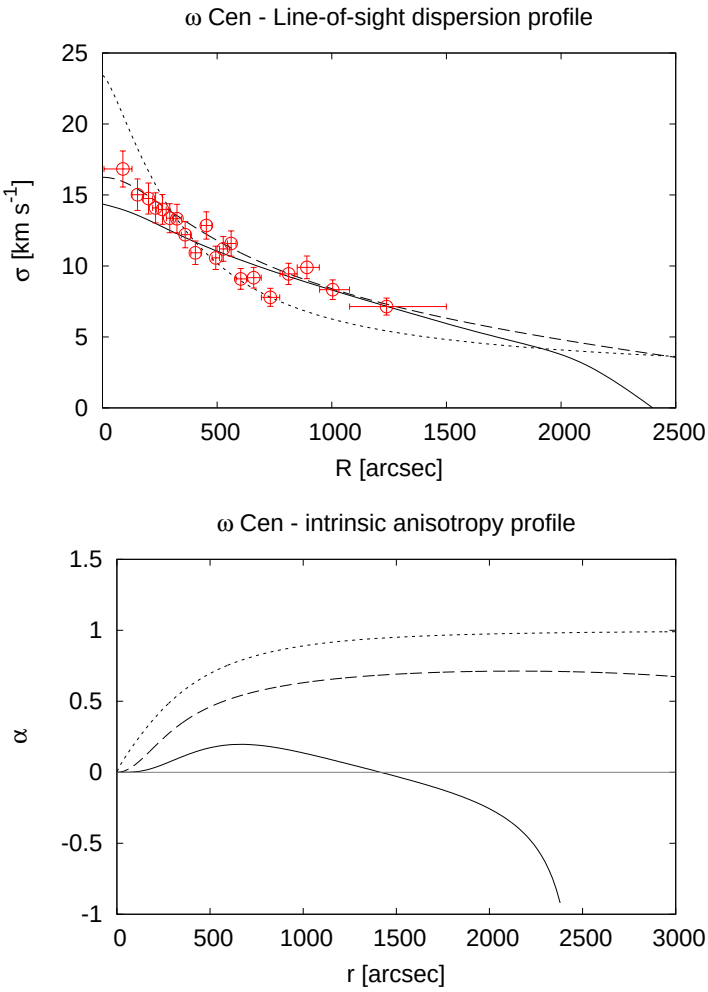

Figure 6.11: Comparison between our rotating quasi-relaxed model (solid lines), spherical radially-biased anisotropic $f^{(\nu)}$ model (from Chapter 4, thin dotted lines), and rotating Wilson (1975) model (from Sollima et al. 2009, dashed lines) for ω Cen. The top panel represents the projected line-of-sight velocity dispersion profile and the bottom panel the intrinsic anisotropy profile α, evaluated along the equatorial plane. A higher degree of radially-biased anisotropy in the central-intermediate region contributes to steepen the central dispersion profile.

produce this controversial kinematic feature, as shown in Chapter 4, while the rotating model here considered is unable to describe the cuspy behavior of the velocity dispersion profile in the central regions (inside $\approx$ 300 arcsec). In Fig. 6.11 we compare our quasi-relaxed model with the best-fit $f^{(\nu)}$ model from Chapter 4 and to the best-fit rotating Wilson (1975) model from Sollima et al. (2009). The top panel shows that, in the central region ($R \lesssim 500$ arcsec $\approx 2R_{\rm h}$), the gradient of the line-of-sight dispersion profile depends strongly on the assumed model: the steeper gradient is associated with the $f^{(\nu)}$ model, which in turn is the model characterized by the strongest radial anisotropy. Note that the spherical $f^{(\nu)}$ model and the rotating Wilson (1975) model both miss the feature

of tangential anisotropy in the outer regions altogether. This is further illustrated by the bottom panel which shows the intrinsic anisotropy parameter α (defined in Eq. (2.19)) profile evaluated along the equatorial plane. Indeed, the rotating models presented in VB12 and applied here are characterized by the presence of only weak radial anisotropy in the intermediate radial range, because they have been constructed under the assumption that the stellar system is quasi-relaxed.

This phase-space property has a counterpart in the predicted ellipticity profile, the shape of which does not reproduce properly the observations. As stated in Sect. 6.3.3, the presence of a large amount of radial anisotropy (directly measured; e.g., see bottom panel of Fig. 6.6) can explain the observed deviations. To add further support to this conclusion, in Fig. 6.10 we compare the ellipticity profile predicted by our model to the profile presented by Sollima et al. (2009) based on a rotating Wilson (1975) model: the latter model is characterized by a higher degree of radial anisotropy (in fact it misses the feature of tangential anisotropy in the outer regions altogether; see Fig. 6.11) and generates deviations from sphericity in the inner regions in better agreement with the observations. Therefore, the structure of ω Cen is determined by the complex interplay between rotation and anisotropy; anisotropy can be naturally present because this cluster is characterized by long relaxation times.

6.4.2 Comparison with previous studies

To our knowledge, an application of non-spherical models to the full set of data available for these clusters, including proper motions, has been made only by van de Ven et al. (2006) for ω Cen and by van den Bosch et al. (2006) for M15, based on a Schwarzschild-type modeling procedure (see Sect. 2.3.2). Remarkably, the best-fit model for M15 is characterized by a total mass and a mass-to-light ratio fully consistent with our results, that is, $4.4 \times 10^5 M_\odot$ and 1.6 $M_\odot/L_\odot$, respectively. In the case of ω Cen, we derive a lower value for the total mass and a higher value for the mass-to-light ratio. Here the discrepancy reflects our estimate of the distance to the object, smaller than distances reported in the literature[7] (by adopting a distance of $d_\odot = 4.8$ kpc, the resulting total mass associated with our rotating model would be $M = 2.28 \times 10^6 M_\odot$, whereas for $d_\odot = 5.2$ kpc, the total mass would be $M = 2.47 \times 10^6 M_\odot$).

In addition, only very few studies have been made of non-spherical rotating models constructed under given physical assumptions. To our knowledge, only three families of models based on a distribution function allowing for internal rotation have been explored in significant detail: those by Prendergast & Tomer (1970), Wilson (1975), and Lupton & Gunn (1987). The first two were originally designed to describe elliptical galaxies and not globular clusters. In fact, the closest and modern paper that we are aware of, for which some comparison with the present article could be made, is that by Sollima et al. (2009), although the application presented there is limited to the line-of-sight kinematics (and thus without consideration of the star proper-motion data). The comparison was provided in the previous subsection.

Therefore, we are left with the task of comparing the results of the dynamical analysis performed in the present work with the results obtained from previous studies based on spherical nonrotating models. This comparison is also interesting, because it shows

[7] For ω Cen, the recent investigation by D'Souza & Rix (2013) assumes a distance of 5.5 kpc, much higher than the distance (4.11 kpc) that we determined in the present work. Based on a discrete kinematic approach, including flattening and rotation, the authors report a value of the total mass of $(4.05 \pm 0.10) \times 10^6 M_\odot$. By assuming an apparent visual magnitude of $m_{\mathrm{V,tot}} = 3.68$ mag (Harris 2010), and by rescaling this value to the distance of 5.5 kpc (to obtain the absolute total luminosity), the corresponding mass-to-light ratio is $M/L = 4.56\, M_\odot/L_\odot$, significantly larger than usually obtained for this cluster.

Table 6.6: Comparison of the structural parameters from the best-fit rotating models with those obtained from spherical models in previous studies.

Cluster	Ref.	C	R_c	M	M/L
47 Tuc	(0)	1.87 ± 0.01	24.6 ± 0.1	6.76 ± 0.04	1.56 ± 0.12
	(1)	2.01 ± 0.00	22.6 ± 0.2	7.18 ± 0.41	1.34 ± 0.08
	(2)	2.57 ± 0.06	32.1 ± 2.6	10.71 ± 0.98	$1.17^{+0.52}_{-0.43}$
	(3)	2.07 ± 0.03	21.6 ± 1.3	...	...
M15	(0)	1.94 ± 0.02	12.9 ± 0.2	4.49 ± 0.07	1.47 ± 0.05
	(1)	1.86 ± 0.01	7.5 ± 0.1	3.98 ± 0.35	1.12 ± 0.10
	(2)	...	...	...	...
	(3)	2.29 ± 0.18	8.4 ± 1.0	...	...
ω Cen	(0)	1.27 ± 0.01	127.8 ± 1.1	24.71 ± 0.20	2.26 ± 0.11
	(1)	1.32 ± 0.01	127.7 ± 2.4	26.45 ± 3.32	1.93 ± 0.24
	(2)	1.43 ± 0.02	164.6 ± 4.5	24.66 ± 2.26	$2.24^{+1.04}_{-0.82}$
	(3)	1.31 ± 0.04	142.2 ± 8.3	...	...

Notes. For each cluster we provide the concentration parameter $C = \log(r_{\rm tr}/R_c)$, the projected core radius R_c in arcsec, the total mass of the cluster M in units of $10^5 M_\odot$, and the V-band mass-to-light ratio M/L in solar units. The values of M and M/L have been rescaled to a common distance for each cluster to allow for a comparison of the different models considered (4.5 kpc, 10.4 kpc, and 5.2 kpc for 47 Tuc, M15, and ω Cen, respectively).

References. (0) This Chapter; (1) spherical King models from Chapter 4; (2) spherical nonrotating Wilson models from McLaughlin & van der Marel 2005; (3) Harris 2010.

to what extent the determination of the structural parameters is sensitive to the model adopted, or, in other words, to what extent some idealized, relatively simple, commonly used models are likely to introduce systematic errors in probing the structure of globular clusters. Table 6.6 summarizes and compares the following derived structural properties: concentration parameter C, core radius R_c, total mass M, and global V-band mass-to-light ratio M/L. In general, the values of the derived structural parameters are consistent with the values derived from the other studies. Spherical nonrotating Wilson models tend to lead to larger truncation radii, as expected.

We note that our rotating models give a good description of the global kinematics and morphology of the three analyzed globular clusters. As a result, the effects of mass segregation are expected to be modest; in addition, we do not have to invoke the presence of dark matter and we do not find any reason to abandon Newtonian dynamics and to move to the MOND (Modified Newtonian Dynamics) framework.

6.5 Conclusions

We have applied a family of self-consistent global dynamical models, recently constructed with the purpose of describing differentially rotating star clusters in a quasi-relaxed state, to three Galactic globular clusters, namely ω Cen, 47 Tuc, and M15, that exhibit evidence for flattening and rotation. For these clusters an extremely rich set of data is available, particularly on their three-dimensional kinematics.

Motivated by the results of the work described in Chapter 4, which showed that kinematical profiles are crucial to determine the dynamical model better representing a given globular cluster, we have given here highest priority to the interpretation of the available kinematical data. This is a particularly challenging test for the models. In turn, the success of the models for the two clusters known to be in a sufficiently well relaxed state allows us to measure their internal structural parameters accurately and reliably, well beyond the reach of simpler and more idealized models.

The main results obtained by the presented analysis are the following:

- For the three most studied globular clusters we have illustrated how such detailed modeling procedure can be implemented to make a test on the adequacy of a physically justified, global, self-consistent family of models to interpret all the available photometric and kinematic data, including a rich set of proper motions. One important technical problem, the inclination and projection of self-consistent models constructed from a nontrivial distribution function, has been resolved by the use of suitable discrete realization in terms of a large number of simulated particles (see Sect. 2.2.2).

- For the well-relaxed cluster 47 Tuc the model that we have identified provides a very good interpretation of the photometric and kinematic data. In particular, the rotation profile is well matched throughout the entire extent of the cluster, showing clearly the position of the maximum rotation velocity, the characteristic rigid rotation behavior in the central region, and the relatively sharp decline in the outer parts. In addition, the proper-motion rotation measured by Anderson & King (2003) is well consistent with the value predicted by our model at the relevant radial positions. The identification of the model comes out naturally and leads to a specific prediction on the ellipticity profile that is in excellent agreement with the observations.

- For the relaxed cluster M15 we provide a global model in good agreement with the data; in particular, the line-of-sight rotation profile in the central regions, characterized by a solid-body behavior, is well accounted for by the model. The possible presence of a fast-rotating core on the small radial scale (where the observed photometric profile shows evidence of a post-core-collapse phase) does not appear to influence the quality of our global description.

- The model selected for ω Cen is unable to reproduce the steep central gradient in the line-of-sight velocity dispersion profile; in addition, the predicted ellipticity profile is somewhat offset with respect to the observed profile. We showed how these features are likely to reflect the condition of only partial relaxation of the cluster, as confirmed by the measured high radial anisotropy. Still, somewhat surprisingly, our model provides a satisfactory global interpretation of the complex three-dimensional kinematics available for this object. In particular, the overall behavior of the anisotropy profile is successfully described, including the presence of tangential anisotropy in the outer parts of the system.

- The results of this study confirm that indeed internal rotation is responsible for the observed flattening for at least two of the three clusters (47 Tuc and M15). For ω Cen there is no doubt that rotation is important; still, the discrepancy between predicted and observed ellipticity profile suggests that pressure anisotropy cooperates in determining its observed morphology.

- We have determined new dynamical estimates of the distances to the stellar systems under consideration. Before, this kind of analysis has been performed only in a few cases (in particular, see van de Ven et al. 2006 and Anderson & van der Marel 2010). It appears that the distance estimates based on dynamical models are generally lower compared to those derived from photometric methods, such as the analyses of variable stars (e.g., see Bono et al. 2008), and from other stellar indicators.

Further interesting insights may come from the study of rotation in different environments, such as in low-mass stellar systems in the Magellanic Clouds, where globular clusters are known to be younger and flatter than the Galactic clusters. In particular, strong differential rotation may be a critical ingredient in determining the structure and internal dynamics of the class of the so-called "ring clusters" (see Hill & Zaritsky 2006 and Werchan & Zaritsky 2011), which are characterized by an off-centered peak density profile. The presence of internal rotation may play an important role also in the dynamics of low-mass stellar systems, in the transition region between classical star clusters and dwarf galaxies (e.g., see the recent spectroscopic study of the rotating ultra-compact dwarf performed by Frank et al. 2011).

We showed that rotation plays an important role in determining the structure of the three considered clusters, but that morphological information (as exemplified by the ellipticity profile of ω Cen) can be decisive in assessing the quality of a model. It remains to be ascertained how frequently is rotation the key dynamical factor and which globular clusters owe their shape instead mainly to external tides or simply to pressure anisotropy. New observational efforts to study the morphology of low-mass stellar systems (in particular, devoted to the measurement of ellipticity profiles, isophotal contours, and quadrupole moments) are thus highly desired.

Finally, we wish to reiterate (see also Sect. 4.4) that many key dynamical issues (such as a reliable estimate of the dark matter content, the search of dynamical signatures of a possible central intermediate-mass black hole, and the evaluation of the effects of mass segregation) can be addressed exclusively by considering appropriate kinematical data in detail (for a recent study with a generally similar approach, but limited to the study of line-of-sight kinematic data, see Sollima et al. 2012).

Part II

An effort to solve observational problems

CHAPTER 7

Measuring accurate radial velocities with FLAMES

The observed flattening of globular clusters could be caused by internal rotation, by the interaction with the external tidal field, or by pressure anisotropy. To determine which of these dynamical ingredients is responsible for the observed shapes of these stellar systems, it is necessary to study their kinematics.

The importance of dealing with good kinematic data is particularly evident in the results shown in Chapters 4 and 6, where the role of pressure anisotropy and of internal rotation was explored for a selected group of globular clusters. Unfortunately, only for a small fraction ($< 20\%$) of the Galactic clusters accurate and well distributed kinematical measurements are available for such a detailed dynamical analysis (see Appendix B). We therefore decided to submit a proposal to the European Southern Observatory (ESO), requesting to measure accurate radial velocities of more than 300 stars in three flattened Galactic globular clusters (NGC 5897, NGC 6273, and NGC 6541) by using FLAMES/GIRAFFE[1]. The proposal has been granted observing time, and observations will be taken during the ESO Period 93 (from April to September 2014).

In this Chapter we describe the motivation of this proposal, and the strategy of the planned observations. The Chapter is organized as follows. In Sect. 7.1 the selection criteria for the target globular clusters are described, and the basic properties of the selected clusters are provided. In Sect. 7.2 the observational strategy is described. Section 7.3 provides a description of the method used to select the stars for which velocities will be measured, and gives some predictions on the expected results.

7.1 Globular clusters selection

To choose the best targets for the proposed analysis, among the clusters for which no kinematical data-sets exist, we adopted the following selection criteria, based on the values of the relevant parameters that are listed in the Harris (2010) catalog:

1. we excluded objects farther than 20 kpc from the Sun, too faint for spectroscopic observations;

2. we excluded the globular clusters indicated as core-collapsed, to avoid the subtle modeling issues that characterize their central regions (as already explained in Chapter 4). However, we did not exclude the clusters that are flagged as possible core-collapsed, but for which a satisfactory fit with King models is feasible;

[1]Proposal ID: 093.D-0628; PI: A. Zocchi; title: "The dynamical origin of the flattening of globular clusters"; CoIs: N. Lützgendorf, M. Hilker, G. Bono, G. Bertin, H. Baumgardt, P. Bianchini, A. Di Cecco, M. Fabrizio, A. Kunder, M. Nonino, N. Neumayer, P. B. Stetson, and A. L. Varri.

Table 7.1: The selected globular clusters.

Globular cluster	$d_\odot$	$\langle v_\mathrm{r} \rangle$	$\log T_\mathrm{c}$	$\log T_\mathrm{M}$	ε		R_h	r_tr
NGC 5897	12.5	101.5±1.0	9.33	9.57	0.08	0.32	123.6	10.14
NGC 6273 (M19)	8.8	135.0±4.1	8.52	9.38	0.27	0.11	79.2	14.57
NGC 6541	7.5	-158.7±2.3	7.55	9.03	0.12	0.09	63.6	13.04

Notes. From left to right, the following quantities are displayed: distance from the Sun (kpc), systemic radial velocity (km s^{-1}), logarithm of the core relaxation time (years), logarithm of the half-mass relaxation time (years), ellipticity from Harris (2010) and from Chen & Chen (2010), projected half-light radius (arcsec), and truncation radius (arcmin).

3. we considered globular clusters with a systemic radial velocity that is significantly different from that of field stars, to easily single out interlopers;

4. we considered globular clusters with estimated truncation radius $6' < r_\mathrm{tr} < 15'$, to properly enclose their extent within the FLAMES field of view. The upper limit was fixed to make it possible to cover the entire extent of the clusters with a single pointing, the lower limit to avoid the selection of small clusters, which would prevent us from allocating a large number of fibers, because of the inevitable spatial proximity of candidate stars, especially in the central region of the systems.

Among the globular clusters satisfying these criteria, we selected three flattened ($\varepsilon > 0.08$) clusters in different relaxation conditions: NGC 6541 is a well relaxed cluster, NGC 6273 (M19) is in an intermediate relaxation condition, and NGC 5897 is partially relaxed; according to the classification introduced in Sect. 1.3.1, therefore, each one of the selected clusters belongs to a different relaxation class. For these three clusters, in Table 7.1 we list the values of the quantities that have been used as selection criteria. NGC 6541 is actually flagged as possibly core-collapsed, but its surface brightness profile can be satisfactorily described by means of spherical isotropic models (see Sect. 7.3.3). NGC 6273 appears to be the most flattened Galactic cluster, according to Harris (2010). NGC 5897 is known to have a stellar tidal tail (Chen & Chen 2010).

The selected clusters thus have different properties which make them excellent representatives of the population of Galactic globular clusters: their analysis will provide information on the dynamical origin of the observed morphologies. We emphasize that this work will provide the first global dynamical description of these globular clusters, for which at the moment no kinematic data-set is available. By comparing the results obtained for these three clusters, we will get clues on the physical factors that govern their dynamics, and on the role they play in different evolutionary phases.

This work will contribute to enlarge the currently small sample of Galactic clusters for which rich kinematic data-sets exist. In particular, if we exclude the three clusters for which very rich data-sets containing more than one thousand stars are available (i.e.: 47 Tuc, ω Cen, and M15, see Table 4.1), with the addition of these three, the number of clusters for which at least 300 radial velocities have been measured will double. This is particularly important also because many measurements of proper motions of stars in several globular clusters will soon be made available by the Gaia mission and by the Hubble Space Telescope: having reliable accurate samples of radial velocities will allow us to study the three-dimensional dynamics of globular clusters, as described in Chapter 6.

7.2 Observational strategy

The proposed spectroscopic observations will be obtained with the multi-object spectrograph FLAMES[2] (Pasquini et al. 2002) mounted at the ESO 8-meter Very Large Telescope (VLT) UT2 Kueyen. FLAMES feeds two different spectrographs, GIRAFFE and UVES, that we plan to use in the offered combined mode. GIRAFFE allows the simultaneous observation of 132 separate objects (including sky fibers) in MEDUSA mode, by means of fibers with an aperture of $1.2''$ on the sky. For our GIRAFFE observations, we selected the HR21 setup that covers the wavelength range 848.4 nm $< \lambda <$ 900.1 nm, and includes the Calcium Triplet; it has central wavelength $\lambda = 875.7$ nm, and resolution R = 16 200. The offered connection with the Red Arm of UVES will also be used, which provides spectra with a resolution R = 47 000 for 8 objects at the time; in this case, we selected the setup centered at 860 nm, which covers a wavelength range similar to the one chosen for GIRAFFE.

7.2.1 Number of stars to be observed

As anticipated at the beginning of this Chapter, we plan to measure radial velocities of $\gtrsim 300$ stars in each of the three flattened Galactic globular clusters with FLAMES. This number of stars is sufficient to accurately sample the kinematics of the systems: with a data-set of this size and with an expected accuracy of ~ 200 m s^{-1} for a single measurement, it is possible to calculate the relevant kinematic profiles with a precision $\lesssim 1$ km s^{-1}, which allows us to discriminate between different dynamical scenarios. We will consider stars distributed across the entire radial extent of the cluster so as to have a global description of its dynamical state (for more details, see Sect. 7.3.2).

To demonstrate the feasibility of this approach, and in particular to determine the number of stars that is necessary to observe in order to reach the proposed objectives, we carried out a test. We sampled a King model distribution function by randomly extracting N data-points that we consider as a "data-set". We chose a King model characterized by $\Psi = 7.00$ and by a central velocity dispersion $\sigma_0 = 5$ km s^{-1}, typical values found for Galactic clusters. We added Gaussian errors of ~ 200 m s^{-1} to each radial velocity, to simulate the expected observational errors. We calculated the velocity dispersion profile from the "data" (see Sect. 3.2.1), by considering bins with an equal number of stars, and compared it with the true velocity dispersion profile, which is calculated directly from the distribution function as shown in Sect. 2.1.2 (see in particular Eq. (2.11)). Figure 7.1 shows the results of this test. We found that $N \sim 300$ stars give an accurate description of the dynamics of the system: by working with fewer data, the resulting profile would be too noisy, whereas with more data the precision of the profiles would not increase significantly.

7.2.2 Signal-to-noise ratio and exposure time

To accomplish the scientific goal of our project, we need radial velocity measurements with an accuracy of about 200 m s^{-1}: with the high resolution grisms, this accuracy can be obtained with signal-to-noise ratios (S/N) of ~ 20, as shown in Fig. 7.2.

We estimated the exposure times needed to obtain such a S/N by using the GIRAFFE Exposure Time Calculator (ETC) provided by ESO[3]. To calculate the necessary time,

[2]For a complete and detailed description of the instrument and of the offered setups, see `http://www.eso.org/sci/facilities/paranal/instruments/flames.html`.

[3]`http://www.eso.org/observing/etc/bin/gen/form?INS.NAME=GIRAFFE+INS.MODE=spectro`

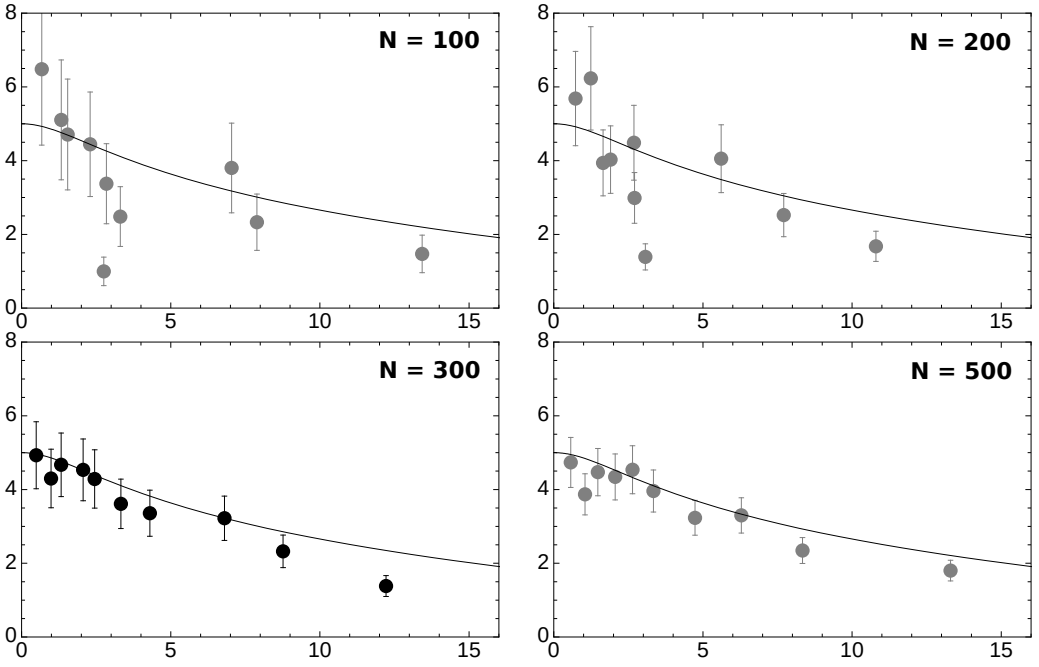

Figure 7.1: Velocity dispersion profiles are calculated using N (specified in each panel) data extracted from a King model, and are shown here with filled circles (black for N = 300); solid lines represent the model velocity dispersion.

among the options given by the ETC, we chose MEDUSA fiber mode with an object-fiber displacement of 0.30″, and the grism HR21 (central wavelength: 875.7 nm). We adopted the following assumptions: black body temperature of 4000 K; 14 days after new moon; airmass = 1.6; seeing = 1.00″ (probability of realization 86%); we also simulated the requested sky transparency (clear sky) by adding 0.1 mag to the object magnitude. By taking into account overheads[4], in order to have Observation Blocks (OBs) with a maximum duration of one hour, we have to consider a maximum continuous exposure time of 2340 s.

We recall that the instrument field of view is more or less as large as the estimated size of each of the selected globular clusters, so that with a single pointing it is possible to place the fibers on stars that are distributed on their entire radial extent. To measure radial velocities for more than 300 stars in each cluster, we will collect, for each of them, three exposures. To properly assess the presence of possible binaries in the samples, we plan to repeat the same measurement at two different epochs, with a time distance of more than 2 weeks. If we consider a limiting magnitude of 19 mag (V-band), we need to combine two OBs to achieve the needed S/N, so we need an exposure time of 2 hours for each exposure, for a total of 6 hours per cluster. We will not need to repeat the same measurements twice: provided that the OBs will be carried out at different epochs, the S/N of each exposure will be high enough (S/N $\sim$ 10) to measure possible velocity shifts.

In summary, we will need a total observing time of 18 hours (6 hours per cluster).

[4]For an observation with FLAMES we calculated the overheads as: 6 min (preset) + 9 min (acquisition) + 1 min (instrument setup) + 1 min (CCD read-out) + 2×[2 min (ThAr calibration) = 1 min (exposure time) + 1 min (readout)] = 21 min = 1260 s.

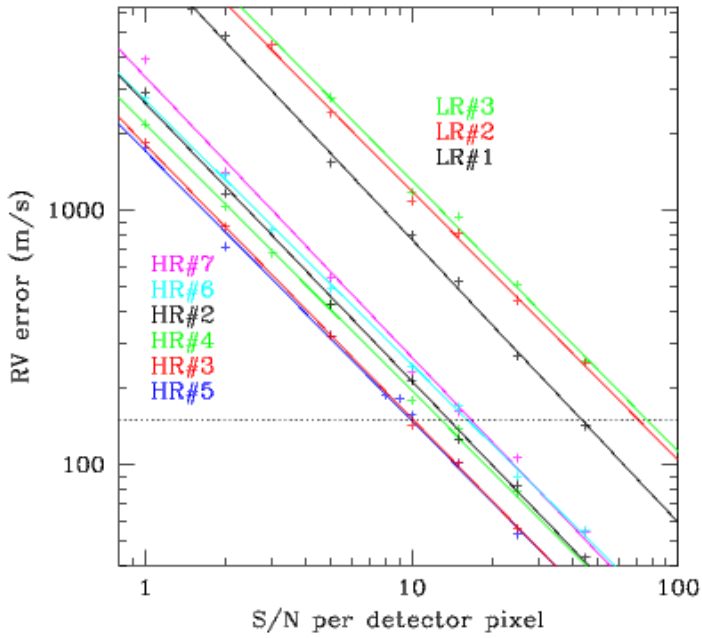

Figure 7.2: The standard deviation of radial velocities measured with FLAMES is simulated and plotted against the S/N of the spectra. Crosses are simulated values; they are fitted by lines in log-log diagram. The correspondent grisms are indicated by the labels (ordered as their corresponding curves); the grism we have requested is not shown in the figure, but has similar properties as the other High Resolution (HR) grisms here represented. This figure is taken from Royer et al. (2002).

Table 7.2: Coordinates of each pointing and total exposure time for FLAMES observations.

Globular cluster	RA	Dec	Exposure time
NGC 5897	15 17 24.50	-21 00 37.0	3.9 h
NGC 6273	17 02 41.38	-26 16 57.2	3.9 h
NGC 6541	18 08 02.36	-43 42 53.6	3.9 h

The coordinates of each pointing and total exposure times are listed in Table 7.2.

We requested the possibility to carry out special ThAr (Thorium-Argon) calibration lamp exposures immediately before and after each science exposure, with the same setup. The reason for this is the fact that, in the selected HR21 setup, the standard simultaneous calibration may show very strong Argon lines that contaminate the science spectra.

7.2.3 Radial velocity measurements and dynamical analysis

We will measure radial velocities by using Calcium Triplet (849.8, 854.2, 866.2 nm), Nickel (886.2 nm), and α elements (e.g. Magnesium: 880.6 nm) lines by using one of the bright target stars as a template for cross-correlation, to overcome the issues that the expected broadening of these lines at such high resolution could cause in the radial velocity measurement.

Then we will identify the interlopers (this can be done easily, because of selection criterion 3, see Sect. 7.1) and we will detect the possible presence of binaries with short orbital periods, by looking for shifts in the velocities obtained for each star at different epochs (since the typical period of binaries in clusters is about a month long, we plan to repeat the measurements with a time distance of about two weeks). After these first steps, we will have identified the final sample of stellar radial velocities that we will use for the subsequent dynamical analysis.

At this point, we will be able to give a first dynamical description of the systems, by calculating their velocity dispersion profiles and their rotation profiles. We recall that, based on the S/N that we are requesting for our observations, we expect to obtain radial velocities with an accuracy of ~ 200 m s^{-1}, which translates into an accuracy of about 1 km s^{-1}on these kinematic profiles. We will use these profiles to test different dynamical models, taking into account the relevant physical factors. We will thus identify the key dynamical ingredient that should be associated with the observed morphology of each cluster, and discuss the implications on the possible formation mechanism of the systems. Finally, we will determine the dynamical mass-to-light ratio and the binary fraction of these systems.

7.3 Stars selected for observations

7.3.1 Selection regions in color-magnitude diagrams

Accurate and extended multiband (B, V, I) photometric catalogs of the sky regions centered on the selected clusters were kindly provided to us by Peter B. Stetson. The typical astrometric accuracy of these catalogs is within the technical requirements for observations with FLAMES (0.30″). We used these catalogs to select the candidate target stars for the observations, with the method described in the following.

First, for each catalog, we constructed the $(B - V, V)$ color-magnitude diagram by considering only the stars located within 2′ from the center of the cluster under examination. This choice allows us to have a well populated color-magnitude diagram, and at the same time it limits the presence of field stars, which could lead us to define too large selection regions in the diagram. We determined a selection region around the red giant branch and another one around the horizontal branch, and we selected as candidate target stars all the stars in the catalog that fall inside these regions in the color-magnitude diagram. Only stars brighter than 19 mag were considered in NGC 5897; in the other two clusters we used the more stringent limit of 18 mag, because for fainter stars it is more difficult to define a selection region in the color-magnitude diagram. In the same way, selection boxes were also defined in the $(V - I, V)$ color-magnitude diagram, and used to further refine the selection, and to eliminate the field stars that were erroneously selected in the first step. For the globular cluster NGC 6273, only the selection boxes around the red giant branch were defined, because its horizontal branch stars are not clearly separable from field stars.

The sample of fiducial member stars that has been identified in this way was then given as input to the Fiber Positioner Observation Support Software (FPOSS), that is, the fiber configuration program for the preparation of FLAMES observations. By means of this program we generated three optimized fiber configurations for each cluster, one for each planned exposure (see Sect. 7.2.2). Some fibers in each configuration were allocated to sky positions, to allow for a proper sky subtraction. UVES fibers were allocated to stars of about 15 mag (V band). We paid particular attention to select some stars in common in different configurations for the same cluster: this will allow us to correct for

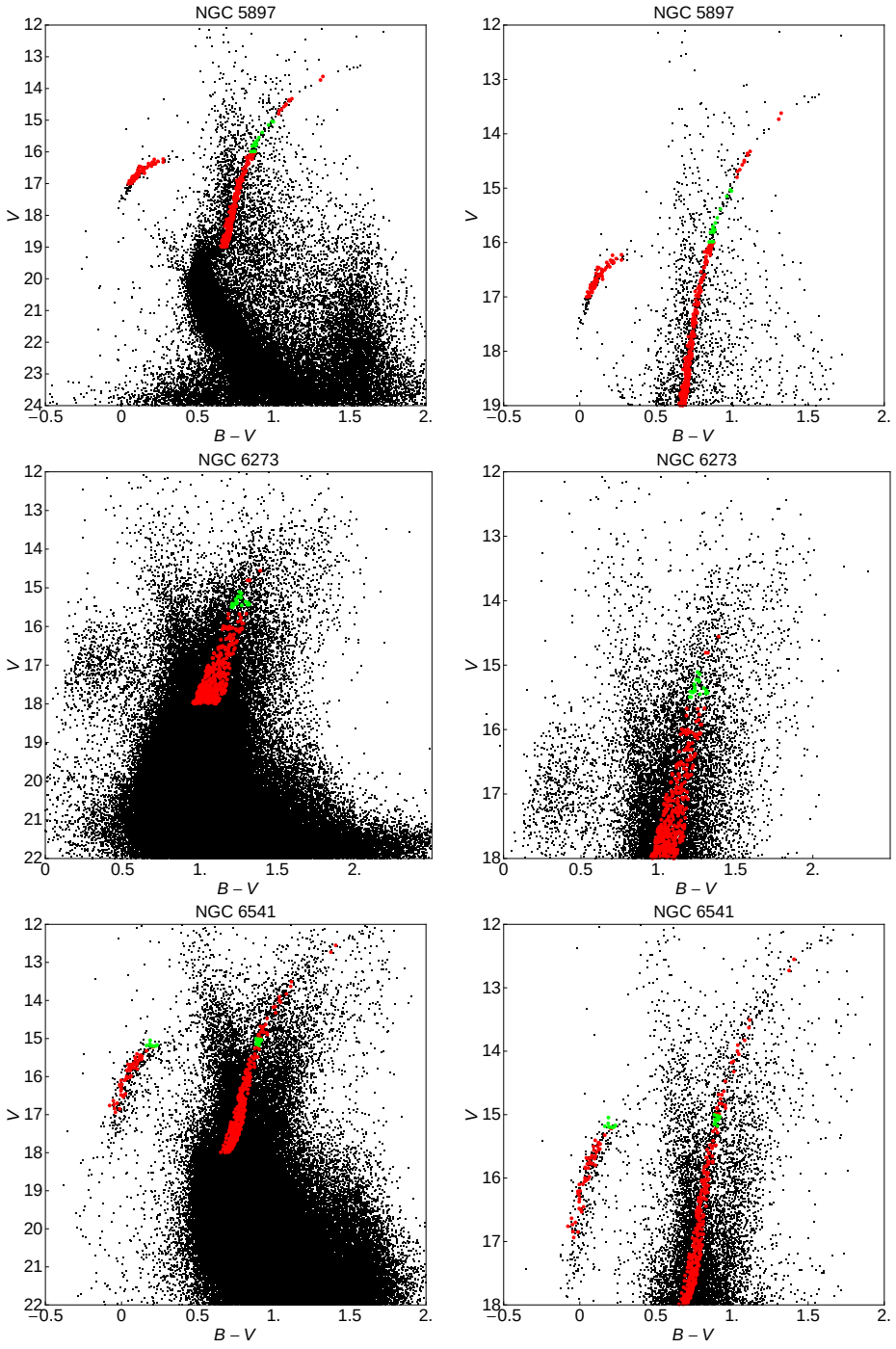

Figure 7.3: Stars selected for the observations in the globular clusters NGC 5897, NGC 6273, and NGC 6541 (from top to bottom, respectively). Left panels show the $(B-V, V)$ color-magnitude diagrams of the three clusters. Red and green dots represent stars for which we will obtain GIRAFFE and UVES spectra, respectively; black dots represent all the other stars present in the original catalogs. Right panels are an enlargement of left panels, restricted to the magnitude range populated by the selected stars.

Table 7.3: Number of allocated GIRAFFE and UVES fibers.

Globular cluster	Number of GIRAFFE fibers	Number of UVES fibers
NGC 5897	348	14
NGC 6273	371	19
NGC 6541	375	20

the presence of possible velocity shifts in the different exposures.

Left panels of Fig. 7.3 show the $(B-V, V)$ color-magnitude diagrams of the three clusters. Red and green dots represent stars for which we will obtain GIRAFFE and UVES spectra, respectively; black dots represent all the stars in the original catalogs. Right panels provide an enlargement of left panels, restricted to the magnitude range populated by the selected stars. In this figure, top panels are relative to NGC 5897, middle panels to NGC 6273, and bottom panels to NGC 6541. In Table 7.3, we list the number of allocated GIRAFFE and UVES fibers for the three clusters.

7.3.2 Spatial distribution of selected stars

In order to properly describe the dynamics of the selected clusters, it is important to obtain radial velocities for stars that are distributed on the entire radial extent of the systems. Of course, the allocation of fibers depends on the number of available targets in the different regions: therefore, the real distribution of the candidate target stars on the plane of the sky might lead to the selection of a sample of stars that does not allow for an ideal coverage of the cluster extent.

Figure 7.4 shows the spatial distribution of stars selected for observations in the three clusters. Top panels refer to NGC 5897: the left panel shows the spatial distribution of the selected stars as compared to that of all the stars present in the original catalog. As in Fig. 7.3, red and green dots represent stars for which we will obtain GIRAFFE and UVES spectra, respectively; blue dots represent the stars that fall in the selection regions defined in the color-magnitude diagram but were not selected by FPOSS, and gray dots represent all the other stars in the original catalog. The top right panel represents the radial distribution of the stars by means of a histogram. The bottom panels provide a similar histogram for NGC 6273 and NGC 6541.

The histograms highlight the different distribution of selected stars in the three clusters. For the low-concentration cluster NGC 5897 it was possible to allocate a very large number of fibers to stars located within the half-light radius of the cluster. Unfortunately, the outermost regions of the cluster are undersampled: only about 50 stars (that is 14% of the total) are located outside a radius of $300''$ (with respect to $R_{\rm h} \approx 123.6''$). The stars selected for NGC 6273 have a flat distribution in radius; only about 40 stars are located within the half-light radius. In the case of NGC 6541, about forty fibers were allocated to stars within the half-light radius, so that the majority of the stars that will be observed are located outside this radius. For the last two clusters, the number of stars inside the half-light radius to which fibers have been allocated is severely limited by crowding.

7.3.3 Predicted properties

A first preliminary description of these clusters is possible, based on their photometric properties. Therefore, some predictions can be made on their kinematic properties.

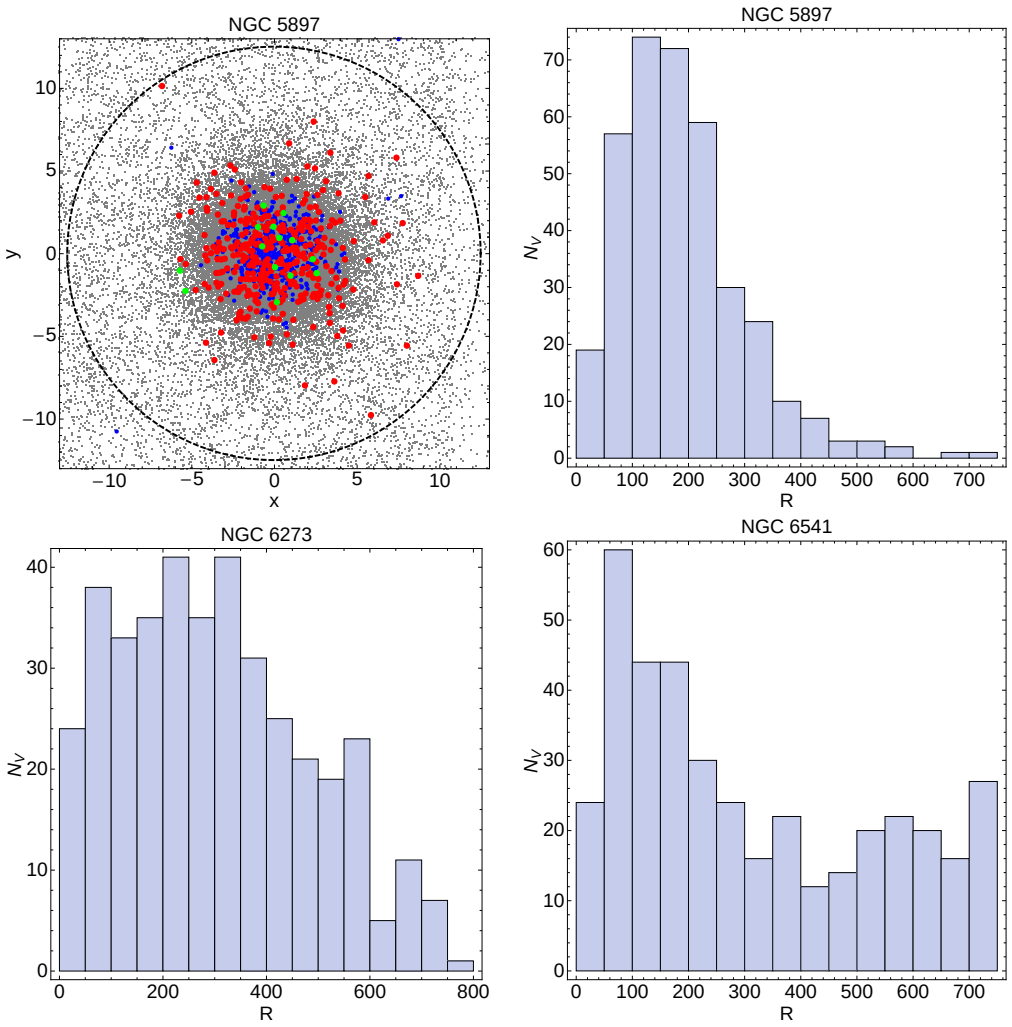

Figure 7.4: Spatial distribution of the stars selected for the observations for NGC 5897, NGC 6273, and NGC 6541. Top panels refer to NGC 5897: the left panel shows the spatial distribution of selected stars as compared to that of all the stars present in the original catalog. As in Fig. 7.3, red and green dots represent stars for which we will obtain GIRAFFE and UVES spectra, respectively; blue dots represent the stars that fall in the selection regions defined in the color-magnitude diagram but were not selected by FPOSS, and gray dots represent all the other stars in the original catalog. Top right panel represents the radial distribution of the stars by means of a histogram. The bottom panels provide a similar histogram for NGC 6273 and NGC 6541.

We considered the surface brightness profiles given by Trager et al. (1995) and we fitted isotropic King (1966) models and anisotropic $f^{(\nu)}$ models (Bertin & Trenti 2003) to these profiles, by following the procedure described in Sect. 3.3.1 and used for the analysis described in Chapter 4. For each cluster, we obtained the best-fit concentration parameter Ψ and the radial and magnitude scales, r_0 and μ_0. The results are shown in the left panels of Fig. 7.5, and the best-fit parameters are listed in Table 7.4.

After the identification of the structural parameters that define the best-fit models,

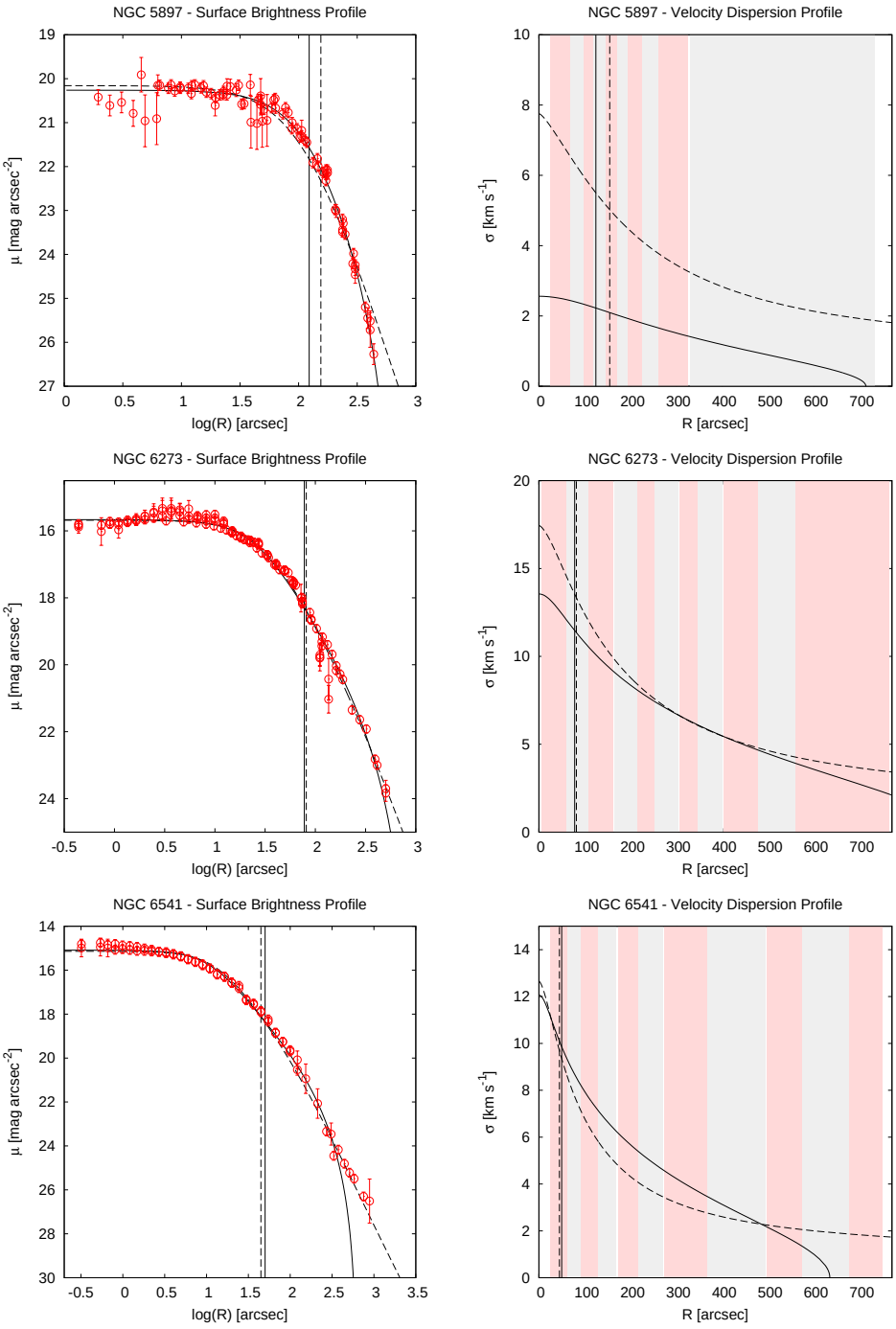

Figure 7.5: Fits by King models and anisotropic non-truncated $f^{(\nu)}$ models to the surface brightness profiles (left) and predictions of the correspondent line-of-sight velocity dispersion profiles (right) of NGC 5897, NGC 6273, and NGC 6541 (from top to bottom, respectively). In all panels, solid lines correspond to the King-model profiles, dashed lines to $f^{(\nu)}$-model profiles; the vertical solid lines mark the position of the King model projected half-light radii, the dashed ones the position of the $f^{(\nu)}$ model projected half-light radii. In right panels, each one of the vertical red and gray stripes covers a radial range in which ≈ 40 stars are located.

Table 7.4: Dimensionless parameters and physical scales of the best-fit models.

			King Models				$f^{(\nu)}$ Models			
NGC	$N_{\rm p}$	M/L	Ψ	r_0	μ_0	σ_0	Ψ	r_0	μ_0	σ_0
(1)	(2)	(3)	(4)	(5)	(6)	(7)	(8)	(9)	(10)	(11)
5897	84	1.868	3.97	104.30	20.26	2.56	3.81	89.61	20.16	7.75
6273	125	1.868	7.00	26.70	15.67	13.55	6.50	102.71	15.68	17.44
6541	69	1.869	7.64	12.00	15.09	12.06	6.90	61.68	15.14	12.65

Notes. For each cluster, given in Col. (1), for King and $f^{(\nu)}$ models, we list: the concentration parameter Ψ (Col. (4) and (8)); the scale radius r_0, expressed in arcsec (Col. (5) and (9)); the V-band central surface brightness μ_0 in mag arcsec^{-2} (Col. (6) and (10)), and the estimated central line-of-sight velocity dispersion σ_0 in km s^{-1}(Col. (7) and (11)). In addition, in Col. (2) we list the total number of points in the surface brightness profile (Trager et al. 1995), and in Col. (3) the mass-to-light ratios in the V band calculated by McLaughlin & van der Marel (2005) are reported.

it is possible to calculate the expected velocity dispersion profiles. If we had kinematic data available, we would obtain the central velocity dispersion from a fit based on each model, and then we would use it to estimate the total mass of the cluster. Here, we proceeded the other way round: we estimated the total mass of the clusters from the total luminosity and a reasonable value for the mass-to-light ratio, derived by McLaughlin & van der Marel (2005) by means of population-synthesis models (see Table 7.4). We calculated the expected central velocity dispersion for each model for the three clusters and used it to set the vertical scale of the velocity dispersion profiles predicted by the models. The right panels of Fig. 7.5 show the expected profiles for the clusters; the radial extent of these panels matches the FLAMES field of view. In Fig. 7.5, each one of the vertical red and gray stripes covers a radial range in which ≈ 40 stars are located. This radial subdivision is shown here to give an idea of how the points in the observed velocity dispersion profiles will be distributed in radius.

For the cluster NGC 5897, the two predicted profiles are clearly different: if we constrain the central scales by means of a fit to real data, we would obtain different masses and mass-to-light ratio estimates for the two models. In any case, the profiles differ significantly in the central parts, inside $\approx 300''$: because our data are mainly concentrated in this region, they will be particularly suited to discriminate between these dynamical models. In other words, our selection of targets should be able to determine the dynamics of this cluster.

For the cluster NGC 6273, the profiles predicted by King and $f^{(\nu)}$ models seem to be very similar especially in the intermediate part of the considered radial region. The distribution of our data ensures that we will have enough accurate data-points in the innermost region to distinguish between the two predicted profiles. From $\approx 200''$ to $\approx 600''$ our data are distributed in a satisfactory manner, but it will not be easy to discriminate the models, because they are too similar to each other in this radial range.

For NGC 6541 the selected models are quite different in the range $50 - 450''$; we expect that data-points in this radial range will have associated errors smaller than the predicted difference between the models, and therefore that it will be possible for us to distinguish them. As for NGC 5897, for this cluster the estimated King truncation radius occurs inside the radial area probed by our data. At variance with the case of NGC 5897, about 40 stars are located outside this radius, opening up the possibility to confirm with

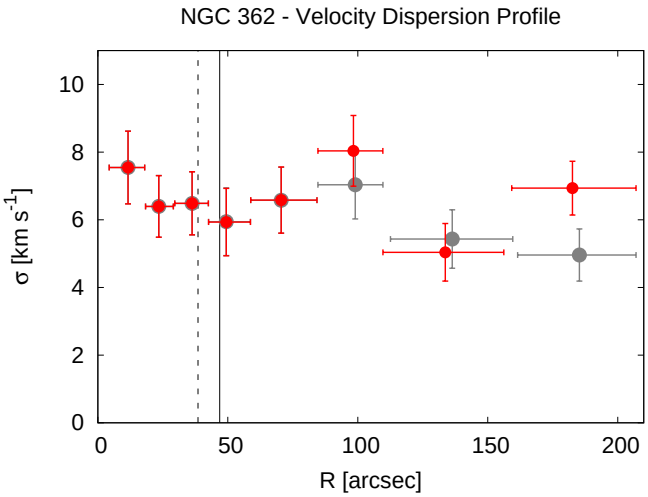

Figure 7.6: Observed velocity dispersion profile, calculated from the data-set published by Fischer et al. (1993) with and without the detected binary stars (indicated with red and gray dots, respectively). The vertical solid line marks the position of the King model projected half-light radius, the dashed one the position of the $f^{(\nu)}$ model projected half-light radius, as calculated in Chapter 4.

kinematics the expected position of the truncation radius of the cluster.

It would be interesting to test the rotating models used in Chapter 6 on the surface brightness profiles of these clusters but, as described there, kinematic data are needed in order to determine their structural parameters. With the FLAMES data we will obtain, this will be possible. In particular, an important goal of this project is to determine if rotation is the key factor responsible for the observed flattening of these systems. With the radial velocities we will measure, it will be possible to calculate the rotation profiles for these clusters. By analogy with the results of Chapter 6, the maximum of the rotation curve might occur at about $2R_{\rm h}$: if this is the case, we will obtain well sampled rotation profiles for NGC 6273 and NGC 6541; for NGC 5897 we should be able to see at least the peak of the curve.

7.3.4 Binaries

We explored the expected effect of binaries on the calculation of velocity dispersion profiles. Among those used in Chapter 4, only the data-set by Fischer et al. (1993) for NGC 362 is published along with a detailed analysis on the possible presence of binary stars within the sample. The authors identify four binaries among the stars for which they measure radial velocities, and exclude them from the subsequent dynamical study (we did the same in Chapter 4). We calculated here the velocity dispersion profile that we would obtain if we had not detected (and eliminated) those stars as binaries. In Fig. 7.6 we compare the velocity dispersion profiles calculated with and without the binaries: when the binaries are included, the velocity dispersion calculated for the radial bins they belong to increases. We stress that a sizable effect in this profile is generated by only four binaries in a sample of 208 velocities. Thus it would be important to properly identify these stars and to exclude them from the dynamical analysis, to avoid exaggerated values observed for the velocity dispersion data-points.

CHAPTER 8

A pilot project with VIMOS

As often emphasized in this Thesis, the availability of kinematic data is a key factor for a satisfactory description of the dynamics of globular clusters. Unfortunately, obtaining accurate large kinematic data-sets is time-demanding. In fact, fiber-fed spectrographs such as FLAMES (see Chapter 7) are often used to measure radial velocities of single stars in globular clusters, but the needed exposure time for these observations is very long, depending on the adopted instrumental setup. Therefore, we submitted a proposal[1] to the European Southern Observatory (ESO), requesting to carry out a pilot project to test the possibility to use the low spectral resolution slit spectrograph VIMOS to measure more (but less accurate) velocities than those possible with FLAMES, and with a similar exposure time.

In particular, we requested to measure velocities for ~ 600 faint stars in the Galactic cluster NGC 6254 (M10), for which some accurate FLAMES data are already available (Carretta et al. 2009). We will use stars in common with the FLAMES sample to calibrate our low-resolution but high S/N data, and we will combine all the kinematic data available for this cluster to study its dynamics in detail. These observations also serve as a test to explore whether many low-resolution measurements, when combined with less numerous but more accurate data, could be useful to obtain reliable dynamical information on the entire extent of globular clusters. The advantage of using VIMOS is its capability to measure many faint stars, which are especially plentiful in the outermost parts of globular clusters. If we will be able to prove that this method is successful, it will be applicable to many nearby globular clusters.

This Chapter is organized as follows. In Sect. 8.1 the selection criteria for the target globular cluster and its basic properties are outlined. In Sect. 8.2 the adopted strategy is illustrated. Section 8.3 gives additional details on the observations. Finally, in Sect. 8.4, we describe the method used to measure radial velocities, and we show the preliminary dynamical analysis of the cluster.

8.1 Target selection

To achieve the goal of this project, we need to target a cluster for which a large data-set of accurate velocity data already exist. The set of Galactic globular clusters that meet this requirement are those listed in Chapter 4. Starting from that set of 13 Galactic clusters, we adopted the following additional criteria.

[1]Proposal ID: 091.D-0610; PI: A. Zocchi; title: "Relaxation, rotation, flattening, central black holes: what is the most important piece in the dynamical puzzle of globular clusters?"; CoIs: N. Lützgendorf, M. Hilker, G. Bono, G. Bertin, P. Bianchini, A. Di Cecco, M. Fabrizio, A. Kunder, M. Nonino, N. Neumayer, P. B. Stetson, and A. L. Varri.

First, we excluded objects located outside the range of declination observable by the Very Large Telescope (VLT), where VIMOS operates: we thus eliminated NGC 2419, NGC 6341, and NGC 7078, located in the Northern hemisphere.

Then, we considered clusters for which the expected value of the central velocity dispersion σ_0 is greater than 5 km s^{-1}, so that the velocity dispersion profile should be measurable also at a relatively large distance from the center. For this selection, we considered the value of this quantity obtained from the King model fitting (see Table 4.2) because it is always lower than that obtained from the $f^{(\nu)}$ models and therefore provides a more stringent constraint. This criterion eliminated from the list five clusters (NGC 288, NGC 3201, NGC 6121, NGC 6218, and NGC 6809).

Among the five remaining candidate targets, we selected NGC 6254 (M10), the one with the lowest number of data available ($N_{\rm V}$ = 147), which is also one of the clusters for which the data extend out to a small fraction of its estimated truncation radius ($R_{\rm V}/r_{\rm tr}$ = 0.55). We made this choice because the existing data-set is large enough to enable a comparison with the new data we obtained, which in turn will contribute to enlarge the existing data-set significantly.

With respect to the selection criteria listed in Sect. 7.1 for the FLAMES observations, here we did not take into account the size of the target, because we plan to obtain multiple exposures of the cluster to measure velocities for a large number of stars. However, we checked that the selected cluster is large enough: a small cluster would prevent us from allocating a large number of slits, because of the inevitable spatial proximity of candidate stars in the central crowded region.

8.2 Observational strategy

The proposed pilot project consists in spectroscopic observations obtained with the multi-object spectrograph VIMOS[2] (Le Fèvre et al. 2003) mounted at the ESO 8-meter Very Large Telescope (VLT) UT3 Melipal. The instrument is made of four identical arms with individual field of view of $7' \times 8'$, with a $0.205''$ pixel size and a gap between each quadrant of $\sim 2'$. Multi-object spectroscopy is carried out using masks (one per quadrant) prepared in Paranal by means of a laser cutting Mask Manufacturing Unit. We decided to carry out our observations with the grism HR-Red, which covers the wavelength range 650 nm $< \lambda <$ 875 nm, thus including the Hα and the Calcium Triplet lines, characterized by spectral resolution R = 2 500. The maximum number of slits per mask for the selected configuration is about 40, so that with a single exposure it is possible to obtain spectra for about 150 objects.

Pre-imaging with VIMOS is mandatory for multi-object spectroscopic observations, even when targets come from a pre-defined catalog. We requested to carry out the pre-imaging run with the B filter, in addition to the required R filter, in order to create a color-magnitude diagram for the target, to properly select member stars and reject field stars.

8.2.1 Signal-to-noise ratio and exposure time

We estimated the exposure times needed to achieve our scientific goals by using the VIMOS Exposure Time Calculator (ETC) provided by ESO[3]. We plan to measure velocities

[2] For a complete and detailed description of the instrument and of the offered setups, see `http://www.eso.org/sci/facilities/paranal/instruments/vimos.html`.

[3] `http://www.eso.org/observing/etc/bin/gen/form?INS.NAME=VIMOS+INS.MODE=imaging`, and `http://www.eso.org/observing/etc/bin/gen/form?INS.NAME=VIMOS+INS.MODE=SPECTRO`,

for almost 600 stars in NGC 6254: to do that, we need to cover the cluster with five pointings, reaching a limiting magnitude of $V = 19$ mag.

Pre-imaging

For the pre-imaging stage, we used both B and R filters to create a color-magnitude diagram. To achieve a S/N of 100, we needed exposure times of 60 s for the B filter, and of 5 s for the R filter. The instrument overhead was calculated as: 6 min (preset) + 3 min (acquisition and instrument setup) + 2×1 min (CCD read-out for all four quadrants) + 2.5 min (change of filter) = 13.5 min = 810 s. An exposure time of 875 s for each of the five pointings, that is, a total exposure time of 1.2 hours, was required to carry out these observations.

Multi-object spectroscopy

By taking into account overheads[4], in order to have Observation Blocks (OBs) with a maximum duration of one hour, we considered a maximum continuous exposure time of 1750 s, which we split into two subsequent exposures to be taken with a given offset; this is done to allow for a more precise sky subtraction.

To accomplish the scientific goal of our project a minimum S/N of ~ 50 is needed; this is reachable with the available exposure time within each OB, with the selected grism HR-Red (central wavelength: $\lambda = 740$ nm). Radial velocities have been measured twice for each configuration, to identify possible binaries or variable stars. Therefore, for each pointing, we used 2 hours of observing time (i.e., 10 hours in total for the five pointings).

8.3 The observations

8.3.1 Exposures

In order to obtain measurements for ≈ 600 stars in NGC 6254, we covered the cluster with five different pointings. Figure 8.1 shows the distribution of these pointings on the cluster; each pointing is indicated with a different color, and the four quadrants of each configuration are shown.

Pre-imaging observations were taken from 5 to 8 April 2013 and were used in combination with the catalog of stars kindly provided by Peter B. Stetson to select the target stars for the allocation of the slits. In Fig. 8.1, red dots indicate the stars to which slits were allocated.

The coordinates of each pointing are listed in Table 8.1. In this table we also report the total exposure time, the date in which the observations were taken, and the number $N_{\rm A}$ of slits that were assigned to targets for each configuration. In total, with an effective exposure of 4.86 h, we obtained spectra for 687 stars. To make a comparison with the observations that we plan to obtain with FLAMES described in Chapter 7 we recall that in that case we are able to obtain at most 375 spectra of stars in a single cluster with an exposure time of 3.9 h. These numbers justify this pilot project: with just one more hour of exposure time, VIMOS would be able to observe a number of objects almost twice the one obtainable with FLAMES.

for the pre-imaging and for the spectroscopic observations, respectively.

[4]For a spectroscopic observation with VIMOS we calculated the overheads as: 6 min (preset) + 15 min (acquisition and instrument setup) + 2×1 min (CCD read-out for all four quadrants) + 5 min (attached flats + arc) = 28 min = 1680 s. Moreover, 170 s turn out to be necessary to perform the offset observation.

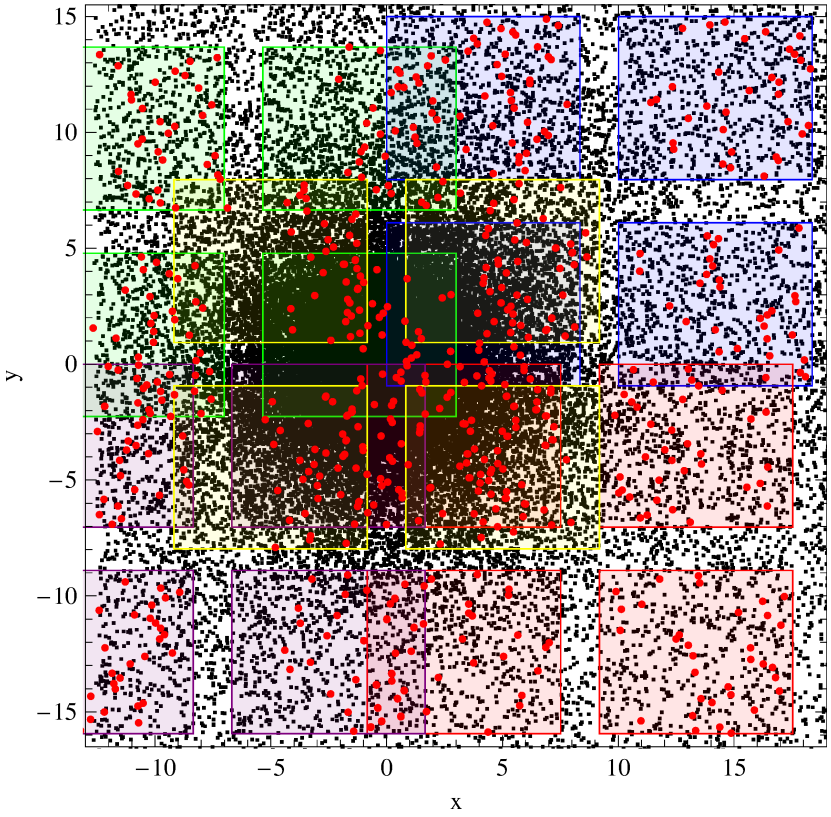

Figure 8.1: Distribution of VIMOS pointings on the globular cluster NGC 6254. Each pointing is marked by a different color. The four quadrants of each configuration are shown. Red dots indicate the stars to which slits were allocated (black dots indicate all the other stars in the cluster).

Table 8.1: Coordinates of each pointing and total exposure time for VIMOS observations.

Pointing	RA	Dec	Exposure time	N_A	Date
0	16 57 33.75	-04 00 18.1	3500 s	140	14 May 2013
1	16 56 32.32	-03 58 59.1	3500 s	139	6 May 2013
2	16 56 35.65	-04 13 59.1	3500 s	139	11 May 2013
3	16 57 39.12	-04 13 59.1	3500 s	133	20-29 May 2013
4	16 57 09.05	-04 06 01.1	3500 s	136	18 Jun 2013

Notes. For each pointing, identified in the first column, we report the coordinates, the total exposure time, the number N_A of slits that were assigned to targets, and the date in which the observations were taken.

8.3.2 Stars selected for the observations

To select the stars for the spectroscopic observation, we followed the same procedure described in Sect. 7.3.1. The left panel of Fig. 8.2 shows the color-magnitude diagram of the cluster: black dots represent the stars in the cluster, red dots represent the stars to

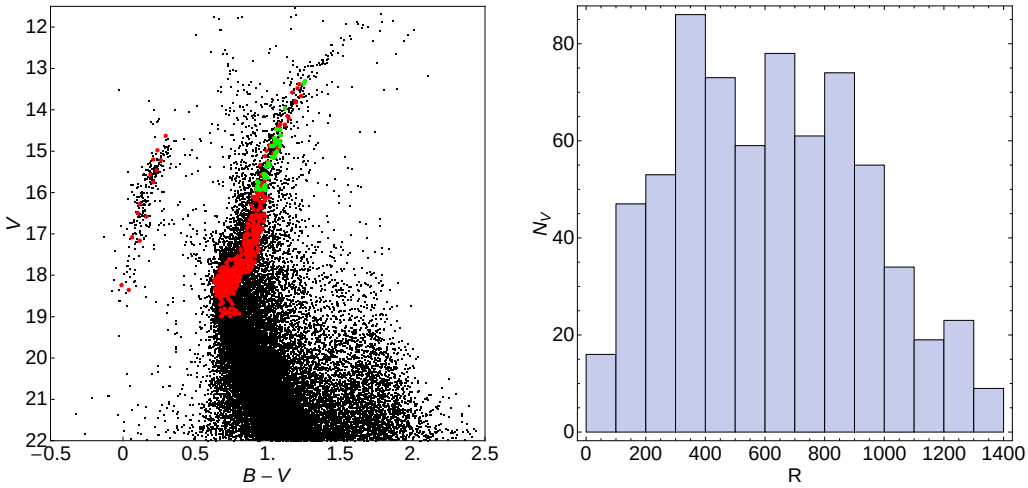

Figure 8.2: Stars selected for the observations in the globular cluster NGC 6254. The left panel shows the stars that have been observed, on the $(B-V, V)$ color-magnitude diagram of the cluster. Red dots represent stars for which we obtained VIMOS spectra, and green dots represent those in common with the FLAMES sample by Carretta et al. (2009); black dots represent all the other stars present in the original catalog of stars. The right panel represents the radial distribution of the stars.

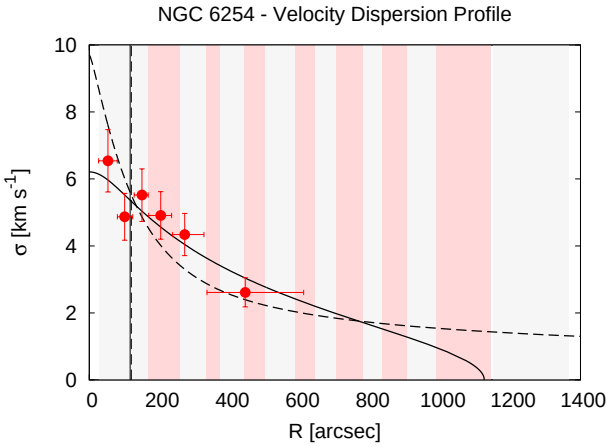

Figure 8.3: Observed velocity dispersion profile, based on the FLAMES sample, and best-fit King and $f^{(\nu)}$ models profiles. Each of the vertical red and gray stripes covers a radial range in which $\approx$ 40 stars from the VIMOS sample are located. This figure shows that our data contributed to double the already observed radial range of the cluster, beyond the estimated truncation radius.

which slits were assigned. We carefully checked that some of the selected stars were also part of the FLAMES sample published by Carretta et al. (2009); these stars are indicated here by green dots.

The histogram in the right panel of Fig. 8.2 shows the distribution of the targets as a function of radial distance from the cluster center. The possibility to allocate slits to

the stars in the cluster is limited by the crowding in the innermost regions, and by the absence of available candidate cluster stars in the outermost parts. Moreover, there is another constraint that prevents us from allocating slits to targets of our choice. In fact, in principle, slits can be positioned at any location in the imaging field of view, but with the selected high-resolution grism the observed spectral range changes slightly, according to the position of the slit. In order to have the Calcium Triplet region of the spectrum for the observed stars, it is necessary to position the slits on one side of the quadrants; in some cases, when no other target was available, we preferred to obtain spectra without the Calcium Triplet, rather than obtain fewer spectra, and we manually assigned slits to stars in the "forbidden" region of the quadrants.

In Chapter 4 we presented the best-fit King and $f^{(\nu)}$ models for this cluster. In particular, we found that its surface brightness is better described by $f^{(\nu)}$ models, whereas the velocity dispersion profile by King models. In Fig. 8.3 we reported the observed velocity dispersion profile, calculated from the FLAMES sample, and the best-fit model profiles. Each one of the vertical red and gray stripes covers a radial range in which ≈ 40 stars from the VIMOS sample are located. From this figure it appears that our data contributed to double the already observed radial range of the cluster, beyond the estimated truncation radius.

8.4 Radial velocity measurements

Data were reduced by means of `Reflex`[5] (Recipe Flexible Execution Workbench), an environment that allows to run ESO VLT pipelines. The data-sets were fed through the workflow which executes the relevant pipeline recipes (or stages) in the correct order; full control of the various recipe parameters is available within the workflow. In this way, the spectra were flat-field corrected, extracted, and wavelength calibrated. A sky correction was also applied to each stellar spectrum. The resulting spectra have dispersion of 0.6 Å/pixel.

Radial velocities were then obtained by using the IRAF[6] `fxcor` cross-correlation task. This task uses the Fourier cross-correlation method developed by Tonry & Davis (1979): the spectrum of an "object" is correlated with a "template" spectrum, and the velocity of the object with respect to the template is obtained. We used as a template one of the stars in our sample: this choice guarantees that the template spectrum is of the same type of the ones of the objects. For the cross-correlation we used the region of the spectrum that contains the Calcium Triplet lines; when this was not available, we used the spectral region around the Hα line.

Each spectrum was treated independently from the others, so that we ended up with two independent measurements of the radial velocity for each star; for a limited number of stars, one of the spectra is affected by some defects and was rejected, leaving us with only one spectrum. The best estimate of the true radial velocity of a star is calculated as the weighted average of the independent measurements; the error on the velocity is calculated as the standard deviation of the independent measurements. As an independent check, we also measured velocities by means of the IRAF task `rvidlines`. We obtained measurements in agreement with those obtained by `fxcor`. Some stars were observed in two different pointings: we used them to correct for shifts in velocity between the different observations.

[5] `http://www.eso.org/sci/software/reflex/`

[6] IRAF (Image Reduction and Analysis Facility) is a collection of software written at the National Optical Astronomy Observatory (NOAO); `http://iraf.noao.edu/`.

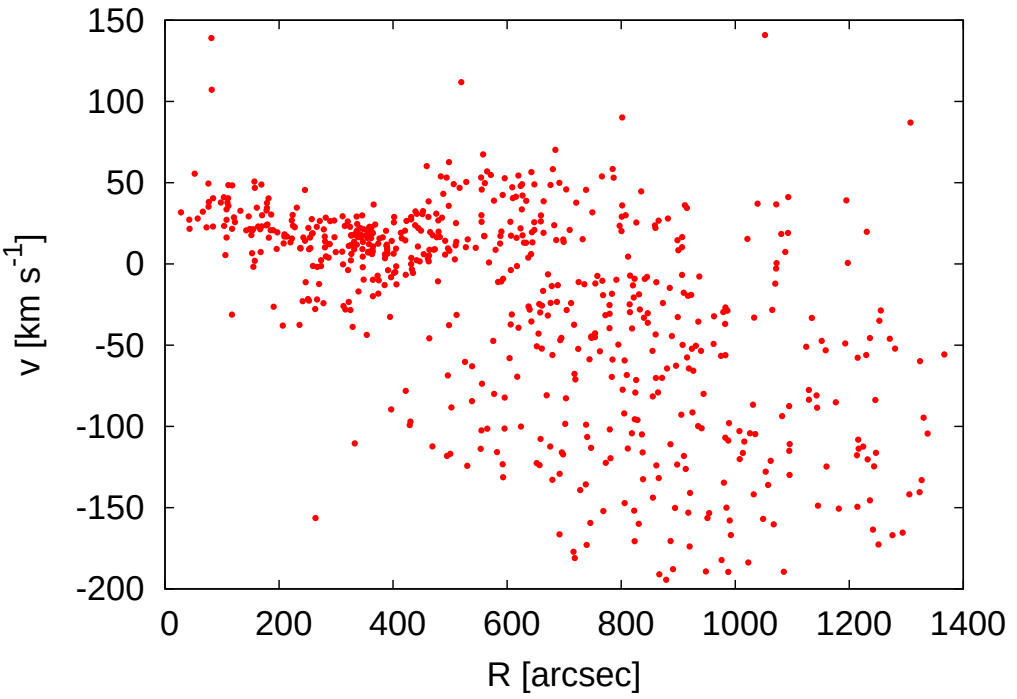

Figure 8.4: Measured radial velocities for stars in M10. The velocities are expressed in km s^{-1}; the reported values are given with respect to the mean of the entire sample.

Figure 8.4 shows the measured values of velocities as a function of the distance from the cluster center. Velocities are given here with respect to the mean of the entire sample. Stars within $400''$ and with velocities around the mean are likely to be member stars of the cluster. A large number of field stars is visible beyond this radius. We notice that despite our effort in choosing fiducial member stars according to their position on the color-magnitude diagram, a lot slits were assigned to field stars. The mean value of the errors on the velocity measurements (≈ 5 km s^{-1}) is comparable to the central velocity dispersion that was obtained for this cluster by means of the FLAMES sample (see Fig. 8.3): this prevents us from obtaining a meaningful dynamical analysis for the cluster. The very large scatter observed for the velocity measurements is partly due to an erroneous calibration of the spectra: we plan to correct this feature in the immediate future.

This pilot project has shown that VIMOS is not an adequate instrument to measure the internal dynamics of small stellar systems. In particular, the large scatter in velocities suggests that, in order to obtain meaningful indications on the dynamics of globular clusters, it is more important to have very accurate velocities than to have a larger and less accurate data-set.

CHAPTER 9

A study of simulated observations

When studying the dynamics of a Galactic globular cluster, we necessarily deal with observations of only a fraction of its stars. Therefore, to provide a good description of the system as a whole, it is particularly important to determine if biases are introduced in the derived properties of the systems, and how to take them into account. A first step of this work is presented in this Chapter.

We consider the results of the numerical simulations of two clusters, run by Mark Gieles and Poul Alexander. From the simulated set of particles, we construct the profiles that correspond to standard photometric and kinematic observations, and then analyze them by means of dynamical models, with the aim of obtaining an estimate of the total mass and of the half-mass radius of the system. At variance with the case of real stellar systems, for the simulations we know the actual properties of the cluster, therefore we can assess whether the dynamical study carried out by means of these profiles offers a good representation of the system.

This Chapter is organized as follows. In Sect. 9.1 we describe the properties of the numerical simulations. In Sect. 9.2 we analyze the case of a cluster of equal mass stars in a tidal field, and we discuss the effects of using only a fraction of the total number of particles to study the dynamics of the system. In Sect. 9.3 we study an isolated cluster with stellar evolution, and we discuss the relation between number density and surface brightness profiles. The work presented here was started in the context of the Gaia Challenge Workshop[1], where the simulations considered here were presented.

9.1 The simulations

In this section we briefly describe the characteristics of the two simulations that we used for the tests described in the following part of the Chapter.

9.1.1 Cluster of equal mass stars in a tidal field

We consider the results of a simulation run by Poul Alexander and Mark Gieles (see Alexander & Gieles 2012) with Aarseth's NBODY6 (Makino & Aarseth 1992; Aarseth 1999, 2003). The starting configuration of the simulation is composed of $N = 65536$ stars with the same mass, distributed according to a Plummer (1911) spherical model. The model does not include primordial binaries, nor a central black hole. The system is assumed to orbit in a tidal field generated by a point-mass galaxy; initially, the ratio of the Jacobi radius to the half-mass radius for the cluster is set to $r_{\rm J}/r_{\rm h} = 100$. The evolution

[1] http://astrowiki.ph.surrey.ac.uk/dokuwiki/doku.php?id=tests:collision

Table 9.1: Basic properties of the simulated cluster of equal mass stars in a tidal field, expressed in code units.

Snapshot	$M_{\rm true}$	$r_{\rm h,true}$	$r_{\rm J,true}$
Y	0.975	1.143	77.513
O	0.238	6.871	48.443

Notes. For the two considered snapshots, listed in the first column, we list: the mass, the half-mass radius, and the Jacobi radius, expressed in N-body units. The subscript "true" is used to indicate the true values of these quantities, as opposed to the estimates that are given in the following.

of the cluster is mainly driven by two-body relaxation; after undergoing core-collapse, the system expands until it fills its Roche-volume.

Here, we consider two snapshots of this evolving system. The first, which we will indicate as "snapshot Y", corresponds to the time, just after core collapse, in which the core radius of the cluster is minimum. The second, indicated as "snapshot O", occurs when $\approx 75\%$ of the stars are lost and the cluster is Roche-filling[2]. The labels, Y and O, are used as a reminder of the age of the system: the first snapshot refers to a young, the second to an old age of the system. Table 9.1 lists some properties of these snapshots.

For each simulation particle, the complete set of coordinates in phase space is available: the three spatial coordinates (x, y, z), and the three velocity coordinates (v_x, v_y, v_z). The units used are those of Heggie & Mathieu (1986): $G = M = r_{\rm vir} = 1$, where G, M, and $r_{\rm vir}$ denote the gravitational constant, the total mass of the initial configuration of the simulation, and the initial virial radius, respectively; they are often refer to as "N-body units". It is possible to translate these units into physical units, by fixing the total mass of the system: in this way, a single simulation could be used to represent systems with similar properties but different scales. In this respect, each simulation particle can be considered as a group of stars, rather than just a single star.

9.1.2 Isolated cluster with stellar evolution

The other N-body model considered in this Chapter has been generated by Mark Gieles (unpublished), starting from a configuration of $N = 10^5$ stars distributed according to a cored "gamma model" (Dehnen 1993; Tremaine et al. 1994), with Kroupa (2001) mass function between 0.1 and 100 $M_\odot$. The model does not include primordial binaries, nor a central black hole; moreover, no tidal interactions are included. The stellar evolution and mass-loss are modeled according to Hurley et al. (2000, 2002). The metallicity of the stars is [Fe/H] = -2.0 in solar units. In this case, we consider a single snapshot, taken at an age of approximately 12 Gyr, comparable to the typical age of Galactic globular clusters (see Sect. 1.3). Table 9.2 lists some properties of this system.

At variance with the case described in Subsection 9.1.1, here we consider each simulation particle as a single star, and we use physical units. For each star in the simulation, the following quantities are given:

- the spatial coordinates (x, y, z), expressed in pc;
- the velocity coordinates $(v_{\rm x}, v_{\rm y}, v_{\rm z})$, expressed in km s^{-1};

[2] A cluster is considered to be Roche-filling when its half-mass radius has become a fixed fraction of the Jacobi radius, $r_{\rm h}/r_{\rm J} = 0.145$ (see Hénon 1965).

Table 9.2: Basic properties of the simulated isolated cluster with stellar evolution.

$M_{\rm true}$	$r_{\rm h,true}$	$\log T_{\rm M,true}$
3.34	9.73	9.84

Notes. From left to right, we list: the mass of the system, expressed in units of $10^4 M_\odot$, the half-mass radius in pc, and the logarithm of the half-mass relaxation time in years. The subscript "true" is used to indicate the true values of these quantities, as opposed to the estimates that are given in the following.

- the mass of the star m, expressed in $M_\odot$;
- the effective temperature $T_{\rm eff}$, in K;
- the bolometric magnitude $M_{\rm bol}$, in mag.

We used the last two quantities to calculate the V magnitude of each star (this quantity will be used to calculate the luminosity density profiles). First, we need to compute the bolometric correction, which can be expressed as a function of the effective temperature by means of the following equation (Cox 2000):

$$BC = -\frac{T_{BC}}{T_{\rm eff}} - 10 \log T_{\rm eff} + \alpha \, . \tag{9.1}$$

Then, this bolometric correction is used to calculate the absolute V magnitude of each star:

$$M_{\rm V} = M_{\rm bol} - BC \, . \tag{9.2}$$

Finally, we calculate the apparent magnitude $m_{\rm V}$ that each star would have by imagining that the simulated cluster be located at a distance $d_\odot \approx 7.9$ kpc, which is a typical value for Galactic clusters. This procedure allows us to obtain values of the apparent magnitudes that are comparable to those usually measured for real clusters, and to explore the effects of realistic observational limitations on the measured profiles (see Sect. 9.3.2).

9.1.3 Projections and calculation of the profiles

We simulated an observation of the clusters by considering a projection on the sky: the direction z indicates the line of sight, and the coordinates (x, y) are on the plane of the sky. We carried out a similar analysis by considering projections along the three coordinates, and we found that our results do not depend on the chosen line-of-sight direction.

For the "projected" systems we then calculated the "observed" profiles that can be used to study their dynamics. Our goal here is to start from simulated observations that provide profiles similar to those that are usually available from real measurements of Galactic globular clusters. In particular, we constructed the projected number density and velocity dispersion profiles; for the second simulation, in addition to the number density, we constructed also the projected mass and (V-band) luminosity density profiles.

For convenience, the density profiles were normalized with respect to the value of their innermost point: this choice does not affect the analysis, because the central density was not used to calculate any of the derived parameters. This choice allows us to compare the density scales obtained for different density profiles for the same system.

Table 9.3: Properties of the samples.

Sample	Description
Y	Young snapshot; all the stars
YC	Young snapshot; 5% of the total stars, distributed as the cluster stars
YR	Young snapshot; 5% of the total stars, randomly distributed
O	Old snapshot; all the stars
OC	Old snapshot; 5% of the total stars, distributed as the cluster stars
OR	Old snapshot; 5% of the total stars, randomly distributed

Table 9.4: Dimensionless parameters and physical scales of the best-fit models.

Label	Model	Ψ	r_0	$\hat{\Sigma}_0$	σ_0
(1)	(2)	(3)	(4)	(5)	(6)
Y	King	8.80 ± 0.01	0.090 ± 0.001	0.039 ± 0.028	0.471 ± 0.003
YC	King	8.80 ± 0.07	0.090 ± 0.005	0.190 ± 0.198	0.434 ± 0.024
YR	King	9.14 ± 0.09	0.060 ± 0.008	0.391 ± 0.125	0.459 ± 0.023
Y	$f^{(\nu)}$	11.20 ± 0.10	0.830 ± 0.013	0.377 ± 0.064	0.595 ± 0.004
YC	$f^{(\nu)}$	11.45 ± 0.74	0.870 ± 0.092	1.734 ± 0.410	0.534 ± 0.029
YR	$f^{(\nu)}$	10.37 ± 0.52	0.920 ± 0.108	1.384 ± 0.399	0.580 ± 0.029
O	King	10.00 ± 0.11	0.220 ± 0.012	1.149 ± 0.031	0.106 ± 0.001
OC	King	10.20 ± 0.52	0.180 ± 0.051	2.184 ± 0.261	0.103 ± 0.006
OR	King	9.88 ± 0.80	0.250 ± 0.131	1.813 ± 0.651	0.097 ± 0.005
O	$f^{(\nu)}$	10.22 ± 0.13	6.580 ± 0.191	1.411 ± 0.092	0.111 ± 0.001
OC	$f^{(\nu)}$	11.78 ± 1.20	4.730 ± 0.760	6.539 ± 0.663	0.102 ± 0.006
OR	$f^{(\nu)}$	11.95 ± 0.80	5.750 ± 0.751	7.046 ± 0.480	0.097 ± 0.005

Notes. For each case, labeled in column (1), for isotropic King and anisotropic $f^{(\nu)}$ models, indicated in Col. (2), we list: the concentration parameter Ψ in Col. (3), the scale radius r_0 in Col. (4), the central (dimensionless) number density $\hat{\Sigma}_0$ in Col. (5), and the central line-of-sight velocity dispersion σ_0 in Col. (6). Formal errors on the various parameters are also recorded (see Sect. 3.3.4).

9.2 Equal mass stars

In this section, we present the results of the tests carried out on the first simulation, which consists of a cluster of equal mass stars in a tidal field, as described in Sect. 9.1.1. We recall that in the following we will refer to the first snapshot as Y, and to the second as O.

9.2.1 Calculated profiles and method

We analyzed the two available snapshots of this simulation by means of three sets of calculated profiles:

1. we consider the entire set of simulated particles to calculate the number density and the velocity dispersion profiles;

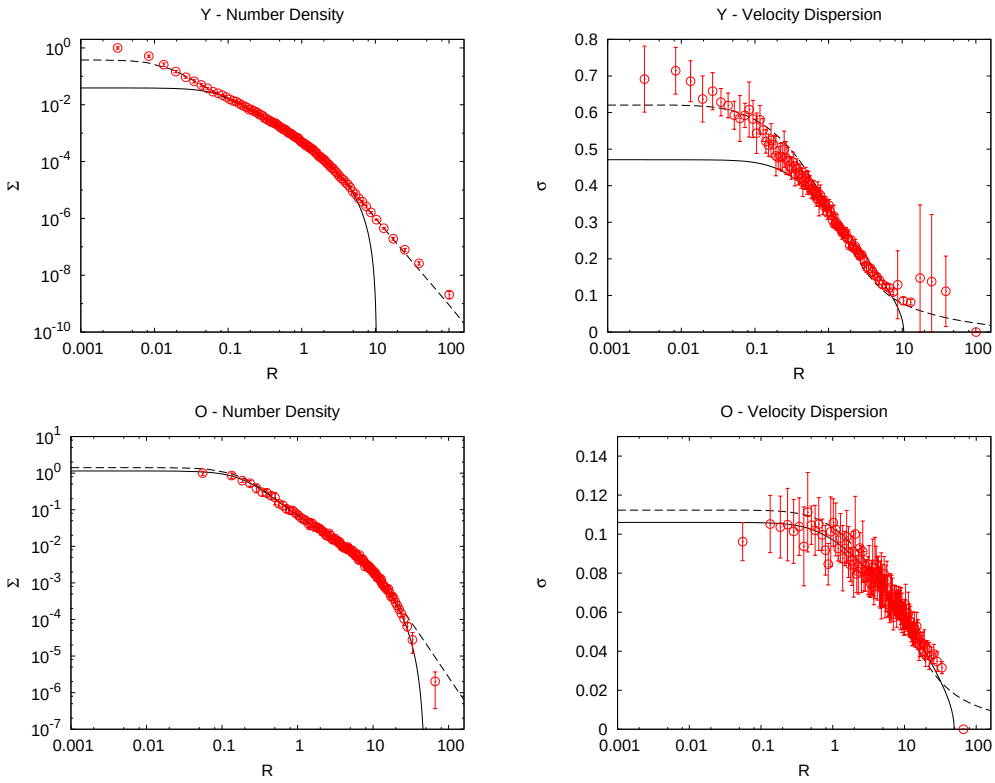

Figure 9.1: Fits by King models and anisotropic $f^{(\nu)}$ models to the number density profiles and to the line-of-sight velocity dispersion profiles of simulated globular clusters. Solid lines correspond to the King-model fits, dashed lines to $f^{(\nu)}$-model fits. The "data" are indicated with circles; for each data-point, errors are shown as vertical error bars (see Sect. 3.3). The top panels refer to snapshot Y, the bottom ones to snapshot O. The profiles here represented were calculated by means of all the available particles in the simulation.

2. we extracted only a fraction ($\approx 5\%$) of the total number of particles from each snapshot, and we calculated the profiles only by means of these particles. We paid attention to select a sample of particles distributed in the same way as the entire set (i.e., we selected more particles in the central region, and fewer in the outermost parts). In the following we refer to this sample as "sample C". Moreover, we randomly extracted from the simulation the same number of particles that are contained in "sample C", and we calculate another set of profiles from them; we indicate this sample as "sample R".

We thus obtain a total of six sets of calculated profiles, three for each snapshot, that we identify by means of the introduced labels (Y, YC, YR; O, OC, OR); Table 9.3 summarizes the properties of the considered samples.

After calculating the number density and velocity dispersion profiles for the three cases for each snapshot, we carried out fits by means of King and $f^{(\nu)}$ models, by following the standard procedure described in Sect. 3.3. The fits determine the concentration parameter Ψ, the central (dimensionless) density $\hat{\Sigma}_0$, the scale radius r_0, and the scale

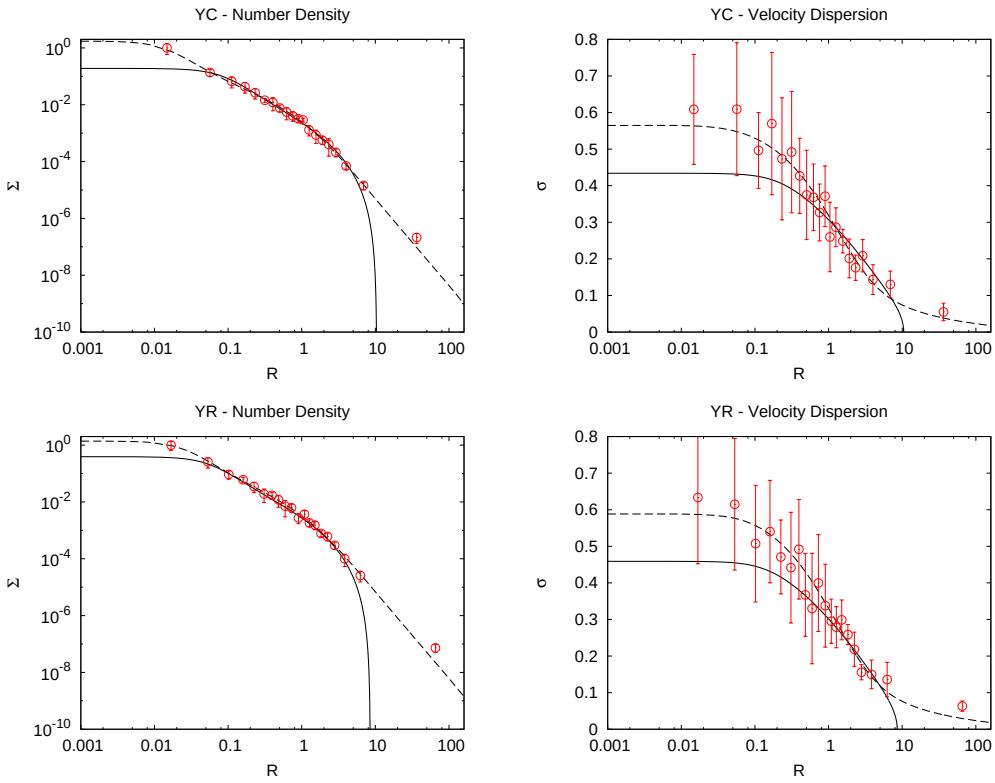

Figure 9.2: Fits by King models and anisotropic $f^{(\nu)}$ models to the number density profiles and to the line-of-sight velocity dispersion profiles calculated for snapshot Y, in the same format as in Fig. 9.1. The top panels show profiles calculated from "sample C", the bottom ones those calculated from "sample R".

velocity σ_0 (i.e. the central velocity dispersion). We then calculated, for each model and for each case, the total mass of the system and the half-mass radius. We recall that all dimensional quantities are expressed in N-body units.

The goal of this test is to determine how well a system could be described by means of profiles calculated from a sample of its particles. For real globular clusters, in fact, we usually observe only a fraction of their total number of stars: it is therefore important to understand the implications of this observational limit on the dynamical description that is achievable for these systems.

9.2.2 Results and discussion

The values of the dimensionless parameters and of the physical scales determined by the fits for the two families of models are presented in Table 9.4. We immediately note that the values of the concentration parameter Ψ identified by the two families of models are larger than those usually found for Galactic globular clusters; this might be related to the fact that these simulations describe post-core-collapse systems[3]. In addition, the

[3]For the core-collapsed globular cluster NGC 7078 (M15), in Chapter 4 we found $\Psi = 8.09$ for King models, and $\Psi = 8.17$ for $f^{(\nu)}$ models.

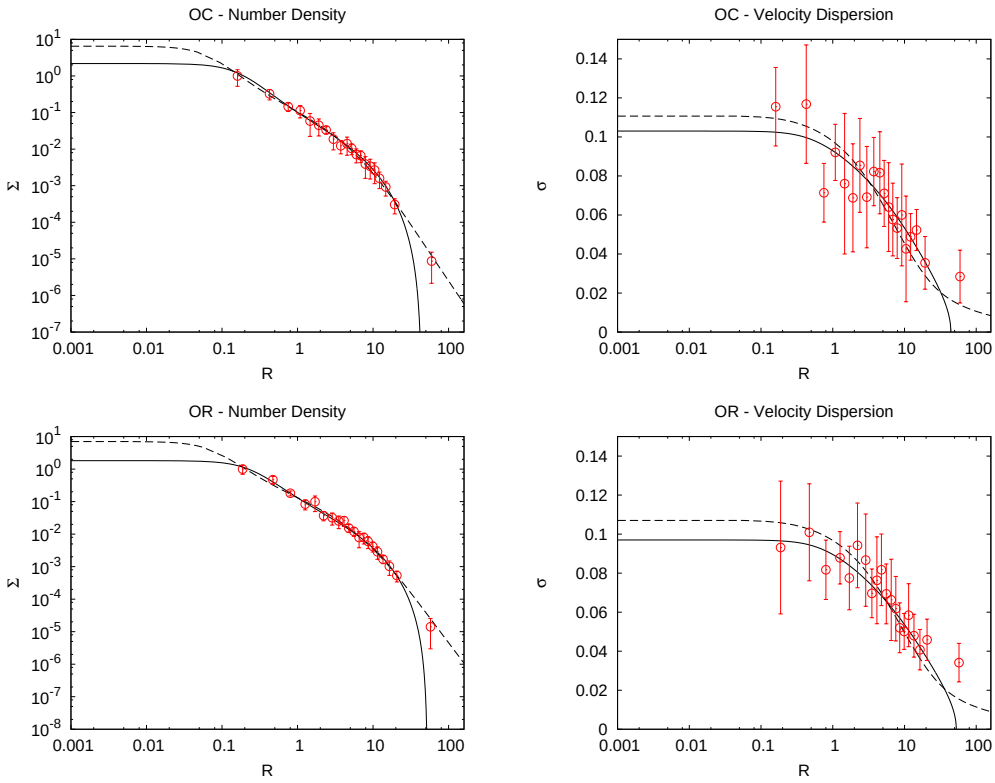

Figure 9.3: Fits by King models and anisotropic $f^{(\nu)}$ models to the number density profiles and to the line-of-sight velocity dispersion profiles calculated for snapshot O, in the same format as in Fig. 9.1. The top panels show profiles calculated from "sample C", the bottom ones those calculated from "sample R".

values of the central number density and of the central velocity dispersion are always larger when determined by $f^{(\nu)}$ models, because that these models are steeper than King models in the central region.

The best-fit number density and line-of-sight velocity dispersion profiles determined by the fitting procedure in the first case (i.e., considering all the particles in the simulation) of the two snapshots, together with the "observed profiles", are shown in Fig. 9.1.

We can see that $f^{(\nu)}$ models perform better in representing the profiles calculated for snapshot Y, while King models are satisfactory only in reproducing those of snapshot O. In particular, for snapshot Y, $f^{(\nu)}$ models are successful in reproducing the number density profiles on their entire radial extent, including the innermost and outermost regions, where King models fail. A similar behavior is observed in the velocity dispersion profiles. In snapshot O, the "observed" profiles are reproduced equally well by both models, even if formally King models perform better. This is in line with the expectation that for partially relaxed systems radially-biased anisotropy could play a role, and that relaxed systems are instead isotropic (see Chapter 4). In a similar way, Figs. 9.2 and 9.3 show the results of the fits to the profiles calculated with "sample C" and "sample R", separately for snapshot Y and O.

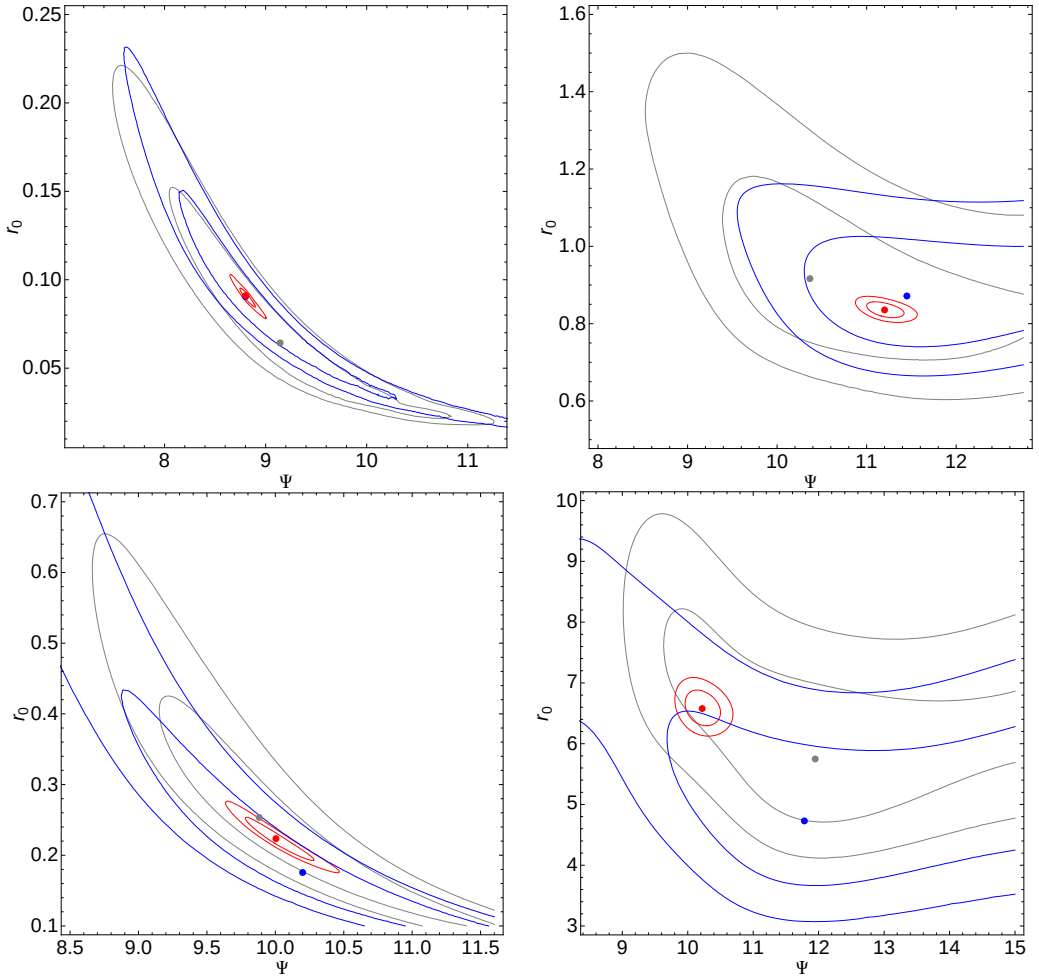

Figure 9.4: Confidence regions on model parameters. Each panel shows the confidence regions, in the parameter space (Ψ, r_0), corresponding to confidence levels of 68.3% and 95.4%; the dot represents the best-fit values of the parameters obtained by minimizing the chi-squared. Top panels refer to snapshot Y, bottom panels to snapshot O; on the left King model parameters are represented, on the right $f^{(\nu)}$ model parameters. Red lines refer to the case in which all the particles have been considered, blue lines to "sample C", and gray lines to "sample R".

To better compare the structural parameters derived in the different cases for each snapshot, we show in Fig. 9.4 the confidence regions in the parameter space (Ψ, r_0), corresponding to confidence levels of 68.3% and 95.4%; the dot represents the best-fit values of the parameters obtained by minimizing the chi-squared. Top panels refer to snapshot Y, bottom panels to snapshot O; on the left King model parameters are represented, on the right $f^{(\nu)}$ model parameters. Red lines refer to the case in which all the particles have been considered, blue lines to "sample C", and gray lines to "sample R". It is apparent that, especially for the King models, the structural parameters (Ψ, r_0) and their confidence regions occupy a strip in parameter space, which is a clear signature of degeneracy: when a more concentrated model is required (larger Ψ), the resulting radial

Table 9.5: Derived quantities for the cluster of equal mass stars in a tidal field.

	King Models				$f^{(\nu)}$ Models			
Label	M	$r_{\rm h}$	$\hat{M}$	$\hat{r}_{\rm h}$	M	$r_{\rm h}$	$\hat{M}$	$\hat{r}_{\rm h}$
Y	0.92 ± 0.02	1.19 ± 0.03	0.94	1.04	1.08 ± 0.07	1.13 ± 0.03	1.11	0.99
YC	0.79 ± 0.18	1.20 ± 0.20	0.81	1.05	0.96 ± 0.51	1.20 ± 0.19	0.98	1.05
YR	0.76 ± 0.24	1.10 ± 0.28	0.78	0.96	1.01 ± 0.35	1.17 ± 0.28	1.04	1.02
O	0.23 ± 0.05	6.84 ± 1.31	0.97	1.00	0.26 ± 0.02	8.22 ± 0.53	1.09	1.2
OC	0.19 ± 0.19	6.16 ± 5.56	0.80	0.90	0.21 ± 0.21	6.57 ± 1.35	0.88	0.96
OR	0.21 ± 0.32	7.31 ± 11.23	0.88	1.06	0.24 ± 0.17	7.33 ± 1.03	1.01	1.07

Notes. For each case, indicated by the label in the first column, we list the total mass M of the cluster and the half-mass radius $r_{\rm h}$, both expressed in N-body units, as calculated from King and $f^{(\nu)}$ models; formal errors on these quantities are recorded. We also list the values of the total mass and of the half-mass radius normalized with respect to the true values, $\hat{M} = M/M_{\rm true}$ and $\hat{r}_{\rm h} = r_{\rm h}/r_{\rm h,true}$ (see Table 9.1).

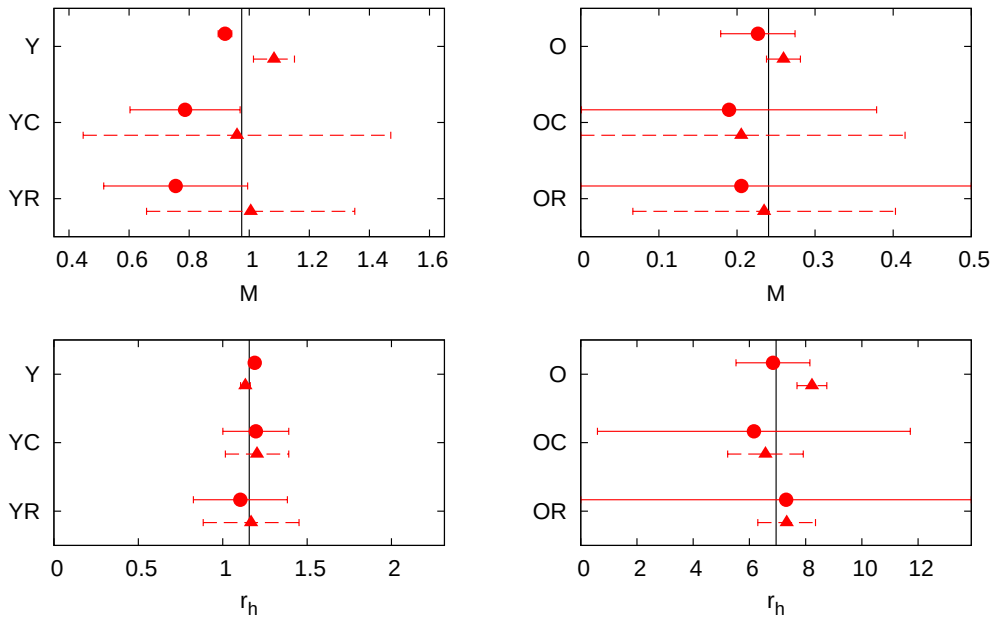

Figure 9.5: Mass and half-mass radius estimates (top and bottom panels, respectively) for snapshot Y and O (left and right panels, respectively). In each panel, the horizontal axis represents the value of the considered quantity (in N-body units), and the vertical axis is used to label the different estimates obtained for that quantity. The true values of mass and half-mass radius of the systems are indicated by the vertical solid lines in the panels. King ($f^{(\nu)}$) model estimates are given as filled circles (triangles), and the corresponding error bars are shown as solid (dashed) lines.

scale shrinks. The area of the parameter space included in the confidence regions increases when going from the first to the third case; this fact is reflected in the increased

Table 9.6: Properties of the samples.

Sample	Description
A	All the stars
L	Stars with $m_{\rm V} < 24$ mag (lower magnitude cut)
U	Stars with $12 < m_{\rm V} < 24$ mag (upper magnitude cut)

magnitude of the calculated errors on the parameters (see Table 9.7).

Derived parameters

As done in Chapter 4, it is interesting to compare the estimates of mass and half-mass radius calculated by means of the different models for the several considered cases. The values obtained for these quantities are listed in Table 9.5. To allow for a more immediate comparison between the values obtained in the various cases, we also show them in Fig. 9.5. In each panel, the horizontal axis represent the value of the considered quantity (in N-body units), and the vertical axis is used to label the different estimates obtained for that quantity. King model ($f^{(\nu)}$ model) estimates are given as filled circles (filled triangles), and the corresponding error bars are shown as solid (dashed) lines. The true values of mass and half-mass radius of the systems are indicated by vertical solid lines in the panels.

The principal observed effect confirms the expectation that when the number of stars used to calculate the "observed" profiles is low (we recall that in this case we considered a fraction of $\approx 5\%$ of the total number of stars), the errors on the derived parameters is large. As already noted in Chapter 4, the estimated value of the total mass is generally larger when calculated by means of $f^{(\nu)}$ models. In particular, for both snapshots, when considering the entire set of particles, King models underestimate the total mass of the cluster, and $f^{(\nu)}$ models overestimate it. In general, we see that the estimates of the half-mass radius for a given snapshot appear to be more stable than those of the mass. For r_h, the maximum difference between estimated and true value is less than 10% the true value; for the mass M, instead, differences up to $\approx 17\%$ of the true value are observed.

9.3 A study of different density profiles

In this section, we present the results of the tests carried out on the second simulation, which consists of a cluster of stars of different masses, where stellar evolution is considered (see Sect. 9.1.2). For this simulation we also consider three different cases, corresponding to different sampling of the stars used for the calculation of the "observed" profiles, as summarized in Table 9.6.

9.3.1 Number, mass and luminosity density

For the cluster under examination, we have enough information to calculate several profiles. In fact, we can calculate the number density (ND), the mass density (MD), and the (V-band) luminosity density (LD) profiles.

First, we consider the entire set of simulated stars, and we label the calculated profiles with the letter A (which stands for "all", to indicate that all the stars are involved in the calculation of the profiles). We carried out fits by means of King and $f^{(\nu)}$ models,

Table 9.7: Dimensionless parameters and physical scales of the best-fit models.

	King models					
Label	Ψ	r_0	$\hat{\Sigma}_0$	σ_0	$\widetilde{\chi}^2_{\rm p}$	$\widetilde{\chi}^2_{\rm k}$
A-ND	7.73 ± 0.05	1.98 ± 0.06	0.78 ± 0.04	1.62 ± 0.01	13.01	23.49
A-MD	7.90 ± 0.03	1.36 ± 0.03	0.84 ± 0.04	1.83 ± 0.01	11.37	19.66
A-LD	7.40 ± 0.05	1.78 ± 0.10	0.04 ± 0.21	1.81 ± 0.01	0.94	22.30
L-ND	7.76 ± 0.08	1.15 ± 0.06	0.93 ± 0.08	1.90 ± 0.02	4.09	2.82
L-MD	7.80 ± 0.02	1.09 ± 0.02	0.89 ± 0.06	1.92 ± 0.03	4.65	3.19
L-LD	7.80 ± 0.14	0.79 ± 0.10	0.73 ± 0.37	2.11 ± 0.03	0.45	7.83
U-ND	7.79 ± 0.06	1.14 ± 0.04	0.92 ± 0.06	1.90 ± 0.02	4.06	7.29
U-MD	7.95 ± 0.06	1.05 ± 0.04	0.88 ± 0.07	1.90 ± 0.03	4.85	1.34
U-LD	7.52 ± 0.26	0.76 ± 0.11	1.16 ± 0.26	2.19 ± 0.03	0.63	9.25

	$f^{(\nu)}$ models					
Label	Ψ	r_0	$\hat{\Sigma}_0$	σ_0	$\widetilde{\chi}^2_{\rm p}$	$\widetilde{\chi}^2_{\rm k}$
A-ND	7.34 ± 0.03	14.41 ± 0.16	0.65 ± 0.03	1.75 ± 0.01	4.42	4.09
A-MD	7.53 ± 0.04	10.26 ± 0.14	0.82 ± 0.05	2.05 ± 0.01	1.76	0.42
A-LD	7.62 ± 0.17	3.80 ± 0.85	0.82 ± 0.75	3.17 ± 0.02	0.31	17.34
L-ND	7.11 ± 0.06	6.94 ± 0.19	0.89 ± 0.06	2.10 ± 0.03	0.62	1.33
L-MD	7.21 ± 0.05	6.80 ± 0.04	0.90 ± 0.05	2.13 ± 0.03	0.63	1.53
L-LD	7.33 ± 0.31	3.81 ± 0.72	1.54 ± 0.50	2.61 ± 0.03	0.21	6.66
U-ND	7.13 ± 0.06	6.97 ± 0.19	0.89 ± 0.06	2.18 ± 0.02	0.56	0.73
U-MD	7.11 ± 0.06	6.50 ± 0.18	0.89 ± 0.06	2.13 ± 0.03	0.61	1.43
U-LD	6.80 ± 0.27	3.77 ± 0.46	1.22 ± 0.22	2.48 ± 0.03	0.23	5.14

Notes. For each case, labeled in the first column of the tables, separately for King and $f^{(\nu)}$ models, we list: the concentration parameter Ψ, the scale radius r_0 in pc, the central (number, mass, or luminosity) dimensionless density $\hat{\Sigma}_0$, and the central line-of-sight velocity dispersion σ_0 in km s^{-1}. Formal errors on the various parameters are also recorded (see Sect. 3.3.4). The last two columns give the minimum value obtained for the reduced chi-squared in the case of the density fit, $\widetilde{\chi}^2_{\rm p}$, and in the case of the kinematic fit, $\widetilde{\chi}^2_{\rm k}$. The top lines in the two parts of the table refer to profiles calculated from the entire set of stars (A), the middle lines refer to profiles calculated when a first magnitude cut is introduced (L), and the bottom lines to those obtained when also the second magnitude cut is operated (U) (see Subsection 9.3.2).

by following the standard procedure described in Sect. 3.3, to obtain the concentration parameter Ψ, the central (dimensionless) density $\hat{\Sigma}_0$, and the scale radius r_0 that provide the best fit to the density profiles. Then, for each of the best fit profiles, we carried out a fit to the velocity dispersion profiles (calculated as prescribed by Pryor & Meylan 1993), thus obtaining also the scale velocity σ_0.

We end up with three best fit models to describe the cluster, shown in Fig. 9.6. The best-fit parameters obtained from these fits are listed in the top lines in the two parts of Table 9.7.

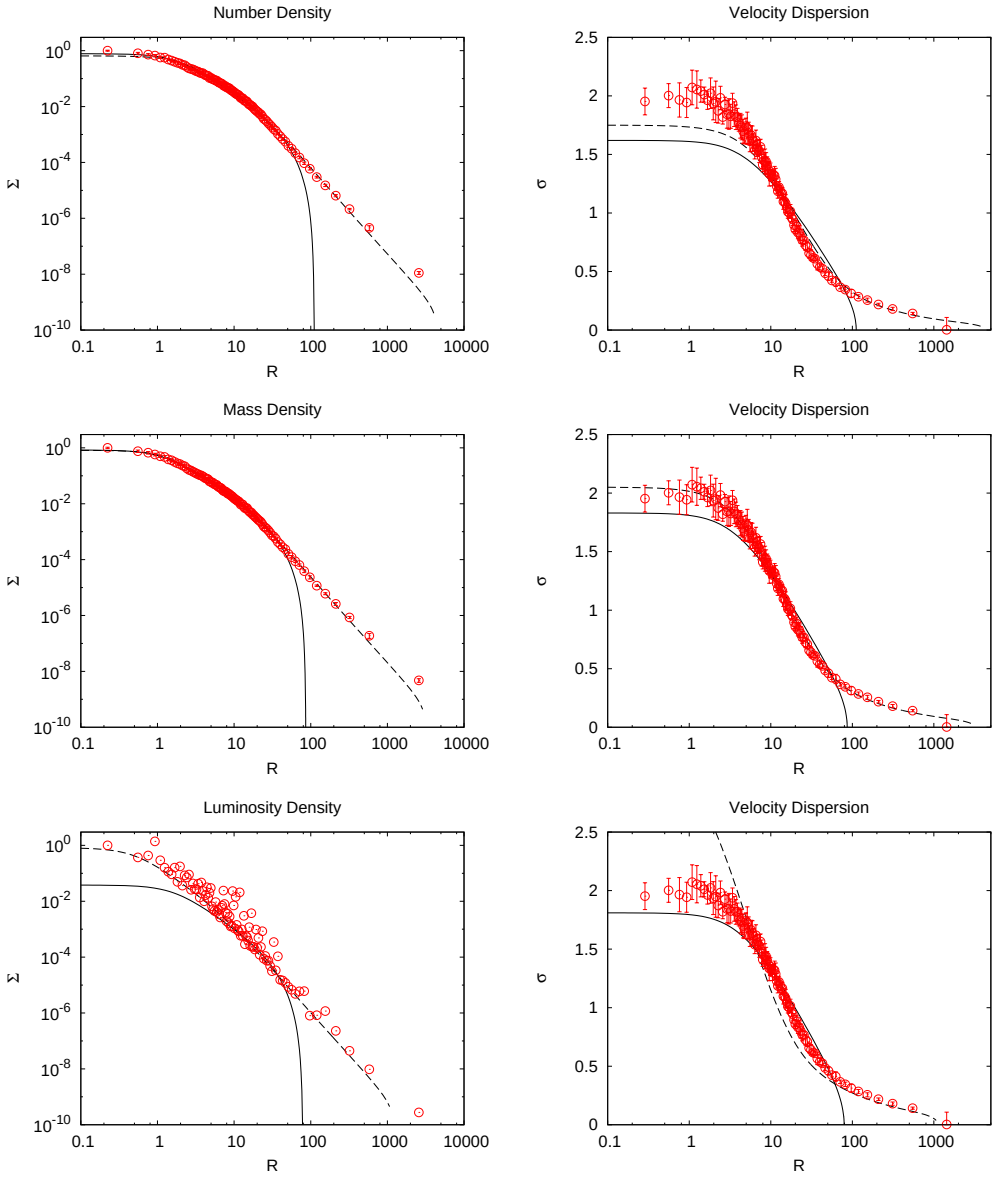

Figure 9.6: Fits by King models and anisotropic $f^{(\nu)}$ models to the simulated globular cluster (case A). Left panels show the fits to the projected density profiles, right panels the corresponding fits to the velocity dispersion profiles. Top panels refer to the number density (ND), middle panels to the mass density (MD), and the bottom panels to the luminosity density (LD). Solid lines correspond to the King-model fits, dotted lines to $f^{(\nu)}$-model fits. The "data" are indicated with circles; for each data-point, errors are shown as vertical error bars (errors for LD are not shown).

For this cluster, it seems that $f^{(\nu)}$ models perform better; this is apparent from Fig. 9.6, as is confirmed by looking at the minimum chi-squared obtained by the different models. When considering the results obtained from King models, we see that the best-fit profiles

systematically underpredict both central density and central velocity dispersion. They are also unable to reproduce the "observed" profiles beyond $R \approx 100$ pc (i.e., $R \approx 10 r_{\rm h}$). If we look at the results obtained by means of $f^{(\nu)}$ models, we immediately notice that the velocity scale determined for the model identified by the ND fit underestimates the central velocity dispersion, whereas the one obtained for the LD best-fit model overestimates it. Only the velocity scale determined for the MD fit reproduces in a satisfactory way the entire "observed" velocity dispersion profile. This result is likely to remind us that the velocity distribution is related to the mass distribution in the cluster. We recall that, unfortunately, for real clusters we cannot measure a mass density profile, but only the number or luminosity density; these profiles strongly depend on the exact distribution of stars in the clusters, and are mainly determined by the distribution of faint (ND) or bright (LD) stars, as explained in Chapter 5.

Finally, we point out that the fact that fits to the LD lead to a low value of the chi-squared does not mean that this profile is particularly adequate to represent the cluster. In fact, this just reflects the fact that the errors on the points in this profiles are large; actually, exactly for this reason, the LD profile does not constrain the model well, and the associated errors on the parameters determined from it are large.

9.3.2 Cut in magnitude

So far, we analyzed the output of this numerical simulation by considering all the stars in the snapshot. Here we introduce magnitude cuts to mimic the limitations that are encountered when observing real clusters.

Eliminating faint stars

First, we eliminate from our sample the stars fainter than 24 mag in V band. This is a typical lower limit to the magnitudes that are observable with currently available instruments and telescopes (for example, see Piotto et al. 2012). In this way, we are discarding the stars that would not be detected in a real cluster. The sample of stars thus obtained is indicated in the following with the letter L (as a reminder that this sample is determined by means of a *lower* limit of brightness).

After calculating the ND, MD, LD, and velocity dispersion profiles for this reduced sample of stars, we carried out the fitting procedure described above. The results are shown in Fig. 9.7, in the same format as in Fig. 9.6. The best-fit parameters obtained from these fits are listed in the middle lines in the two parts of Table 9.7.

These fits confirm that $f^{(\nu)}$ models perform better in reproducing the "observed" profiles. In this case, the best-fit $f^{(\nu)}$ models determined from the ND and MD fits lead to the determination of a velocity scale close to the innermost part of the velocity dispersion profile. The model determined by the LD profile, even if characterized by a lower σ_0 with respect to the one obtained in the previous section, still overpredicts the central value of velocity dispersion.

By inspecting the best-fit values obtained for the parameters Ψ and r_0 from the ND and LD profiles, we find a situation similar to the one described in Chapter 5: the best-fit model identified by means of the LD profile is more concentrated (it has larger Ψ and smaller r_0) with respect to the one obtained by means of the ND profile. When detected for the globular cluster NGC 6341 (M92), this feature was considered to be a signature of mass segregation.

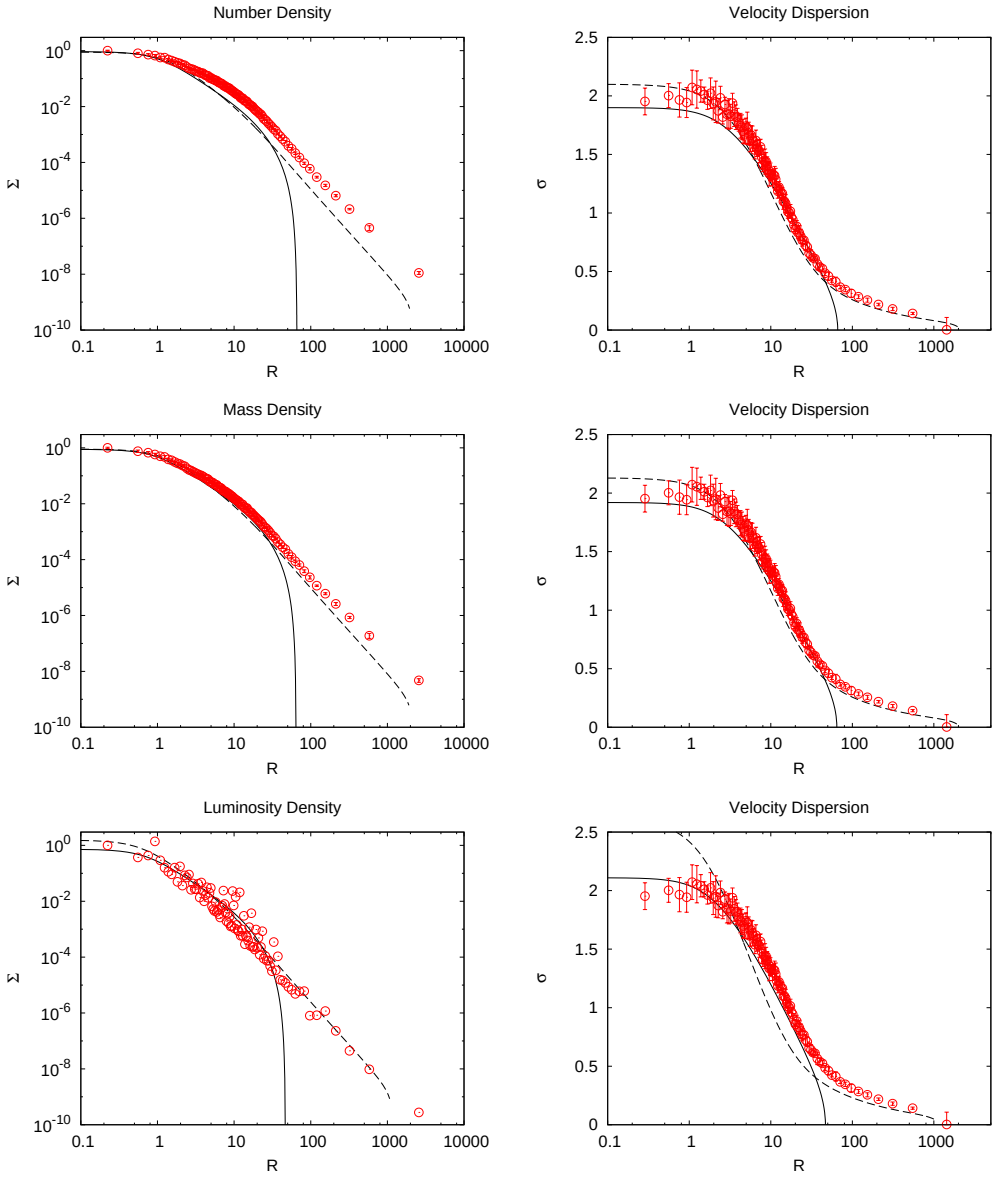

Figure 9.7: Fits by King models and anisotropic $f^{(\nu)}$ models to the simulated globular cluster, after the operation of a magnitude cut (case L), in the same format as in Fig. 9.6.

Eliminating bright stars

Starting from the sample obtained by eliminating faint stars, another cut in magnitude can be imposed, to eliminate the stars brighter than a certain limit. Here we decided to keep only stars fainter than 12 mag. This is to emulate what is usually done to eliminate the fluctuations in the surface brightness that are introduced by the presence of bright stars. In the following, we identify the sample obtained by means of this *upper* brightness

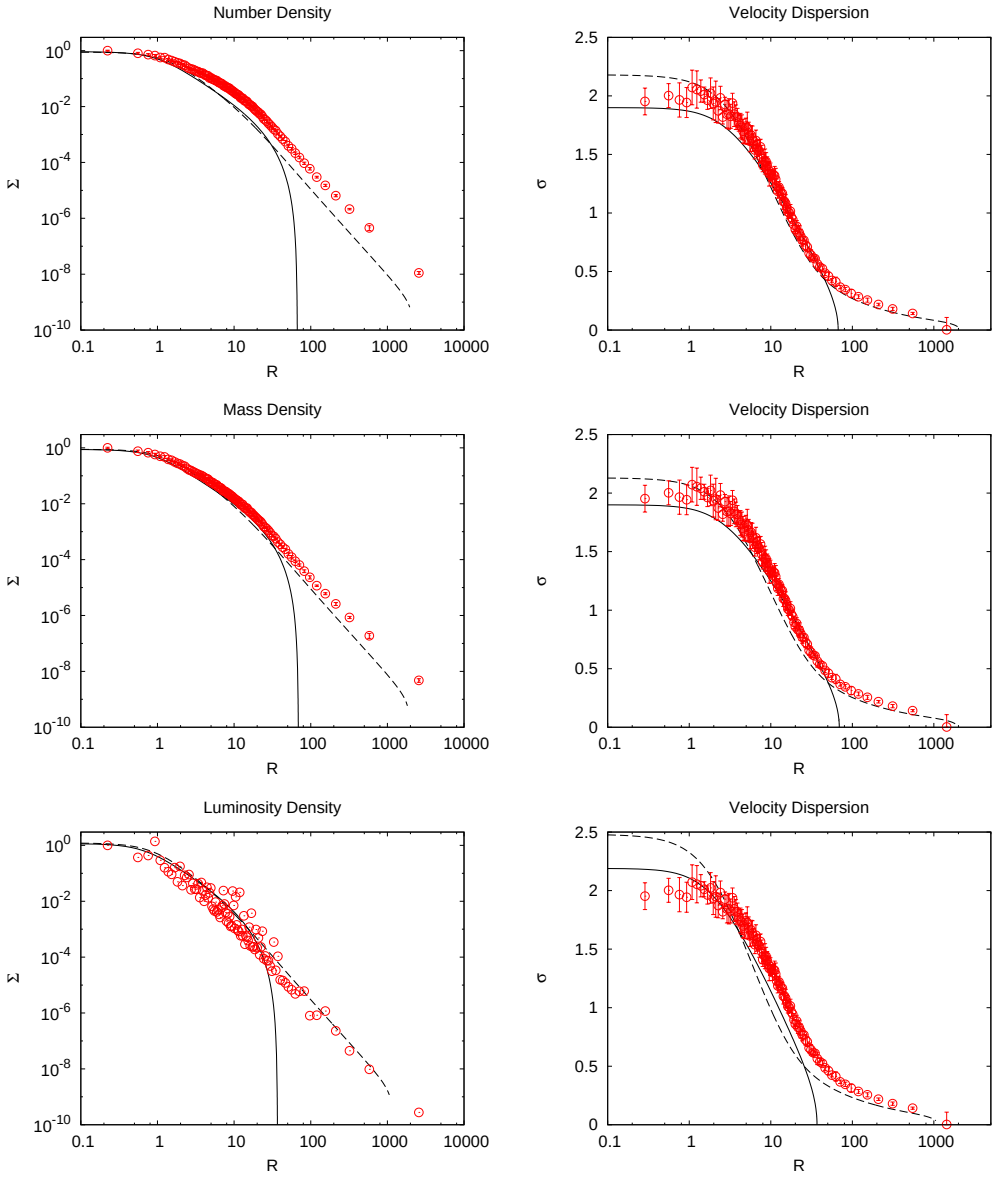

Figure 9.8: Fits by King models and anisotropic $f^{(\nu)}$ models to the simulated globular cluster, after the operation of a double magnitude cut (case U), in the same format as in Fig. 9.6.

cut with the letter U.

The results of the fits to the profiles calculated for this sample of stars are shown in Fig. 9.8, in the same format as in Fig. 9.6. The best-fit parameters obtained from these fits are listed in the bottom lines in the two parts of Table 9.7.

As already noted for real clusters (see Chapter 5), the number density profile is only very slightly affected by the elimination of the brightest stars in the sample. Instead, some differences are seen in the values of best-fit parameters obtained for the LD and

Table 9.8: Derived parameters for the isolated cluster with stellar evolution.

	King models						
Label	M	$r_{\rm h}$	$\log T_{\rm M}$	$r_{\rm tr}$	$\hat{M}$	$\hat{r}_{\rm h}$	$\log \hat{T}_{\rm M}$
A-ND	3.18 ± 0.26	11.76 ± 1.05	9.97	111.61	0.95	1.21	1.01
A-MD	3.03 ± 0.19	9.06 ± 0.56	9.79	86.51	0.91	0.93	0.99
A-LD	3.08 ± 0.35	8.63 ± 0.96	9.76	79.37	0.92	0.89	0.99
L-ND	2.58 ± 0.38	7.00 ± 1.06	9.59	66.22	0.77	0.72	0.97
L-MD	2.55 ± 0.17	6.80 ± 0.33	9.57	64.58	0.76	0.70	0.97
L-LD	2.22 ± 0.64	4.89 ± 1.53	9.33	46.81	0.66	0.50	0.95
U-ND	2.59 ± 0.29	7.05 ± 0.97	9.60	67.12	0.78	0.72	0.98
U-MD	2.56 ± 0.34	7.24 ± 0.50	9.61	69.15	0.77	0.74	0.98
U-LD	2.03 ± 0.85	3.96 ± 1.85	9.18	36.89	0.61	0.41	0.93

	$f^{(\nu)}$ models						
Label	M	$r_{\rm h}$	$\log T_{\rm M}$	κ	$\hat{M}$	$\hat{r}_{\rm h}$	$\log \hat{T}_{\rm M}$
A-ND	3.80 ± 0.13	12.88 ± 0.24	10.06	1.32	1.14	1.32	1.02
A-MD	3.54 ± 0.14	9.00 ± 0.18	9.81	1.31	1.06	0.92	1.00
A-LD	3.09 ± 0.94	3.31 ± 0.80	9.14	1.31	0.93	0.34	0.93
L-ND	2.79 ± 0.23	6.41 ± 0.31	9.55	1.34	0.84	0.66	0.97
L-MD	2.74 ± 0.15	6.19 ± 0.12	9.52	1.33	0.82	0.64	0.97
L-LD	2.24 ± 0.80	3.41 ± 0.91	9.10	1.32	0.67	0.35	0.92
U-ND	3.00 ± 0.23	6.42 ± 0.31	9.56	1.33	0.90	0.66	0.97
U-MD	2.68 ± 0.22	6.01 ± 0.25	9.50	1.34	0.80	0.62	0.97
U-LD	2.28 ± 0.64	3.70 ± 0.87	9.15	1.36	0.68	0.38	0.93

Notes. For each case, labeled in the first column of the tables, for King and $f^{(\nu)}$ models, we list: the estimated total mass of the cluster M in units of $10^4 M_\odot$, the half-mass radius $r_{\rm h}$ in pc, and the logarithm of the half-mass relaxation time $\log T_{\rm M}$ expressed in years. In addition, for King models we show the estimated truncation radius $r_{\rm tr}$ in pc, and for $f^{(\nu)}$ models the instability parameter κ (see Sect. 4.3.4). In the last columns we list the values of the total mass, of the half-mass radius, and of the relaxation time normalized with respect to the true values, $\hat{M} = M/M_{\rm true}$, $\hat{r}_{\rm h} = r_{\rm h}/r_{\rm h,true}$, and $\log \hat{T}_{\rm M} = \log T_{\rm M}/\log T_{\rm M,true}$ (see Table 9.2).

MD profiles, with respect to those determined for cases A and L.

9.3.3 Derived parameters

For the best-fit models, we calculate the total mass of the cluster, the half-mass radius, and the half-mass relaxation time and we compare them with the true values, listed in Table 9.2. In addition, for King models we estimated the truncation radius $r_{\rm tr}$, and for $f^{(\nu)}$ models the instability parameter κ (Polyachenko & Shukhman 1981; see Sect. 4.3.4, and in particular Eq. (4.1)). We list these quantities in Table 9.8.

Before discussing the results, we describe a final test that we carried out to simulate what can be achieved by means of more realistic kinematic data-sets. In Chapters 7

Table 9.9: Derived parameters for red giant branch stars velocity dispersion.

	King models				
Label	σ_0	M	$\log T_{\rm M}$	$\hat{M}$	$\log \hat{T}_{\rm M}$
A-ND	1.62 ± 0.21	3.20 ± 1.07	9.97	0.96	1.01
A-MD	1.66 ± 0.22	2.50 ± 0.79	9.75	0.75	0.99
A-LD	1.65 ± 0.22	2.55 ± 0.93	9.73	0.76	0.99
L-ND	1.69 ± 0.22	2.04 ± 0.79	9.55	0.61	0.97
L-MD	1.70 ± 0.22	2.09 ± 0.63	9.54	0.63	0.97
L-LD	1.76 ± 0.23	1.54 ± 0.81	9.27	0.46	0.94
U-ND	1.69 ± 0.22	2.06 ± 0.73	9.56	0.62	0.97
U-MD	1.70 ± 0.22	2.06 ± 0.76	9.57	0.62	0.97
U-LD	1.79 ± 0.24	1.35 ± 0.89	9.11	0.40	0.93

	$f^{(\nu)}$ models				
Label	σ_0	M	$\log T_{\rm M}$	$\hat{M}$	$\log \hat{T}_{\rm M}$
A-ND	1.64 ± 0.22	3.33 ± 0.96	10.03	1.00	1.02
A-MD	1.69 ± 0.22	2.42 ± 0.71	9.74	0.72	0.99
A-LD	1.94 ± 0.26	1.16 ± 0.65	8.97	0.35	0.91
L-ND	1.74 ± 0.23	1.91 ± 0.61	9.48	0.57	0.96
L-MD	1.75 ± 0.23	1.85 ± 0.54	9.45	0.55	0.96
L-LD	1.92 ± 0.26	1.21 ± 0.73	8.99	0.36	0.91
U-ND	1.74 ± 0.23	1.91 ± 0.61	9.48	0.57	0.96
U-MD	1.75 ± 0.23	1.82 ± 0.59	9.43	0.54	0.96
U-LD	1.88 ± 0.25	1.31 ± 0.68	9.06	0.39	0.92

Notes. For each case, labeled in the first column, for both King and $f^{(\nu)}$ models, we list: the value of the central velocity dispersion σ_0 obtained by means of a fit to the velocity dispersion that is calculated by considering only red giant branch stars, in km s^{-1}, the calculated total mass of the cluster M in units of $10^4\ M_\odot$, and the logarithm of the half-mass relaxation time $T_{\rm M}$ expressed in years. In the last columns we list the values of the total mass and of the relaxation time normalized with respect to the true values, $\hat{M} = M/M_{\rm true}$ and $\log \hat{T}_{\rm M} = \log T_{\rm M}/\log T_{\rm M,true}$ (see Table 9.2).

and 8 we described the proposals that we submitted to ESO in order to measure radial velocities of stars in Galactic globular clusters. We showed that, with a reasonable observing time, it is possible to measure accurate velocities for stars located on the red giant branch in the color-magnitude diagram of the clusters. To recreate a similar situation, we selected the red giant branch stars from the simulated cluster, and we calculated the velocity dispersion profile by using only the 247 stars thus identified. Then, we performed the kinematic fit to this new profile to determine the central velocity dispersion.

We found that the values of σ_0 obtained for the best-fit models determined by different density profiles are rather stable, when the velocity dispersion is measured by taking into account only red giant branch stars. The σ_0 values are smaller than those obtained when all the stars are considered, and the formal errors are larger. From these values

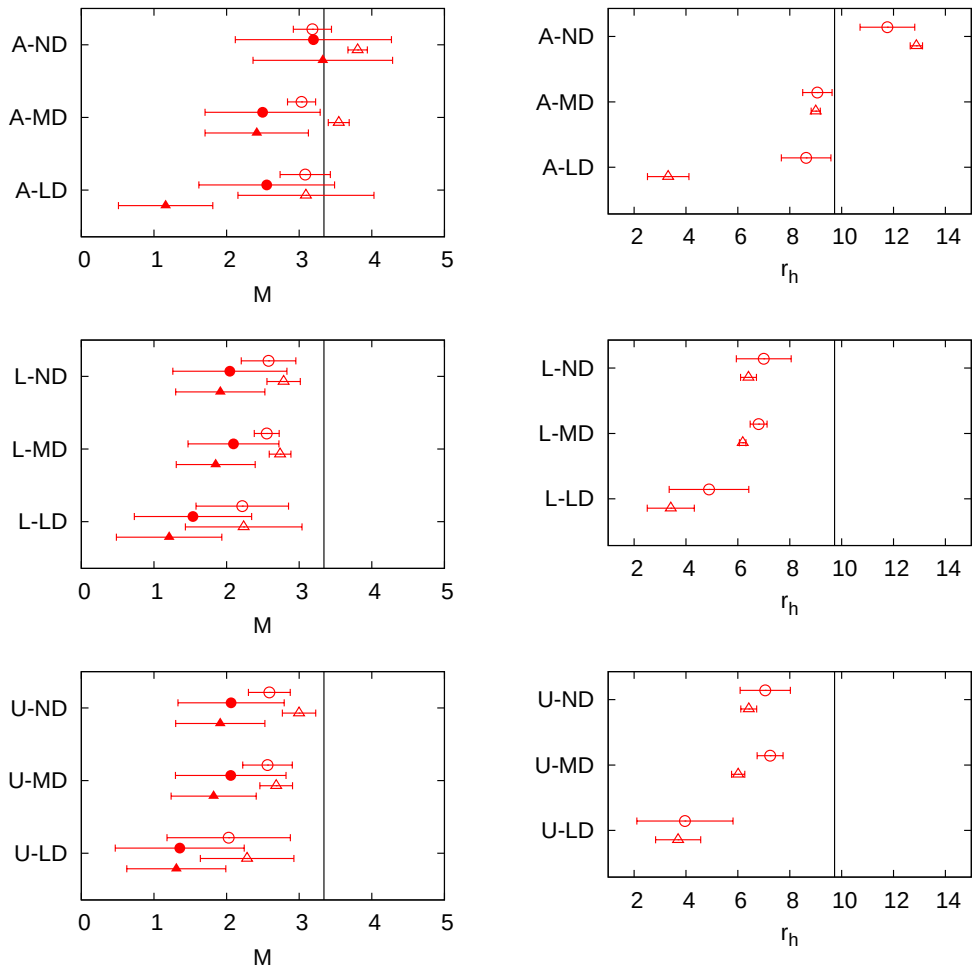

Figure 9.9: Mass and half-mass radius estimates (left and right panels, respectively) for case A, in which all the stars are considered (top panels), and for cases L and U, in which cuts in magnitude are operated (middle and bottom panels). In each panel, the horizontal axis represent the value of the considered quantity (in units of $10^4\ M_\odot$ for M, and of pc for r_h), and the vertical axis is used to label the different estimates obtained for that quantity. The true values of the total mass and of the half-mass radius of the systems are indicated by vertical solid lines in the panels. King model ($f^{(\nu)}$ model) estimates are given as empty circles (empty triangles), and the corresponding error bars are shown as horizontal lines. The values obtained when the velocity scale is determined by considering only the red giant branch stars are indicated as filled symbols in the left panels.

of the velocity scale, we also estimated the total mass of the cluster: even if σ_0 is rather stable, the derived values of the mass may change significantly, because they depend on structural parameters that are different when determined from different density profiles. Table 9.9 lists the values of these quantities.

An easier to read representation of the values of the mass and of the half-mass radius obtained from the fits is given by Fig. 9.9. By inspecting the figure, it is evident that when a cut in magnitude is operated and the faint stars in the cluster are rejected, the

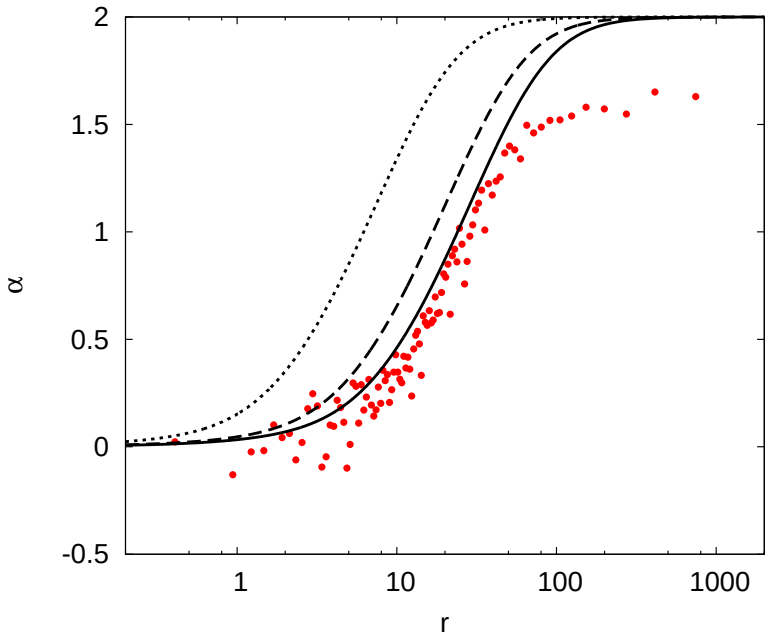

Figure 9.10: Comparison between the anisotropy profile calculated from the simulated stars (represented here with red dots) and the profiles predicted by the models. The solid line represents the anisotropy profile associated with the best-fit $f^{(\nu)}$ model obtained for the ND profile, the dashed line the one obtained for the MD profile, and the dotted line the one obtained for the LD profile.

estimated value for the total mass of the cluster decreases significantly. We thus may argue that in dealing with real data we tend to underestimate the total mass of clusters.

Contrary to what we found in Sect. 9.2, here the values of the half-mass radius change significantly when different profiles are used. This means that, in general, a subsample of stars does not give a good representation of a real system, unless some corrections are introduced to account for the effects noted in this Section.

Finally, we make one last check that confirms that indeed $f^{(\nu)}$ models provide a better description of the "observed" cluster, with respect to King models. We consider the best-fit models obtained in the case in which all the stars were used to calculate the profiles (A), and we study the corresponding intrinsic anisotropy profile $\alpha(r)$. Moreover, the information we have for the simulated stars allow us to calculate the same quantity for our "data" (for real data this is not usually possible, as explained in Sect. 3.2.3). In Fig. 9.10 we provide a comparison of these profiles. The "observed" anisotropy is represented by red dots; the solid line represents the anisotropy profile associated with the best-fit $f^{(\nu)}$ model obtained for the ND profile, the dashed line the one obtained for the MD profile, and the dotted line the one obtained for the LD profile. It is evident that the "observed" anisotropy profile is remarkably similar to the predicted ones, even if some discrepancies are observed. The simulated system appears to be isotropic in the center and radially anisotropic in the outermost parts, and therefore it conforms well to the anisotropic $f^{(\nu)}$ models.

CHAPTER 10

Global line profiles

The observed spectrum of a stellar system can be considered as the convolution of a suitably chosen template spectrum and a broadening function. This broadening function is commonly referred to as the line profile (Franx & Illingworth 1988; van der Marel & Franx 1993), and is dominated by the motions of the stars along the line of sight. Another contribution to the broadening of the observed spectrum is associated with the instrumental error of the measurement; this is usually approximated by a Gaussian function. Gaussian parametrizations of the instrumental broadening, of the line-of-sight velocity distribution, and therefore also of the observed line profiles, have been almost universally employed in the literature. Only with very accurate data a more detailed description is justified. In fact, there are situations in which the line-of-sight velocity distribution of a stellar system is not expected to be a Gaussian. The possibility to recover the true shape of the line-of-sight velocity distribution of a given system could be very important in the study of its dynamics.

The line-of-sight velocity distribution, as an observable, has been used to study the dynamics of elliptical galaxies (Tonry & Davis 1979; Bender 1990; Rix & White 1992; Cappellari & Emsellem 2004) and, more recently, of ultra compact dwarfs (see for example Frank et al. 2011, and references therein); we recall that this is analogous to the analyses of H I line profiles that have been carried out for a long time to probe the dynamics of spiral galaxies (see for example Tully & Fisher 1977). The observations that provide such information are usually carried out by means of slit spectroscopy: the slit includes a large part of the stellar system, for which a spectrum is obtained. This type of observations might then be possible for extragalactic globular clusters. A comparison with what we know about the Galactic globular clusters could give us important information on the dynamical evolution of these systems.

In this Chapter we describe a study that we performed to test if it is possible to detect the expected differences in the line-of-sight velocity distributions of systems in different dynamical conditions, by means of accurate spectroscopic observations. In particular, we test if the presence of rotation leads to line profiles with specific signatures.

The Chapter is organized as follows. In Sect. 10.1 we outline the method used. In Sect. 10.2 we describe the procedure used to calculate the line-of-sight velocity distributions for three clusters, by means of three different models. In Sect. 10.3 we summarize our results.

10.1 Method and objectives

We decided to consider the three Galactic globular clusters studied in Chapter 6, that is, 47 Tuc (NGC 104), M15 (NGC 7078), and ω Cen (NGC 5139). We calculated the ex-

pected shape of their line-of-sight velocity distributions for each of three available models: spherical isotropic King (1966) and Wilson (1975) models, and non-spherical rotating models (Varri & Bertin 2012, see Appendix A for details on these models).

The three clusters have been chosen as prototypes for this test, because in our Galaxy they are the ones for which the largest data-sets are available, and for which a detailed analysis by means of rotating models has been made. Isotropic King and rotating models have been chosen for this test because they describe systems that are structurally very different, and for which we may anticipate that the line-of-sight velocity distributions should be distinguishable from each other. In addition, spherical nonrotating Wilson models have been added to this analysis, because they are somewhat intermediate between the other two: they are isotropic like King models, and they have the same truncation prescription used for the rotating models.

In order to properly compare line-of-sight velocity distributions calculated for the three different models for the three clusters, we proceeded as follows.

1. We carried out fits to the surface brightness and velocity dispersion profiles, as described in Sect. 3.3 (see also Chapters 4 and 6); the best-fit parameters determined in this way define the models that better represent the observations.
2. Once the model parameters have been determined, we sampled the corresponding distribution functions.
3. We then calculated the line-of-sight velocity distributions and scaled them by means of the velocity scale determined by the fits.
4. We convolved the line-of-sight velocity distributions with a Gaussian function, to simulate the effect of the measurement errors.

The best-fit parameters[1] are listed in Table 10.1.

10.2 Calculation of the line profiles

Considering models defined by a distribution function $f(\mathbf{x}, \mathbf{v})$, for a particular line of sight through the system the line-of-sight distribution function $l(\mathbf{x}_\perp, v_\parallel)$ is calculated as:

$$l(\mathbf{x}_\perp, v_\parallel) = \frac{\int f(\mathbf{x}, \mathbf{v})\, d^2 v_\perp\, dx_\parallel}{\int f(\mathbf{x}, \mathbf{v})\, d^3 v\, dx_\parallel}\,, \tag{10.1}$$

where the subscript $\parallel$ indicates the components along the line of sight, and the subscript $\perp$ those on the plane of the sky. We note that the integral at the denominator of the fraction is the projected mass density (see Eq. (2.16)) of the system. In this Chapter, we consider the global line-of-sight velocity distribution, calculated for the entire system; it can be expressed as:

$$\mathscr{L}(v_\parallel) = \int f(\mathbf{x}, \mathbf{v})\, d^2 v_\perp\, d^3 x\,. \tag{10.2}$$

We notice that, by integrating this function over the velocity component $v_\parallel$, we obtain the mass of the system. In the following we will drop the subscript, and indicate this function simply as $\mathscr{L}(v)$.

[1] The values of these quantities obtained for King and rotating models were also listed in Tables 4.2, 4.5 and 6.3. In the case of the rotating models, we adopted for the masses the values listed in Table 6.6, because they have been calculated by assuming for each cluster the value of the distance that was also used to calculate the masses of the other models.

Table 10.1: Model parameters and physical scales.

Globular cluster	Model (1)	Ψ (2)	r_0 (3)	σ_0 (4)	$V_{\rm rot}^{\rm max}$ (5)	M (6)
47 Tuc	K	8.58	23.10	12.27	...	7.18
	W	7.40	28.21	13.36	...	6.59
	R	7.60	24.41	13.35	3.26	6.76
M 15	K	8.09	7.72	11.83	...	3.98
	W	7.10	11.84	11.65	...	4.11
	R	6.80	13.33	12.52	3.00	4.49
ω Cen	K	6.27	136.85	14.83	...	26.45
	W	4.88	181.54	15.46	...	26.19
	R	5.80	134.54	15.87	5.80	24.71

Notes. For each cluster we list: the concentration parameter Ψ in Col. (2), the scale radius r_0 in arcsec in Col. (3), the central velocity dispersion in km s^{-1}in Col. (4), the maximum of the line-of-sight rotation profile $V_{\rm rot}^{\rm max}$ in km s^{-1}in Col. (5), and the estimated total mass of the cluster in units of 10^5 $M_\odot$ in Col. (6). In Col. (1) we indicate the family of models used to derive the parameters: K indicates King (1966) models, W Wilson (1975) isotropic nonrotating models, and R rotating models (Varri & Bertin 2012).

After selecting a model in each family by means of the fitting procedure described in the previous Section, we proceed to calculate the related line-of-sight velocity distribution. For the non-spherical rotating models it is particularly difficult to define the projections and to calculate the necessary integrals, so we decided to use an alternative "numerical" method. This procedure is applied to the three models, to calculate the profiles in a uniform way. Therefore, we start by sampling the distribution functions and by calculating the relevant profiles from the obtained discrete samples of points. In the remaining of this Section, we describe in detail the steps that have been followed.

10.2.1 Sampling of a distribution function

The procedure used to generate a sample of points from a distribution function can be summarized in two steps. First, we start by sprinkling the particles in space, as a random realization of the mass density distribution of the model; at this stage, it is important to carefully determine the radial positions of the particles with the appropriate statistical weight. Secondly, we give each particle a velocity with random direction and magnitude, but drawn from the appropriate velocity distribution at that point in space. The order of these two steps is important: only after the position of a particle in space is known, is it possible to determine the potential energy of that particle, and which velocities are admissible in order to keep the particle bound, and to assign to each velocity the correct statistical weight.

The details given below refer to the procedure used to sample the distribution functions of the spherical models, but this method can be generalized and applied also to the non-spherical models.

Sprinkling particles in space

We define the cumulative mass of the cluster as

$$m(r) = \int_0^r dr\, 4\pi r^2 \rho(r) \,, \tag{10.3}$$

where ρ is the mass density of the cluster, and is calculated from Eq. (2.8). The fractional mass contained within radius r is defined as

$$\hat{m}(r) = \frac{m(r)}{M} \,, \tag{10.4}$$

where M is the total mass of the cluster; based on this definition, the fractional mass $\hat{m}$ takes values between 0 and 1 (at the center and at the truncation radius, respectively).

To sample points that are distributed in radius according to the cumulative mass function, we spin a random number generator to obtain a random number $\hat{m}_i$, with $0 \leq \hat{m}_i \leq 1$, and we consider it to be the fractional mass contained within the radius r_i of the particle i, so that $\hat{m}(r_i) = \hat{m}_i$. Since we want to know r_i, we need to invert $\hat{m}(r)$ to obtain a function $r(\hat{m})$, so that we can calculate the needed radius as $r_i = r(\hat{m}_i)$. We then generate two additional random numbers, k_1 and k_2, that are used to calculate the angles $\phi = 2\pi k_1$ and $\theta = \arccos(1 - 2k_2)$; with these, we can finally calculate the three spatial coordinates:

$$x = r \sin\theta \cos\phi \tag{10.5}$$

$$y = r \sin\theta \sin\phi \tag{10.6}$$

$$z = r \cos\theta \tag{10.7}$$

At this point, we have generated the first three coordinates of the particle in the phase space.

Assigning a velocity vector to each particle

After calculating the potential energy at the radial position determined in the previous step, we calculate the maximum value that is possible to assign to the velocity magnitude, that is, the escape velocity:

$$v_{\rm escape} = \sqrt{-2\psi(r)} \,. \tag{10.8}$$

If the distribution function is isotropic, the probability distribution for the velocities at given radius can be calculated as:

$$g(v)dv \propto v^2 f(r, v), \tag{10.9}$$

where $f(r, v)$ is the distribution function of the considered model. We also calculate the maximum of this probability distribution, $g_{\rm max}$.

At this point, we generate the velocities by means of rejection techniques. We generate a random number v_i uniformly in the interval between 0 and $v_{\rm escape}$. We generate another random number k (such that $0 \leq k \leq 1$); if $k < g(v)/g_{\rm max}$ we keep the generated velocity, otherwise we reject v_i, and we repeat this step by generating another v_i. The normalization factor of $g_{\rm max}$ used in this procedure ensures that the acceptance probability $g(v)/g_{\rm max}$ has a maximum value of one, which makes the algorithm as efficient as

possible. We can calculate the three velocity components by analogy with the treatment of the spatial coordinates.

To check that the generated points are actually distributed according to the adopted distribution function, we calculated the density and velocity dispersion profiles (both intrinsic and projected) from the generated points, and we compared them with those calculated directly by integrating the distribution function.

10.2.2 The line-of-sight velocity distribution

To calculate the line-of-sight velocity distribution we are interested in, we will consider all the stars in the sample. We do not calculate this function in correspondence of a specific radius, because a very large number of generated point would be needed to carry out a similar analysis: in fact, we would need to select only the stars located within a defined and narrow radial range, and to calculate the line-of-sight velocity distribution only for this subsample of stars, and we would need the chosen radial range to be well populated, in order to calculate the function. For the moment, therefore, we just considered the case in which the line profile is calculated for the entire system, which is the normal case to be considered first in actual observations.

We assume the line-of-sight direction to be parallel to the x axis. We consider the velocity component $v_{\rm x}$, and we divide the velocity range into equal-size bins. Finally, we calculate the line-of-sight velocity distribution by counting the number of stars that fall into each bin. The function thus obtained depends on the dimensionless velocities determined by the models, and its normalization is determined by the total number of stars.

Physical scales for the different models

In order to obtain line-of-sight velocity distributions that represent the real clusters, we need to scale the functions by using the velocity scales obtained by the fits. We thus obtain a function that describes how the velocities expressed in km $s^{-1}$are distributed in the systems.

Moreover, we need to introduce an appropriate normalization, to allow for an adequate comparison of the different cases: in fact, in principle, the line-of-sight velocity distribution can be calculated starting from a different number of generated points, and by using a different number of bins in the velocity. We chose to normalize the line-of-sight velocity distribution calculated for a specific model so that the area under the curve is equal to the total mass calculated by that model for the cluster[2].

Figure 10.1 shows the line-of-sight velocity distributions $\mathscr{L}(v)$ calculated for 47 Tuc, M15, and ω Cen (from top to bottom, respectively), and scaled as described. In each panel, the red line represents the function calculated by means of King models, the blue line the one calculated by nonrotating isotropic Wilson models, and the black line the one by rotating models.

By looking at Fig. 10.1, it is possible to identify the main characteristics of the line-of-sight velocity distribution for the three different models. The function $\mathscr{L}(v)$ is similar for the two isotropic models, but a careful inspection reveals that for Wilson models (blue lines) the function is steeper. For the rotating models, the double peak characteristic of rotation is visible.

[2]Another possibility would be to scale the models so that they all have the same mass: this has been checked, but the results do not change significantly.

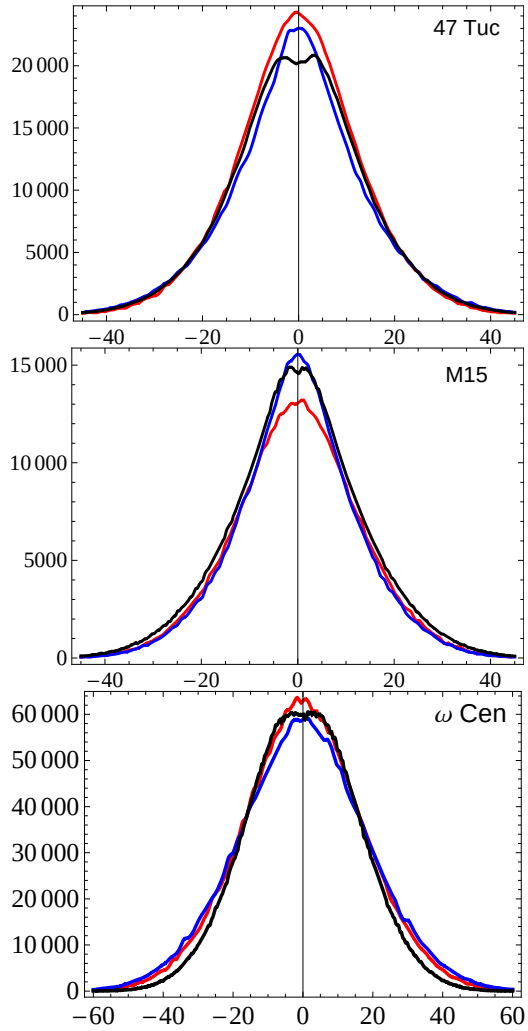

Figure 10.1: Line-of-sight velocity distributions calculated for 47 Tuc, M15, and ω Cen (from top to bottom, respectively). Each function has been scaled as described in the main text. The velocities are expressed in km s^{-1}. In each panel, the red line represent the function calculated by means of King models, the blue line the one calculated by nonrotating isotropic Wilson models, and the black line the one calculated by rotating models.

10.2.3 Convolution with a Gaussian function to simulate the observational errors

To simulate the effects introduced by measurement errors, we carried out a convolution of the line-of-sight velocity distribution, $\mathscr{L}(v)$, with the Gaussian:

$$G(v) = \frac{1}{\sqrt{2\pi}\sigma_{\rm v}} \mathrm{e}^{-v^2/(2\sigma_{\rm v}^2)} \ . \tag{10.10}$$

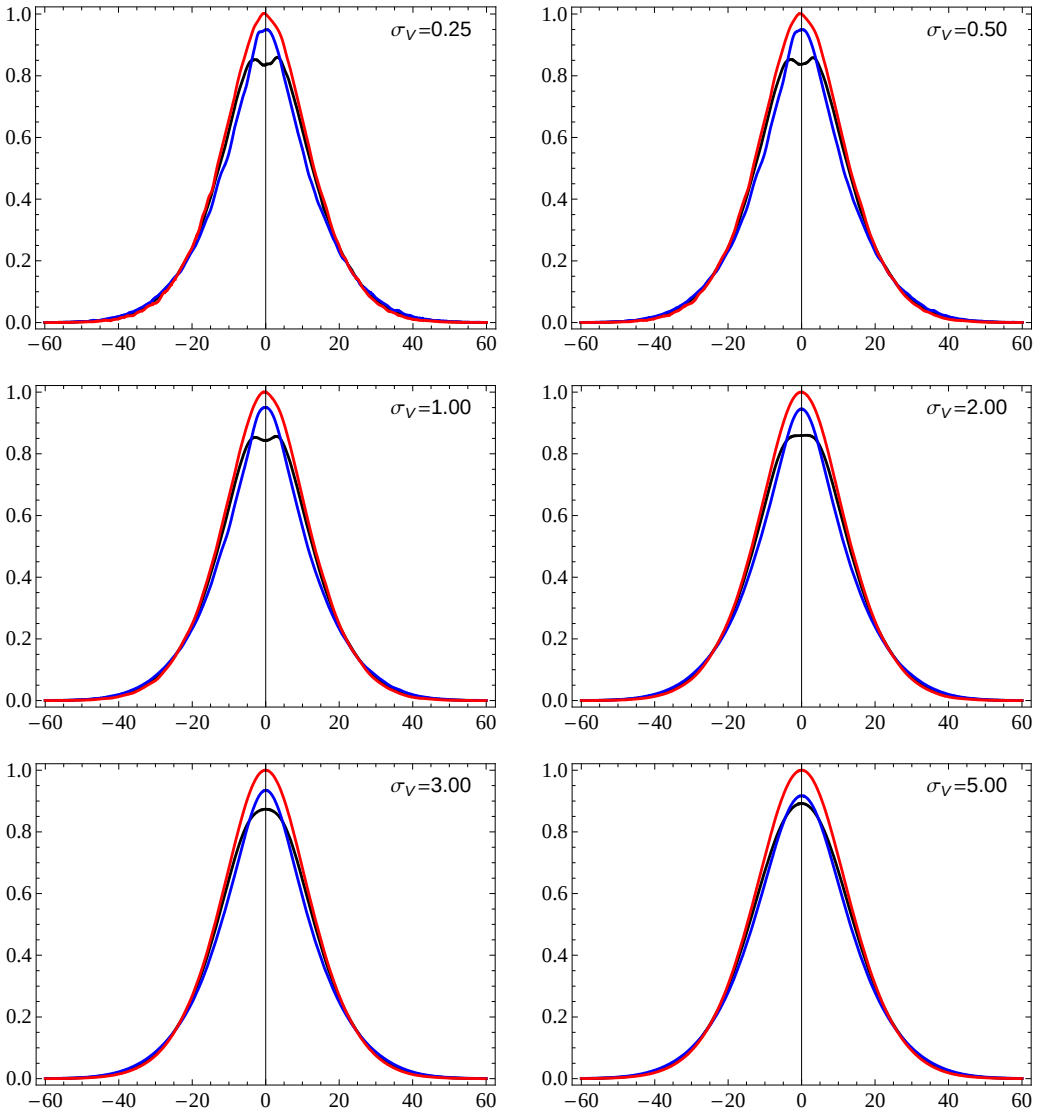

Figure 10.2: Line profiles calculated for 47 Tuc as the convolution between the line-of-sight velocity distribution and the Gaussian that represents the measurement error. The values of the parameter σ_v of the Gaussian are 0.25, 0.5, 1, 2, 3, and 5 km s^{-1}, from left to right and from top to bottom. The velocities are expressed in km s^{-1}; in each panel, the red line represent the function calculated by means of King models, the blue line the one calculated by Wilson models, and the black line the one calculated by rotating models.

We express the convolution as:

$$C(v) = \int_{-\infty}^{+\infty} \mathscr{L}(u)G(v-u)du \; . \tag{10.11}$$

We explored the effect of this convolution on the shape of the calculated line profiles

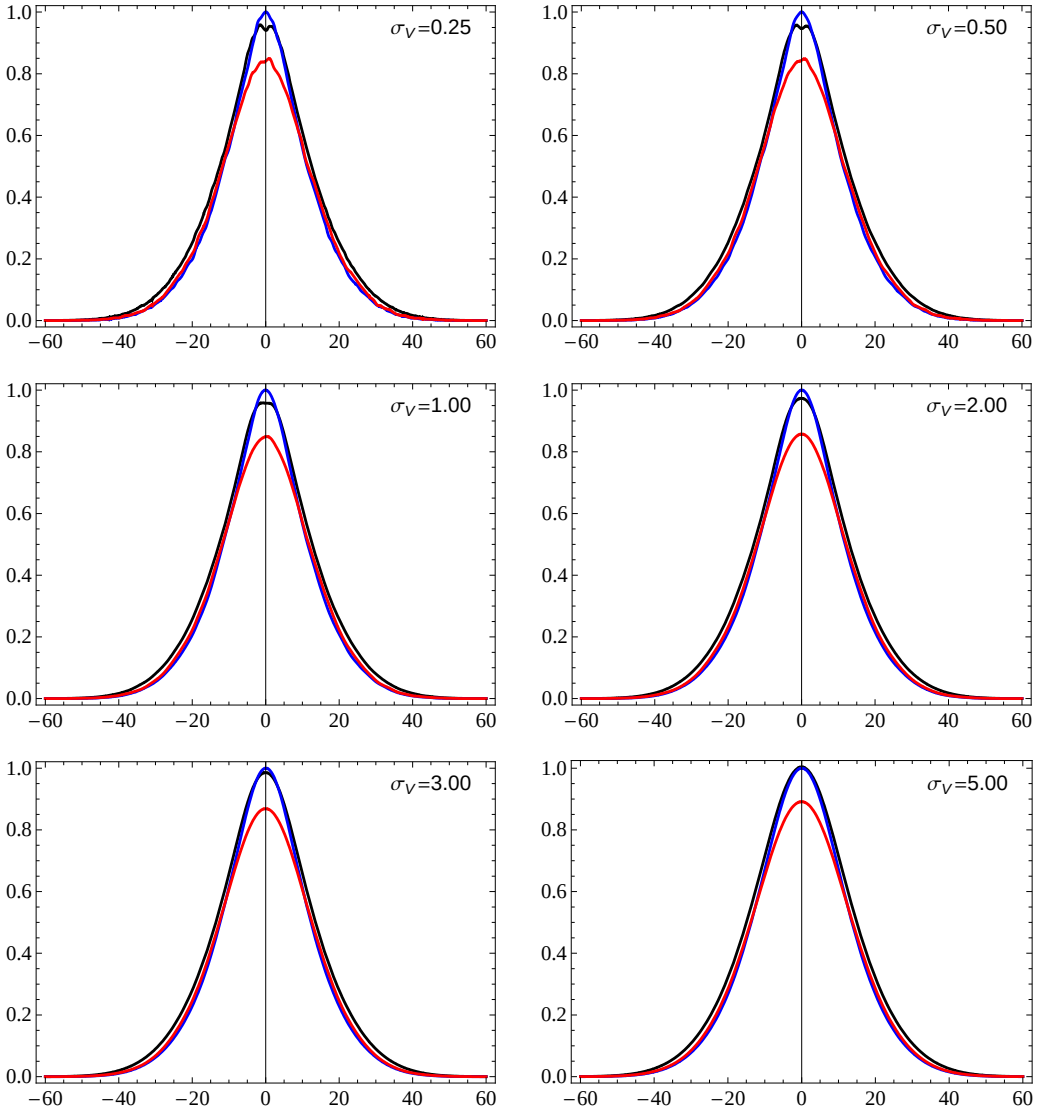

Figure 10.3: Line profiles calculated for M15 as the convolution between the line-of-sight velocity distribution and the Gaussian that represents the measurement error. The format is the same used in Fig. 10.2.

by changing the value of the parameter σ_v in the Gaussian that represents the measurement error: we present our results in the next Section.

10.3 Results and discussion

Figures 10.2, 10.3, and 10.4 show the functions $C(v)$ calculated for 47 Tuc, M15, and ω Cen, respectively. In each of the panels shown in these figures, we represent the functions $C(v)$ after dividing them by the same factor so that the peak of one of them is

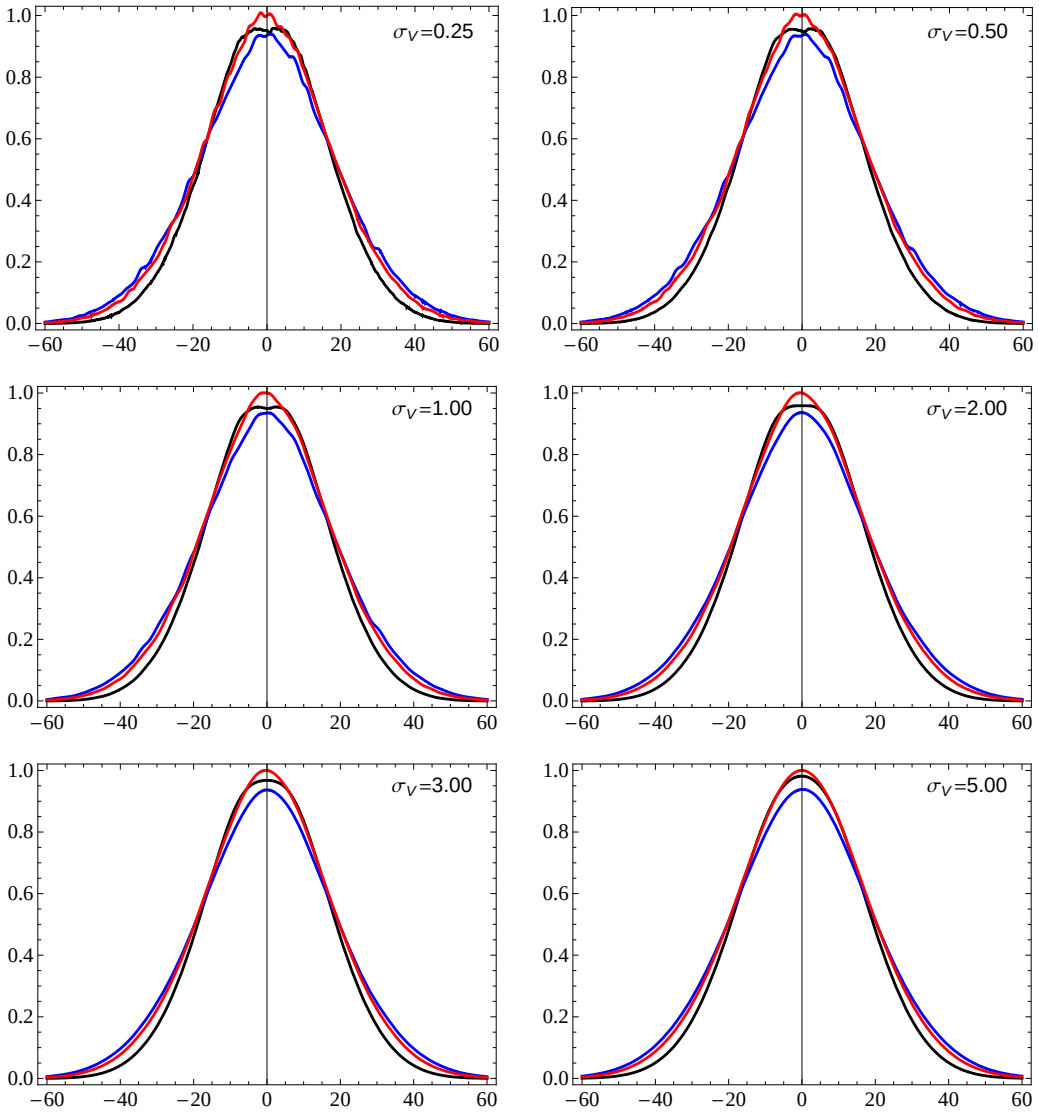

Figure 10.4: Line profiles calculated for ω Cen as the convolution between the line-of-sight velocity distribution and the Gaussian that represents the measurement error. The format is the same used in Fig. 10.2.

normalized to unity. This allows for an easier comparison of the functions obtained for different values of $\sigma_{\rm v}$. In each figure, the values of the parameter $\sigma_{\rm v}$ of the Gaussian are 0.25, 0.5, 1, 2, 3, and 5 km s^{-1}, from left to right and from top to bottom, as indicated on each panel. The red lines represent the function calculated by means of King models, the blue lines the ones calculated by nonrotating isotropic Wilson models, and the black lines the ones by rotating models.

We thus see that the characteristic double peak found in the line-of-sight velocity distribution of the rotating model is completely smoothed away for $\sigma_{\rm v} \geq 2$ km s^{-1}.

For M15, this feature is hardly visible also for lower values of $\sigma_{\rm v}$. For ω Cen, we see that before reaching a value of $\sigma_{\rm v}$ that makes this feature disappear, a flattening in the function $C(v)$ of rotating models is clearly apparent (the curve becomes "squarish"). In any case, for $\sigma_{\rm v} \geq 2$ km s^{-1} the functions $C(v)$ calculated for the three different models are no longer distinguishable.

These results show that, unfortunately, this tool is not particularly promising in applications to the study of the dynamics of globular clusters. For these systems, the internal dynamics can be reasonably well described by means of the models considered in this analysis. In this Chapter we showed that even if the models are structurally different, the expected line profiles are very similar, and the characteristic features could be identified, with some difficulty, only by means of extremely accurate data.

Nonetheless, the line-of-sight velocity distribution may turn out to be a useful tool to exclude some models with peculiar phase-space structure that sometimes are invoked in studies based on pure orbit analysis (e.g., of features interpreted in terms of the presence of central black holes).

Future directions

Starting from the detailed study of the dynamics of globular clusters presented in this Thesis, a number of projects can be imagined, as a natural extension of the line of research followed so far. In particular, the following issues will be addressed in the near future:

Study of the morphology of globular clusters by means of ellipticity profiles: In this Thesis we addressed the issue of determining the cause of the significant deviations from spherical symmetry (White & Shawl 1987; Chen & Chen 2010) that are observed for globular clusters, by determining which dynamical ingredient (among tides, pressure anisotropy, and rotation) account for the observed morphology. We focused on pressure anisotropy and rotation and found that the available data are often not adequate for the purpose. To properly test different dynamical scenarios, we therefore plan to extend the currently available ellipticity profiles of globular clusters, by means of archival data and new observations. In fact, in only very few cases the existing profiles cover a large portion of the radial extent of the clusters. We also plan to obtain isophotal contours for Galactic clusters, to properly characterize the deviations from symmetry. These data will be used in combination with kinematical data, to provide a more detailed description of these systems.

Determining the importance of tidal interactions: Among the dynamical ingredients that can be considered responsible for the observed morphology of globular clusters, we did not consider tidal interactions with the external tidal fields: we plan to explore the role of this important factor in the future. The three-dimensional external tidal field should induce a stretching along the direction pointing toward the center of the host galaxy (van den Bergh 2008). The tidal field might also induce the preferential loss of stars on radial orbits, which would lead to a tangentially-biased anisotropy in velocity space especially in the outer parts of the system (Baumgardt & Makino 2003). A new family of models, in which the external tidal field is taken into account in a self-consistent way, has been proposed recently (Bertin & Varri 2008; Varri & Bertin 2009) and will be employed to study the importance of tidal effects.

Unique signatures of the presence of intermediate-mass black holes: Despite the great observational effort devoted to it (see Lützgendorf et al. 2013b, and references therein), conclusive evidence for the existence of intermediate-mass black holes in globular clusters is still lacking (for example, see Vesperini & Trenti 2010). Model degeneracy is currently limiting progress in this field; we plan therefore to look for features (observable with currently available telescopes) that could discriminate between the effects produced by an intermediate-mass black hole on the dynamics of

the entire system and those generated by other dynamical factors. To do this, we plan to carry out dedicated N-body simulations with and without a central black hole, and to identify the best signature that should be looked for in observations to confirm the presence of intermediate-mass black holes in globular clusters, or to rule it out completely. By considering different initial conditions for the simulations, we also plan to determine whether the clusters with an intermediate-mass black hole evolve towards a similar configuration, or not.

Quantifying the presence of mass segregation in globular clusters: We plan to use accurate and radially extended kinematical measurements to determine the cumulative and local dynamical mass-to-light ratio profiles of globular clusters, and therefore the detailed distribution of matter. We will study the observations by means of multi-mass dynamical models and by comparing them with dedicated N-body simulations. Hence, the results will be compared with the mass-to-light ratio distribution expected from studies of stellar populations, opening the way to address the important issue of the presence of mass segregation. By analyzing the mass-to-light ratio radial profile, we will quantify to what extent dynamical models with multiple mass components are required.

Dark matter in small stellar systems: Globular clusters are usually considered to be simple stellar systems, free of dark matter. However, only accurate and radially extended kinematical measurements can give a definitive proof that dark matter is negligible for these systems: we plan to address this issue in future investigations. A similar study is also planned for ultra-compact dwarf galaxies, which show high dynamical mass-to-light ratios that can be explained by some kind of unseen matter, either dark matter, or an intermediate-mass black hole, or massive stellar remnants from a top-heavy initial mass function (Mieske et al. 2008). The results collected by the planned dynamical studies of individual systems in the different classes will serve as important empirical clues for the general problem of cosmological interest of understanding the mechanisms at the basis of the formation and evolution of these stellar systems. We recall that in this context, globular clusters have already been considered as interesting targets to test non-standard dynamical frameworks (in particular, see the recent test of Modified Newtonian Dynamics performed on NGC 2419 by Ibata et al. 2011).

Appendices

APPENDIX A

Definition of some dynamical models

A.1 Spherical isotropic King models

The King (1966) one-component, spherical, isotropic models are based on the following distribution function:

$$f_{\rm K} = \begin{cases} A\left[\exp(-aE) - \exp(-aE_0)\right] & E \leq E_0 \\ 0 & E > E_0 \end{cases} , \tag{A.1}$$

where A, a, E_0 are positive constants, defining two scales and one dimensionless parameter, and E represents the specific energy $E = v^2/2 + \Phi(r)$, where $\Phi(r)$ is the mean-field gravitational potential, to be determined from the Poisson equation. The quantity E_0 is a threshold energy, above which the stars are considered unbound; it can be translated into a truncation radius, $r_{\rm tr}$, for the system, considering that $E_0 = \Phi(r_{\rm tr})$.

We recall that a radial scale r_0 can be defined as

$$r_0 = \left(\frac{9}{4\pi G a \rho_0}\right)^{1/2} , \tag{A.2}$$

where ρ_0 is the central mass density. The other dimensional scale is the total mass of the cluster or, as an alternative, its central velocity dispersion.

By introducing the dimensionless potential $\psi(r) = a[\Phi(r_{\rm tr}) - \Phi(r)]$, the escape velocity is a function of radius that can be expressed as $v_{\rm escape} = \sqrt{2\psi/a}$. The dimensionless concentration parameter is given by the central dimensionless potential $\Psi = \psi(0)$ or, alternatively, by the index

$$c = \log\left(\frac{r_{\rm tr}}{r_0}\right) , \tag{A.3}$$

because these two quantities are in a one-to-one relation.

The quantity listed in the Harris (2010) catalog as concentration parameter, in this Thesis indicated with C, is defined using the standard core radius $R_{\rm c}$ in place of r_0 in Eq. (A.3). The values of C for a model identified by $\Psi \gtrsim 4$ are slightly larger than the corresponding values of c; in fact, for these models $0.8 \lesssim R_{\rm c}/r_0 \lesssim 1$.

The mass density and the velocity dispersion are calculated from the distribution function by means of Eq. (2.8) and Eq. (2.11), respectively:

$$\rho[\psi(r)] = \hat{A}\, {\rm e}^{\psi}\, \gamma\left(\frac{5}{2}, \psi\right) \tag{A.4}$$

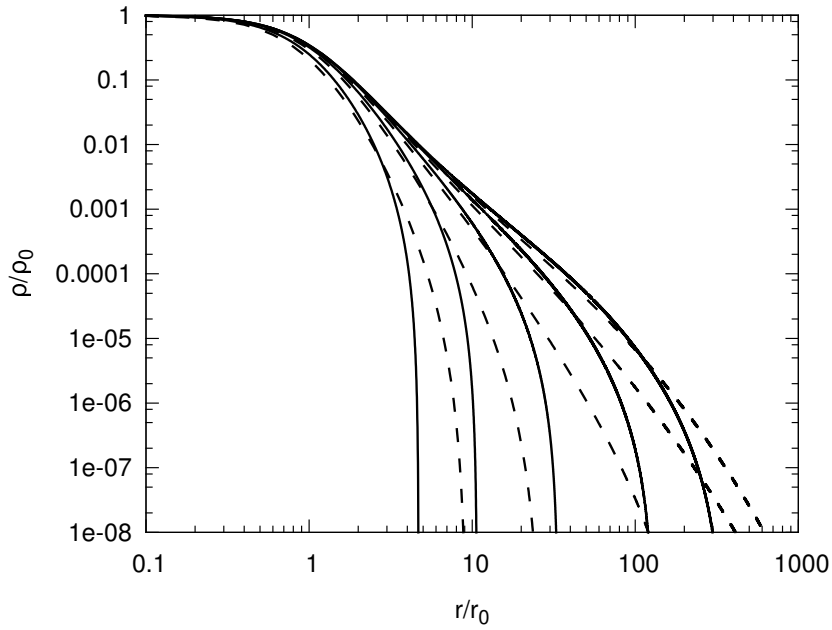

Figure A.1: Normalized mass density as a function of the dimensionless radius for King (solid lines) and spherical Wilson (dashed lines) models characterized by $\Psi = 3, 5, 7, 9, 11$ (from left to right).

$$\sigma^2[\psi(r)] = \frac{6}{5a}\,\frac{\gamma\,(7/2,\psi)}{\gamma\,(5/2,\psi)}\,, \tag{A.5}$$

where γ is the incomplete gamma function (see Abramowitz & Stegun 1972), $\hat{A}$ is a constant, and σ^2 is the squared (total) velocity dispersion. From the previous equations it is evident that the density and the velocity dispersion depend on the radial coordinate only implicitly, through the dimensionless potential.

A.2 Spherical isotropic Wilson models

Wilson (1975) modified the distribution function by including a dependence on the angular momentum, to generate axisymmetric models to describe elliptical galaxies. By reducing his distribution function to the spherical limit, the following distribution function, dependent only on the energy E is obtained:

$$f_{\rm W}(E) = \begin{cases} A\,\{\exp(-aE) - \exp(-aE_0)[1 - a(E - E_0)]\} & E \leq E_0 \\ 0 & E > E_0\ . \end{cases} \tag{A.6}$$

This distribution function defines one-component, spherical and isotropic models. In this Thesis, we refer to these models as "spherical Wilson models", by following the notation used by McLaughlin & van der Marel (2005).

For these models, a radial scale r_0 and a concentration parameter c can be defined in the same way as for the King models (Eqs. A.2 and A.3). By analogy to King models, in

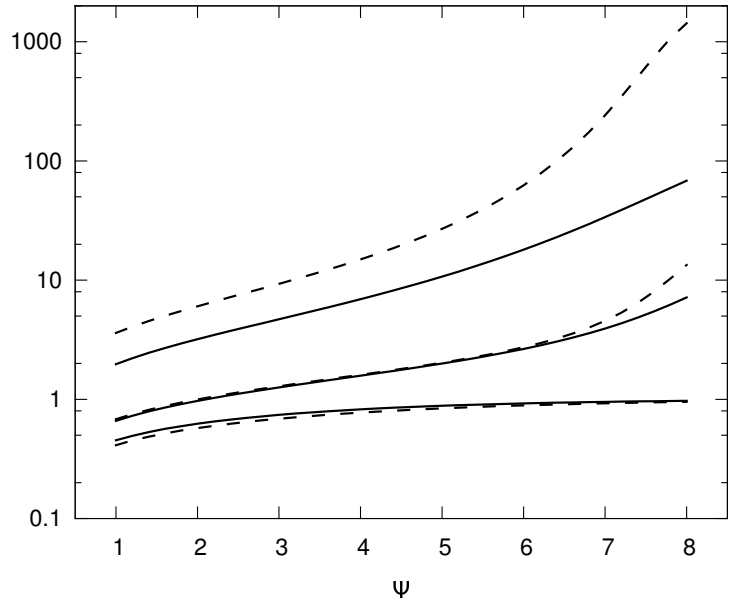

Figure A.2: Relation between relevant radii and the concentration parameter Ψ for King (solid lines) and spherical Wilson (dashed lines) models. From bottom to top, the lines represent the dimensionless core radius $R_{\rm c}/r_0$, the dimensionless half-mass radius $r_{\rm M}/r_0$, and the dimensionless truncation radius $r_{\rm tr}/r_0$ (see Sect. 1.1 for a definition of these quantities).

this case the mass density and the velocity dispersion profiles can be written as:

$$\rho[\psi(r)] = \hat{A}\,\mathrm{e}^{\psi}\,\gamma\left(\frac{7}{2},\psi\right) \tag{A.7}$$

$$\sigma^2[\psi(r)] = \frac{6}{7a}\,\frac{\gamma\,(9/2,\psi)}{\gamma\,(7/2,\psi)}\,, \tag{A.8}$$

where γ is the incomplete gamma function and $\hat{A}$ is a constant. As in the case of King models, the density and the velocity dispersion depend on the radial coordinate only implicitly, through the dimensionless potential.

The main difference with respect to King (1966) models is in the adopted truncation prescription: models defined by Eq. (A.6) are similar to King models in the core, but have a larger (but still finite) radial extent. This is shown in Fig. A.1, where intrinsic density profiles for five models of the two families are compared: in each case, the Wilson profiles have a larger radial extent with respect to the corresponding King models with the same concentration parameter Ψ. Figure A.2 shows the values taken by the dimensionless core, half-mass, and truncation radius as a function of Ψ. Remembering that c is defined by Eq. (A.3), the difference found in the relation between $r_{\rm tr}/r_0$ and Ψ indicates that the one-to-one relation between Ψ and c for the two families of models is different.

A.3 Anisotropic $f^{(\nu)}$ models

Several families of dynamical models have been developed to represent the final state of numerical simulations of the violent relaxation process thought to be associated with the formation of bright elliptical galaxies via collisionless collapse (for a review, see Bertin & Stiavelli 1993). These models show a characteristic anisotropy profile, with an inner isotropic core and an outer envelope dominated by radially-biased anisotropic pressure. They provide a good representation of the photometric and kinematic properties of elliptical galaxies. Here we will refer to the family of spherical, anisotropic, non-truncated $f^{(\nu)}$ models (which have been revisited recently in detail by Bertin & Trenti 2003).

The distribution function that defines these models depends on specific energy E and angular momentum J:

$$f^{(\nu)} = \begin{cases} A \exp\left[-aE - d\left(\frac{J^2}{|E|^{3/2}}\right)^{\nu/2}\right] & E \leq 0 \\ 0 & E > 0 \ , \end{cases} \tag{A.9}$$

where A, a, d, and ν are positive constants, defining two scales and two dimensionless parameters. For applications, as described by Bertin & Trenti (2003), the dimensionless parameter ν can be fixed at $\nu = 1$. Therefore, similarly to the King models, after integration of the relevant Poisson equation the $f^{(\nu)}$ models are a one-parameter family of models, parametrized by their central concentration, which can be expressed by the central dimensionless potential $\Psi = -a\Phi(0)$. The physical scales can be expressed as:

$$\begin{aligned} r_0 &= d^{-1/\nu} a^{-1/4} \\ M_0 &= d^{-3/\nu} a^{-9/4} \ . \end{aligned} \tag{A.10}$$

To calculate the mass density, the dimensionless Poisson equation

$$\frac{1}{\hat{r}^2}\frac{d}{d\hat{r}}\left(\hat{r}^2 \frac{d\psi}{d\hat{r}}\right) = -\frac{1}{\Gamma}\hat{\rho}(\hat{r}, \psi) \ , \tag{A.11}$$

where $\psi = -a\Phi$, $\hat{r} = r/r_0$ and $\hat{\rho} = \rho\, r_0^3/M_0$, is solved by assuming the boundary conditions $\psi(\hat{r} = 0) = \Psi$ and $\psi'(\hat{r} = 0) = 0$, and by considering $\Gamma = \Gamma(\Psi)$ as an eigenvalue, to be determined so that $\psi \sim \hat{r}^{-1}$ for large $\hat{r}$. The mass density depends on the radial coordinate both explicitly and implicitly, through ψ; it can be calculated numerically by means of the following expression:

$$\rho(\hat{r}, \psi) = \frac{2\pi A}{\mathrm{e}^{\psi}} \left(-\frac{2\psi}{a}\right)^{3/2} \int_0^{\pi} \int_0^1 \mathrm{e}^{B(k,\theta)} k^2 \sin\theta \, dk d\theta \ , \tag{A.12}$$

where

$$B(k, \theta) = k^2\psi - \frac{\hat{r}^{\nu} \left(k \sin\theta\right)^{\nu} 2^{\nu/2}}{(-\psi)^{\nu/4} \left(1 - k^2\right)^{3\nu/4}} \ , \tag{A.13}$$

$k = v\sqrt{a/2\psi}$, and the angular momentum is expressed as $J^2 = r^2 v^2 \sin^2\theta$. The intervals of integration are determined by the condition on the vanishing of the distribution function and by the choice of spherical coordinates. An example of the mass density profiles obtained for these models is shown in Fig. A.3; by inspecting the figure, it is possible to notice that at large radii the profiles all have the same slope $\sim \hat{r}^{-4}$.

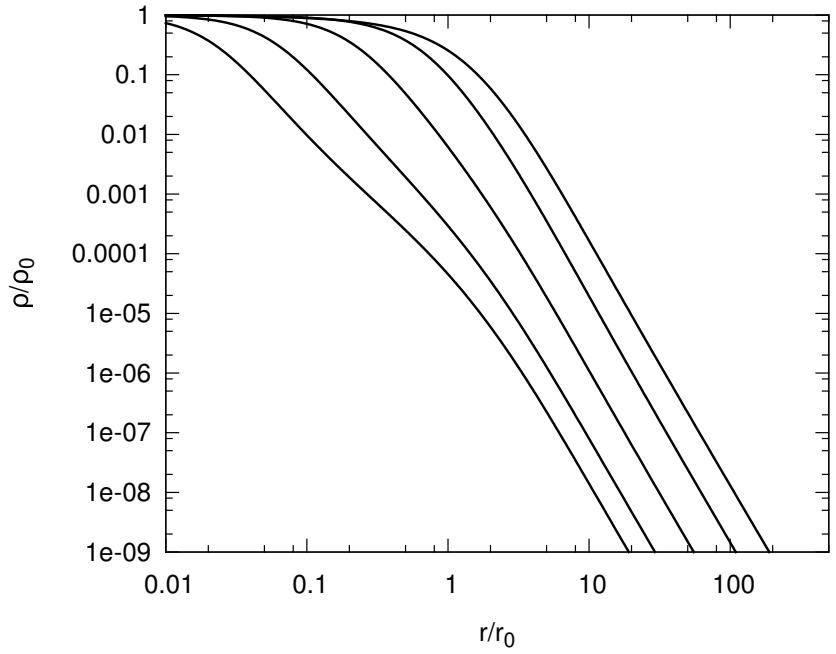

Figure A.3: Normalized mass density as a function of the dimensionless radius for $f^{(\nu)}$ models characterized by $\Psi = 3, 5, 7, 9, 11$ (from top to bottom).

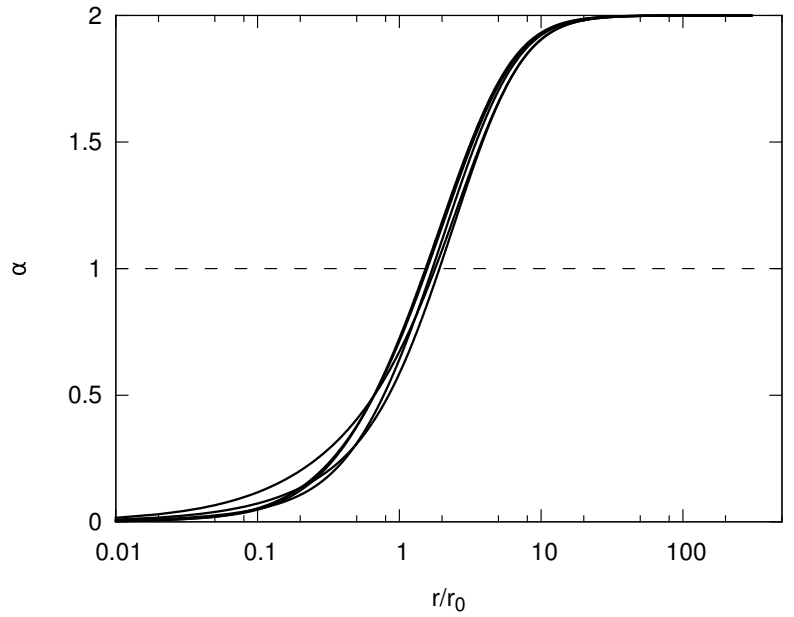

Figure A.4: Anisotropy profile as a function of the dimensionless radius for $f^{(\nu)}$ models characterized by $\Psi = 3, 5, 7, 9, 11$.

The radial and tangential components of the velocity distribution are calculated as:

$$\sigma_{\rm r}^2(\hat{r},\psi) = \frac{1}{\rho(\hat{r},\psi)}\frac{2\pi A}{{\rm e}^{\psi}}\left(-\frac{2\psi}{a}\right)^{5/2}\int_0^{\pi}\int_0^1 {\rm e}^{B(k,\theta)}k^4\cos^2\theta\sin\theta\,dkd\theta \tag{A.14}$$

and

$$\sigma_{\rm t}^2(\hat{r},\psi) = \frac{1}{\rho(\hat{r},\psi)}\frac{2\pi A}{{\rm e}^{\psi}}\left(-\frac{2\psi}{a}\right)^{5/2}\int_0^{\pi}\int_0^1 {\rm e}^{B(k,\theta)}k^4\sin^3\theta\,dkd\theta\ , \tag{A.15}$$

respectively. These quantities are used to calculate the anisotropy function α, defined in Eq. (2.19). For every model in this family, two particular types of behavior are found, in agreement with the expectations on the results of violent relaxation: in the central region $\alpha \approx 0$, that is, the system is isotropic; in the external region $\alpha \approx 2$, that is, the anisotropy is radially-biased. This is illustrated in Fig. A.4, where this function is shown for five models characterized by $\nu = 1$ and different values of Ψ. This plot shows that models with very different values of the parameter Ψ have remarkably similar anisotropy functions. The anisotropy radius, defined as the radius r_α at which $\alpha = 1$, takes similar values for the models in this family (typically the value of r_α/r_0 is between 1 and 2). The ratio between the anisotropy radius and the half-mass radius is $r_\alpha/r_{\rm M} < 2$, and indicates that the onset of the radial anisotropy occurs well inside these systems.

By definition, these models are non-truncated and, because of this, are likely to be less suited to describe the outer parts of globular clusters. A study of globular clusters based on truncated $f^{(\nu)}$ models is planned for the future.

We recall that the surface brightness profiles for concentrated models ($\Psi \gtrsim 7$) are very close to de Vaucouleurs profile, while for low values of Ψ the models exhibit a sizable core.

A.4 Rotating models

The family of self-consistent axisymmetric models introduced by Varri & Bertin (2012) has been specifically designed to describe quasi-relaxed stellar systems with finite global angular momentum. These models are global, finite-mass solutions of the self-consistent problem associated with the distribution function

$$f_{\rm WT}^{\rm d}(I) = \begin{cases} A{\rm e}^{(-aE_0)}\left[{\rm e}^{-a(I-E_0)} - 1 + a(I-E_0)\right] & E \le E_0 \\ 0 & E > E_0\ , \end{cases} \tag{A.16}$$

in which the integral of the motion $I = I(E, J_z)$ is defined as

$$I(E,J_z) = E - \frac{\omega J_z}{1 + bJ_z^{2c}}, \tag{A.17}$$

where ω, b, and $c > 1/2$ are positive constants. The subscript WT in the distribution function is a reminder that the form of the function is that of the corresponding spherical isotropic nonrotating models characterized by Wilson truncation, while the superscript d indicates that this distribution function defines models characterized by differential rotation. A full description of the physical arguments that have led to this choice of distribution function is provided in Varri & Bertin (2012). The integral of the motion reduces to $I \sim E$ for high values of J_z and to the Jacobi integral $I \sim H = E - \omega J_z$ for low values of J_z. Therefore, the models are characterized by differential rotation, approximately rigid in the center and vanishing in the outer parts.

The models are defined by four dimensionless parameters:

- Ψ, the concentration parameter, is defined as the depth of the dimensionless potential well at the center of the clusters. Large values of this parameter determine spatially extended configurations, in terms of the relevant units of length (see Varri & Bertin (2012) for details);

- $\chi = \omega^2/(4\pi G\rho_0)$ is the rotation-strength parameter. Configurations characterized by a given value of concentration and increasing values of the rotation strength parameter χ are progressively more compact because of the adopted truncation prescription in phase space;

- $\bar{b}$ and c determine the shape of the rotation profile. The effect of taking a larger value of $\bar{b}$ is to produce models in which the solid-body rotation covers a wider radial range; this parameter determines the shape of the line-of-sight rotation profile, in particular, it regulates the radial position of the velocity peak. A variation of c does not introduce significant differences, therefore to simplify the investigation it is possible to set $c = 1$.

Different rotation regimes are identified, depending on the value assumed by the rotation-strength parameter. Of particular interest for this Thesis is the "moderate rotation regime", corresponding to small values of the parameter χ. Models in this regime have non-monotonic ellipticity profiles, and have values of $V_{\rm rot}/\sigma$ comparable to those observed in Galactic globular clusters (see Sect. 1.2 and Chapter 6).

For these models, the velocity dispersion tensor is characterized by isotropy in the central region, weak radial anisotropy in the intermediate regions, and tangential anisotropy in the outer parts. The behavior of the pressure tensor in the external regions of a configuration was not assigned *a priori* in the definition of the models: it results from the requirement of self-consistency and from the relevant truncation prescription in phase space.

APPENDIX B

Radial velocity data-sets for Galactic globular clusters

As shown in Chapter 4, the possibility to analyze kinematic profiles, in addition to the usually considered photometric ones, is crucial to properly describe the dynamics of globular clusters. Of particular importance are the measurements of line-of-sight (radial) velocities of single stars. Unfortunately, this kind of kinematic data is currently available for only a small fraction of the Galactic globular clusters, and often the number of stars for which velocities have been measured is quite small.

In Table B.1 we provide a list of the published data-sets of radial velocities for stars in Galactic globular clusters. This list only contains globular clusters with a fairly rich kinematical information available (radial velocity measurements for at least 40 stars). In Table B.1, for each considered globular cluster (indicated in the first column), each line corresponds to a different data-set, whose reference is indicated in the last column of the table. For each cluster, the different data-sets are here presented in chronological order: the first line corresponds to the oldest data-set, the last one to the most recent. For each data-set, we give the total number of velocity data-points available $N_{\rm V}$, the number of velocity data-points contained within the projected half-mass radius $N_{\rm V,h}$, the ratio of the radius of the outermost velocity point to the projected half-light radius $R_{\rm V}/R_{\rm h}$, and ratio of the radius of the outermost velocity point to the truncation radius $R_{\rm V}/r_{\rm tr}$ (the values considered for the half-mass radius and for the truncation radius are those given in the Harris 2010 catalog[1]). Moreover, by following the procedure described by Pryor & Meylan (1993), we calculated the mean velocity $\langle v_{\rm r} \rangle$, the global velocity dispersion σ_c, and the associated errors for velocities in every data-set.

In some cases, it is not enough to consider just one data-set to obtain a global satisfactory description of the kinematics of a cluster, and several data-sets need to be combined. To do this, two important factors need to be taken into account. First, it is necessary to identify stars that are in common between the data-sets, in order to avoid to consider them twice; usually, the velocity measurements with the smallest error are then taken as the velocities of such stars. Secondly, the values of the calculated mean velocities of each data-set are used to identify the presence of a possible shift between the samples, and to correct it.

Table B.2 offers a more compact description of the data-sets available for these globular clusters. For each cluster, the values of the concentration parameter C, the logarithm of the core relaxation time $\log T_{\rm c}$, and the logarithm of the half-mass relaxation time

[1] In the latest version of the Harris (2010) catalog, the values of the truncation radii are not listed; we calculated them from the available values of the core radius $R_{\rm c}$ and of the concentration parameter C (see Appendix A.1), as: $r_{\rm tr} = R_{\rm c}\, 10^C$; for the three core-collapsed globular clusters in Table B.2, for which the concentration parameter is arbitrarily set to $C = 2.50$, the value of $r_{\rm tr}$ calculated in this way is only considered as indicative.

$\log T_{\rm M}$ are recorded (as listed in the Harris 2010 catalog). By considering, for each globular cluster, a data-set containing all the available data, we also list the total number of velocity data-points available $N_{\rm V}$, the total number of velocity data-points inside the projected half-light radius $N_{\rm V,h}$, the ratios of the radius of the outermost velocity point $R_{\rm V}$ to the projected half-light radius $R_{\rm h}$ and to the truncation radius $r_{\rm tr}$. Table B.2 is organized in four parts: in the first part we list post-core-collapse globular clusters, in the second part those with a total number of kinematic data that we consider insufficient for a proper dynamical analysis, in the third part those with an insufficient number of data inside the half-light radius, and in the fourth part those having a satisfactory number of velocity data-points (in particular, these clusters match the criteria listed in Sect. 4.1.1). In each part of the table, globular clusters are listed in order of increasing number of total stellar velocity data $N_{\rm V}$. The values listed in this table regard the largest data-set that is in principle attainable by combining all the available data-sets for each cluster. This is not always the best way to obtain a reliable set of data-points to be used to calculate the kinematic profiles of interest (for some additional comments, see for example Sect. 4.1.2). The exact combinations of data-sets that have been used in the work presented in this Thesis are described in the relevant Chapters.

Table B.1: Radial velocity data-sets.

Globular cluster	$N_{\rm V}$	$N_{\rm V,h}$	$\langle v_{\rm r} \rangle$ [km s^{-1}]	σ_c [km s^{-1}]	$R_{\rm V}/R_{\rm h}$	$R_{\rm V}/r_{\rm tr}$	Ref.
NGC 104	640	537	-18.46 $\pm$ 0.46	11.47 $\pm$ 0.33	4.53	0.34	(1)
	147	55	-16.86 $\pm$ 0.78	9.40 $\pm$ 0.55	3.88	0.29	(2)
	2072	302	-16.84 $\pm$ 0.16	6.83 $\pm$ 0.12	19.07	1.43	(3)
NGC 288	24	18	-46.48 $\pm$ 0.59	2.79 $\pm$ 0.42	2.61	0.44	(4)
	124	27	-43.73 $\pm$ 0.20	2.11 $\pm$ 0.15	3.41	0.58	(5)
	110	43	-44.30 $\pm$ 0.28	2.85 $\pm$ 0.20	5.61	0.95	(2)
	133	44	-45.09 $\pm$ 0.22	1.64 $\pm$ 0.20	5.61	0.95	(3)
NGC 362	206	92	223.28 $\pm$ 0.45	6.36 $\pm$ 0.32	4.21	0.33	(6)
NGC 1851	186	0	319.90 $\pm$ 0.36	4.93 $\pm$ 0.26	21.21	1.66	(7)
	124	0	320.26 $\pm$ 0.33	3.70 $\pm$ 0.24	20.7	1.62	(8)
NGC 1904	58	5	205.61 $\pm$ 0.44	3.30 $\pm$ 0.31	10.75	0.87	(2)
	145	2	206.13 $\pm$ 0.26	3.07 $\pm$ 0.18	14.46	1.17	(7)
NGC 2419	166	39	-20.85 $\pm$ 0.36	4.14 $\pm$ 0.27	14.66	1.74	(9)
NGC 2808	124	7	102.64 $\pm$ 0.88	9.76 $\pm$ 0.62	8.41	0.74	(10)
	71	4	92.98 $\pm$ 0.65	5.38 $\pm$ 0.48	12.31	1.09	(11)
	62	0	101.25 $\pm$ 0.95	7.41 $\pm$ 0.68	14.09	1.24	(12)
NGC 3201	399	201	494.37 $\pm$ 0.19	3.69 $\pm$ 0.15	10.37	1.27	(13)
	149	72	495.03 $\pm$ 0.32	3.82 $\pm$ 0.22	2.98	0.36	(2)
NGC 4590	121	29	-93.10 $\pm$ 0.27	2.93 $\pm$ 0.19	6.69	0.68	(2)
	50	12	-94.21 $\pm$ 0.75	5.14 $\pm$ 0.53	14.34	1.45	(3)
NGC 5024	142	5	-62.79 $\pm$ 0.31	3.03 $\pm$ 0.27	16.2	1.16	(3)
	19	0	-61.13 $\pm$ 1.47	3.30 $\pm$ 1.80	13.33	0.95	(14)

Continued on next page

Table B.1 – Continued from previous page

Globular cluster	$N_{\rm V}$	$N_{\rm V,h}$	$\langle v_{\rm r} \rangle$ [km s^{-1}]	σ_c [km s^{-1}]	$R_{\rm V}/R_{\rm h}$	$R_{\rm V}/r_{\rm tr}$	Ref.
NGC 5053	71	30	291.18 ± 0.37	1.04 ± 0.28	2.61	0.59	(15)
	16	3	43.62 ± 1.46	3.67 ± 5.04	3.03	0.69	(14)
NGC 5139	471	202	232.91 ± 0.64	13.78 ± 0.45	4.47	0.46	(16)
	1589	344	231.37 ± 0.29	11.28 ± 0.21	5.98	0.62	(17)
	649	307	233.38 ± 0.52	13.19 ± 0.37	2.93	0.3	(18)
	318	0	234.15 ± 0.56	9.90 ± 0.39	14.57	1.51	(19)
	75	0	233.70 ± 0.86	7.36 ± 0.61	6.09	0.63	(20)
	160	0	233.32 ± 0.61	7.64 ± 0.43	10.72	1.11	(21)
NGC 5272	77	4	-141.91 ± 0.47	3.37 ± 0.39	8.81	0.71	(14)
NGC 5466	66	49	116.06 ± 1.86	12.47 ± 1.52	1.69	0.25	(22)
NGC 5904	136	18	53.49 ± 0.43	5.03 ± 0.31	6.61	0.5	(2)
NGC 6121	177	108	70.87 ± 0.27	3.48 ± 0.20	3.37	0.28	(23)
	103	69	71.63 ± 0.41	4.16 ± 0.29	2.65	0.22	(2)
	200	55	71.53 ± 0.25	3.06 ± 0.21	10.37	0.87	(3)
NGC 6171	66	37	-34.13 ± 0.44	3.37 ± 0.33	3.67	0.33	(24)
	33	0	-35.36 ± 0.75	4.30 ± 0.54	6.04	0.55	(2)
NGC 6205	123	10	-247.10 ± 0.52	5.76 ± 0.37	7.92	0.64	(25)
	293	0	-245.26 ± 0.35	4.79 ± 0.28	14.05	1.13	(14)
	113	31	-244.77 ± 0.57	6.10 ± 0.41	7.03	0.57	(26)
NGC 6218	242	59	-40.98 ± 0.24	2.96 ± 0.20	10.4	1.06	(3)
NGC 6254	147	47	73.75 ± 0.41	4.98 ± 0.29	5.22	0.55	(2)
NGC 6341	295	44	-121.05 ± 0.31	5.37 ± 0.22	13.93	1.14	(27)
	64	0	-121.01 ± 0.59	4.68 ± 0.41	9.45	0.77	(28)
	58	0	-115.67 ± 0.76	3.37 ± 0.76	13.85	1.14	(14)
NGC 6397	103	103	19.18 ± 0.55	4.84 ± 0.42	0.37	0.07	(1)
	144	49	19.26 ± 0.27	3.24 ± 0.19	4.83	0.89	(2)
NGC 6656	130	49	-148.77 ± 0.59	6.64 ± 0.42	2.09	0.22	(29)
	345	114	-144.92 ± 0.32	5.00 ± 0.27	8.41	0.89	(3)
NGC 6752	146	42	-26.27 ± 0.44	5.33 ± 0.31	5.41	0.19	(30)
	325	60	-26.23 ± 0.26	4.46 ± 0.20	15.33	0.54	(3)
NGC 6809	156	66	174.85 ± 0.31	3.91 ± 0.22	3.56	0.66	(2)
	723	306	177.35 ± 0.13	2.45 ± 0.11	7.83	1.45	(3)
NGC 6838	39	19	-23.14 ± 0.39	2.39 ± 0.28	3.47	0.65	(2)
	17	3	-20.87 ± 0.91	3.36 ± 0.68	5.2	0.98	(14)
NGC 7078	1777	1298	-107.45 ± 0.25	9.53 ± 0.19	16.94	0.62	(31)
	84	12	-107.37 ± 0.62	5.64 ± 0.44	11.26	0.41	(2)
	98	0	-108.54 ± 0.88	5.86 ± 1.00	19.4	0.71	(14)

Continued on next page

Table B.1 – Continued from previous page

Globular cluster	$N_{\rm V}$	$N_{\rm V,h}$	$\langle v_{\rm r} \rangle$ [km s^{-1}]	σ_c [km s^{-1}]	$R_{\rm V}/R_{\rm h}$	$R_{\rm V}/r_{\rm tr}$	Ref.
NGC 7089	61	20	-4.56 $\pm$ 1.02	7.95 $\pm$ 0.72	8.03	0.68	(32)
	71	0	-1.70 $\pm$ 0.82	4.51 $\pm$ 0.74	102.87	8.76	(14)
NGC 7099	16	16	-186.95 $\pm$ 0.98	3.78 $\pm$ 0.71	0.76	0.04	(33)
	27	27	-185.89 $\pm$ 0.78	3.71 $\pm$ 0.60	0.89	0.05	(1)
	125	4	-184.40 $\pm$ 0.25	2.69 $\pm$ 0.18	11.2	0.61	(34)
	193	32	-183.81 $\pm$ 0.31	3.34 $\pm$ 0.25	11.19	0.61	(3)
	65	13	-185.30 $\pm$ 0.37	2.97 $\pm$ 0.27	9.34	0.51	(2)
IC 4499	43	11	31.41 $\pm$ 0.37	1.82 $\pm$ 0.33	6.9	0.87	(35)
Pal 13	22	7	24.11 $\pm$ 0.50	2.18 $\pm$ 0.35	5.42	0.89	(37)
	66	7	25.76 $\pm$ 0.41	2.32 $\pm$ 0.34	15.84	2.6	(38)

Notes. From left to right, we list: the number of velocity data-points available for each data-set and inside the projected half-mass radius, the mean velocity and the velocity dispersion (with associated errors), and the ratio of the radius of the outermost velocity point to the projected half-light and truncation radius. The sources of each kinematical data-set are listed in the last column.

References. (1) Gebhardt et al. (1995); (2) Carretta et al. (2009); (3) Lane et al. (2011); (4) Pryor et al. (1991); (5) Scarpa et al. (2007a); (6) Fischer et al. (1993); (7) Scarpa et al. (2011); (8) Carretta et al. (2011); (9) Ibata et al. (2011); (10) Carretta et al. (2006); (11) Moni Bidin et al. (2011); (12) Gratton et al. (2011); (13) Cote et al. (1995); (14) Smolinski et al. (2011); (15) Yan & Cohen (1996); (16) Mayor et al. (1997); (17) Reijns et al. (2006); (18) Pancino et al. (2007); (19) Sollima et al. (2009); (20) Scarpa & Falomo (2010); (21) Da Costa (2012); (22) Shetrone et al. (2010); (23) Peterson et al. (1995); (24) Piatek et al. (1994); (25) Mészáros et al. (2009); (26) Johnson & Pilachowski (2012); (27) Drukier et al. (2007); (28) Mészáros et al. (2009); (29) Peterson & Cudworth (1994); (30) Carretta et al. (2007); (31) Gebhardt et al. (2000); (32) Pryor et al. (1986); (33) Zaggia et al. (1992); (34) Scarpa et al. (2007b); (35) Hankey & Cole (2011); (36) Frank et al. (2012); (37) Côté et al. (2002); (38) Bradford et al. (2011); (39) Jordi et al. (2009).

Table B.2: Combined radial velocity data-sets.

Globular cluster	C	$\log T_{\rm c}$	$\log T_{\rm M}$	$N_{\rm V}$	$N_{\rm V,h}$	$R_{\rm V}/R_{\rm h}$	$R_{\rm V}/r_{\rm tr}$
NGC 6397	2.50	4.94	8.60	247	152	4.83	0.89
NGC 7099 (M30)	2.50	6.37	8.88	425	92	11.2	0.61
NGC 6752	2.50	0.17	1.91	470	102	15.33	0.54
IC 4499	1.21	9.21	9.73	43	11	6.9	0.87
NGC 6838 (M71)	1.15	7.54	8.43	56	22	5.2	0.98
NGC 5466	1.04	9.35	9.76	66	49	1.69	0.25
NGC 5272 (M3)	1.89	8.31	9.79	77	4	8.81	0.71
NGC 5053	0.74	9.81	9.87	87	33	3.03	0.69
Pal 13	0.66	9.60	9.44	88	14	15.84	2.6
NGC 6171 (M107)	1.53	8.06	9.00	99	37	6.04	0.55
NGC 7089 (M2)	1.59	8.48	9.40	132	20	102.87	8.76
NGC 5904 (M5)	1.73	8.28	9.41	136	18	6.61	0.5
NGC 5024 (M53)	1.72	8.73	9.76	161	5	16.2	1.16
NGC 4590 (M68)	1.41	8.45	9.27	171	29	14.34	1.45
NGC 1904 (M79)	1.70	7.83	8.95	203	7	14.46	1.17
NGC 2808	1.56	8.24	9.15	257	11	14.09	1.24
NGC 1851	1.86	7.43	8.82	310	0	21.21	1.66
NGC 6205 (M13)	1.53	8.51	9.30	492	34	14.05	1.13
NGC 6254 (M10)	1.38	8.21	8.90	147	47	5.22	0.55
NGC 2419	1.37	9.87	10.63	166	39	14.66	1.74
NGC 362	1.76	7.76	8.93	206	92	4.21	0.33
NGC 6218 (M12)	1.34	8.19	8.87	242	59	10.4	1.06
NGC 288	0.99	8.99	9.32	319	132	5.61	0.95
NGC 6341 (M92)	1.68	7.96	9.02	417	44	13.93	1.14
NGC 6656 (M22)	1.38	8.53	9.23	475	163	8.41	0.89
NGC 6121 (M4)	1.65	7.90	8.93	479	232	10.37	0.87
NGC 3201	1.29	8.61	9.27	548	273	10.37	1.27
NGC 6809 (M55)	0.93	8.90	9.29	879	372	7.83	1.45
NGC 7078 (M15)	2.29	7.84	9.32	1959	1310	19.4	0.71
NGC 104 (47 Tuc)	2.07	7.84	9.55	2859	894	19.07	1.43
NGC 5139 (ω Cen)	1.31	9.60	10.09	3262	853	14.57	1.51

Notes. From left to right, the following quantities are displayed: concentration parameter, logarithm of the core relaxation time (years), logarithm of the half-mass relaxation time (years), total number of velocity data-points available, number of velocity data-points inside the projected half-light radius, ratio of the radius of the outermost velocity point to the projected half-light radius, and ratio of the radius of the outermost velocity point to the truncation radius. The source of each of the kinematical data-sets here combined is given in the last column of Table B.1 (see main text for further details).

Bibliography

Aarseth, S. J. 1999, *Publ. Astron. Soc. Pac.*, 111, 1333

Aarseth, S. J. 2003, Gravitational N-Body Simulations (Cambridge University Press, Cambridge UK)

Abramowitz, M. & Stegun, I. A. 1972, Handbook of Mathematical Functions (Dover Books on Advanced Mathematics, New York)

Aguilar, L., Hut, P., & Ostriker, J. P. 1988, *Astrophys. J.*, 335, 720

Aihara, H., Allende Prieto, C., An, D., et al. 2011, *Astrophys. J. Suppl.*, 193, 29

Alexander, P. E. R. & Gieles, M. 2012, *Mon. Not. R. Astron. Soc.*, 422, 3415

Anderson, J. & King, I. R. 2003, *Astron. J.*, 126, 772

Anderson, J. & van der Marel, R. P. 2010, *Astrophys. J.*, 710, 1032

Andreuzzi, G., Buonanno, R., Fusi Pecci, F., Iannicola, G., & Marconi, G. 2000, *Astron. Astrophys.*, 353, 944

Ashman, K. M. & Zepf, S. E. 2008, Globular Cluster Systems (Cambridge University Press, Cambridge UK)

Bahcall, J. N. & Wolf, R. A. 1976, *Astrophys. J.*, 209, 214

Barmby, P., McLaughlin, D. E., Harris, W. E., Harris, G. L. H., & Forbes, D. A. 2007, *Astron. J.*, 133, 2764

Baumgardt, H., Grebel, E. K., & Kroupa, P. 2005, *Mon. Not. R. Astron. Soc.*, 359, L1

Baumgardt, H. & Makino, J. 2003, *Mon. Not. R. Astron. Soc.*, 340, 227

Bedin, L. R., Piotto, G., Anderson, J., et al. 2004, *Astrophys. J. Lett.*, 605, L125

Bellazzini, M. 1998, *New Astron.*, 3, 219

Bellazzini, M., Bragaglia, A., Carretta, E., et al. 2012, *Astron. Astrophys.*, 538, A18

Bellazzini, M., Ibata, R., Ferraro, F. R., & Testa, V. 2003, *Astron. Astrophys.*, 405, 577

Bellazzini, M., Ibata, R. A., Chapman, S. C., et al. 2008, *Astron. J.*, 136, 1147

Bellini, A., Piotto, G., Bedin, L. R., et al. 2009, *Astron. Astrophys.*, 507, 1393

Bellini, A., van der Marel, R. P., & Anderson, J. 2013, *Mem. Soc. Astron. Italiana*, 84, 140

Bender, R. 1990, *Astron. Astrophys.*, 229, 441

Bertin, E. & Arnouts, S. 1996, *Astron. Astrophys. Supp. Ser.*, 117, 393

Bertin, G. 2000, Dynamics of Galaxies (Cambridge University Press, Cambridge)

Bertin, G., Ciotti, L., & Del Principe, M. 2002, *Astron. Astrophys.*, 386, 149

Bertin, G., Saglia, R. P., & Stiavelli, M. 1988, *Astrophys. J.*, 330, 78

Bertin, G. & Stiavelli, M. 1993, Reports on Progress in Physics, 56, 493

Bertin, G. & Trenti, M. 2003, *Astrophys. J.*, 584, 729

Bertin, G. & Varri, A. L. 2008, *Astrophys. J.*, 689, 1005
Bianchini, P., Varri, A. L., Bertin, G., & Zocchi, A. 2013, *Astrophys. J.*, 772, 67
Bono, G., Stetson, P. B., Sanna, N., et al. 2008, *Astrophys. J. Lett.*, 686, L87
Bradford, J. D., Geha, M., Muñoz, R. R., et al. 2011, *Astrophys. J.*, 743, 167
Cappellari, M. 2002, *Mon. Not. R. Astron. Soc.*, 333, 400
Cappellari, M. 2008, *Mon. Not. R. Astron. Soc.*, 390, 71
Cappellari, M. & Emsellem, E. 2004, *Publ. Astron. Soc. Pac.*, 116, 138
Carretta, E., Bragaglia, A., Gratton, R. G., et al. 2006, *Astron. Astrophys.*, 450, 523
Carretta, E., Bragaglia, A., Gratton, R. G., et al. 2009, *Astron. Astrophys.*, 505, 117
Carretta, E., Bragaglia, A., Gratton, R. G., Lucatello, S., & Momany, Y. 2007, *Astron. Astrophys.*, 464, 927
Carretta, E., Lucatello, S., Gratton, R. G., Bragaglia, A., & D'Orazi, V. 2011, *Astron. Astrophys.*, 533, A69
Castellani, V., Calamida, A., Bono, G., et al. 2007, *Astrophys. J.*, 663, 1021
Chen, C. W. & Chen, W. P. 2010, *Astrophys. J.*, 721, 1790
Chun, S.-H., Kim, J.-W., Sohn, S. T., et al. 2010, *Astron. J.*, 139, 606
Correnti, M., Bellazzini, M., Dalessandro, E., et al. 2011, *Mon. Not. R. Astron. Soc.*, 417, 2411
Côté, P., Djorgovski, S. G., Meylan, G., Castro, S., & McCarthy, J. K. 2002, *Astrophys. J.*, 574, 783
Cote, P., Welch, D. L., Fischer, P., & Gebhardt, K. 1995, *Astrophys. J.*, 454, 788
Cox, A. N. 2000, Allen's astrophysical quantities (Springer Verlag, Berlin)
Da Costa, G. S. 2012, *Astrophys. J.*, 751, 6
Dalessandro, E., Lanzoni, B., Beccari, G., et al. 2011, *Astrophys. J.*, 743, 11
D'Antona, F., Bellazzini, M., Caloi, V., et al. 2005, *Astrophys. J.*, 631, 868
D'Antona, F. & Caloi, V. 2004, *Astrophys. J.*, 611, 871
Davies, M. B., Piotto, G., & de Angeli, F. 2004, *Mon. Not. R. Astron. Soc.*, 349, 129
Davis, T. A., Bureau, M., Cappellari, M., Sarzi, M., & Blitz, L. 2013, *Nature*, 494, 328
Dehnen, W. 1993, *Mon. Not. R. Astron. Soc.*, 265, 250
den Brok, M., van de Ven, G., van den Bosch, R., & Watkins, L. 2014, *Mon. Not. R. Astron. Soc.*, 438, 487
D'Ercole, A., Vesperini, E., D'Antona, F., McMillan, S. L. W., & Recchi, S. 2008, *Mon. Not. R. Astron. Soc.*, 391, 825
Di Cecco, A., Becucci, R., Bono, G., et al. 2010, *Publ. Astron. Soc. Pac.*, 122, 991
Di Cecco, A., Zocchi, A., Varri, A. L., et al. 2013, *Astron. J.*, 145, 103
Dinescu, D. I., Girard, T. M., & van Altena, W. F. 1999, *Astron. J.*, 117, 1792
Djorgovski, S. 1993, in Astronomical Society of the Pacific Conference Series, Vol. 50, Structure and Dynamics of Globular Clusters, ed. S. G. Djorgovski & G. Meylan, 373
Drukier, G. A., Cohn, H. N., Lugger, P. M., et al. 2007, *Astron. J.*, 133, 1041
D'Souza, R. & Rix, H.-W. 2013, *Mon. Not. R. Astron. Soc.*, 429, 1887
Ebisuzaki, T., Makino, J., Tsuru, T. G., et al. 2001, *Astrophys. J. Lett.*, 562, L19
Elson, R. A. W., Fall, S. M., & Freeman, K. C. 1987, *Astrophys. J.*, 323, 54
Emsellem, E., Monnet, G., & Bacon, R. 1994, *Astron. Astrophys.*, 285, 723
Evans, I. N., Primini, F. A., Glotfelty, K. J., et al. 2010, *Astrophys. J. Suppl.*, 189, 37
Fall, S. M. & Frenk, C. S. 1985, in IAU Symposium, Vol. 113, Dynamics of Star Clusters, ed. J. Goodman & P. Hut, 285–296

Fan, X. 2006, *New Astron. Rev.*, 50, 665
Ferrarese, L. & Merritt, D. 2000, *Astrophys. J. Lett.*, 539, L9
Ferraro, F. R., Lanzoni, B., Dalessandro, E., et al. 2012, *Nature*, 492, 393
Ferraro, F. R., Messineo, M., Fusi Pecci, F., et al. 1999, *Astron. J.*, 118, 1738
Ferraro, F. R., Pecci, F. F., Cacciari, C., et al. 1993, *Astron. J.*, 106, 2324
Ferraro, F. R., Sollima, A., Rood, R. T., et al. 2006, *Astrophys. J.*, 638, 433
Fiestas, J., Spurzem, R., & Kim, E. 2006, *Mon. Not. R. Astron. Soc.*, 373, 677
Fischer, P., Welch, D. L., Mateo, M., & Cote, P. 1993, *Astron. J.*, 106, 1508
Forbes, D. A. & Bridges, T. 2010, *Mon. Not. R. Astron. Soc.*, 404, 1203
Frank, M. J., Hilker, M., Baumgardt, H., et al. 2012, *Mon. Not. R. Astron. Soc.*, 423, 2917
Frank, M. J., Hilker, M., Mieske, S., et al. 2011, *Mon. Not. R. Astron. Soc.*, 414, L70
Franx, M. & Illingworth, G. D. 1988, *Astrophys. J. Lett.*, 327, L55
Fridman, A. M. & Polyachenko, V. L. 1984, Physics of gravitating systems. II - Nonlinear collective processes: Nonlinear waves, solitons, collisionless shocks, turbulence. Astrophysical applications
Gebhardt, K., Pryor, C., O'Connell, R. D., Williams, T. B., & Hesser, J. E. 2000, *Astron. J.*, 119, 1268
Gebhardt, K., Pryor, C., Williams, T. B., & Hesser, J. E. 1995, *Astron. J.*, 110, 1699
Geyer, E. H., Nelles, B., & Hopp, U. 1983, *Astron. Astrophys.*, 125, 359
Giersz, M. & Heggie, D. C. 2011, *Mon. Not. R. Astron. Soc.*, 410, 2698
Glebbeek, E., Gaburov, E., de Mink, S. E., Pols, O. R., & Portegies Zwart, S. F. 2009, *Astron. Astrophys.*, 497, 255
Gratton, R. G., Carretta, E., & Bragaglia, A. 2012a, *Astron. Astrophys. Rev.*, 20, 50
Gratton, R. G., Lucatello, S., Carretta, E., et al. 2011, *Astron. Astrophys.*, 534, A123
Gratton, R. G., Villanova, S., Lucatello, S., et al. 2012b, *Astron. Astrophys.*, 544, A12
Griffin, R. F. 1967, *Astrophys. J.*, 148, 465
Griffin, R. F. & Gunn, J. E. 1974, *Astrophys. J.*, 191, 545
Grillmair, C. J., Freeman, K. C., Irwin, M., & Quinn, P. J. 1995, *Astron. J.*, 109, 2553
Grillmair, C. J. & Johnson, R. 2006, *Astrophys. J. Lett.*, 639, L17
Gunn, J. E. & Griffin, R. F. 1979, *Astron. J.*, 84, 752
Hankey, W. J. & Cole, A. A. 2011, *Mon. Not. R. Astron. Soc.*, 411, 1536
Harris, W. E. 2010, ArXiv e-prints
Harris, W. E., Harris, G. L. H., & Alessi, M. 2013, *Astrophys. J.*, 772, 82
Harris, W. E., Harris, G. L. H., Barmby, P., McLaughlin, D. E., & Forbes, D. A. 2006, *Astron. J.*, 132, 2187
Harris, W. E., Harris, G. L. H., Holland, S. T., & McLaughlin, D. E. 2002, *Astron. J.*, 124, 1435
Harris, W. E. & van den Bergh, S. 1981, *Astron. J.*, 86, 1627
Heggie, D. & Hut, P. 2003, The Gravitational Million-Body Problem: A Multidisciplinary Approach to Star Cluster Dynamics (Cambridge University Press, Cambridge UK)
Heggie, D. C. & Giersz, M. 2008, *Mon. Not. R. Astron. Soc.*, 389, 1858
Heggie, D. C. & Mathieu, R. D. 1986, in Lecture Notes in Physics, Berlin Springer Verlag, Vol. 267, The Use of Supercomputers in Stellar Dynamics, ed. P. Hut & S. L. W. McMillan, 233
Hénon, M. 1965, Annales d'Astrophysique, 28, 62
Hesser, J. E. & Bell, R. A. 1980, *Astrophys. J. Lett.*, 238, L149
Hill, A. & Zaritsky, D. 2006, *Astron. J.*, 131, 414

Hurley, J. R., Pols, O. R., & Tout, C. A. 2000, *Mon. Not. R. Astron. Soc.*, 315, 543
Hurley, J. R., Tout, C. A., & Pols, O. R. 2002, *Mon. Not. R. Astron. Soc.*, 329, 897
Ibata, R., Bellazzini, M., Chapman, S. C., et al. 2009, *Astrophys. J. Lett.*, 699, L169
Ibata, R., Sollima, A., Nipoti, C., et al. 2011, *Astrophys. J.*, 738, 186
Illingworth, G. 1976, *Astrophys. J.*, 204, 73
Johnson, C. I. & Pilachowski, C. A. 2012, *Astrophys. J. Lett.*, 754, L38
Jordi, K. & Grebel, E. K. 2010, *Astron. Astrophys.*, 522, A71
Jordi, K., Grebel, E. K., Hilker, M., et al. 2009, *Astron. J.*, 137, 4586
King, I. 1961, *Astron. J.*, 66, 68
King, I. R. 1966, *Astron. J.*, 71, 64
King, I. R., Hedemann, Jr., E., Hodge, S. M., & White, R. E. 1968, *Astron. J.*, 73, 456
Knigge, C., Leigh, N., & Sills, A. 2009, *Nature*, 457, 288
Kochanek, C. S. 1996, *Astrophys. J.*, 457, 228
Kroupa, P. 2001, *Mon. Not. R. Astron. Soc.*, 322, 231
Küpper, A. H. W., Kroupa, P., Baumgardt, H., & Heggie, D. C. 2010, *Mon. Not. R. Astron. Soc.*, 407, 2241
Lane, R. R., Kiss, L. L., Lewis, G. F., et al. 2010, *Mon. Not. R. Astron. Soc.*, 406, 2732
Lane, R. R., Kiss, L. L., Lewis, G. F., et al. 2011, *Astron. Astrophys.*, 530, A31
Lane, R. R., Küpper, A. H. W., & Heggie, D. C. 2012, *Mon. Not. R. Astron. Soc.*, 423, 2845
Lanzoni, B., Mucciarelli, A., Origlia, L., et al. 2013, *Astrophys. J.*, 769, 107
Lardo, C., Bellazzini, M., Pancino, E., et al. 2011, *Astron. Astrophys.*, 525, A114
Le Fèvre, O., Saisse, M., Mancini, D., et al. 2003, in Society of Photo-Optical Instrumentation Engineers (SPIE) Conference Series, Vol. 4841, Instrument Design and Performance for Optical/Infrared Ground-based Telescopes, ed. M. Iye & A. F. M. Moorwood, 1670–1681
Lee, K. H., Lee, H. M., Fahlman, G. G., & Lee, M. G. 2003, *Astron. J.*, 126, 815
Lehmann, I. & Scholz, R.-D. 1997, *Astron. Astrophys.*, 320, 776
Leon, S., Meylan, G., & Combes, F. 2000, *Astron. Astrophys.*, 359, 907
Leonard, P. J. T., Richer, H. B., & Fahlman, G. G. 1992, *Astron. J.*, 104, 2104
Little, B. & Tremaine, S. 1987, *Astrophys. J.*, 320, 493
Lupton, R. H. & Gunn, J. E. 1987, *Astron. J.*, 93, 1106
Lupton, R. H., Gunn, J. E., & Griffin, R. F. 1987, *Astron. J.*, 93, 1114
Lützgendorf, N., Kissler-Patig, M., Gebhardt, K., et al. 2013a, *Astron. Astrophys.*, 552, A49
Lützgendorf, N., Kissler-Patig, M., Gebhardt, K., et al. 2012, *Astron. Astrophys.*, 542, A129
Lützgendorf, N., Kissler-Patig, M., Neumayer, N., et al. 2013b, *Astron. Astrophys.*, 555, A26
Lützgendorf, N., Kissler-Patig, M., Noyola, E., et al. 2011, *Astron. Astrophys.*, 533, A36
Mackey, A. D. & Gilmore, G. F. 2003a, *Mon. Not. R. Astron. Soc.*, 338, 120
Mackey, A. D. & Gilmore, G. F. 2003b, *Mon. Not. R. Astron. Soc.*, 338, 85
Mackey, A. D. & Gilmore, G. F. 2003c, *Mon. Not. R. Astron. Soc.*, 340, 175
Madau, P. & Rees, M. J. 2001, *Astrophys. J. Lett.*, 551, L27
Madrid, J. P., Harris, W. E., Blakeslee, J. P., & Gómez, M. 2009, *Astrophys. J.*, 705, 237
Makino, J. & Aarseth, S. J. 1992, *Publ. Astron. Soc. Jpn.*, 44, 141
Mayor, M., Meylan, G., Udry, S., et al. 1997, *Astron. J.*, 114, 1087
McLaughlin, D. E., Anderson, J., Meylan, G., et al. 2006, *Astrophys. J. Suppl.*, 166, 249
McLaughlin, D. E. & van der Marel, R. P. 2005, *Astrophys. J. Suppl.*, 161, 304

McNamara, B. J., Harrison, T. E., & Anderson, J. 2003, *Astrophys. J.*, 595, 187
McNamara, B. J., Harrison, T. E., & Baumgardt, H. 2004, *Astrophys. J.*, 602, 264
Merritt, D., Meylan, G., & Mayor, M. 1997, *Astron. J.*, 114, 1074
Mészáros, S., Dupree, A. K., & Szalai, T. 2009, *Astron. J.*, 137, 4282
Meylan, G. & Heggie, D. C. 1997, *Astron. Astrophys. Rev.*, 8, 1
Meylan, G. & Mayor, M. 1986, *Astron. Astrophys.*, 166, 122
Meylan, G. & Mayor, M. 1991, *Astron. Astrophys.*, 250, 113
Meylan, G., Mayor, M., Duquennoy, A., & Dubath, P. 1995, *Astron. Astrophys.*, 303, 761
Michie, R. W. 1963, *Mon. Not. R. Astron. Soc.*, 125, 127
Mieske, S., Hilker, M., Jordán, A., et al. 2008, *Astron. Astrophys.*, 487, 921
Milone, A. P., Bedin, L. R., Piotto, G., et al. 2008, *Astrophys. J.*, 673, 241
Milone, A. P., Piotto, G., Bedin, L. R., et al. 2012, *Astrophys. J.*, 744, 58
Miocchi, P., Lanzoni, B., Ferraro, F. R., et al. 2013, *Astrophys. J.*, 774, 151
Mohr, J. J., Armstrong, R., Bertin, E., et al. 2012, in Society of Photo-Optical Instrumentation Engineers (SPIE) Conference Series, Vol. 8451, Society of Photo-Optical Instrumentation Engineers (SPIE) Conference Series
Moni Bidin, C., Villanova, S., Piotto, G., & Momany, Y. 2011, *Astron. Astrophys.*, 528, A127
Murphy, B. W., Cohn, H. N., & Lugger, P. M. 2011, *Astrophys. J.*, 732, 67
Noyola, E. & Baumgardt, H. 2011, *Astrophys. J.*, 743, 52
Noyola, E. & Gebhardt, K. 2006, *Astron. J.*, 132, 447
Noyola, E., Gebhardt, K., & Bergmann, M. 2008, *Astrophys. J.*, 676, 1008
Noyola, E., Gebhardt, K., Kissler-Patig, M., et al. 2010, *Astrophys. J. Lett.*, 719, L60
Odenkirchen, M., Grebel, E. K., Dehnen, W., et al. 2003, *Astron. J.*, 126, 2385
Odenkirchen, M., Grebel, E. K., Rockosi, C. M., et al. 2001, *Astrophys. J. Lett.*, 548, L165
Olszewski, E. W., Saha, A., Knezek, P., et al. 2009, *Astron. J.*, 138, 1570
Osborn, W. 1971, The Observatory, 91, 223
Pancino, E., Galfo, A., Ferraro, F. R., & Bellazzini, M. 2007, *Astrophys. J. Lett.*, 661, L155
Pasquato, M. & Bertin, G. 2010, *Astron. Astrophys.*, 512, A35
Pasquini, L., Avila, G., Blecha, A., et al. 2002, The Messenger, 110, 1
Peterson, R. C. & Cudworth, K. M. 1994, *Astrophys. J.*, 420, 612
Peterson, R. C., Rees, R. F., & Cudworth, K. M. 1995, *Astrophys. J.*, 443, 124
Piatek, S., Pryor, C., McClure, R. D., Fletcher, J. M., & Hesser, J. E. 1994, *Astron. J.*, 107, 1397
Piotto, G. 2009, in IAU Symposium, Vol. 258, IAU Symposium, ed. E. E. Mamajek, D. R. Soderblom, & R. F. G. Wyse, 233–244
Piotto, G., Bedin, L. R., Anderson, J., et al. 2007, *Astrophys. J. Lett.*, 661, L53
Piotto, G., Milone, A. P., Anderson, J., et al. 2012, *Astrophys. J.*, 760, 39
Piotto, G., Milone, A. P., Marino, A. F., et al. 2013, *Astrophys. J.*, 775, 15
Piotto, G., Villanova, S., Bedin, L. R., et al. 2005, *Astrophys. J.*, 621, 777
Plummer, H. C. 1911, *Mon. Not. R. Astron. Soc.*, 71, 460
Polyachenko, V. L. & Shukhman, I. G. 1981, *Soviet. Astron.*, 25, 533
Portegies Zwart, S. F., Baumgardt, H., Hut, P., Makino, J., & McMillan, S. L. W. 2004, *Nature*, 428, 724
Prendergast, K. H. & Tomer, E. 1970, *Astron. J.*, 75, 674
Press, W. H., Teukolsky, S. A., Vetterling, W. T., & Flannery, B. P. 2007, Numerical Recipes: The Art of Scientific Computing, Third Edition (Cambridge University Press, Cam-

bridge)
Pryor, C., Hartwick, F. D. A., McClure, R. D., Fletcher, J. M., & Kormendy, J. 1986, *Astron. J.*, 91, 546
Pryor, C., McClure, R. D., Fletcher, J. M., & Hesser, J. E. 1991, *Astron. J.*, 102, 1026
Pryor, C. & Meylan, G. 1993, in Astronomical Society of the Pacific Conference Series, Vol. 50, Structure and Dynamics of Globular Clusters, ed. S. G. Djorgovski & G. Meylan, 357
Reijns, R. A., Seitzer, P., Arnold, R., et al. 2006, *Astron. Astrophys.*, 445, 503
Rhode, K. L. 2012, *Astron. J.*, 144, 154
Richer, H. B., Harris, W. E., Fahlman, G. G., et al. 1996, *Astrophys. J.*, 463, 602
Rix, H.-W. & White, S. D. M. 1992, *Mon. Not. R. Astron. Soc.*, 254, 389
Royer, F., Blecha, A., North, P., et al. 2002, in Society of Photo-Optical Instrumentation Engineers (SPIE) Conference Series, Vol. 4847, Astronomical Data Analysis II, ed. J.-L. Starck & F. D. Murtagh, 184–194
Sandage, A. R. 1953, *Astron. J.*, 58, 61
Sandquist, E. L., Bolte, M., & Hernquist, L. 1997, *Astrophys. J.*, 477, 335
Scarpa, R. & Falomo, R. 2010, *Astron. Astrophys.*, 523, A43
Scarpa, R., Marconi, G., Carraro, G., Falomo, R., & Villanova, S. 2011, *Astron. Astrophys.*, 525, A148
Scarpa, R., Marconi, G., Gilmozzi, R., & Carraro, G. 2007a, The Messenger, 128, 41
Scarpa, R., Marconi, G., Gilmozzi, R., & Carraro, G. 2007b, *Astron. Astrophys.*, 462, L9
Schechter, P. L., Mateo, M., & Saha, A. 1993, *Publ. Astron. Soc. Pac.*, 105, 1342
Schödel, R., Ott, T., Genzel, R., et al. 2002, *Nature*, 419, 694
Schwarzschild, M. 1979, *Astrophys. J.*, 232, 236
Shetrone, M., Martell, S. L., Wilkerson, R., et al. 2010, *Astron. J.*, 140, 1119
Sills, A., Lombardi, Jr., J. C., Bailyn, C. D., et al. 1997, *Astrophys. J.*, 487, 290
Smolinski, J. P., Lee, Y. S., Beers, T. C., et al. 2011, *Astron. J.*, 141, 89
Sollima, A., Bellazzini, M., & Lee, J.-W. 2012, *Astrophys. J.*, 755, 156
Sollima, A., Bellazzini, M., Smart, R. L., et al. 2009, *Mon. Not. R. Astron. Soc.*, 396, 2183
Sollima, A., Ferraro, F. R., Bellazzini, M., et al. 2007, *Astrophys. J.*, 654, 915
Sollima, A., Lanzoni, B., Beccari, G., Ferraro, F. R., & Fusi Pecci, F. 2008, *Astron. Astrophys.*, 481, 701
Spitzer, L. 1987, Dynamical evolution of globular clusters (Princeton University Press, Princeton, NJ)
Spitzer, Jr., L. & Chevalier, R. A. 1973, *Astrophys. J.*, 183, 565
Spitzer, Jr., L. & Harm, R. 1958, *Astrophys. J.*, 127, 544
Spitzer, Jr., L. & Hart, M. H. 1971, *Astrophys. J.*, 164, 399
Stetson, P. B. 1987, *Publ. Astron. Soc. Pac.*, 99, 191
Stetson, P. B., Bruntt, H., & Grundahl, F. 2003, *Publ. Astron. Soc. Pac.*, 115, 413
Stetson, P. B., Vandenberg, D. A., & Bolte, M. 1996, *Publ. Astron. Soc. Pac.*, 108, 560
Strader, J., Chomiuk, L., Maccarone, T. J., et al. 2012, *Astrophys. J. Lett.*, 750, L27
Testa, V., Zaggia, S. R., Andreon, S., et al. 2000, *Astron. Astrophys.*, 356, 127
Tonry, J. & Davis, M. 1979, *Astron. J.*, 84, 1511
Trager, S. C., King, I. R., & Djorgovski, S. 1995, *Astron. J.*, 109, 218
Tremaine, S., Richstone, D. O., Byun, Y.-I., et al. 1994, *Astron. J.*, 107, 634
Trenti, M. & Bertin, G. 2005, *Astron. Astrophys.*, 429, 161

Trenti, M. & Bertin, G. 2006, *Astrophys. J.*, 637, 717
Trenti, M., Bertin, G., & van Albada, T. S. 2005, *Astron. Astrophys.*, 433, 57
Tully, R. B. & Fisher, J. R. 1977, *Astron. Astrophys.*, 54, 661
van de Ven, G., van den Bosch, R. C. E., Verolme, E. K., & de Zeeuw, P. T. 2006, *Astron. Astrophys.*, 445, 513
van den Bergh, S. 2008, *Astron. J.*, 135, 1731
van den Bosch, R., de Zeeuw, T., Gebhardt, K., Noyola, E., & van de Ven, G. 2006, *Astrophys. J.*, 641, 852
van den Bosch, R. C. E., Gebhardt, K., Gültekin, K., et al. 2012, *Nature*, 491, 729
van der Marel, R. P. & Anderson, J. 2010, *Astrophys. J.*, 710, 1063
van der Marel, R. P. & Franx, M. 1993, *Astrophys. J.*, 407, 525
van Leeuwen, F., Le Poole, R. S., Reijns, R. A., Freeman, K. C., & de Zeeuw, P. T. 2000, *Astron. Astrophys.*, 360, 472
Vandenberg, D. A., Bolte, M., & Stetson, P. B. 1996, *Ann. Rev. Astron. Astrophys*, 34, 461
Varri, A. L. & Bertin, G. 2009, *Astrophys. J.*, 703, 1911
Varri, A. L. & Bertin, G. 2012, *Astron. Astrophys.*, 540, A94
Vasilevskis, S., van Leeuwen, F., Nicholson, W., & Murray, C. A. 1979, *Astron. Astrophys. Supp. Ser.*, 37, 333
Vesperini, E., McMillan, S. L. W., D'Antona, F., & D'Ercole, A. 2010, *Astrophys. J. Lett.*, 718, L112
Vesperini, E. & Trenti, M. 2010, *Astrophys. J. Lett.*, 720, L179
Villanova, S., Piotto, G., King, I. R., et al. 2007, *Astrophys. J.*, 663, 296
Volonteri, M. 2010, *Astron. Astrophys. Rev.*, 18, 279
Walker, A. R., Kunder, A. M., Andreuzzi, G., et al. 2011, *Mon. Not. R. Astron. Soc.*, 415, 643
Wang, S. & Ma, J. 2013, *Astron. J.*, 146, 20
Watkins, L. L., van de Ven, G., den Brok, M., & van den Bosch, R. C. E. 2013, *Mon. Not. R. Astron. Soc.*, 436, 2598
Wen, Z. L., Han, J. L., & Liu, F. S. 2009, *Astrophys. J. Suppl.*, 183, 197
Werchan, F. & Zaritsky, D. 2011, *Astron. J.*, 142, 48
White, R. E. & Shawl, S. J. 1987, *Astrophys. J.*, 317, 246
Wilkinson, M. I. & Evans, N. W. 1999, *Mon. Not. R. Astron. Soc.*, 310, 645
Wilkinson, M. I., Kleyna, J., Evans, N. W., & Gilmore, G. 2002, *Mon. Not. R. Astron. Soc.*, 330, 778
Wilson, C. P. 1975, *Astron. J.*, 80, 175
Woodley, K. A., Goldsbury, R., Kalirai, J. S., et al. 2012, *Astron. J.*, 143, 50
Wybo, M. & Dejonghe, H. 1995, *Astron. Astrophys.*, 295, 347
Wybo, M. & Dejonghe, H. 1996, *Astron. Astrophys.*, 312, 649
Yan, L. & Cohen, J. G. 1996, *Astron. J.*, 112, 1489
Zaggia, S. R., Capaccioli, M., Piotto, G., & Stiavelli, M. 1992, *Astron. Astrophys.*, 258, 302
Zocchi, A., Bertin, G., & Varri, A. L. 2012, *Astron. Astrophys.*, 539, A65
Zonoozi, A. H., Küpper, A. H. W., Baumgardt, H., et al. 2011, *Mon. Not. R. Astron. Soc.*, 411, 1989

List of Publications

As of April 2014

Refereed publications

- "Rotating globular clusters"
  Bianchini, P., Varri, A. L., Bertin, G., **Zocchi, A.**, *Astrophys. J.*, 772, 67-85 (2013)
  (Chapter 6)

- "On the density profile of the globular cluster M92"
  Di Cecco, A., **Zocchi, A.**, Varri, A. L., Monelli, M., Bertin, G., Bono, G., Stetson, P. B., Nonino, M., Buonanno, R., Ferraro, I., Iannicola, G., Kunder, A., Walker, A. R., *Astron. J.*, 145, 103-113 (2013)
  (Chapter 5)

- "A dynamical study of Galactic globular clusters in different relaxation conditions"
  Zocchi, A., Bertin, G., Varri, A. L., *Astron. Astrophys.*, 539, A65 (2012)
  (Chapter 4)

Publications in conference proceedings

- "The flattening of globular clusters: internal rotation or velocity anisotropy?"
  Bianchini, P., Varri, A. L., Bertin, G., **Zocchi, A.**, *Memorie della Società Astronomica Italiana*, 84, 183 (2013)